

Manipulation of Photoluminescence
from
Semiconductor Nanocrystals
by
Bandgap Engineering and Surface Plasmons

Dissertation

zur Erlangung des Doktorgrades

des Fachbereichs Chemie
der Universität Hamburg

vorgelegt von

Xuedan Ma

Hamburg, 10. Juni 2011

This page is intentionally left blank.

Gutachter der Dissertation

Prof. Dr. Alf Mews (Hamburg)

Prof. Dr. Horst Weller (Hamburg)

Gutachter der Disputation

Prof. Dr. Alf Mews (Hamburg)

Prof. Dr. Marc H. Prosenc (Hamburg)

Dr. Hauke Heller (Hamburg)

Datum der Disputation

22. Juli 2011

This page is intentionally left blank.

Abstract

Optical behaviors of semiconductor nanocrystals (NCs) strongly depend on the trap states on the nanocrystal surface or in their surroundings. Excited charge carriers can possibly be captured by such trap states, leading to the so-called fluorescence intermittency (or blinking) of NCs. To develop a further understanding of these optical properties and modify the photoluminescence (PL) of the NCs, two different strategies were applied in this work.

In the first approach, NC surfaces were passivated by the growth of semiconductor shells around the core NCs. Depending on the relative alignment of the band structures in the cores and shells, two different types of core-shell NCs were synthesized. The type I core-shell NCs studied here were multishell NCs, composed of CdSe cores coated with nominally 2 monolayers (MLs) CdS, 3.5 MLs $\text{Cd}_{0.5}\text{Zn}_{0.5}\text{S}$ and 2 MLs ZnS shells. Due to these protective wider bandgap semiconductor shells, the synthesized multishell NCs exhibited greatly enhanced photostability and quantum efficiency as compared to the core CdSe NCs. On the other hand, using CdTe NCs as cores, type II CdTe/CdSe and CdTe/CdS core-shell NCs were synthesized. In contrast to the type I core-shell NCs, charge carriers in type II core-shell NCs are spatially separated. Calculations of the electron and hole wavefunctions showed that in these type II core-shell NCs, holes were mainly located in the CdTe cores, whereas the electrons were either located in the CdSe shells in the case of CdTe/CdSe NCs or delocalized over the whole NCs in the case of CdTe/CdS NCs. In both type II core-shell NCs, a dramatic increase in the lifetime and a red shift of the PL wavelength were observed with the growth of shells.

In the second approach, PL properties of NCs were modified by the surface plasmons of nearby metallic nanostructures. The first type of metallic nanostructure used in this work was self-assembled AuNP film. To tune the distance between the AuNP films and NCs, homogeneous silica shells with different thicknesses were grown on the surface of CdSe multishell NCs. Increased PL intensity, decreased PL lifetime, strong blinking suppression, and appearance of gray states of the NCs coupled to AuNP films were observed by measuring the NCs at the single particle level. These observations can be explained by the metallic nanostructure induced change of the excitation and recombination rates in NCs in the framework of a simple model. To further correlate the PL properties of NCs with the relative geometries of the NCs and metallic nanostructures, hybrid nanostructures comprised of individual NCs and AuNPs were prepared and investigated with confocal microscopy and transmission electron microscopy. Similarly, an increase in the PL intensity, a decrease in the PL lifetime, and blinking suppression were observed for the NCs in the close vicinity of AuNPs. In addition, an increase of the recombination rate with the decrease of the silica shell thickness was observed, and the experimental data was compared with the simulation results from the Gersten-Nitzan model and the

3D FDTD method.

Zusammenfassung

Die optischen Eigenschaften von Halbleiter-Nanokristallen sind stark abhängig von Ladungsträger-Zuständen an der Nanokristalloberfläche oder in der Nanokristallumgebung. Angeregte Ladungsträger können in solchen Zuständen gefangen werden, was wiederum zum sogenannten Blinken von Nanokristallen, dem zeitliche Wechseln zwischen Emission und Nicht-Emission von Licht, führen kann. Um ein tieferes Verständnis von diesen optischen Eigenschaften zu erlangen und um die Photolumineszenzeigenschaften von Nanokristallen gezielt zu modifizieren zu können, wurden in der vorliegenden Arbeit zwei unterschiedliche Strategien verfolgt.

Im ersten Ansatz wurden die Nanokristalloberflächen durch das Wachstum von Schalen aus Halbleitermaterialien um den Kern des Nanokristalls passiviert. Abhängig von der relativen Anordnung der Bandstrukturen der Kern- und Schalematerialien wurden zwei unterschiedliche Arten von Kern-Schale-Teilchen synthetisiert. Bei den hier untersuchten Typ I Kern-Schale-Nanokristallen handelt es sich um Mehrschalenschichtenstrukturen aus einem CdSe-Kern beschichtet mit Schalen von nominell 2 Monolagen (ML) CdSe, 3.5 ML Cd_{0.5}Zn_{0.5}S und 2 ML ZnS. Diese schützenden Schalen aus Halbleitermaterialien größerer Bandlücke führten zu einer stark erhöhten Photostabilität und Quantenausbeute der Kern-Schale-Nanokristalle verglichen mit reinen Kern-Nanokristallen. Des Weiteren wurden Typ II CdTe/CdSe und CdTe/CdS Kern-Schale-Nanokristalle synthetisiert. Im Gegensatz zum Fall der Typ I Kern-Schale-Nanokristalle sind Ladungsträger in den Typ II Kern-Schale-Nanokristallen räumlich getrennt. Berechnungen der Elektron- und Lochwellenfunktionen zeigten dass in den Typ II Kern-Schale Nanokristallen die Löcher vorwiegend in den CdTe-Kernen lokalisiert sind, während die Elektronen entweder, im Fall von CdTe/CdSe-Nanokristallen, in der CdSe-Schale lokalisiert waren, oder, im Fall von CdTe/CdS-Nanokristallen, über dem gesamten Nanokristall delokalisiert waren. Für beide Arten von Typ II Kern-Schale-Nanokristallen wurde einhergehend mit dem Wachstum der Schalen eine drastische Zunahme der Lebensdauer und eine Rotverschiebung der Photolumineszenzwellenlänge beobachtet.

Im zweiten Ansatz wurden die Photolumineszenzeigenschaften von Nanokristallen durch Oberflächenplasmonen in benachbarten Metallnanostrukturen modifiziert. In dieser Arbeit wurden zunächst selbstorganisierte Filme von Gold-Nanopartikeln als metallische Nanostrukturen verwendet. Um den Abstand zwischen dem Film und Nanokristallen gezielt einzustellen, wurden CdSe-Mehrschalenschichten-Nanokristalle mit homogenen Schalen unterschiedlicher Dicke aus SiO₂ ummantelt. In Messungen an einzelnen, mit den Gold-Nanopartikeln wechselwirkenden Nanokristallen wurde eine erhöhte Photolumineszenzintensität, eine Verringerte Photolumineszenzlebensdauer, eine Unterdrückung des Blinkens sowie das Auftreten sogenannter Grau-Zustände beobachtet. Diese Beobachtungen können innerhalb eines einfachen Modells durch die von den metallischen Nanostrukturen induzierte Änderung der Anregungs- und

Rekombinationsraten der Nanokristalle erklärt werden. Um eine weitergehende Korrelation zwischen den Photolumineszenzeigenschaften von Nanokristallen und den relativen Geometrien der Nanokristalle und Metall-Nanostrukturen zu erlangen, wurden hybride Nanostrukturen bestehend aus einzelnen Nanokristallen und Gold-Nanopartikeln hergestellt und mittels konfokaler Mikroskopie und Transmissionselektronenmikroskopie untersucht. Wiederum wurden für Nanokristalle in naher Umgebung zu Gold-Nanopartikeln eine Erhöhung der Photolumineszenzintensität, eine Reduktion der Photolumineszenzlebensdauer und eine Unterdrückung des Blinkens beobachtet. Zusätzlich wurde eine Erhöhung der Rekombinationsrate für Abnehmende SiO₂-Schalendicke beobachtet, und die experimentellen Daten wurde mit der Simulation Ergebnisse aus dem Gersten-Nitzan Modell und die 3D FDTD-Methode verglichen.

Table of Contents

Abstract	I
Table of Contents	V
List of Figures	VII
Abbreviations	XI
1 Introduction	1
2 Theoretical background	3
2.1 Synthesis of semiconductor nanocrystals and gold nanoparticles	3
2.1.1 General growth mechanism	3
2.1.2 Synthesis of II-VI semiconductor nanocrystals	4
2.1.3 Synthesis of gold nanoparticles	6
2.2 Electronic and optical properties of semiconductor nanocrystals	7
2.2.1 Crystal structures	7
2.2.2 Electronic structures	7
2.2.3 Size-dependent optical properties	11
2.2.4 Blinking and power law	16
2.2.5 Recombination dynamics	18
2.2.6 Wavefunction engineering – core-shell heterostructures	21
2.3 Electronic and optical properties of gold nanoparticles	23
2.3.1 Electronic structures	23
2.3.2 Dielectric functions	23
2.3.3 Interaction of light with gold nanoparticles	25
2.4 Interaction between semiconductor nanocrystals and metals	29
2.4.1 Enhancement or quenching? – General considerations	29
2.4.2 Interaction mechanism – different theoretical models	30
3 Experimental Setup	37
3.1 Principles of confocal microscopy	37
3.1.1 Confocal microscopy	37
3.1.2 Signal-to-noise ratio	38
3.1.3 Point-spread function and resolution	40
3.2 Experimental setup	43
3.2.1 Illumination part	44
3.2.2 Detection part	56

Table of Contents

4	Core-shell semiconductor nanocrystals	65
4.1	Type I core-shell semiconductor nanocrystals	65
4.1.1	Experimental	65
4.1.2	Results and discussion	67
4.2	Type II core-shell semiconductor nanocrystals	70
4.2.1	Experimental	70
4.2.2	Results and discussion	71
5	Semiconductor nanocrystals on gold nanoparticle films	79
5.1	Samples: preparation and characterization	79
5.1.1	Silica coated semiconductor nanocrystals	80
5.1.2	Self-assembled gold nanoparticle films	83
5.1.3	Sample preparation for optical measurements	85
5.2	Optical measurements of individual semiconductor nanocrystals . . .	86
5.3	Theoretical interperation	93
6	Semiconductor nanocrystals attached to gold nanoparticles	101
6.1	Samples: preparation and characterization	101
6.1.1	Silica coated gold nanoparticles	102
6.1.2	Sample preparation	106
6.2	Optical measurements of individual semiconductor nanocrystals . . .	108
6.3	Correlation between optical and structural properties	113
7	Summary and outlook	123
	Appendix	i
	Bibliography	v
	Acknowledgements	xvii

List of Figures

2.1	Growth rate and size distribution	4
2.2	The crystalline structures of zinc blende and wurtzite structures	7
2.3	Density of states for various dimensionalities	8
2.4	Semiconductor band structures	11
2.5	Discrete energy levels in semiconductor nanocrystals	13
2.6	Auger ionization and recombination in semiconductor nanocrystals	17
2.7	Recombination processes in semiconductor nanocrystals	18
2.8	Band structure of core-shell NCs	21
2.9	Lattice strain in CdSe-ZnS core-shell NCs	22
2.10	Band Structure of gold	23
2.11	Dielectric function of gold	25
2.12	Extinction, scattering, and absorption spectra calculated from Mie theory	28
2.13	Comparison between spectra calculated from FDTD and Mie theory	29
2.14	Lifetime of fluorophores as a function of distance from a Au mirror in the CPS model	31
2.15	Geometry of the Gersten-Nitzan model	32
2.16	Lifetime vs. distance calculated from the Gersten-Nitzan model and CPS model	33
2.17	Layout of monitors used in the FDTD simulation	35
3.1	Principles of confocal microscopy	38
3.2	Calculation of the point spread function	41
3.3	Setup of the scanning confocal microscope	44
3.4	Total internal reflection and numerical aperture of a fiber	45
3.5	Beam shape after leaving a diode laser	47
3.6	Coupling of a fiber to a laser beam coupler/collimator	48
3.7	Transmission characteristics of different filters	51
3.8	Three main types of beamsplitters	52
3.9	Finite corrected and infinity corrected optical systems	54
3.10	Schematic of the action of a piezo actuator	55
3.11	Quantum efficiency of SPADs	57
3.12	Principle of a spectrograph	58
3.13	Diffraction grating schematics	59
3.14	P-type MOS capacitor and potential well	62
3.15	The bucket analogy used to describe CCD operation	62
3.16	Charge transfer in CCD	63

List of Figures

4.1	Reaction setup	66
4.2	Absorption and PL spectra of CdSe and multishell NCs	67
4.3	TEM images of CdSe and multishell NCs	68
4.4	scanned PL images of CdSe core and multishell NCs	68
4.5	Time traces from individual CdSe core NC and multishell NC	69
4.6	Decay curve from a multishell NC	70
4.7	Relative positions of valence and conduction band edges in different II-VI semiconductor materials	71
4.8	Absorption and PL spectra of CdTe/CdSe core-shell NCs	72
4.9	Quantum efficiency of CdTe/CdSe core-shell NCs	72
4.10	Decay curves and lifetimes of CdTe/CdSe core-shell NCs	73
4.11	Wavefunctions in CdTe/CdSe core-shell NCs	74
4.12	Absorption and PL spectra of CdTe/CdS core-shell NCs	75
4.13	Scanned PL images of CdTe/CdS core-shell NCs	75
4.14	Time traces of CdTe/CdS core-shell NCs	76
4.15	Decay curves of CdTe/CdS core-shell NCs	77
4.16	Wavefunctions of CdTe/CdS core-shell NCs	78
5.1	SiNCs synthesized from different amounts of NCs	80
5.2	SiNCs synthesized from different amounts of TEOS	81
5.3	Surface modification of SiNCs with APS	81
5.4	Surface modification of SiNCs with THPAP	82
5.5	SiNCs with core NCs or silica shells dissolved	82
5.6	Absorption and emission spectra of SiNCs and their photobrightening .	83
5.7	Preparation of AuNP films	83
5.8	Extinction spectrum and size distribution of AuNPs	84
5.9	Absorption spectra and SEM images of AuNP films	85
5.10	AFM images of Au526 film	85
5.11	Scanned PL images of SiNCs on different substrates	86
5.12	PL spectra of individual SiNCs	87
5.13	Time traces and count rate histograms of SiNCs on different substrates	88
5.14	Histograms of PL intensity of SiNCs on different substrates	88
5.15	On- and off-time probability density	89
5.16	PL decay curves and rate distributions	90
5.17	Lifetime distributions of SiNCs on different substrates	91
5.18	PL intensity – lifetime distributions	92
5.19	Extinction spectrum of Au526 from FDTD simulation	93
5.20	Extinction spectrum of Au590 from FDTD simulation	94
5.21	Local field enhancement factor	95
5.22	Radiative decay rates calculated from FDTD method and Gersten- Nitzan model	97
5.23	Local electric field intensity distribution close to a dipole	97
5.24	Radiative decay rates calculated from FDTD method and CPS model .	98
5.25	Schematic of the theoretical model	99
6.1	TEM images of different sized AuNPs	103

6.2	TEM images of AuNPs before and after purification	103
6.3	Extinction spectra of different sized AuNPs in water	104
6.4	TEM images of AuNP@SiO ₂ synthesized from different conditions . . .	105
6.5	TEM images of AuNPs coated with polymers	105
6.6	TEM images of AuNP@SiO ₂ surface modified with APS and PAH . . .	106
6.7	TEM images and PL spectra of NCs	107
6.8	TEM images and PL spectra of NWs	108
6.9	Correlation between optical and TEM measurements	109
6.10	Time traces and CRHs of individual NCs attached to AuNPs	110
6.11	TEM images of Au@SiO ₂ and AuNP dimer	111
6.12	Histograms from isolated NCs	112
6.13	Decay curves and rate distributions of NCs with and without AuNPs .	113
6.14	Local electric field enhancement factor distributions	114
6.15	Average lifetime and normalized decay rate vs. silica shell thickness .	115
6.16	Orientation of dipole	116
6.17	Distance dependent lifetimes calculated from 3D FDTD and Gersten- Niztan model	118
6.18	Local electric field intensity enhancement factor distribution near a linear dipole	119
6.19	Silica shell thickness dependent lifetimes calculated from experiments and FDTD simulations	119
6.20	On-time fraction of NCs attached to AuNP@SiO ₂	120

This page is intentionally left blank.

Abbreviations

2D	2 dimensional
3D	3 dimensional
AFM	Atomic Force Microscopy
CCD	Charge Coupled Device
CdS	Cadmium Sulfide
CdSe	Cadmium Selenide
CdTe	Cadmium Telenide
cw	Continuous-wave
DOS	Density of States
EDX	Energy Dispersive X-Ray
eV	Electron Volt
FWHM	Full width at Half Maximum
HRTEM	High Resolution Transmission Electron Microscopy
IRF	Instrument Response Function
ML	Monolayer
NA	Numerical Aperture
NC	Semiconductor Nanocrystal
NP	Nanoparticle
ns	Nanosecond
ODE	octadecene
PL	Photoluminescence
ps	Picosecond
PSF	Point Spread Function
QE	Quantum Efficiency
rpm	Round per Minute
SEM	Scanning Electron Microscopy
SILAR	Successive Ion Layer Adsorption and Reaction
SNR	Signal-to-Noise Ratio
SPAD	Single-Photon Avalanche Diode
TBP	tributylphosphine
TCSPC	Time-Correlated Single Photon Counting
TEM	Transmission Electron Microscopy
TEOS	tetraethyl orthosilicate
TOP	trioctylphosphine
TOPO	trioctylphosphine oxide
TTTR	Time-Tagged Time-Resolved
WZ	Wurtzite
ZB	Zinc Blende
ZnS	Zinc Sulfide

This page is intentionally left blank.

Chapter 1

Introduction

Semiconductor nanocrystals (NCs), also known as quantum dots, are small crystalline semiconductor materials with sizes on the order of a few nanometers. In this size range, the NCs are smaller than the bulk Bohr exciton diameter. As a result, one of the major features of the NCs is the quantum confinement effect, which makes the optical and electronic properties of the NCs determined not only by their compositions, but also by their sizes and shapes. For this reason, NCs represent a new class of materials with size dependent electronic and optical properties.

Decrease of the NC size also leads to a high surface-to-volume ratio. The incompletely bonded atoms on the surface of the NCs act as surface-related trap states, by which charge carriers can be trapped and consequently the overlap of electron-hole wavefunctions are reduced, resulting in the reduction of the photoluminescence (PL). In addition, although the theoretical mechanism remains unclear, observation of PL blinking at the single NC level is commonly attributed to the temporal trap of charge carriers by these trap states. Hence, to develop further applications of NCs, it becomes crucial to eliminate the influence from these surface trap states.

One important strategy is to improve the surface passivation of the NCs by modifying the surface ligands of the NCs or by growing a shell of a second semiconductor around core NCs, resulting in the so-called core-shell NCs. Especially in the second manner, by the careful choice of the core and shell materials, not only the PL intensity and stability of the NCs can be significantly improved, but also different electronic structures accompanying unique PL properties can be obtained. To specify, overcoating core NCs with epitaxial layers of shell materials with wider bandgap than that of the core NCs can form type I core-shell NCs. In this type of NCs, both electrons and holes are confined in the cores. The shells passivate the NC surface, enhancing the photostability. Alternatively, when core NCs are coated with shell materials of which either the valence band (VB) edge or the conduction band (CB) edge is located in the bandgap of the cores, the charge carriers are spatially separated between the core and the shell. This type of NCs is referred to as type II core-shell NCs. Since the corresponding energy gap is determined by the energy separation between the CB edge of one semiconductor and the VB edge of the other, red shift of the PL wavelength by shell growth is observed. Therefore, it is possible to manipulate the PL wavelength of the type II core-shell NCs towards spectral ranges (e.g. the near-infrared range) that would otherwise not be available with a single material. In addition, due to the reduced overlap of electron-hole wavefunc-

tions, the PL lifetime of the NCs is strongly prolonged. This property makes type II core-shell NCs suitable for photovoltaic technologies.

Another strategy to manipulate the PL of NCs is based on the interactions between NCs and nearby metallic nanostructures. Under certain circumstances, surface plasmons can be generated in metallic nanostructures and have complex effects on the PL of nearby NCs. An extensive search of the literature reveals that PL from NCs can either be enhanced or quenched by nearby metallic nanostructures, depending on several parameters including the geometry, size, and composition of the metallic nanostructures, the distance between the NCs and the metals, as well as the spectral overlap between the emission spectrum of the NCs and the surface plasmon resonance spectrum of the metallic nanostructure. To understand the interaction mechanism, it is necessary to eliminate the effects of ensemble averaging. Single NC spectroscopy has been extensively employed in the observation of many fundamental phenomena of NCs, such as blinking and spectral diffusion of single NCs. Therefore, in this study, confocal microscopy has been used to investigate NCs at the single particle level. Precise analysis of the exciton-plasmon interaction also requires detailed structural information about the investigated system. In this study, different metallic nanostructures are carefully designed to modify the PL of NCs and characterized by various technologies, including SEM, TEM, and AFM. By combining the structural information with the optical properties of individual NCs measured with a confocal microscope, mechanism of the interaction is studied in detail.

This work is aimed at the manipulation of PL from NCs by chemical coating of shell materials on the NCs and by surface plasmons from metallic nanostructures. It includes three main parts. The first part includes chapter 2 and chapter 3, where the fundamental knowledges used in this study and information about the home-built confocal microscope are introduced. The second part is chapter 4, in which synthesis procedures of type I and type II core-shell NCs are established. Their properties are discussed both at the ensemble and single NC level. The last part consists of chapter 5 and chapter 6, mainly about the manipulation of PL from NCs by surface plasmons in nearby metallic nanostructures. In chapter 5, influence of gold nanoparticle (AuNP) films prepared by the self-assembly of AuNPs on glass covers is studied. When the distance between NCs and AuNP films was adjusted to 10 nm, enhanced PL intensity, decreased lifetime, and gray states from the NCs can be observed. In addition, blinking of the individual NCs was also suppressed. These phenomena are explained on the basis of a simple model. In order to precisely correlate the geometry of the metallic nanostructures with the optical properties of NCs, hybrid nanostructures comprising individual NCs and AuNPs were prepared and investigated by both TEM and optical microscopy, as introduced in chapter 6. These NCs also showed enhanced PL intensity. In addition, distance dependent lifetime reduction of the NCs was observed, which was compared with the calculations from the Gersten-Nitzan model and the 3D FDTD method.

Chapter 2

Theoretical background

In order to understand current theories addressing the optical properties of NCs and AuNPs, as well as to interpret our experimental results, this chapter will describe the theoretical backgrounds used in this work. To start with, synthetic methods of colloidal NCs and AuNPs will be briefly reviewed. Next, after introducing the basic crystal and electronic structures, the optical properties of NCs with emphasis on blinking and recombination dynamics will be described in detail. The third part deals with the electronic and optical properties of AuNPs, with emphasis on the different methods of describing the optical behaviors of AuNPs under illumination. Having established the basic knowledge of NCs and AuNPs, the last part will discuss about the current understanding of the interaction mechanism between the two.

2.1 Synthesis of semiconductor nanocrystals and gold nanoparticles

The ultimate technique for the fabrication of nanoscale materials should be able to control the size, shape, and monodispersity of the nanostructures. So far, the variety of physical and chemical methods used to prepare those nanostructures can be divided into two main classifications [Ban04]: the top-down approaches, mainly including lithography which is limited to structures with dimensions on the order of tens of nanometers, and the bottom-up approaches, including molecular beam epitaxy (MBE) deposition and colloidal synthesis. In this work, only colloidal nanostructures are studied.

2.1.1 General growth mechanism

In theory the growth process of colloidal particles involves at least two stages: the nucleation stage and the particle growth stage. Although in real reactions the different stages coexist and it is difficult to isolate each stage for independent study, the growth mechanism for each stage is usually analyzed separately.

Following the classical model of LaMar and Dinegar [LaM50], in a diffusion controlled system, the growth rate as a function of particle size is given by [Sug87,

Rog08]

$$\frac{dr}{dt} = \frac{2\sigma DC_\infty}{d_m^2 k_B T} \cdot \frac{1}{r} \cdot \left(\frac{1}{r^*} - \frac{1}{r} \right), \quad (2.1)$$

where σ is the surface tension, D the diffusion constant of reaction monomers, C_∞ the vapour pressure of a flat surface, d_m the density of monomers in the crystal, and T the temperature. In particular, r^* denotes the critical size when the growth is in equilibrium (zero growth rate). For particles with sizes smaller than r^* , the growth rate is negative and they will dissolve, whereas for those particles with sizes larger than r^* the rate is positive and they will continue growing. Fig. 2.1 (red curve) shows the dependence of the growth rate on the size of the particle. Obviously, there is a maximum rate at the radius of $2r^*$.

Sugimoto [Sug87, Kun05] further suggested that the size distribution of the particles is determined by

$$\frac{d^2r}{dt^2} \propto \frac{1}{r^2} \left(\frac{2r^* - r}{r^*r} \right) \frac{dr}{dt}. \quad (2.2)$$

The right side of the above equation is also plotted in Fig. 2.1 (blue curve). When $r > 2r^*$, $\frac{d^2r}{dt^2}$ is negative, and the size distribution will be narrow. This conclusion can be interpreted in this way: if the radii of the particles in the solution are larger than $2r^*$, then from the growth rate curve in Fig. 2.1 we can tell that the smaller particles will grow faster than the larger ones. Therefore, the size distribution becomes narrower and this is called the size focusing regime. In contrast, when the particle sizes are smaller than $2r^*$ (but still larger than r^*), $\frac{d^2r}{dt^2}$ becomes positive and the size distribution increases. This is called defocussing or Ostwald ripening. In this regime, the smaller particles will typically shrink and eventually disappear, while the larger ones continue growing.

However, in a real reaction, the critical size r^* changes with the concentration of free monomers in the solution. In a closed system (no monomers added during the reaction), the monomer concentration decreases with time and consequently r^* increases. To prevent the system from entering into the defocussing regime ($r^* < r < 2r^*$) and obtain particles with uniform sizes, in some cases [Pen98] repeated injections of fresh monomers into the reaction system are necessary.

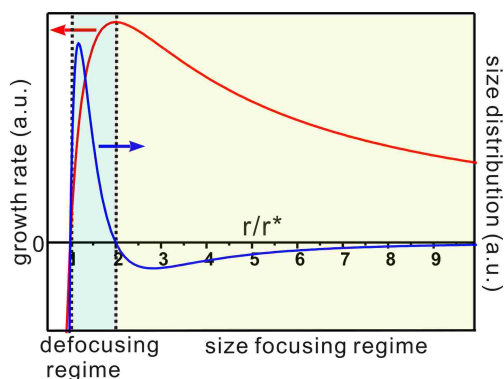


Figure 2.1: Growth rate (red curve) and size distribution (blue curve) as a function of particle size.

2.1.2 Synthesis of II-VI semiconductor nanocrystals

Until now, many different methods have been explored for the controlled synthesis of colloidal II-VI NCs. Depending on the medium in which NCs are synthesized, those synthetic approaches can be classified into three general groups: in organic phase [Mur93], in aqueous solvents [Che86, Rog00, Rog07], and in normal/inverse

2.1. Synthesis of semiconductor nanocrystals and gold nanoparticles

micelles [McB20, Pil00]. Although the latter two methods are advantageous in the sense that reactions are carried out under mild conditions and that post-synthesis processing of the NCs in aqueous solvents can be performed, the relatively limited availability and wide size distributions of those NCs have limited their applications. Using organic phase provides the possibility to tune the reaction temperature over a wide range and the synthesized NCs usually have better crystalline structures and PL qualities. In the following discussion, the focus will therefore be on NCs synthesized in an organic phase.

One of the most important methods in the preparation of II-VI NCs is proposed by Murray et al. in 1993 [Mur93]. In this method, organometallic precursors of cadmium (dimethyl cadmium, CdMe_2) and trioctylphosphine selenide (TOP:Se) are injected into a hot ($280 - 300^\circ\text{C}$) coordinating solution of trioctylphosphine oxide (TOPO). Subsequent size-selective precipitation reduces the particle size distribution and removes impurities. The method is highly reproducible and the synthesized CdSe NCs have high quality in terms of crystallinity and uniformity. Later, this method was further improved by Katari et al. [Kat94], who replaced TOP with tributylphosphine (TBP) and avoided Ostwald ripening.

However, one of the limitations of the organometallic approaches is the use of organometallic compounds, such as CdMe_2 , which is highly hazardous, especially at high temperatures. Therefore, access to the high quality yet expensive CdSe NCs was once limited to a dozen groups in the world, motivating researchers in the field to explore alternative methods. Peng and coworkers introduced the greener approach, which replaces the CdMe_2 with cadmium oxide (CdO) and other inorganic cadmium salts [Pen01, Qu01], and the coordinating solvents (such as TOPO) with non-toxic, non-coordinating solvents (such as octadecene, ODE) [Yu02, Bat02]. Despite the striking simplicity of the method, it produces NCs with crystallinity and optical properties at least comparable to those synthesized through the traditional organometallic approaches. In addition, the accessible size range of NCs from the greener approach is significantly larger.

Another alternative method to the organometallic approach is the single precursor approach. Here, a single compound containing both anionic and cationic components required within the NCs as precursors is used, such as alkylthiocarbamate complexes. A comprehensive review of this topic is given by Ref. [Mal01].

In order to further enhance the PL quantum efficiency and photostability, or to tune the emission wavelength to near-infrared range, the NC cores are commonly passivated with layers of inorganic semiconductor materials to form core-shell NCs. Early reports of this kind of core-shell architecture include CdS on CdSe [Pen97] and ZnS on CdSe [Hin96, Dab97]. Later, to overcome the problem of lattice mismatch between the core and shell materials yet still being able to passivate the core NCs, synthesis of highly luminescent core-shell-shell NCs were reported by several groups [Rei03, Tal04, Xie05]. During the subsequent shell growth onto the core NCs, it is critical to prevent nucleation of the shell material as well as the ripening of the core NCs. Typically, low precursor concentrations and reaction temperatures are used to avoid this. In real reactions, this is achieved by adding the calculated amount of shell precursors slowly (e.g. by syringe pumps) at temperatures lower than 150°C . With the introduction of the successive ion layer adsorption and reaction (SILAR)

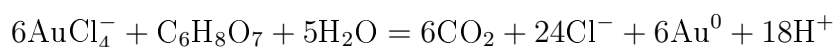
method [Li03, Xie05], which is based on the formation of one monolayer (ML) at a time by alternating injections of cationic and anionic precursors, it is possible to precisely control the shell thickness without loss of NC size monodispersity. Some “giant” NCs with very thick shell (> 10 ML) have been successfully synthesized with this method and exhibit fundamentally different optical properties [Che08, Mah08]. Detailed properties of core-shell NCs will be discussed in section 2.2.6.

NCs synthesized in organic phase are essentially capped with non-polar ligands (such as TOPO, TOP), making them insoluble in water. Hence, to make them compatible with biological manipulations, various strategies, mainly including surface ligand exchange, encapsulation of the NCs within amphiphilic polymers, and formation of silica shells on NC surface, have been used to disperse these hydrophobic NCs into water [Med05].

2.1.3 Synthesis of gold nanoparticles

Due to the long tradition of their applications, a wealth of approaches are currently available for the syntheses of colloidal gold nanoparticles (AuNPs) [Dan04]. Here, the few most widely used methods will be reviewed.

One of the most popular protocols for synthesizing AuNPs was first introduced in 1951 by Turkevich et al. [Tur51]. In this method, HAuCl_4 is reduced by sodium citrate through the following reaction [Hu06]:



The resulting citrate-stabilized AuNPs usually have diameters of 10 – 20 nm. This method was further refined to produce AuNPs with sizes ranging from 15 to 150 nm by controlling the ratio of citrate to HAuCl_4 [Fre73]. However, large AuNPs synthesized with this method usually have a broad size distribution.

The reproducible synthesis of large, uniform AuNPs with pre-chosen size had remained a difficult task before the introduction of the seed-mediated growth method [Bro00, Jan01, RF06]. This method uses small AuNPs (e.g. 12 nm in size) as seeds and allows the synthesis of monodisperse, spherical AuNPs up to 200 nm simply by varying the ratio of seed to metal salt and applying multiple growth steps.

In general, most of the large AuNPs reported in literature are not single crystals [Hu06]. Instead they are multiply twinned¹ particles with quasispherical, polyhedral morphologies.

On the other hand, to produce small AuNPs (< 10 nm), important methods include the delicate Schmid method [Sch81], with which monodisperse Au clusters with diameters of 1.4 ± 0.4 nm can be produced, and the widely-used Brust-Schiffrin method [Bru94], which generates hydrophobic AuNPs capped with thiol ligands and 1 – 3 nm in size.

¹Crystal twinning refers to the phenomena that two separate crystals share a common crystallographic plane.

2.2 Electronic and optical properties of semiconductor nanocrystals

2.2.1 Crystal structures

Depending on the reaction conditions, II-VI semiconductor nanocrystals can grow in the form of either zinc blende (ZB) or wurtzite (WZ) structures. As shown in Fig. 2.2, the ZB structure is a face centered cubic (FCC) structure¹ with the atoms of the two elements located at the coordinates $(0, 0, 0)$ and $(a/4, a/4, a/4)$, respectively (a is the lattice constant), and the stacking sequence is ABCABC. The WZ structure is a hexagonal close packed structure based on the stacking sequence of ABAB, and coordinates of the two kinds of atoms are $(0, 0, 0)$ and $(2a/3, a/3, a/2)$. Compared to the ZB structure, the WZ structure has lower symmetry.

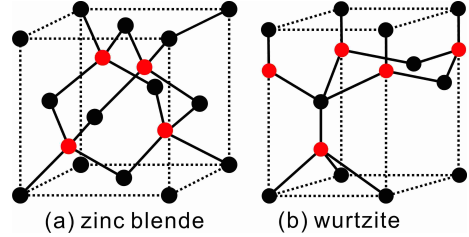


Figure 2.2: The crystalline structures of zinc blende and wurtzite structures.

One important experimental parameter that can influence the NC structure is the reaction temperature. At low reaction temperatures, formation of ZB structure is preferential, whereas at high temperatures the NCs usually grow in the WZ structure [Yeh92, Wei00a]. Additionally, the bonding strength and steric effects of the ligands during the reaction also influence the resultant crystal structures [Yu03b].

On the other hand, the structures of very small clusters (e.g., CdSe clusters with sizes smaller than 2 nm) are usually described with the concept of magic number of atoms, details about which can be found in Ref. [Sch86, Sch87].

2.2.2 Electronic structures

Density of states. As a first approximation, electrons in a bulk material can be considered as “free”, meaning that the interactions between the electrons themselves and between the electrons and crystal lattice can be neglected. However, with the decrease of size, the motion of electrons is restricted and the corresponding energy levels become discrete. In order to obtain a more quantitative view, the concept of density of states (DOS), which is defined as the number of available electronic states per unit interval of wavenumbers [Sch04], is introduced. For a three-dimensional bulk material, the DOS is given by [Kun05]

$$\rho_{3D}(E) = \frac{\sqrt{2}m^{*3/2}}{\pi^2\hbar^3}\sqrt{E}, \quad (2.3)$$

with m^* being the effective mass of electrons or holes, and the energy E is measured from the bottom of the conduction band (CB) for electrons and from the top of the valence band (VB) for holes. Notice here $\rho_{3D}(E)$ is a continuous square-root function

¹Also known as the cubic close packed (CCP) structure.

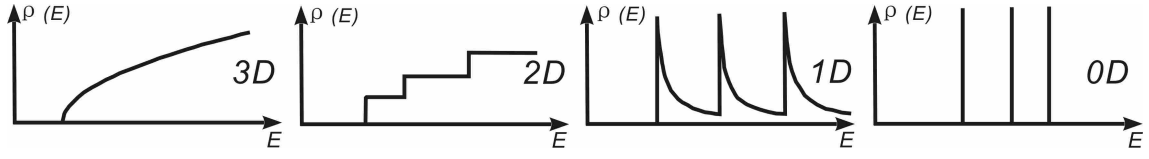


Figure 2.3: Schematic of density of states for various dimensionalities.

of energy. In the case of two- and one-dimensional structures¹, the corresponding DOS are given by

$$\rho_{2D}(E) = \frac{m^*}{\pi \hbar^2} \sum_{n_x, y, z} \Theta(E - E_{n_x, y, z}) \quad (2.4)$$

and

$$\rho_{1D}(E) = \frac{\sqrt{2m^*}}{\pi \hbar} \sum_{n_x, n_y} \frac{\Theta(E - E_{n_x, n_y})}{\sqrt{E - E_{n_x, n_y}}} \quad (2.5)$$

respectively. Here $E_{n_x, y, z}$ is the confinement energy along the x, y, and z directions, whereas $\Theta(E - E_{n_x, y, z})$ is the Heavyside function defined by

$$\Theta(E - E_{n_x, y, z}) = \begin{cases} 0 & \text{if } E < E_{n_x, y, z}, \\ 1 & \text{if } E > E_{n_x, y, z}. \end{cases} \quad (2.6)$$

Further reduction in dimensionality ends up in zero-dimensional structures (quantum dots). The DOS of a quantum dot is characterized by a series of discrete δ -functions. Fig. 2.3 schematically depicts the evolution of the DOS as the dimensionality is reduced.

Quantum confinement. In a semiconductor material, excitons are produced by pairing of an electron (from the conduction band) and a hole (from the valence band) due to the Coulomb interaction. As discussed above, due to the finite size of NCs, their energetic states differ dramatically from those of the corresponding bulk material. In order to evaluate the impact of the size, the Bohr radius of a particle² is commonly utilized as a convenient length scale. It is defined as

$$a_B = \varepsilon \frac{m_0}{m^*} a_0, \quad (2.7)$$

where ε represents the dielectric constant of the material, m_0 and a_0 the electron mass and Bohr radius, respectively, and m^* the effective mass of the particle. Because of the interaction of electrons/holes with host atoms and other electrons and holes, typically the effective mass of an electron/hole in a semiconductor differs from the mass of a free electron/hole. Table 2.1 lists the effective mass, exciton Bohr radius and bandgap of the semiconductor materials used in this work.

¹The so called “quantum wells” and “quantum wires”.

²Here the term “particle” refers to electrons, holes and excitons.

2.2. Electronic and optical properties of semiconductor nanocrystals

Table 2.1: Important parameters for semiconductor materials used in this work [Mad99].

	electron effective mass (m_0)	hole effective mass hh/lh ¹ (m_0)	exciton Bohr radius (nm)	bandgap (eV)
CdSe (WZ)	0.13	1.79/0.48	4.9	1.732
CdTe	0.11	0.63	7.5	1.475
CdS (WZ)	0.18	5/0.7	2.8	2.5
ZnS (WZ)	0.28	1.4	1.7	3.8

Depending on the values of NC radius (R) and its Bohr radii for the electron (a_e), the hole (a_h), and the exciton (a_{exc}), three different limits can be considered [Efr82]. These include:

1. Weak confinement regime. When R is larger than both a_e and a_h , only the quantization of the center-of-mass motion of the exciton is considered.
2. Intermediate confinement regime. When R is between a_e and a_h , only one particle is strongly confined while the other is not. Since usually the effective mass of the electron is smaller than that of the hole, we have $a_h < R < a_e$.
3. Strong confinement regime. When $R < a_{exc}, a_e, a_h$, both the electron and hole are strongly confined by the NC boundary. NCs used in this work have sizes smaller than their Bohr radius. Hence, the following discussion will mainly deal with this regime.

Band structures. The time-independent Schrödinger equation for an electron in a bulk crystalline solid is

$$\left[\frac{-\hbar^2}{2m_0} \nabla^2 + V(r) \right] \Psi(r) = E\Psi(r), \quad (2.8)$$

where m_0 is the free electron mass, $-i\hbar\nabla$ the momentum operator, $V(r)$ the operator for the potential, $\Psi(r)$ the wavefunction and E the eigenvalue of energy. According to Bloch's theorem [Ash76], the eigenfunctions of eq. (2.8) have the form of

$$\Psi_{nk}(r) = e^{ikr} u_{nk}(r). \quad (2.9)$$

Here, u_{nk} is the Bloch lattice function which has the periodicity of the lattice, and n and k are the band index and wavevector, respectively. The relation between E and k calculated by solving eq. (2.8) is called the band structure of the material (also known as the dispersion curves). The full details of the band structure are in general quite complex and difficult to calculate. Several theoretical approaches, including the effective mass approximation (EMA) [Efr82], tight-binding methods [Lip90], and empirical pseudo-potential method [Vis05] have been extensively employed for calculating the band structures in solids. The EMA is the oldest and least computationally demanding approach. In the following, the band structure of NCs will be discussed in the framework of the EMA consideration.

Even for NCs in the strong confinement regime, their physical sizes are still considerably larger than the lattice constants of the material. For example, CdSe NCs

¹hh: heavy hole. lh: light hole. Details about holes will be discussed in the following part.

have an exciton Bohr radius of 4.9 nm, which is much larger than the lattice constants (WZ: $a = 0.430$ nm, $c = 0.702$ nm [Wes88]). Therefore, it is reasonable to treat the NCs as macroscopic crystals with crystalline structures the same as the bulk material, and the EMA can be utilized in the nanocrystal problems. In the EMA, the electrons and holes are assumed to behave like free particles with an effective mass $m_{e,h}^*$. In order to reveal the principle quantum confinement effects with the EMA, we will only consider the simplest situation, in which the potential barrier at the surface of the NC is infinite, i.e.

$$V(r) = \begin{cases} 0 & \text{if } |r| \leq a, \\ \infty & \text{if } |r| > a. \end{cases} \quad (2.10)$$

Here a denotes the radius of the spherical potential well. In this way the problem can be simplified to a particle-in-a-box problem [Gap98]. By solving eq. (2.8), the band structures for the conduction and valence bands are given by [Nor04]

$$E_c(k) = \frac{\hbar^2 k^2}{2m_e^*} + E_g \quad (2.11)$$

$$E_v(k) = \frac{-\hbar^2 k^2}{2m_h^*} \quad (2.12)$$

Here, E_g is the bulk bandgap of the semiconductor and the energies are given relative to the top of the valence band.

As shown in Fig. 2.4a, the band structures from this approximation have parabolic forms. In most compound semiconductors, like the case shown in Fig. 2.4a, the maximum of the valence band and the minimum of the conduction band occur at the same point in the k -space. Such semiconductors are called direct bandgap semiconductors. The semiconductors used in this work, including CdSe, CdTe, and CdS, have direct bandgaps. However, if the extrema of the conduction and valence bands are reached at different points in the k -space, then the semiconductor is called indirect bandgap semiconductors. Typical examples are Si and Ge. Additionally, from eq. (2.11) and (2.12) we can derive

$$\frac{1}{m^*} = \frac{1}{\hbar^2} \left. \frac{d^2 E}{dk^2} \right|_{k=0}, \quad (2.13)$$

which indicates that the effective mass accounts for the curvature of the bands at $k = 0$.

However, in reality, the band structures of II-VI semiconductors are more complicated than the model proposed above. Take the most studied CdSe as an example. The electronic configuration of Cd is $[\text{Kr}]4d^{10}5s^2$, and the conduction band arising from $5s$ orbitals in Cd is only twofold degenerate at the point $k = 0$. Therefore, for the electrons near the bottom of the conduction band, it is sufficient to consider only a single parabolic band given in eq. (2.11). As to the valence band of CdSe, it arises from the $4p$ orbitals of Se whose electronic configuration is $[\text{Ar}]3d^{10}4s^2 4p^4$, and is sixfold degenerate at $k = 0$. As a result for holes, the underlying valence band has a much more complicated structure. For CdSe with ZB structures, due to

2.2. Electronic and optical properties of semiconductor nanocrystals

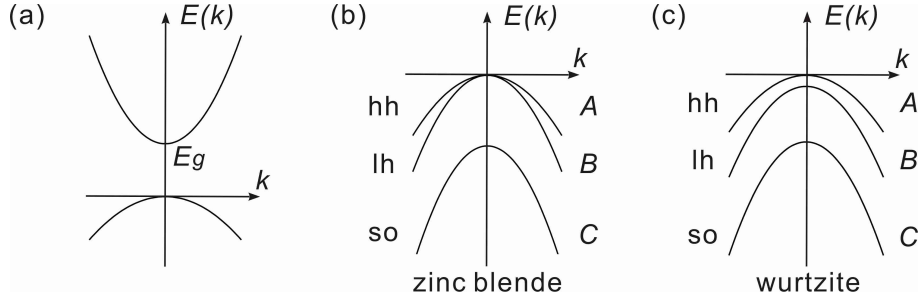


Figure 2.4: (a) A schematic illustration of the conduction and valence band structures of a direct bandgap semiconductor calculated from the EMA. (b) The valence band structure of a zinc blend type semiconductor at $k = 0$. (c) The valence band structure of a wurtzite type semiconductor at $k = 0$.

spin-orbit coupling the parabolic valence band is further split into three subbands referred to as the heavy-hole (hh), light hole (lh), and split-off-hole (so) subbands, as shown in Fig. 2.4b. They are also referred to as the A , B , and C subbands. For the WZ structures (Fig. 2.4c), due to the lack of inversion symmetry as previously mentioned in section 2.2.1 and the crystal field splitting resulting from the unique c -axis in the lattice, the degeneracy of the A and B subbands at $k = 0$ is lifted [Nor04].

Once we know the band structures in one potential, we can consider particles in a crystal composed of periodic units separated by a lattice translation constant b , so that the potential is also periodic with respect to b

$$V(r) = V(r + b), \quad (2.14)$$

and

$$u_{nk}(r) = u_{nk}(r + b). \quad (2.15)$$

Therefore, wavenumbers k_1, k_2 that differ by a value $2\pi n/b$ ($n = \pm 1, \pm 2, \pm 3, \dots$) would appear to be equivalent. In band theory, each of the following intervals

$$-\frac{\pi}{b} < k < \frac{\pi}{b}; \quad \frac{\pi}{b} < k < \frac{3\pi}{b}; \quad \frac{3\pi}{b} < k < \frac{5\pi}{b}; \dots, \quad (2.16)$$

contains the full set of the nonequivalent k values and is called the Brillouin Zone [Gap98]. Typically, only the first Brillouin zone is considered and the extended band structure with $|k| > \pi/b$ is modified to yield structures also in the first Brillouin zone.

2.2.3 Size-dependent optical properties

Fermi's golden rule. When treating the optical properties of NCs, one often has to deal with the transition of charges. The transition rate between electronic states can be understood in term of Fermi's golden rule, which for a transition from

state $|i\rangle$ to state $|f\rangle$ has the general form [Gap98]

$$\Gamma_{i \rightarrow f} = \frac{2\pi}{\hbar} |\langle \psi_f | H_{\text{int}} | \psi_i \rangle|^2 \rho_f(E). \quad (2.17)$$

Here, ψ_f and ψ_i are the wavefunctions of the final and initial states, and H_{int} is the interaction Hamiltonian. The whole term $\langle \psi_f | H_{\text{int}} | \psi_i \rangle$ is called the matrix element of the transition and it describes the overlap of the initial and final states. Additionally, ρ_f denotes the density of the final states. From the formula, we can see that stronger coupling between the initial and final states and higher density of final states lead to faster transition.

Size-dependent bandgap. In semiconductors, the bandgap (E_g) is the minimum energy required to excite an electron from the valence band into the conduction band. Here, we discuss how the corresponding energy states and the bandgap change when the size of NCs is decreased to be comparable to the exciton Bohr radius. According to the EMA [Efr82, Gap98], for a spherical NC with radius R and infinite potential barrier at the surface, the Hamiltonian operator without Coulomb interaction and the energies for different quantized states are given by

$$H = -\frac{\hbar^2}{2m_e^*} \nabla_e^2 - \frac{\hbar^2}{2m_h^*} \nabla_h^2 + V_e(r_e) + V_h(r_h), \quad (2.18)$$

$$E_{n,l}^{e,h} = \frac{\hbar^2 \alpha_{n,l}^2}{2m_{e,h}^* R^2}, \quad (2.19)$$

where $\alpha_{n,l}$ is the n th zero of the spherical Bessel function of order l [Nor04]. V_e , V_h and r_e , r_h are the confining potentials and coordinates of the electrons and holes, respectively. From eq. (2.19), one can derive that the energy levels of the NCs are discrete and with the decrease of the NC size, the energy of the quantized states increases (Fig. 2.5). The lowest quantized energy state with $n = 1$ and $l = 0$ is

$$E_{1,0} = \frac{\pi^2 \hbar^2}{2m_{e,h}^* R^2}. \quad (2.20)$$

Therefore, the lowest excited state energy E of NCs is related to the bulk bandgap E_g by

$$E = E_g + \frac{\pi^2 \hbar^2}{2R^2} \left[\frac{1}{m_e^*} + \frac{1}{m_h^*} \right]. \quad (2.21)$$

In order to include the Coulomb interaction between the electrons and holes, the Hamiltonian in eq. (2.18) is further modified to [Gap98]

$$H = -\frac{\hbar^2}{2m_e^*} \nabla_e^2 - \frac{\hbar^2}{2m_h^*} \nabla_h^2 + V_e(r_e) + V_h(r_h) - \frac{e^2}{\varepsilon |r_e - r_h|}, \quad (2.22)$$

where ε is the bulk dielectric constant of the semiconductor material. As a result, the corresponding energy E should also include the Coulomb interaction energy.

Several groups have worked on the calculation of the lowest excited state energy in

2.2. Electronic and optical properties of semiconductor nanocrystals

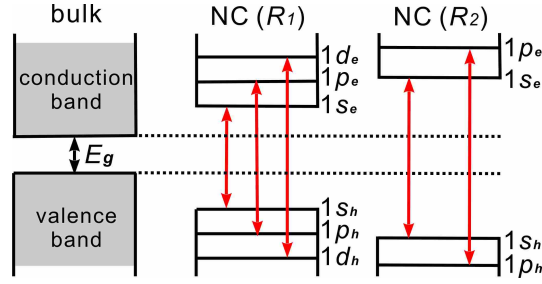


Figure 2.5: A schematic illustration of the discrete energy levels in NCs. The lowest excited state energy of NCs is larger than the bulk bandgap, and with the decrease of the NC size ($R_1 > R_2$), the corresponding energy increases. In addition, due to the optical selection rule, only certain transitions are possible.

NCs. On the basis of EMA, Brus et al. [Bru84] calculated the Coulomb interaction in first order perturbation theory and derived that the energy of the lowest excited state is

$$E = E_g + \frac{\pi^2 \hbar^2}{2R^2} \left[\frac{1}{m_e^*} + \frac{1}{m_h^*} \right] - \frac{1.8e^2}{\epsilon R}. \quad (2.23)$$

Later using Ritz's variational technique, Kayanuma et al. [Kay88] found that the energy should be represented as

$$E = E_g + \frac{\pi^2 \hbar^2}{2R^2} \left[\frac{1}{m_e^*} + \frac{1}{m_h^*} \right] - \frac{1.786e^2}{\epsilon R} - 0.248 \frac{\mu e^4}{2\epsilon^2 \hbar^2}, \quad (2.24)$$

where μ is the reduced mass

$$\mu = \frac{m_e^* m_h^*}{m_e^* + m_h^*}. \quad (2.25)$$

From eq. (2.23) and (2.24), it can be seen that by decreasing the size of NCs, the lowest excited state energy of NCs is expected to increase (Fig. 2.5).

It is important to keep in mind that the EMA holds only if the energies of the electrons and holes are close to the bottom of the conduction band and top of the valence band, respectively, because then the band structures can be approximated by the simple parabolic band forms. Details of the band-edge exciton fine structures can be found in Ref. [Efr04, Efr00]. Although the EMA method is not valid for all types of NCs, it still provides reasonable, quantitative descriptions of the size-dependent optical properties of NCs.

Absorption and photoluminescence. Common techniques used to characterize the energy level structures of NCs include absorption and emission spectroscopies. Both absorption and emission processes follow the optical selection rule, which requires that for interband optical transitions between energy levels labeled by the quantum numbers $n_e l_e$ (for electrons) and $n_h l_h$ (for holes), the conditions $\Delta n = 0$ and $\Delta l = 0$ must be fulfilled [Nor04]. Additionally, the angular quantum number should not change during the transition. As a result, the three lowest energy

Chapter 2. Theoretical background

transitions occur between the following electron-hole states (Fig. 2.5):

$$1s_e \leftrightarrow 1s_h, \quad 1p_e \leftrightarrow 1p_h, \quad \text{and} \quad 1d_e \leftrightarrow 1d_h. \quad (2.26)$$

The absorption of a photon with energy $h\nu \geq E_g$ by the NC leads to the excitation of an electron to the conduction band leaving a hole in the valence band. The peak positions in the absorption spectrum indicate the excited electron-hole pair states, with the first peak position (lowest energy) providing an estimate of the bandgap of the NCs. As discussed above, with the decrease of NC size the bandgap of the NC increases, which is observed as a blue shift of the absorption spectrum as well as the absorption peaks.

Different expressions have been used to describe the absorption by materials [Kun05]. For example, the exponential attenuation law is often used to represent the absorption of light by a solid:

$$I = I_0 e^{-\alpha l}, \quad (2.27)$$

where α is called the absorption coefficient and l is the thickness of the solid. Another commonly used method is the Lambert-Beer law:

$$A = \varepsilon c l, \quad (2.28)$$

with A being the absorbance, ε the molar extinction coefficient, and c and l the concentration of particles and path length of the light. The two equations can be correlated by the following equation

$$A = \log\left(\frac{I_0}{I}\right). \quad (2.29)$$

The absorption coefficient α is directly proportional to the oscillator strength $f_{i,f}$ of the transition, which is given by [Sat10]

$$f_{i,f} = \frac{2m}{E_f - E_i} |\langle \Psi_f | \hat{e} \cdot \vec{p} | \Psi_i \rangle|^2. \quad (2.30)$$

Here Ψ_i , Ψ_f and E_i , E_f are the wavefunctions and energies of the initial and final states in the transition, \hat{e} and \vec{p} the polarization vector of the light and momentum operator, respectively. The oscillator strength is often normalized by the volume of the NCs. In the strong confinement regime, the overlap of electron and hole wavefunctions increases with decreasing NC size, and consequently the excitonic oscillator strength per unit volume also increases [Kay88, Bry88]. This is why, even at room temperature for small NCs with narrow size distribution, distinct excitonic features can be observed in the absorption spectra. However, the total oscillator strength over the whole volume decreases as the size of the NC decreases [Bry88, Don09], which is shown experimentally in the work of Yu et al. [Yu03a], who empirically correlated the molar extinction coefficient at the first excitonic absorption peak with the size of NCs.

When excitons are created by absorption of photons with energies higher than

2.2. Electronic and optical properties of semiconductor nanocrystals

the bandgap, they will lose their excess energy and relax to the band edge by interaction with phonons. Exciton-phonon interaction is of great importance because it determines the absorption and emission linewidths as well as the Stokes shift (i.e., the difference in energy between absorption and emission peaks). In bulk materials, these relaxation processes (typically in the time regime of 100 fs to 10 ps [Rog08]) are much faster than the subsequent radiative and nonradiative recombination processes. However, in NCs the discrete energy levels would require exact resonance between the optical phonon energy and the NC energy level spacing. Besides, the level spacing is relatively large when compared to the typical energy of phonons in bulk materials. These facts lead to the assumption that the carrier relaxation rate in NCs would be much slower than in bulk, and this problem is known as the “phonon bottleneck” [Rog08]. Much interest has been aroused in this area [Efr95, Ura01, Pan08, Sve09] because if the charge carrier relaxation in NCs is really slowed down as compared to bulk materials, then NCs would be promising candidates for applications in solar cells. However, the existence of the phonon bottleneck phenomena remains a controversial subject [Pre08]. One can refer to Ref. [Rog08, Gap98] and the references in them for further reading.

When NCs are excited by a photon with an even higher energy ($> 2E_g$), the generated electron and hole may release their energy through the excitation of a second exciton. Thus, a biexciton is formed and the internal quantum efficiency is greater than 100%. This phenomena is called the carrier multiplication (another topic still under debate) and details about it can refer to the reviews from McGuire et al. [McG08], Nozik [Noz08], and Beard [Bea11].

Compared to absorption, the photoluminescence (PL) of NCs is much more complicated, because it is very sensitive to the relaxation process of the exciton as well as the bandgap electronic states. Aside from the emission from band edge (band edge emission), sometimes charge carriers can be captured at trap states. Emission from those states (trap state emission) further complicates the situation. Many experimental and theoretical works have been devoted to the understanding of the trap states, details about which will be discussed in the next section.

When measuring a PL spectrum from NCs in solvent with a fluorometer, an additional noise signal may pop up: the high order Rayleigh scattering peak [Zha08], which is caused by the diffraction from gratings. According to the grating equation (see eq. 3.45), the noise signal would appear at multiples of the excitation wavelength. As a result, the PL scanning range is usually chosen to start several nanometers larger than the excitation wavelength and stop before the second order Rayleigh scattering wavelength.

PL spectrum of single NCs provides information on the bandgap electronic states which would otherwise be hidden in the ensemble average. The PL spectral line shape is determined by dephasing dynamics of the excited state [Gap98]. Consider a simple example of an oscillator set into motion by an electric field $E(t)$ with a frequency ω_0 . When the oscillation is damped and decays exponentially with a constant dephasing rate Γ , then the inverse Fourier transformation (\hat{f}) shows that

the line shape of the spectrum follows a Lorentzian [SÖ1, Wik11]

$$\begin{aligned}
 E(t) &= E_0 e^{-i\omega_0 t} \cdot e^{-\Gamma t} \xrightarrow{\text{inverse Fourier}} \\
 I(\omega) &= \hat{f}(\omega) = \frac{1}{2\pi} \int_{-\infty}^{\infty} E(t) e^{-it\omega} dt = \frac{E_0}{\sqrt{2\pi}} \frac{\Gamma}{(\omega - \omega_0)^2 + \Gamma^2}, \quad (2.31)
 \end{aligned}$$

where ω_0 is the resonant frequency and Γ is the half-width at half-maximum (HWHM). In this study, spectra from single NCs are fitted by Lorentzians. However in real ensemble systems, size, shape and local environment of NCs differ from one to another, and as a result an inhomogeneous broadening of the PL spectrum is typically observed. In the analysis, usually a Gaussian distribution of subbands from individual NCs is assumed.

2.2.4 Blinking and power law

Trap states. Optical properties of NCs are strongly dependent on the trap states of the NCs because trapping usually decreases the overlap of the electron-hole wavefunctions and increases the recombination time. A survey of the literature indicates that there are mainly two groups of trap states that have been investigated most frequently: the surface-related trap states and the intrinsic trap states.

With diminishing NC size, the ratio of the number of atoms at the surface divided by the total number of atoms, which is called the surface-to-volume ratio (P), increases. Equations to estimate P for cubic and spherical nanoparticles can be found in Ref. [Rod06, Jor92]. Since the atoms on the surface of the NCs remain incompletely bonded, the direct consequence of the increase of P is that surfactants can easily bind to the NC surface if the binding energies are favorable (for most cation rich surfaces), or sometimes dangling bonds are formed on the NC surface (for some anion rich surfaces¹). If these trap states are energetically positioned within the bandgap of NCs, charge carriers can be trapped, usually leading to nonradiative recombinations. Among the theories that have been used to describe how the surface trap states are involved in capturing the charge carriers are the models proposed by Chestnoy et al. [Che86], who argued that the electrons can be located by both shallow and deep traps while the latter vary less with changes in NC size than the former, and by Bawendi et al. [Baw92] who proposed a state mixing of the exciton orbitals and surface trap states.

Another important type of trap states is the intrinsic trap states. Theoretical analyses [Nir95, Efr96] have shown that due to shape anisotropy in wurtzite structures and electron-hole exchange interaction, the band edge excitonic state ($1S_{3/2}1S_e$) splits into five sublevels labeled by the projection of the total angular momentum along the unique crystal axis N_m : ± 2 , $\pm 1^L$, $\pm 1^U$, 0^L , and 0^U . Among them, ± 2 and 0^L states are optically forbidden. Therefore, relaxation of electron-hole pairs into these states leads to dark excitons.

Both types of trap states have been used to explain many experimental results.

¹For example, in CdSe NCs, deep trap states are usually formed on the Se^{2-} rich facets, because these anions do not easily bind to ligands [Und01].

2.2. Electronic and optical properties of semiconductor nanocrystals

In some work, the observed phenomena is attributed to the interplay between the surface and intrinsic trap states [Mor07, Cal05].

Blinking and power law. PL blinking (or intermittency) refers to the fact that in the PL time traces (or trajectory) of single fluorophores, which give the temporal evolution of the PL intensity, the emitting states are interrupted by dark periods in a large range of timescales. In 1913, Bohr predicted the possible existence of these “quantum jumps” in a three level system [Lee09]. However, it was not until 1996 that Nirmal et al. [Nir96] first observed blinking in single NCs. A few years later, by defining the on- (or off-) time as the interval of time when no signal falls below (or surpasses) a chosen threshold intensity, Kuno et al. [Kun00] first found that, in CdSe NCs, the probability distributions of both on- and off-time follow an inverse power law:

$$P(t) = A \cdot t^{-\alpha}. \quad (2.32)$$

Such behavior can span over many decades in probability density and time. Furthermore, the exponent α typically has values in the range of 1 to 2, peaking at about 1.5 [Ste09], depending on the threshold values and binning time [Kun01, Cro10]. The off-state exponent α_{off} is relatively insensitive to experimental conditions such as temperature and excitation intensity [Shi01, Ban99]. In contrast, a truncation effect has been observed in the on-time probability distributions [Shi01, Ban99, Ste05a], indicating a secondary mechanism leading to the shorter maximum on-time. On- and off-times are reported either to be uncorrelated [Kun01] or weakly correlated [Ste05b].

To understand the physical mechanisms behind the observed blinking and power law behavior of individual NCs, a number of models have been developed, among which the Auger ionization model, proposed by Efros and Rosen [Efr97] soon after the observation of blinking from single NCs, remains fundamental and important. According to this model, due to the strong spatial confinement of the electronic wavefunctions of electrons and holes in NCs, the probability of NCs carrying two excitons is significantly increased. Energy from the recombination of one electron-hole pair would be transferred to the remaining charge carriers, leading to the ejection of

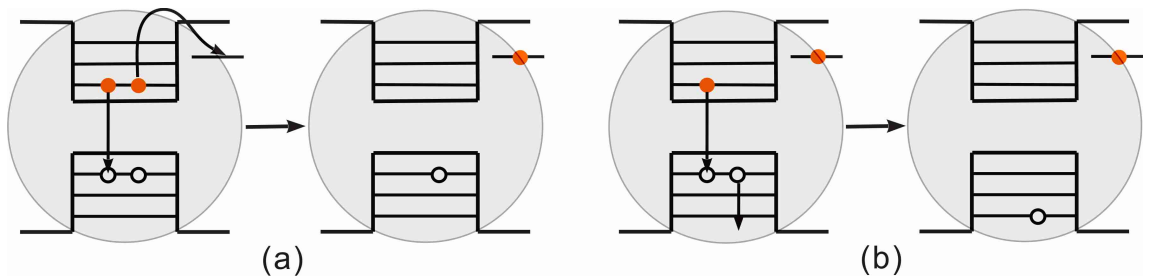


Figure 2.6: A scheme presenting (a) Auger ionization in which an electron is ejected, leaving behind a charged NC; (b) nonradiative Auger recombination whereby the energy from electron-hole recombination is transferred to the remaining hole.

electrons or holes to the surrounding trap states¹. As a result, a charged NC is generated and this process is known as the Auger ionization (Fig. 2.6a). Due to the remaining charge in the NC, the subsequently excited electron-hole pairs can recombine nonradiatively through Auger recombination processes: the recombination energy is transferred to the remaining charge that is re-excited to a higher-energy state (Fig. 2.6b). Experiments show that the Auger recombination time (10 – 400 ps in CdSe NCs) decreases with the size of NCs and is significantly shorter than the radiative decay time [Kli03]. As a result, once the NC is charged, nonradiative Auger recombination dominates and the NC remains dark. Only when the NC is neutralized is the PL restored. Although the model explains why blinking occurs in NCs, the main limitation is that it predicts single switching rates between the on- and off-states and corresponding exponential distributions of on- and off-time, rather than the power law distributions.

A series of modifications to this theory have been proposed. Among them are the multiple trap model of Verberk et al. [Ver02], the spectral diffusion model from Shimizu et al. [Shi01] (later developed by Tang et al. [Tan05]), the spatial diffusion model of Margolin et al. [Mar06], and the fluctuating barrier model of Kuno et al. [Kun01]. Details about the different models can refer to a number of comprehensive reviews [Fra08, G06, Lee09, Cic07].

2.2.5 Recombination dynamics

At low excitation intensities, a photon with energy higher than the bandgap of NCs produces an electron-hole pair, which then relaxes nonradiatively to the band edge states through intraband exciton-phonon interactions (see section 2.2.3).

Once there, as shown in Fig. 2.7, there are several competing interband recombination processes the NC can undertake to return to the ground state. In a simple picture, the electron and hole recombine radiatively (k_r), producing a photon. According to Fermi's golden rule, the spontaneous transition rate between an excited state $|j\rangle$ and a ground state $|0\rangle$ is given by [vD05]

$$\Gamma_j = \frac{e^2}{3\pi\epsilon_0 m^{*2} \hbar c^3} \omega_j |\langle 0 | \mathbf{p} | j \rangle|^2, \quad (2.33)$$

where ϵ_0 is the permittivity of free space, m^* the effective mass of electron, ω_j the frequency of the emitted light. By certain approximation, it is found that the matrix element of the momentum $\langle 0 | \mathbf{p} | j \rangle$ is independent of the size of NCs. As a result, the radiative decay rate is expected to be linearly proportional to the emission frequency ω_j . In other words, at a given temperature,

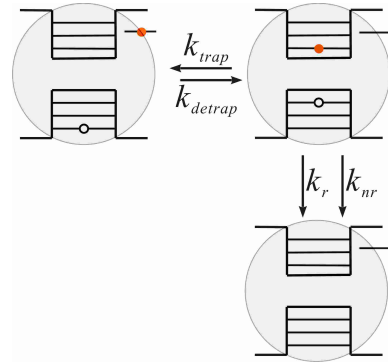


Figure 2.7: A simplified scheme describing the band edge recombination processes in NCs.

¹Since the effective mass of holes are larger than that of electrons, usually electrons are ejected.

2.2. Electronic and optical properties of semiconductor nanocrystals

smaller NCs have shorter radiative lifetimes. This has been both theoretically demonstrated [vD05, Cal07] and experimentally observed [vD05, Don09]. Furthermore, radiative decay rate is also sensitive to the external environment. It has been shown that the radiative decay rate of CdSe NCs increases with the refractive index of the medium [Wui04, Bro04].

In addition to radiative decay, electron-hole pairs can also recombine through non-radiative processes (k_{nr}), which include electron-phonon interactions (section 2.2.3) and Auger recombination processes (section 2.2.4). Another important process influencing the recombination dynamics is the trapping of charge carriers at surface or intrinsic trap states of NCs (k_{trap}). For example, several groups have detected temperature dependent lifetime of CdSe NCs, and this is explained by the “dark/bright exciton” model: temperature dependent redistribution of excitons between the bright ($N_m = 1^L$) and dark ($N_m = 2$) states leads to the strong dependence of recombination lifetime on temperature [Rog08]. Here, it should be noted that trapping of charge carriers does not necessarily lead to off-states of NCs in time traces. Instead, it depends on how much the trap states decrease the overlap of electron-hole wavefunctions and, therefore, the corresponding recombination rates.

The most common technique used to monitor the recombination dynamics is the time-correlated single photon counting (TCSPC). In this method, a pulsed laser excites the sample. The time difference between the excitation pulse and the observed photon is measured and stored in a histogram. After certain integration time, the resultant histogram with the time difference as the x-axis and the corresponding number of detected photons as y-axis gives the so-called decay curve. The effective resolution of a TCSPC measurement is characterized by its instrument response function (IRF), which contains the laser pulse shape, the temporal dispersion in the detection system, and the timing resolution of the detector [Bec05]. Details about the detectors will be discussed in the next chapter.

To get a general idea about the recombination dynamics, we assume the recombination rates for the radiative and nonradiative processes are k_r and k_{nr} , respectively. As a result the depopulation of the excited state follows

$$\frac{dN_2}{dt} = -(k_r + k_{nr})N_2, \quad (2.34)$$

where N_2 is the excited state population. With $N_2(0)$ as the initial population of the excited state, one can derive

$$N_2 = N_2(0)e^{-(k_r+k_{nr})t}. \quad (2.35)$$

This is a single exponential function, and the observed lifetime τ and quantum efficiency QE of NCs are defined by

$$\tau = \frac{1}{k_r + k_{nr}}, \quad (2.36)$$

$$\text{QE} = \frac{k_r}{k_r + k_{nr}}. \quad (2.37)$$

Chapter 2. Theoretical background

However, in real NCs, due to the various recombination processes mentioned above, the recombination dynamic is much more complicated than a single exponential function. Schlegel et al. [Sch02] and Fisher et al. [Fis04] both observed that the PL decay rates fluctuated with time and were closely related to the PL intensity. In such a case, it is more accurate to describe the recombination processes with a continuous distribution of decay rates rather than as a sum of several discrete rates. As a result, the decay curves can be considered as arising from a superposition of weighted exponential functions [Lin80, BS05], and can be written as

$$I(t) = I_0 \cdot \int_0^{\infty} e^{-t/\tau} \rho(\tau) d\tau. \quad (2.38)$$

The function $\rho(\tau)$ representing the probability density of the decay rates is the inverse Laplace transform of $I(t)$ and is normalized by $\int_0^{\infty} \rho(\tau) d\tau = 1$. Finally, the decay rate distribution function $G(\tau)$ is defined as $G(\tau) = \tau\rho(\tau)$.

In principle, $\rho(\tau)$ can be recovered directly from the experimental decay curves through an inverse Laplace transform. However, this is an ill-conditioned problem, and corresponding to one decay curve there may be many different rate distributions [Sch02, BS05]. To reconstruct $\rho(\tau)$ from decay curve analysis, one approach is to use a mathematical function to describe it. For example, van Driel et al. [vD07] used a log-normal distribution function as $\rho(\tau)$ and successfully fitted decay curves from NCs. In this work, however, we fitted the decay curves with a more commonly used function: the stretched exponential function¹

$$I(t) = I_0 \cdot e^{-(t/\tau_{1/e})^{\beta_s}}, \quad (2.39)$$

where the stretching exponent β_s ($0 < \beta_s \leq 1$) reflects the width of the decay rate distribution involved in the recombination process. Small β_s values are related to broad rate distributions whereas $\beta_s = 1$ means single exponential behavior. $\tau_{1/e}$ is the decay time when the PL intensity $I(t)$ drops to $1/e$ of the initial intensity I_0 . From these two parameters one can further calculate the average lifetime $\langle\tau\rangle$ by [Sch02, Lin80]

$$\langle\tau\rangle = \left(\frac{\tau_{1/e}}{\beta_s}\right) \Gamma\left(\frac{1}{\beta_s}\right). \quad (2.40)$$

Here, Γ is the gamma function. In order to recover $\rho(\tau)$ from the stretched exponential function, following Ref. [Lin80] we make

$$\int_0^{\infty} e^{-t/\tau} \rho(\tau) d\tau = e^{-(t/\tau_{1/e})^{\beta_s}}. \quad (2.41)$$

Applying the inverse Laplace transform to eq. (2.41), with the following substitutions

¹Also known as the Kohlrausch-Williams-Watts (KWW) function.

2.2. Electronic and optical properties of semiconductor nanocrystals

$$\beta = \beta_s, \quad x = \frac{\tau_{1/e}}{\tau}, \quad s = \frac{t}{\tau_{1/e}}, \quad (2.42)$$

we obtain

$$\rho(\tau) = \frac{\tau_{1/e}}{\tau^2} \cdot \lambda\left(\frac{\tau_{1/e}}{\tau}, \beta_s\right). \quad (2.43)$$

Here, λ is defined by

$$\lambda(x, \beta) = \frac{1}{\pi} \int_0^{\infty} e^{-xu} e^{-u^\beta \cos \pi\beta} \sin(u^\beta \sin \pi\beta) du \quad (2.44)$$

when $\beta \neq 1/2$. If $\beta = 1/2$, then

$$\lambda(x, \beta) = \frac{1}{2} \pi^{-1/2} x^{-3/2} e^{-1/4x}. \quad (2.45)$$

Usually the rate distribution is represented as $G(\tau) = \tau\rho(\tau)$.

The correlation between the decay rate and PL intensity was further revealed by the work of Zhang et al. [Zha06] and Biebricher et al. [Bie06]. Especially in the latter work, a time-tagged time-resolved (TTTR) single photon counting technique was applied. This method allows access both to the arrival time of emitted photons relative to the excitation pulse and to the start of data acquisition. It was observed that both the PL lifetime and intensity distributed continuously. Although the correlation between the two was nonlinear, in general, higher intensity exhibited longer lifetime, which is consistent with Ref. [Sch02]. As a consequence, it was suggested that instead of the discrete on-/off-states, the NCs probably had continuous emissive states due to a distribution of trap states on the surface.

2.2.6 Wavefunction engineering – core-shell heterostructures

As mentioned in section 2.1.2, shells of wider bandgap semiconductors, such as CdS and ZnS, are commonly grown onto CdSe NCs to protect them from interaction with the environment. In such NCs, the electrons and holes are localized in the same material (here in the core), and heterostructures like this are called type I core-shell NCs (Fig. 2.8a). In contrast, when the conduction and valence bands of the core and shell materials are staggered, then the electrons and holes are spatially separated in the core and shell, leading to the type II core-shell NCs (Fig. 2.8b).

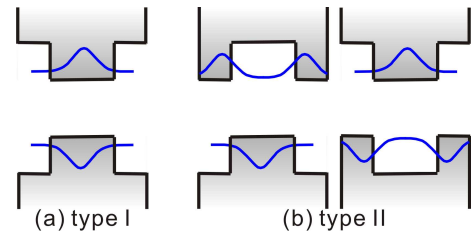


Figure 2.8: Schematic illustration of band structures and wavefunctions in (a) type I and (b) type II core-shell NCs.

For common type I core-shell NCs (with wider bandgap material as the shell), the quantum efficiency and photostability are usually enhanced compared to the core NCs. This is because the dangling bonds on

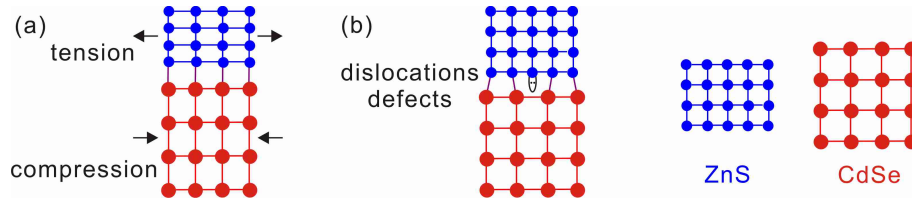


Figure 2.9: Schematic of ways in which lattice strains are eased in (a) coherent and (b) incoherent epitaxial growth of CdSe-ZnS core-shell NCs. Modified from [Smi10].

the core NC surfaces are passivated by the shell. Sometimes this could be indicated by the disappearance of the trap state emission in the PL spectra with the growth of shell. Since both the electron and hole wavefunctions are mainly confined to the core, bandgap of this type of core-shell NCs is determined by the core NCs. As a result, no significant shift of the absorption band edge and PL peak should occur. However, broadening of the spectra is usually observed because of the inevitable broadening of the NC size distribution during the shell growth.

Different from type I core-shell NCs, the bandgap of type II NCs is determined by the energy separation between the conduction band edge of the core (shell) and the valence band edge of the shell (core), and thus is very sensitive to both the core size and shell thickness. Usually strong redshift of the emission peak can be observed during the course of the shell growth. Therefore, type II core-shell NCs can be potential candidates for near-infrared biomedical applications. In addition, due to the reduced spatial overlap between the charge carrier wavefunctions, a significant increase in recombination lifetime can be detected, which may be of great interest for photovoltaic devices.

When choosing a proper shell material, lattice mismatch is another critical parameter aside from band offset. It is believed that two types of epitaxial growth can occur in core-shell NCs: the coherent type and the incoherent type. The former (Fig. 2.9a) corresponds to the shell growth in which distortions or strains caused by the shell are tolerated by the deformation of NCs. Although lattice strain is distributed over a large fraction of the NC atoms, no dislocation or defect is formed. This type of core-shell NCs is usually observed in very small core NCs with any shell thickness [Smi09] or NCs with very thin shell [Dab97], depending on how deformable the materials composing the core-shell NCs are¹. Meanwhile, for the incoherent type (Fig. 2.9b), strain is eased by the formation of dislocations and quenching defects near the core-shell interface, and the core and shell materials form own crystalline domains, respectively. Such structure usually leads to lower PL quantum efficiency. To overcome this problem, sometimes an alloyed layer is introduced between the core and the shell [Xie05, Wan09], and the resultant NCs can be grouped into another new arising, interesting type of NCs – the alloyed NCs [Reg10].

¹For example, CdTe has a larger deformation potential than CdSe [Smi10].

2.3 Electronic and optical properties of gold nanoparticles

2.3.1 Electronic structures

Knowing the fundamental facts of the electronic structures of Au helps to develop an understanding of the optical properties of AuNPs. Au is classified as a noble metal (IB) and has a FCC lattice structure, with a lattice constant of 4.08 Å. Its electronic configuration is $[\text{Xe}]4f^{14}5d^{10}6s^1$, indicating a completely filled 5d shell and half filled 6s band. Such electronic configuration makes Au highly electrically conductive, and the concentration of free electrons in gold reaches $5.98 \times 10^{28} \text{ m}^{-3}$ [Dul04].

Theoretical chemistry of Au is thoroughly reviewed in Ref. [Pyy04]. Among many of the properties, the band structure of gold has been studied ever since the 1970s [Chr71]. As shown in Fig. 2.10, the d bands are located a few eV below the Fermi level, whereas the broad conduction band (derived from $6s^1p$ hybridized atomic orbitals) crosses the Fermi level near the X, L, and Σ points of the Brillouin zone and displays the characteristics of quasi-free electron behavior. Two different types of electron transitions happen in Au: (1) the intraband or indirect transitions, which takes place within a single band at low energy; (2) the interband or direct transitions occurring at higher energies (above 1.8 eV at the X point and 2.4 eV at the L point) between the d bands and sp band without any change in the crystal momentum $\hbar k$ [Chr71]. Both types of transitions contribute to the dielectric constant of Au, as we will discuss in section 2.3.2.

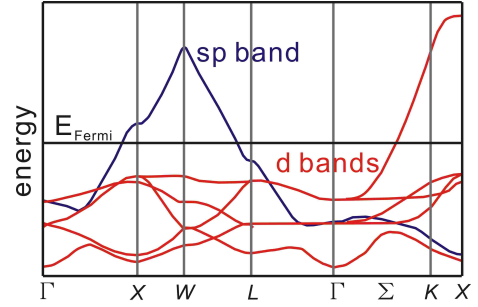


Figure 2.10: Band structure of gold. [Chr71]

2.3.2 Dielectric functions

The dielectric response of a metal to the electromagnetic field is described by a wavelength dependent complex dielectric function

$$\varepsilon(\omega) = \varepsilon' + i\varepsilon''. \quad (2.46)$$

Here, the real part ε' represents the degree to which the metal polarizes in response to the applied external electric field, while the imaginary part ε'' determines the relative phase shift of this induced polarization with respect to the external field [Sha07].

The Drude-Sommerfeld model is often used to roughly estimate the dielectric function of metals. The basic assumption in the Drude model is that the free electrons in the metal can be considered as a classical gas of electrons performing a diffusive motion. An external electric field with amplitude \mathbf{E}_0 and frequency ω

Chapter 2. Theoretical background

is applied to accelerate the free electrons, which then experience collisions with the lattice, other free electrons, and defects. The equation of motion is then [Nov06]

$$m_e \frac{\partial^2 \mathbf{r}}{\partial t^2} + m_e \Gamma \frac{\partial \mathbf{r}}{\partial t} = e \mathbf{E}_0 e^{-i\omega t}, \quad (2.47)$$

where m_e and e are the effective mass and charge of the free electrons. The damping rate in the framework of the Drude model is $\Gamma = \langle v \rangle_{th} / l$, where $\langle v \rangle_{th}$ is the average thermal velocity of the free electrons and l is the average distance traveled by the electron between collisions. However, in reality, only electrons close to the Fermi surface respond to the applied electric field and those lying deep within the Fermi sea tend not to change their electronic states [Dre03]. In consideration of this, Sommerfeld incorporated corrections into the expression for the damping rate, which is then given by $\Gamma = v_F / l$, where v_F is the Fermi velocity. It should be noted that in eq. (2.47) no restoring force is considered since the electrons are taken as free. Solving eq. (2.47) yields [Nov06]

$$\begin{aligned} \varepsilon(\omega) &= 1 - \frac{\omega_p^2}{\omega^2 + i\Gamma\omega} \\ &= 1 - \frac{\omega_p^2}{\omega^2 + \Gamma^2} + i \frac{\Gamma\omega_p^2}{\omega(\omega^2 + \Gamma^2)}. \end{aligned} \quad (2.48)$$

Here ω_p is the bulk plasma frequency and is given by

$$\omega_p^2 = \frac{ne^2}{m_e \varepsilon_0}, \quad (2.49)$$

with n as the density of free electrons in the metal.

Although the Drude-Sommerfeld model describes the contribution from the nearly free conduction electrons accurately, the response of the bound 5d electrons is neglected. In order to supplement the influence of the interband transitions from the bound 5d electrons, the equation of motion for a bound electron is modified from eq. (2.47) to

$$m \frac{\partial^2 \mathbf{r}}{\partial t^2} + m\gamma \frac{\partial \mathbf{r}}{\partial t} + \alpha \mathbf{r} = e \mathbf{E}_0 e^{-i\omega t}, \quad (2.50)$$

where m is the effective mass of the bound electrons, γ the damping rate of the bound electrons, and α the restoring force constant of the potential. Again, by solving eq. (2.50), we find the contribution of the bound electrons to the dielectric function to be

$$\begin{aligned} \varepsilon_{\text{inter}}(\omega) &= 1 + \frac{\tilde{\omega}_p^2}{(\omega_0^2 - \omega^2) - i\gamma\omega} \\ &= 1 + \frac{\tilde{\omega}_p^2(\omega_0^2 - \omega^2)}{(\omega_0^2 - \omega^2)^2 + \gamma^2\omega^2} + i \frac{\gamma\tilde{\omega}_p^2\omega}{(\omega_0^2 - \omega^2)^2 + \gamma^2\omega^2}. \end{aligned} \quad (2.51)$$

Here, $\omega_0 = \sqrt{\alpha/m}$ and $\tilde{\omega}_p = \sqrt{\tilde{n}e^2/m\varepsilon_0}$, with \tilde{n} being the density of the bound electrons [Nov06].

2.3. Electronic and optical properties of gold nanoparticles

Table 2.2: Material parameters used in the calculation of the dielectric function of gold [Oka01, Bor99].

ω_p	$13.8 \times 10^{15} \text{ s}^{-1}$	Γ	$1.075 \times 10^{14} \text{ s}^{-1}$
$\tilde{\omega}_p$	$45 \times 10^{14} \text{ s}^{-1}$	γ	$9 \times 10^{14} \text{ s}^{-1}$
ω_0	$2\pi c/\lambda$	λ	450 nm

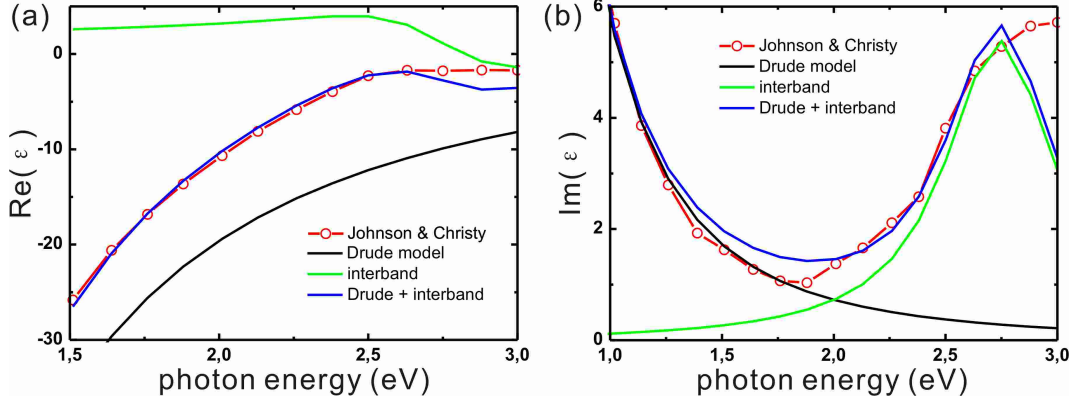


Figure 2.11: Real (a) and imaginary (b) parts of the dielectric function of gold from experimental data [Joh72] and theoretical models.

In order to estimate the accuracy of the theoretical models, dielectric functions for the nearly free electrons (eq. (2.48)) and bound electrons (taking interband transition into account (eq. (2.51))), as well as measured values taken from the paper of Johnson and Christy [Joh72] are plotted together in Fig. 2.11. Parameters used for the calculation are listed in Table 2.2. In the calculation, a constant offset $\epsilon_\infty = 6$, which accounts for the influence of all higher-energy interband transitions not considered in the discussed model, is added to eq. (2.51) [Nov06]. From Fig. 2.11 we can see that the sum of the Drude-Sommerfeld model and the interband transition contribution fits the experimental values well for energy below 2.6 eV, especially for the real part. For the energy below 1.8 eV, the imaginary part clearly follows the Drude-Sommerfeld model, whereas above 1.8 eV, the contribution from the interband transition becomes significant.

The dielectric functions discussed above are for bulk gold. As the size of AuNPs decreases (< 10 nm), the quantization of the electronic states becomes important and quantum size effects dominates. Therefore, additional correction to the dielectric function needs to be introduced for accurate work, and detailed discussion can refer to Ref. [Gen80, Kaw66].

2.3.3 Interaction of light with gold nanoparticles

When a AuNP is irradiated by light, the external electric field causes the conduction electrons to oscillate relative to the much heavier and therefore effectively immobile positive ionic cores, inducing polarization. This collective oscillation of the electrons

Chapter 2. Theoretical background

is called localized surface plasmon (LSP) and it has attracted great interests for centuries. The scientific research on AuNPs dates at least back to 1856 when Michael Faraday demonstrated the preparation of ruby-red gold colloids [Far57], some of which are still preserved in the Faraday Museum in London [Roy].

Classical electrodynamic methods provide both qualitative and quantitative solutions to the optical properties of AuNPs by utilizing their bulk dielectric functions. To start with, a simple quasistatic model, the Rayleigh approximation [Ray71, Ray07], in honor of Lord Rayleigh¹, will be discussed. For AuNPs with diameters much smaller than the wavelength of light, the electric field of the light around the AuNPs can be taken to be constant, and the interaction can be simply treated electrostatically. The induced polarizability α of AuNPs with radius R can be calculated by the Clausius-Mossotti formula [Jac99]:

$$\alpha = 4\pi\epsilon_0 R^3 \frac{\epsilon - \epsilon_m}{\epsilon + 2\epsilon_m} \quad (2.52)$$

where ϵ and ϵ_m are the dielectric functions of the AuNPs and the surrounding medium, respectively. If we set $k = 2\pi/\lambda$, using the dielectric function given in eq. (2.46), the scattering and absorption cross sections² are [Boh83]

$$C_{sca} = \frac{8}{3}\pi k^4 R^6 \frac{(\epsilon' - \epsilon_m)^2 + \epsilon''^2}{(\epsilon' + 2\epsilon_m)^2 + \epsilon''^2} \quad (2.53)$$

$$C_{abs} = 12\pi k R^3 \frac{\epsilon''\epsilon_m}{(\epsilon' + 2\epsilon_m)^2 + \epsilon''^2} \quad (2.54)$$

Since the real part ϵ' of the dielectric function of Au is negative, it is possible to have $\epsilon' = -2\epsilon_m$ fulfilled. This is called plasmon resonance and the absorption and scattering cross sections reach maxima under this condition. Referring to Fig. 2.11, we can derive the higher the dielectric constant of the medium, the longer the plasmon resonant wavelength. For example, according to this model, the plasmon resonance for AuNPs in vacuum ($\epsilon_m = 1$) and glass ($\epsilon_m \approx 4.6$) should occur at 480 nm and 520 nm, respectively.

It should be noted that the quasistatic model only works for very small AuNPs ($2R < 25$ nm), because when the size of AuNPs is beyond the Rayleigh approximation, the conduction electrons under the influence of electric field do not all move in phase anymore and retardation effects due to phase shift of the electrodynamic field over the nanoparticle size play a more significant role [Mei83, Gho07]. Consequently, with the increase of the AuNP size the plasmon resonance red shifts while at the same time substantially broadens.

Aside from the Rayleigh approximation, the interaction of light with AuNPs can also be obtained by solving Maxwell's equations. In 1908, Gustav Mie³ presented a complete solution to Maxwell's equations that describes the scattering and absorption spectra of single, isolated spheres with arbitrary sizes [Mie08]. According to

¹*12.11.1842 in Langford Grove, England; †30.6.1919 in Witham, England

²In some references, the scattering and absorption efficiencies are used, which are obtained by normalizing the cross sections with the particles' geometrical cross section.

³*29.9.1868 in Rostock, Germany; †13.2.1957 in Freiburg, Germany

2.3. Electronic and optical properties of gold nanoparticles

Mie theory, the extinction, scattering and absorption cross sections for AuNPs with radius R radiated by light with wavelength λ are given by [Boh83]

$$C_{ext} = \frac{2\pi R^2}{x^2} \sum_{n=1}^{\infty} (2n+1) \text{Re}(a_n + b_n) \quad (2.55)$$

$$C_{sca} = \frac{2\pi R^2}{x^2} \sum_{n=1}^{\infty} (2n+1) (|a_n|^2 + |b_n|^2) \quad (2.56)$$

$$C_{abs} = C_{ext} - C_{sca} \quad (2.57)$$

Here, x is defined by $x = 2\pi R n_m / \lambda$, with n_m being the refractive index of the surrounding medium. n is the multipole order ($n = 1$ the dipole oscillation, $n = 2$ the quadrupole oscillation, ...), and a_n and b_n are the scattering coefficients given by

$$a_n = \frac{m\psi_n(mx)\psi'_n(x) - \psi_n(x)\psi'_n(mx)}{m\psi_n(mx)\xi'_n(x) - \xi_n(x)\psi'_n(mx)} \quad (2.58)$$

$$b_n = \frac{\psi_n(mx)\psi'_n(x) - m\psi_n(x)\psi'_n(mx)}{\psi_n(mx)\xi'_n(x) - m\xi_n(x)\psi'_n(mx)} \quad (2.59)$$

in which $m = n_{Au}/n_m$, where $n_{Au} = \sqrt{\varepsilon(\omega)}$ is the complex refractive index of the Au, and $\psi_n(x)$ and $\xi_n(x)$ are Ricatti-Bessel cylindrical functions.

When the size of AuNPs is much smaller than the wavelength of light ($2R < 25$ nm), the electric dipole oscillation ($n = 1$) dominates and eq. (2.55) and (2.56) can be simplified to [Pap79, H93]

$$C_{ext} = \frac{24\pi^2 R^3}{\lambda} \frac{\varepsilon'' \varepsilon_m^{3/2}}{(\varepsilon' + 2\varepsilon_m)^2 + \varepsilon''^2} \quad (2.60)$$

$$C_{sca} = \frac{256\pi^6 R^6}{\lambda^4} \frac{(\varepsilon' - \varepsilon_m)^2 + \varepsilon''^2}{(\varepsilon' + 2\varepsilon_m)^2 + \varepsilon''^2} \quad (2.61)$$

The result is identical to that from the Rayleigh approximation (eq. (2.53)). Again, plasmon resonance happens when $\varepsilon' = -2\varepsilon_m$ is fulfilled. However, for large AuNPs, contributions from the higher orders of n become more important. Since the higher order modes appear at lower energies, the plasmon resonance red shifts with increasing AuNP size. Under such condition, the complete Mie theory should be applied.

Fig. 2.12 shows the effect of higher order modes on different-sized AuNPs. The spectra are computed with Mathematica™. For the small AuNP ($R = 25$ nm, Fig. 2.12a), spectra from $n = 5$ (solid curves) fit very well with those from $n = 1$ (dashed curves), whereas for AuNP with $R = 100$ nm (Fig. 2.12b), the difference is apparent. However, both two sets of spectra ($n = 1$ and $n = 5$) are red shifted as compared to the spectra of the smaller AuNP. It is also worth noting that in larger AuNPs scattering instead of absorption becomes dominant.

Although Mie theory provides efficient, exact solution to Maxwell's equations for single, isolated spherical particles, it neglects the polydispersity of size and the inter-particle interactions. Moreover, developments in wet chemistry techniques as well as

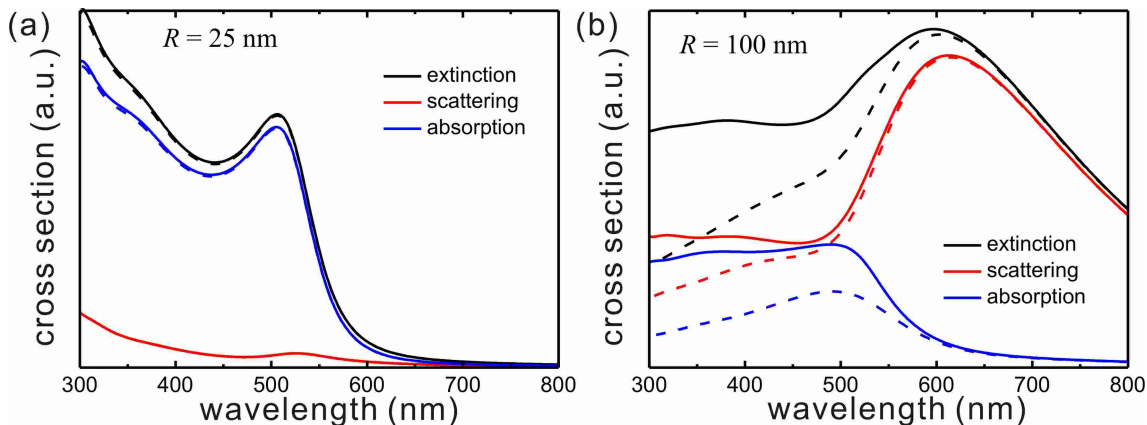


Figure 2.12: Extinction, scattering, and absorption spectra calculated from Mie theory for AuNPs with radius (a) $R = 25$ nm and (b) $R = 100$ nm. The solid curves correspond to multiple order of 5, and the dashed ones to multiple order of 1.

the application of modern lithographic techniques have stimulated increasing interest in the optical properties of nonspherical nanostructures, making the development of more accurate theories necessary. That is why modern numerical methods that can treat arbitrary nanostructures and environments have experienced a tremendous improvement in the past decade. Among the numerical methods that have been introduced to describe metallic nanostructures are the finite-difference time-domain method (FDTD) [Yee66, Taf00] and the frequency-domain approaches, including discrete dipole approximation (DDA) [Dra94, Dra00] and multiple multipole method (MMP) [Mor02, Nov97].

In this work, many simulations are performed with the aid of the FDTD method implemented in available software packages (Lumerical Solutions, Inc., Canada). The FDTD method is basically an algorithm used to solve Maxwell's equation on a discretized spatial grid through consecutive time steps. It can provide exact solutions of Maxwell's equations concerning both the near-field and far-field optical properties of nanostructures with arbitrary size and shape, although sometimes the accuracy of the simulation is limited by the time step intervals and grid size used in the calculation. Details about this method could refer to the book by Taflove and Hagness [Taf00]. Fig. 2.13 compares results computed from the complete Mie theory and FDTD method. For large AuNPs (Fig. 2.13b), the difference between the two methods become apparent.

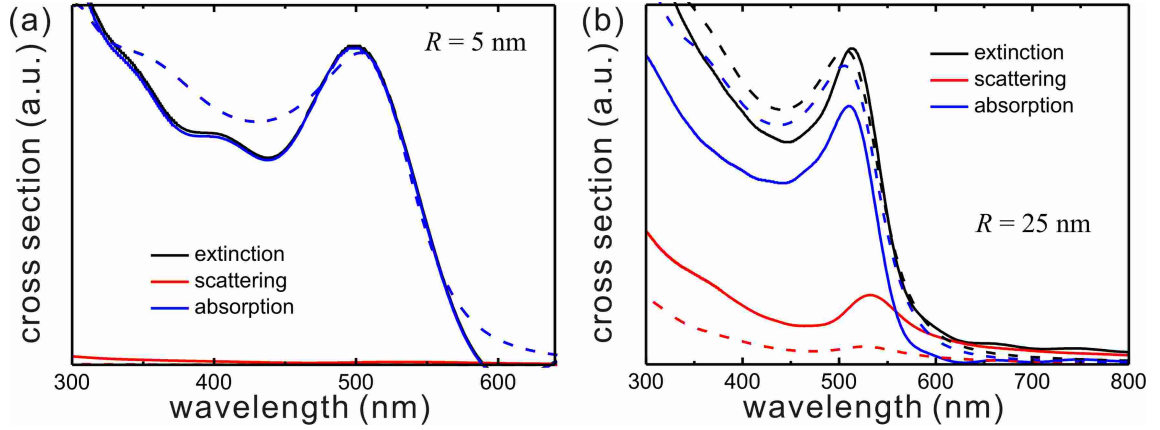


Figure 2.13: Extinction, scattering, and absorption spectra calculated from FDTD method (solid curves) and complete Mie theory (dashed curves) for AuNPs with radius (a) $R = 5$ nm and (b) $R = 25$ nm.

2.4 Interaction between semiconductor nanocrystals and metals

Ever since the pioneering experiments carried out by Drexhage and coworkers [Dre70a, Dre74], numerous experimental and theoretical investigations have been performed to elucidate the underlying interaction mechanism between fluorophores and metals. In particular, the theoretical works range from classical electromagnetic models [Cha78, For84, Mos85, Bar98] to quantum mechanical descriptions [Mor74, Phi75, Bha09]. From these studies, it has become clear that the complex interaction depends on many factors. Nevertheless, only main aspects of this topic and theoretical models related to this work will be discussed here.

2.4.1 Enhancement or quenching? – General considerations

In a simplified case, a fluorophore can be represented by a two-level system with transition frequency ω_{em} . When illuminated by weak¹ electromagnetic radiation with frequency $\omega_{exc} \geq \omega_{em}$, the fluorophore undergoes at least two processes: excitation and emission. The presence of metal nanostructures in close proximity can alter both processes.

For the excitation stage, the excitation rate k_{exc} depends on both the absorption coefficient of the fluorophore $\sigma(\omega_{exc})$ and the local electric field $E(\omega_{exc})$ at the position of the fluorophore [Ged10]:

$$k_{exc} \propto \sigma(\omega_{exc}) |E(\omega_{exc})|^2. \quad (2.62)$$

Because of their large extinction coefficients, metal nanostructures can interact strongly with incident light, and the local electric field surrounding the fluorophore

¹No saturation of the optical transition happens.

is usually altered compared with that in the absence of metal. The change of the electric field is sensitive to the excitation frequency ω_{exc} , the distance and orientation of the fluorophore relative to the metal, and the size and geometry of the metal nanostructures.

As compared to excitation, the behavior of emission is more complicated due to the possibilities of various channels to the ground state (section 2.2.5). In general, however, we can assume that there are only radiative and nonradiative decays (neglecting the possibility of Auger ionization which, as commonly assumed, leads to the off-states of NCs). Therefore, the quantum efficiency (QE) of the fluorophore (in the on-state) is in fact determined by the balance of radiative (k_r) and nonradiative (k_{nr}) decay rates. With the metal nanostructures in vicinity, the density of final states (states after the emission of photons) is increased [Ged10], and, following Fermi's golden rule in eq. (2.17), we can conclude that k_r also increases. Meanwhile, additional nonradiative channels due to excitation of plasmons in the metal might also be created. Thus, both k_r and k_{nr} , and consequently QE and lifetime of the fluorophores, will be altered.

Although it is difficult to separate the effects of the excitation and emission processes, it is reasonable to treat them as two subsequent processes due to the often present intraband relaxation. The various effects of a metal nanostructure on the fluorescence intensity of a nearby fluorophore can then be summarized as [Ang06]

$$\gamma = k_{exc} \cdot \text{QE} = k_{exc} \cdot \frac{k_r}{k_r + k_{nr}}. \quad (2.63)$$

Thus, metal nanostructures can lead to either fluorescence enhancement or quenching of nearby fluorophores, depending on the relative magnitudes of the competing effects.

2.4.2 Interaction mechanism – different theoretical models

Although many models persist in the literature, most of them are based on classical electromagnetic theories. A complete list of these models is too exhaustive to be given here. Thus, only those models that are most frequently used or related to this work will be presented. When describing the interaction of fluorophores with metals using the classical approach, it is a common strategy to treat the fluorophores as oscillating dipoles.

CPS model. Some of the early experiments on the effect of metal films on a fluorophore were reported in the 1960s by Drexhage [Dre70a, Dre70b, Dre74], who observed characteristic oscillations in the lifetime as the distance between a fluorophore and a thick (≥ 100 nm) metal mirror was varied from about 5 to 600 nm. Later, based on Sommerfeld's solution to the problem of a radiating antenna emitting near the surface of the earth [Som49], Chance, Prock, and Silbey (CPS) [Cha75, Cha78] provided a comprehensive analysis of these results, and their theory was found to be in excellent accord with Drexhage's results and with many other experimental works. Fig. 2.14a shows one set of experimental data from Drexhage [Dre74] and the best fitting from the CPS model. In addition, they predicted that,

2.4. Interaction between semiconductor nanocrystals and metals

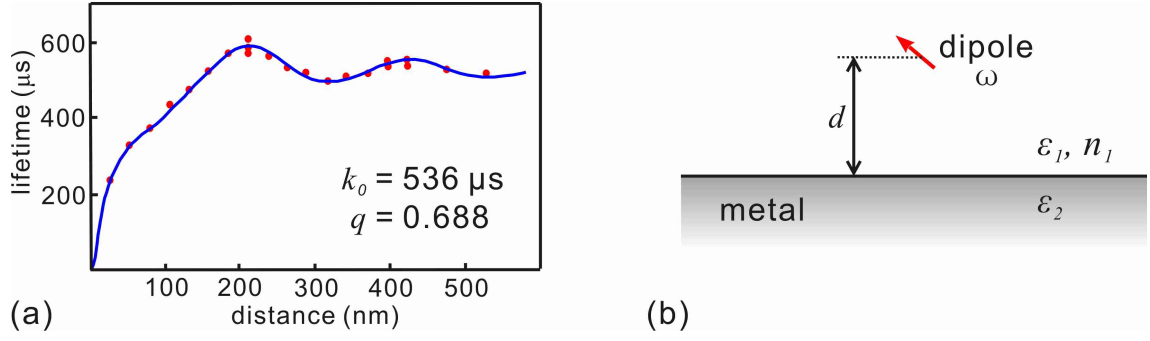


Figure 2.14: (a) Lifetime of isotropically distributed fluorophores as a function of distance from a thick Au mirror. The points represent experimental data from Drexhage [Dre74], and the solid curve represents the best fitting using the CPS model. (From [Cha75]) (b) Geometry of the CPS model.

in the short distance region (typically below 20 nm), the lifetime and quantum efficiency would decrease dramatically due to energy transfer.

The detailed geometry of the CPS model is shown in Fig. 2.14b. An oscillating dipole with transition frequency ω is located at a distance d from the metal surface. The surrounding medium and the metal film have dielectric constants as $\varepsilon_1 = n_1^2$ and ε_2 , respectively. Therefore, the wavenumber in the medium is $k_1 = \omega n_1/c$. By considering the interference between the source radiation from the fluorophore and that reflected by the metal film at the dipole position, the radiative (k_r) and nonradiative (k_{nr}) decay rates in the presence of the metal for dipoles oriented perpendicular (\perp) or parallel (\parallel) to the metal surface are normalized to the decay rate in the absence of metal (k_0) [Cha78]:

$$\frac{k_{r,\perp}}{k_0} = q - \frac{3}{2}q \mathbf{Im} \int_0^1 R^{\parallel} e^{-2l_1 k_1 d} \frac{u^3 du}{l_1} \quad (2.64)$$

$$\frac{k_{nr,\perp}}{k_0} = (1 - q) - \frac{3}{2}q \mathbf{Im} \int_1^{\infty} R^{\parallel} e^{-2l_1 k_1 d} \frac{u^3 du}{l_1} \quad (2.65)$$

$$\frac{k_{r,\parallel}}{k_0} = q + \frac{3}{4}q \mathbf{Im} \int_0^1 [(1 - u^2)R^{\parallel} + R^{\perp}] e^{-2l_1 k_1 d} \frac{u du}{l_1} \quad (2.66)$$

$$\frac{k_{nr,\parallel}}{k_0} = (1 - q) + \frac{3}{4}q \mathbf{Im} \int_1^{\infty} [(1 - u^2)R^{\parallel} + R^{\perp}] e^{-2l_1 k_1 d} \frac{u du}{l_1} \quad (2.67)$$

Here, q is the quantum efficiency, and

$$l_j = -i(\varepsilon_j/\varepsilon_1 - u^2)^{\frac{1}{2}} \quad (2.68)$$

$$R^{\parallel} = \frac{\varepsilon_1 l_2 - \varepsilon_2 l_1}{\varepsilon_1 l_2 + \varepsilon_2 l_1} \quad (2.69)$$

$$R^{\perp} = \frac{l_1 - l_2}{l_1 + l_2} \quad (2.70)$$

Matlab[®] scripts for the computing of these equations are included in Appendix A.

Gersten-Nitzan model. To evaluate the influence of surface geometry on the decay rate of a fluorophore, Gersten and Nitzan analyzed the case when an excited fluorophore was placed close to a small metal sphere (or spheroid) [Ger80, Ger81b, Ger81a]. In general, the model indicates the existence of excitation enhancement due to the increase of local electric field when the fluorophore is close enough to the metal. Additionally, energy transferred from the fluorophore excites different surface plasmon modes in the metal particles, among which only the dipolar surface plasmon can radiate whereas the other modes result in dissipation, i.e., nonradiative losses. Thus, nonradiative decay rate is increased.

According to the model, it is assumed that there is an oscillating dipole with frequency ω and intrinsic radiative decay rate $k_{r,\text{intrins}}$ (in the absence of metal particles) located at a distance d from the metal particle surface (Fig. 2.15). The radiative decay rate (k_r) and energy transfer rate (k_{ET}) for the dipole oriented perpendicular to the metal particle surface can then be calculated by [Ger81a]

$$k_{r,\perp}(r, d) = \frac{\omega^3 |\mu_0|^2}{3\hbar c^3 |1 - \Delta(\perp)|^2} \left| 1 + 2 \left(\frac{r}{r+d} \right)^3 \frac{\varepsilon(\omega) - \varepsilon_m}{\varepsilon(\omega) + 2\varepsilon_m} \right|^2, \quad (2.71)$$

$$k_{ET,\perp}(r, d) = -\frac{|\mu_0|^2}{2\hbar r^3 |1 - \Delta(\perp)|^2} \sum_{n=1}^{\infty} (2n+1) \frac{(n+1)^2}{n} \cdot \text{Im} \frac{1}{\varepsilon(\omega) + \varepsilon_m \cdot (n+1)/n} \left(\frac{r}{r+d} \right)^{2n+4}, \quad (2.72)$$

with μ_0 the intrinsic dipole moment of an isolated fluorophore, and the molecular polarizability α and $\Delta(\perp)$ calculated by [Dul04]

$$|\mu_0| = \sqrt{\frac{3\hbar c^3}{\omega^3} k_{r,\text{intrins}}} \quad (2.73)$$

$$\alpha = \frac{3c^3}{2\omega^4} k_{r,\text{intrins}} \quad (2.74)$$

$$\Delta(\perp) = \frac{\alpha}{(r+d)^3} \sum_{n=1}^{\infty} \frac{\varepsilon(\omega) - \varepsilon_m}{\varepsilon(\omega) + \varepsilon_m \cdot (n+1)/n} (n+1)^2 \left(\frac{r}{r+d} \right)^{2n+1}. \quad (2.75)$$

Here r represents the metal particle radius, and $\varepsilon(\omega)$ and ε_m are the dielectric functions of the metal and the medium at frequency ω , respectively. Similarly, in

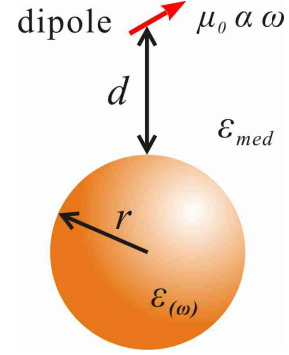


Figure 2.15: Geometry of the Gersten-Nitzan model.

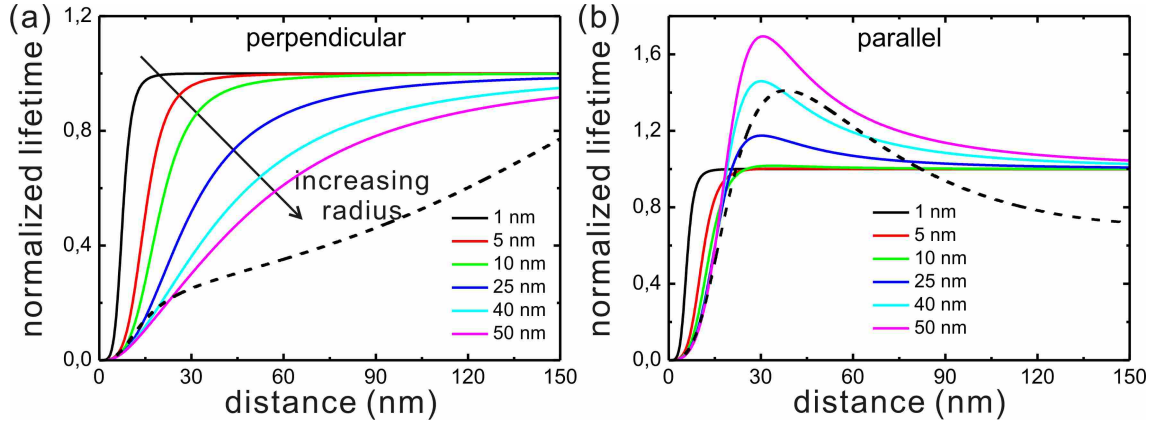


Figure 2.16: Normalized lifetime as a function of distance between perpendicularly (a) or parallelly (b) oriented dipoles and different-sized AuNPs calculated from the Gersten-Nitzan model. The dashed line is calculated from the CPS model for dipoles located at different distances from a Au film. The dipole has a unity quantum efficiency and transition wavelength of 600 nm. The surrounding medium is air.

the case when the dipole is parallel to the metal particle surface, it holds that

$$k_{r,\parallel}(r, d) = \frac{\omega^3 |\mu_0|^2}{3\hbar c^3 |1 - \Delta(\parallel)|^2} \left| 1 - \frac{\varepsilon(\omega) - \varepsilon_m}{\varepsilon(\omega) + 2\varepsilon_m} \left(\frac{r}{r+d} \right)^3 \right|^2 \quad (2.76)$$

$$k_{ET,\parallel}(r, d) = -\frac{|\mu_0|^2}{4\hbar r^3 |1 - \Delta(\parallel)|^2} \sum_{n=1}^{\infty} (n+1)(2n+1) \cdot \text{Im} \frac{1}{\varepsilon(\omega) + \varepsilon_m \cdot (n+1)/n} \left(\frac{r}{r+d} \right)^{2n+4} \quad (2.77)$$

with

$$\Delta(\parallel) = \frac{\alpha}{2r^3} \sum_{n=1}^{\infty} n(n+1) \frac{\varepsilon(\omega) - \varepsilon_m}{\varepsilon(\omega) + \varepsilon_m \cdot (n+1)/n} \left(\frac{r}{r+d} \right)^{2n+4}. \quad (2.78)$$

The total nonradiative decay rate k_{nr} of the dipole close to the metal nanoparticle is calculated by

$$k_{nr} = k_{nr,\text{intrins}} + k_{ET}, \quad (2.79)$$

with $k_{nr,\text{intrins}}$ as the nonradiative decay rate of the dipole without the nearby metal nanoparticle. Following these equations, the radiative and nonradiative decay rates can be computed with algebraic programs such as Mathematica™ (Appendix B).

Fig. 2.16 shows the dependence of normalized lifetime on the distance between dipoles and AuNPs (solid curves, Gersten-Nitzan model) or a Au film (dashed curve, CPS model). It is clear that orientation of the dipole influences the total lifetime and, with the increase in distance, the influence of metal on the dipole decreases. The Gersten-Nitzan model predicts that, especially for the perpendicularly oriented dipoles, as the size of AuNP increases, the lifetime becomes closer to that calculated

from the CPS model for a Au film. This is because when the sphere radius is much larger than the distance between the dipole and the AuNP, the AuNP appears to be a flat surface to the dipole, which is also true in the case when the dipole is close enough to the AuNPs (at very small distances).

Radiating plasmon model. Recently, a qualitative, relatively easy to understand model, the radiating plasmon model, was proposed by Lakowicz et al. [Asl05, Lak05, Zha07b]. Within this model, nonradiative energy transfer from the fluorophore to the metal, which is much faster than the radiative and nonradiative decay rates of the fluorophores in the absence of metal, occurs. Unlike the Gersten-Nitzan model, this model suggests that the transferred energy does not necessarily result in dissipation. Instead, the excited plasmon can decay through emission of photons into the far field, as is the case with highly scattering metal nanoparticles, and leads to an overall increase in the emission as well as a reduction in the lifetime. On the contrast, for those poorly scattering metal nanoparticles, the plasmons will decay nonradiatively, resulting in the quenching of the fluorescence. Therefore, in the radiating plasmon model, the relative contribution of scattering to the overall extinction somehow decides the extend to which the plasmons can radiate to the far field [Ged10].

FDTD method. As is briefly discussed in section 2.3.3, compared to quasistatic analytical solutions such as the Gersten-Nitzan model, the FDTD method is a rigorous computational method providing an exact solution of Maxwell's equations, calculating the complete electromagnetic field that is only limited by the time step intervals and grid size in the calculation. In addition, alternative shapes and geometries as well as different materials that are the same as in the real systems can be easily incorporated in the simulation. Therefore, it is often used to simulate both the near and far field optical properties of metal nanostructures. However, only limited studies [Cho07, Cho08, Kam07] have used this method in simulating the interactions between fluorophores and metals.

The reason that FDTD method can be used in analyzing the decay rates and eventually quantum efficiency of fluorophores close to metal nanostructures is because, for dipoles with unity intrinsic quantum efficiency ($QE = 1$, no nonradiative decay), the decay rate of the excited state is related to the power radiated by the dipole by the following equation [Nov06]

$$\frac{\gamma}{\gamma_0} = \frac{P}{P_0}. \quad (2.80)$$

Here γ , γ_0 and P , P_0 are the decay rates and radiated powers of the dipole with and without nearby metal nanostructures, respectively. This can be further specified by [Kam07]

$$\frac{\gamma_{tot}}{\gamma_0} = \frac{P_{tot}}{P_0}, \quad (2.81)$$

$$\frac{\gamma_{rad}}{\gamma_0} = \frac{P_{rad}}{P_0}, \quad (2.82)$$

2.4. Interaction between semiconductor nanocrystals and metals

where γ_{tot} and γ_{rad} are the total and radiative decay rates of the dipole close to metal nanostructures. P_{tot} is the total power radiated by the dipole in the proximity of metals, and it both goes into radiation (P_{rad}) and dissipation.

In a real simulation, the fluorophore is modeled by a radiating dipole source. As shown in Fig. 2.17, to calculate P_{tot} and P_{rad} , two sets of monitors, each containing six (four in the 2D FDTD simulation) frequency-domain power monitors to form a closed box, are used. The big box with both the dipole and metal nanostructures inside it is used to compute P_{rad} by integrating the real part of the Poynting vector over all six surfaces. The small one contains only the dipole and is used for the calculation of P_{tot} . [Cho08, Kam07] Before each simulation, it is important to test the numerical error by calculating the ratio of P_{rad} and P_0 in the absence of metal, since theoretically $P_{rad} = P_0$. FDTD scripts for computing P_{rad} and P_{tot} are given in Appendix C.

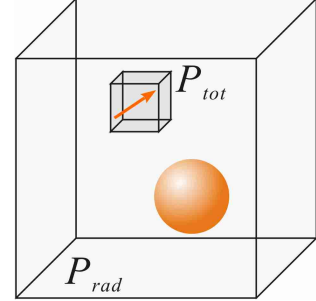


Figure 2.17: Schematic of the layout of monitors used in the FDTD simulation.



This page is intentionally left blank.

Chapter 3

Experimental Setup

A complete and precise understanding of the optical properties of NCs requires direct observation at the single particle level, since when measured from an ensemble, many of the properties can be masked due to sample inhomogeneities caused by different particle sizes, shapes, and surface states. The advent of single molecule techniques has enabled the discovery of many striking phenomena in NC optical properties, such as blinking [Mir96], spectral diffusion [Emp96] and PL intensity correlated lifetime fluctuation [Sch02, Fis04]. During this study, a homebuilt scanning confocal microscope was used extensively to investigate the PL properties of individual NCs. This chapter begins with a brief discussion of confocal microscopy. A detailed description of the specific scanning confocal microscope used in this work follows.

3.1 Principles of confocal microscopy

Invention of the confocal microscope is usually attributed to Marvin Minsky, who patented the principle of confocal imaging in 1957 [Min57]. Today, confocal microscopy is applied in many scientific disciplines, because compared to conventional wide-field light microscopy, the confocal microscopy provides not only improved signal-to-noise ratio, but also an increase in both lateral and axial resolutions. In addition, the localization property of the confocal scanning scheme allows real-time investigation of individual objects.

3.1.1 Confocal microscopy

The method of obtaining information in a confocal microscope is fundamentally different from that in a conventional wide-field microscope, in which the entire sample is bathed in light. A scanning confocal microscope incorporates two principle ideas: point by point illumination of the sample and rejection of out-of-focus light by a pinhole [Paw95]. Fig. 3.1 shows the basic configuration of a confocal microscope. A collimated laser beam is reflected by a (dichroic) beamsplitter and then focused by a microscope objective to a diffraction limited spot on the sample. The light coming back from the sample is then collected by the objective, passes through the beamsplitter and is focused onto a pinhole which is placed in the conjugated focal

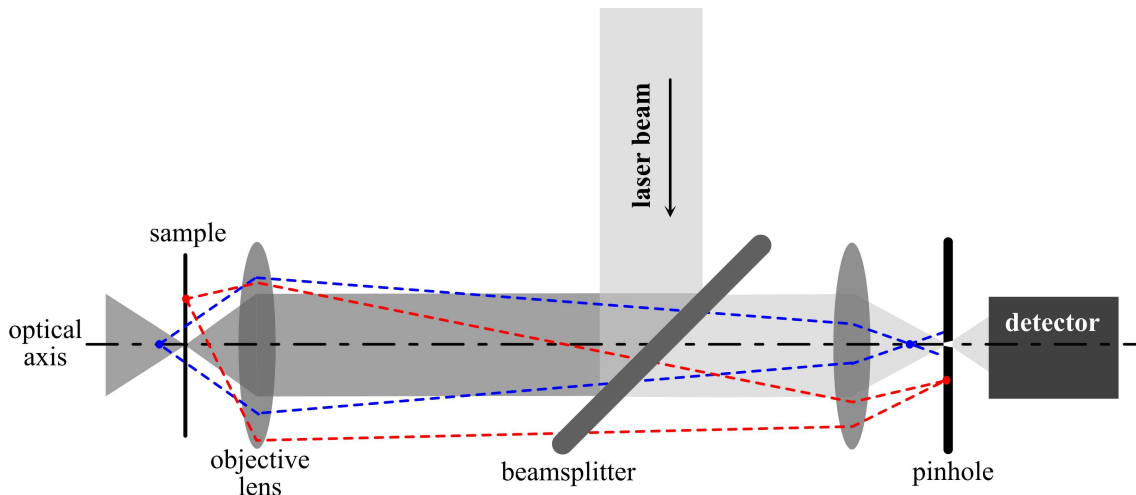


Figure 3.1: Schematic of confocal microscopy. Only the point at the focus of the objective is imaged onto the pinhole and detected. Beams from laterally displaced positions will be blocked by the pinhole (red beam path) and from positions displaced along the optical axis will not be focused in the detection plane (blue beam path).

plane of the sample. As a result, this pinhole acts as a spatial filter, rejecting all out-of-focus light and allows only the light from the focused spot to reach the detector right behind the pinhole. Many detectors, such as the single-photon avalanche diodes (SPAD), have very small active areas and can thus be used without an additional pinhole [Nov06].

Because the confocal microscope is a point detection device, in order to build up an image either the sample or the laser beam must be scanned point by point. The majority of commercial scanning confocal microscope employ some form of beam scanning, which is typically faster than sample scanning. One widely used method is to scan the laser beam by galvanometers. In some other cases, acousto-optical cells or Nipkow disks are used, which enable production of real-time images at video rates or faster. On the other hand, although scanning the sample requires more time, the fact that the laser beam is stationary on the optical axis removes specific aberrations and distortions, and makes optical performance of the system superior. In our homebuilt scanning confocal microscope, the laser beam is stationary on the optical axis and the sample is raster scanned with the help of a piezo stage, about which will be discussed in detail in section 3.2.1.4.

3.1.2 Signal-to-noise ratio

In the detection of single fluorophores, which usually emit a limited number of photons, signal-to-noise ratio (SNR) is one of the major factors influencing image and spectrum quality. Although it is often confused with the signal-to-background ratio (SBR), in practice SNR is the parameter which ultimately determines the information capacity of the measurements [Cox86] and limits the resolution [San95]. Due to its design, the confocal microscopy provides improved SNR when compared

to the conventional wide-field light microscopy [San94].

In a fluorescence measurement, assume s is the number of photons originating from the illuminated fluorophore per unit-time and unit-excitation power, b the background signal originating from scattering or fluorescence of the medium per unit-time, unit-excitation power, and unit-volume, and V is the excitation volume of the background signal. As a result, after illuminating a single fluorophore for time t with an excitation power P , the signal S collected with a detection efficiency E would be $s \cdot t \cdot P \cdot E$, and the background B would be $b \cdot t \cdot P \cdot V$, which yields SBR as:

$$\text{SBR} = \frac{S}{B} = \frac{s \cdot t \cdot P \cdot E}{b \cdot t \cdot P \cdot V} = \frac{s \cdot E}{b \cdot V}. \quad (3.1)$$

In order to define SNR, main sources of noises should be considered. In fluorescence measurements, the signal intensity is typically low. As a result, electronic noises in the instrumentation or fluctuations in the illumination intensity could be neglected, and the shot noise N_s dominates. SNR can thus be written as

$$\text{SNR} = \frac{S}{N_s} = \frac{s \cdot t \cdot P \cdot E}{N_s}. \quad (3.2)$$

The shot noise is due to the quantum nature of photons. Because independent photons hit the sensor at randomly distributed time intervals, detected electrical current fluctuates with time. This random distribution of the arriving photons is known as Poisson distribution, and as a result, shot noise is equal to the square root of the total number of photons collected. There are two main sources that contribute to shot noise: (1) photons originally generated by the light source, fluorophores and their medium, i.e. S and B , and (2) dark current from the detector. The dark current is due to the thermal generation of electrons and holes within the detector, regardless of whether or not the sensor is irradiated. Taking d as the dark current count per unit-time, shot noise is given by

$$N_s = \sqrt{S + B + d \cdot t} = \sqrt{(s \cdot P \cdot E + b \cdot P \cdot V + d) \cdot t}. \quad (3.3)$$

From eq. (3.2) and eq. (3.3) we can see that for a specific sample with certain s , there are several possibilities to improve the SNR:

1. increase detection efficiency E ;
2. increase integration time t ;
3. increase excitation power P ;
4. decrease excitation volume of the background signal V .

Although longer integration time or higher excitation power improves SNR even though they have no influence on SBR, in reality there is a greater probability of photo-bleaching or saturation effects of the fluorophores. That is why increasing detection efficiency and decreasing excitation volume of background signal are so essential [Doo03]. In a confocal microscope, only signals from the focal area are detected, and the excitation volume of the background signal V is optimized to the diffraction limit. Hence, the SNR of a confocal microscope is improved over a wide-field light microscope.

3.1.3 Point-spread function and resolution

Like a wide-field light microscope, the resolution of a confocal microscope is limited by the diffraction of light, which means that even the image of an infinitely small point by an ideal lens (i.e., a lens without optical aberrations) will be smeared out into a blur spot of finite size. This is because on propagation from the source to the image, only part of the plane wave as well as spectrum components from the source could be collected, which makes accurate reconstruction of the source impossible [Nov06]. The intensity distribution in the image of a point source can be quantitatively described by the point spread function (PSF). In general, the narrower the PSF, the better the resolution of a system. In the following, a brief description of the standard derivation of PSF from classical theories will be shown.

Assume that a thin circular lens with focal length f and radius a is illuminated by a uniform plane wave U_0 with wavelength λ , and that the light fields right before and behind the lens are $U_1(x_1, y_1)$ and $U_2(x_2, y_2)$ (Fig. 3.2). When the light wave passes through the lens and is focused onto the focal plane, two main optical behaviors happen: transmission through the lens and diffraction after the lens.

During the transmission, the optical lens changes both the phase and amplitude of the radiation field, so that the transmittance of a lens $t(x, y)$ can be written as [Gu96]:

$$t(x, y) = P(x, y) \exp[-i\phi(x, y)]. \quad (3.4)$$

Here, $P(x, y)$ and $\phi(x, y)$ represent the amplitude and phase changes of the incident light, respectively, and $P(x, y)$ is sometimes referred to as the pupil function of the lens. Since $U_1(x_1, y_1) = U_0$, by its definition, transmittance can also be written as:

$$t(x, y) = \frac{U_2(x_2, y_2)}{U_1(x_1, y_1)} = \frac{U_2(x_2, y_2)}{U_0}. \quad (3.5)$$

For a thin lens with uniform refractive index, the displacement of the beam before and after the lens is usually neglected, i.e. $x_1 = x_2 = x$, $y_1 = y_2 = y$. With the paraxial approximation, the transmittance of a thin lens can be derived to be [Gu96]

$$t(x, y) = P(x, y) \exp\left[\frac{i\pi(x^2 + y^2)}{\lambda f}\right], \quad (3.6)$$

and the light field behind the lens to be

$$U_2(x_2, y_2) = U_0 P(x, y) \exp\left[\frac{i\pi(x^2 + y^2)}{\lambda f}\right]. \quad (3.7)$$

Once we know the light field behind the lens, starting from Maxwell's equations, the diffraction pattern of the light wave can be calculated from the classical diffraction theories, about which Born et al. [Bor99] have discussed in detail. Assume z is the distance between the plane right behind the lens and the observation plane, and $U_3(x_3, y_3)$ is the light field on the observation plane. With the Kirchhoff diffraction formula, under the condition that the distance between the lens and the observation plane z is much larger than the distance between the observation point and the optical axis (Fresnel approximation), the field at the observation plane can be

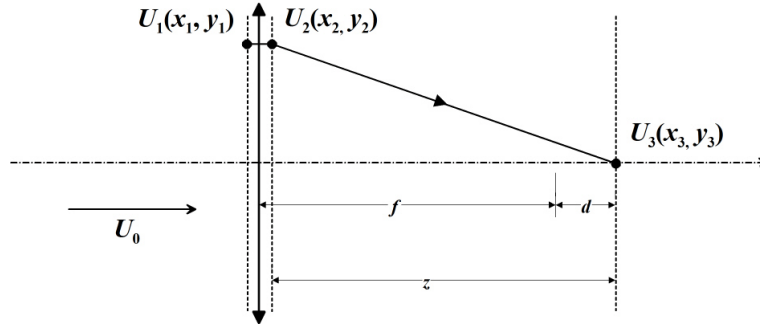


Figure 3.2: Schematic of the variables used for the calculation of the point spread function. A uniform plane wave is transmitted through a thin lens and then focused by the lens onto an observation plane.

expressed as [Gu96]

$$U_3(x_3, y_3) = \frac{i \exp(-\frac{2\pi iz}{\lambda})}{\lambda z} \iint_{-\infty}^{\infty} U_2(x_2, y_2) \exp\left\{-\frac{i\pi}{\lambda z} [(x_3 - x_2)^2 + (y_3 - y_2)^2]\right\} dx_2 dy_2. \quad (3.8)$$

From eq. (3.7) and (3.8), the intensity distribution of the light field in the vicinity of the focal plane (i.e. PSF) can be derived. Several important terms must, however, be introduced first:

1. Numerical aperture of the lens: $\text{NA} = n \cdot \sin \alpha \approx n \cdot a/f$, where α is defined as half the angle of the cone of light focused by the lens, and n is the refractive index of the medium.
2. Lateral coordinate: $\nu = 2\pi \cdot r \cdot \text{NA}/\lambda$, where $r = (x^2 + y^2)^{1/2}$ is the radial coordinate relative to the optical axis.
3. Axial coordinate: $u = 2\pi \cdot d \cdot \text{NA}^2/(\lambda \cdot n)$, where $d = z - f$.
4. Fresnel number: $N = a^2/(\lambda \cdot f)$.

For a circular lens, the lateral intensity distribution of the light field in the focal plane (i.e. $f = z$ and $u = 0$) is given by

$$I(\nu) = |U_3(\nu, u = 0)|^2 = (\pi N)^2 \left[\frac{2J_1(\nu)}{\nu} \right]^2, \quad (3.9)$$

where $J_1(\nu)$ is a Bessel function of the first order and the first kind, and the term in square bracket is known as the Airy function [Nov06]. Similarly, the intensity distribution along the optical axis is

$$I(u) = |U_3(\nu = 0, u)|^2 = (\pi N)^2 \left[\frac{\sin(u/4)}{u/4} \right]^2. \quad (3.10)$$

Chapter 3. Experimental Setup

One will notice that both the lateral and axial intensity distribution show an oscillatory side lobe structure surrounding the main peak [Mö5]. For the lateral distribution, approximately 80% of the incident energy is confined to the central main peak [Gu96], and the first node is located at $\nu_0 = 1.22\pi$. Hence

$$r_0 = \frac{0.61\lambda}{\text{NA}}, \quad (3.11)$$

which defines the width of the PSF in lateral direction and is also referred to as the Airy disk radius. In the case of axial distribution, the first node is located at $u_0 = 4\pi$, and hence the depth of field is given by

$$d_0 = \frac{2n\lambda}{\text{NA}^2}. \quad (3.12)$$

The resolution of a microscope determines the ability to distinguish between two objects. The Rayleigh criterion, often used to define sufficient resolution, states that two points should be considered to be just resolved if the intensity maximum of one is located at the first intensity minimum of the other [Bor99]. For this to happen, the drop in intensity between the maxima should be 26%. For conventional wide-field microscopy, the lateral resolution limit is exactly the Airy disk radius (eq. (3.11)). Although the values change, the situation along the optical axis is similar.

However, in the case of a confocal microscope, the total point spread function PSF_{con} is the product of the excitation point spread function PSF_{exc} and the detection point spread function PSF_{det} ,

$$\text{PSF}_{con} = \text{PSF}_{exc} \cdot \text{PSF}_{det}, \quad (3.13)$$

Here, PSF_{exc} corresponds to the intensity distribution of the laser spot that is focused by the objective and scans the sample, whereas PSF_{det} is the intensity distribution of the light focused by a lens on the pinhole (see Fig. 3.1). In fluorescence measurements, the excitation and detection PSFs are slightly different due to the Stokes shift. Taking the ratio of the excitation and detection wavelength as $\gamma = \lambda_{exc}/\lambda_{det}$, it can be derived that the lateral resolution in a confocal microscope is given by [Mö5]

$$r_{0,con} = \frac{1}{\sqrt{1+\gamma^2}} \cdot \frac{0.61\lambda_{exc}}{\text{NA}}. \quad (3.14)$$

In a simplified case where $\lambda_{exc} = \lambda_{det} = \lambda$, the lateral resolution is

$$r_{0,con} = \frac{0.61\lambda}{\sqrt{2}\text{NA}}, \quad (3.15)$$

which is a factor of $1/\sqrt{2}$ smaller than for conventional wide-field microscopy (eq. (3.11)). Similarly, the axial resolution in a confocal microscope is

$$d_{0,con} = \frac{1}{\sqrt{1+\gamma^2}} \cdot \frac{2n\lambda_{exc}}{\text{NA}^2} \quad (3.16)$$

and can be simplified to

$$d_{0,con} = \frac{\sqrt{2}n\lambda}{\text{NA}^2} \quad (3.17)$$

when λ_{exc} is considered to be equal to λ_{det} .

In conclusion, the main benefit of a confocal microscope is that, since it blocks the out-of-focus background signals, both the lateral and axial resolution limits can be greatly improved. Take the confocal microscope in this work as an example. The samples are illuminated by a Gaussian shaped laser beam with the excitation wavelength 470 nm, and an air objective with $\text{NA} = 0.95$ is used. The resolution limits in the lateral and axial directions are calculated to be about 200 nm and 700 nm, respectively. In practice, however, effects like aberrations, light scattering and absorption by the optical components of the microscope decrease the resolution and cause the PSF to deviate from its ideal form.

3.2 Experimental setup

The best approach to optical design is to “deliver efficiency through simplicity”. Table 3.1 lists typical intensity losses in the beam path of a confocal microscope. In our setup, only those optical elements which are absolutely necessary are used and placed in the optimal location along the optical axis, which makes the microscope rather compact and easy to maintain. A simplified schematic of the microscope is shown in Fig. 3.3. The light from a laser is spatially filtered by a fiber, and after passing through several optical components that adjust the spectrum, polarizability and intensity of the beam, is reflected by a beamsplitter and directed into a microscope objective by an elliptical plane mirror.² The microscope objective focuses the light to a single spot on the sample. Light produced by the interaction between the laser beam and the sample is collected by the same objective, filtered by longpass filters, and finally focused onto detectors. In the following the setup will be discussed separately in two main parts: the illumination part (Fig. 3.3a) and the detection part (Fig. 3.3b).

Table 3.1: Typical intensity losses in the beam path of a confocal microscope [Paw95].

element	loss(%)
single-mode fiber	< 60
multi-mode fiber	< 20
fiber collimator	< 20
mirror	1 – 3
dichroic mirror	10 – 30
filter ¹	1 – 2
$\lambda/4$ wave plate	4
beamsplitter	2
beam expander	4
lens	1 – 3

¹Here only intensity loss due to reflection is counted.

²For brevity not shown in the picture.

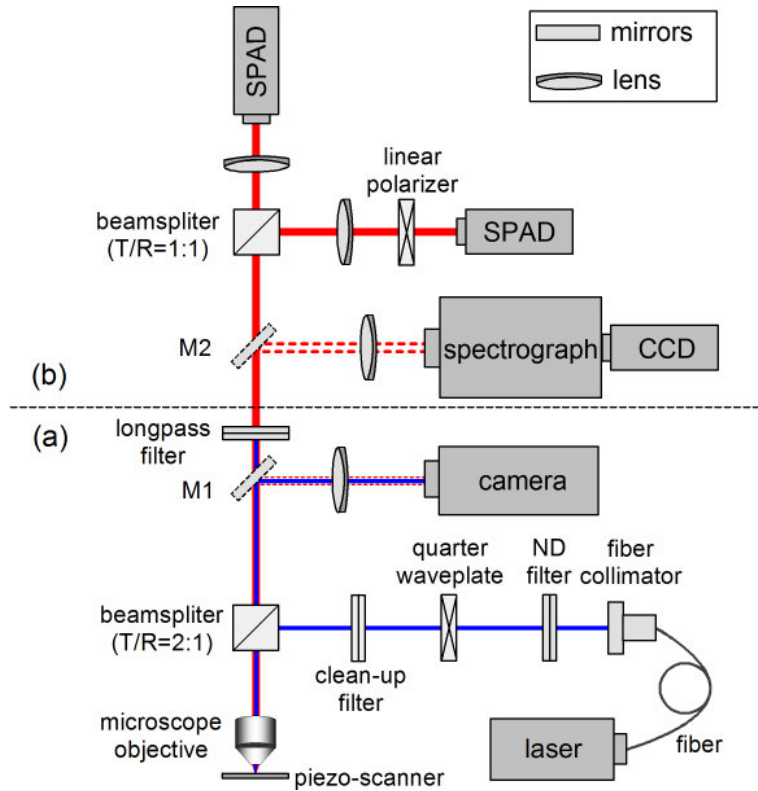


Figure 3.3: Setup of the scanning confocal microscope, which is mainly composed by two parts: (a) the illumination part and (b) the detection part. The lenses plotted with dashed lines are flexible so that they can be easily removed from or put back in the way of the beam path.

3.2.1 Illumination part

3.2.1.1 The laser system

The role of the laser system is to provide a coherent, intensity stable source of Gaussian beam (TEM_{00} mode) for the microscope. The confocal microscope shown in Fig. 3.3 uses a laser, fiber, and fiber collimator to accomplish this goal.

Laser. Laser can produce beams of light which are highly monochromatic, coherent and collimated. Basics of laser can be found in many text books. When selecting a laser for use in confocal microscopy, important performance specifications of the laser that must be evaluated include its wavelength, output power, beam stability (including intensity, wavelength and beam position stability), polarization property, and mode structure. During this work, mainly a picosecond diode laser head (LDH-D-C-470, PicoQuant GmbH) coming with an integrated laser beam coupler (60SMS-1-4-A11-01, Schäfter + Kirchhoff GmbH) together with a driver (PDL 800-D, PicoQuant GmbH) is used to generate both pulsed and continuous-wave (cw) laser beams. In the cw mode, a maximum power of 10.8 mW could be obtained. In the pulsed mode, repetition rates from 31.25 kHz to 80 MHz with peak power up to

500 mW can be selected. The central wavelength shifts slightly from 470 nm with different laser powers and operation modes (cw or pulsed). Pulse width of the beam also depends on the laser power, with a minimum of 70 ps at very low power. Since lifetimes of NCs in this work are typically on the order of ns, such a pulse width of the laser beam is sufficient. The laser driver has a sync output which allows triggering of time-correlated single photon counting (TCSPC) system (PicoHarp 300, PicoQuant GmbH) for lifetime measurements. Because diode lasers producing blue emission usually have high pumping efficiency (typically 10 mW of blue emission from an input of less than 10 W [Paw95]), they do not require water cooling.

Fiber. Among many of their wide applications, fibers in confocal microscopes are mainly used either for laser delivery and/or as a detection aperture. As an optical waveguide, fibers can guide a light beam from one place to another by the process of so-called total internal reflection. As shown in Fig. 3.4a, when a light beam is incident from a denser medium on an interface separating two media ($n_1 > n_2$) with the angle of incidence θ_1 and the angle of refraction θ_2 , from the Snell's law of refraction

$$\frac{\sin \theta_1}{\sin \theta_2} = \frac{n_2}{n_1}, \quad (3.18)$$

we have $\theta_2 > \theta_1$. For an incident angle $\theta_1 = \theta_c$ such that

$$\sin \theta_c = \frac{n_2}{n_1}, \quad (3.19)$$

the refracted light just grazes the interface. This angle is referred to as the critical angle, and for incident angles greater than θ_c , the light is reflected back into the denser medium nearly without loss. (Although in practice, loss from scattering and absorption usually exists.)

The basic structure of a frequently used type of fiber (the so-called step index fiber) is shown in Fig. 3.4b, which consists of a core of glass with circular cross-section, surrounded by a cladding zone of a different glass having a slightly lower refractive index. With this simplified schematic, one can derive the numerical aperture (NA) of a fiber with the Ray-optical treatment, which treats the core-cladding interface as an ideal mirror. Consider a beam enters the fiber from a medium (usually air)

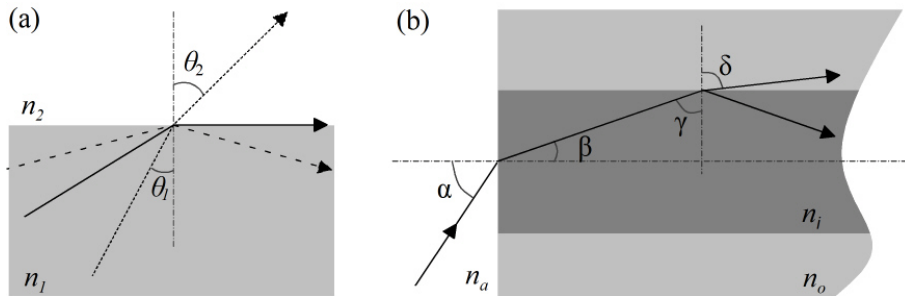


Figure 3.4: (a) Principle of total internal reflection; (b) Sketch for the calculation of numerical aperture of a fiber.

Chapter 3. Experimental Setup

of refractive index n_a , and the fiber core has a refractive index n_i , which is slightly greater than the cladding refractive index n_o . Applying Snell's law, we have

$$n_a \sin \alpha = n_i \sin \beta, \quad (3.20)$$

$$n_i \sin \gamma = n_o \sin \delta. \quad (3.21)$$

Assume the fiber axis to be perpendicular to the front face, hence $\beta + \gamma = 90^\circ$. From eq. (3.19), the limiting angle for total internal refraction is

$$\sin \gamma_{\min} = \frac{n_o}{n_i}. \quad (3.22)$$

With $n_a = 1$ for air, from the above equations we can obtain

$$\sin \alpha_{\max} = \sqrt{n_i^2 - n_o^2}. \quad (3.23)$$

This square-root value is called the NA of the fiber, i.e. $\text{NA} = \sqrt{n_i^2 - n_o^2}$, and is a measure of the light-collecting ability of a fiber. One of the single-mode fibers we use in the setup has a NA of 0.12, indicating a maximum acceptance angle of about $\pm 7^\circ$. Only beam coming within a cone of this angle will be guided in the fiber. This is why, in most cases, in order to reduce back-reflection, APC (angled physical contact) fibers have their ends polished to an angle of 8° , which is slightly larger than the maximum acceptance angle α_{\max} .

Not all the light that is able to enter the fiber, however, will be guided through. Due to different entering angles, plane waves interfere with each other either constructively or destructively. Only plane waves traveling with specific paths or angles can propagate in the fiber. These are called modes of the fiber. A detailed electromagnetic analysis of modes with Maxwell's equations [Gha08, Mit10] is beyond the scope of this thesis. However, it is useful to consider several important parameters derived from the resulting modal field:

1. V number. It is given by [Mit10]

$$V = k_0 \cdot a \cdot \text{NA}, \quad (3.24)$$

where k_0 is the wavenumber in vacuum, a the fiber core radius, and NA the numerical aperture of the fiber. The larger the V number, the more modes a fiber supports. The particular value $V = 2.405$ marks the transition point, below which the fiber is supposed to be single-mode. The corresponding wavelength is called the cutoff wavelength, which is defined by

$$\lambda_{\text{cutoff}} = \frac{2\pi \cdot a \cdot n_i \cdot \sqrt{2\Delta}}{2.405}, \quad (3.25)$$

Here, Δ is defined to be $\Delta = (n_i^2 - n_o^2)/(2n_i^2)$. For wavelengths shorter than λ_{cutoff} , two or more modes are guided within the fiber. Technically, multimode and single-mode fibers mainly differ in the diameter of the core. λ_{cutoff} of our fiber is 470 nm, which is the same as the wavelength of the laser beam. Hence,

- only a single mode can propagate through the fiber.
2. Mode-field diameter (MFD): diameter of the beam profile at exit of the fiber. For a single-mode fiber, the field of which is approximated well by a Gaussian distribution, the MFD can be approximated to be

$$\text{MFD} = \frac{2\lambda}{0.82 \pi \text{NA}}. \quad (3.26)$$

The factor 0.82 is incorporated because NA is typically given at the 5% level of the Gaussian profile while the MFD at its 13.5%. In our case, with $\lambda = 470$ nm and $\text{NA} = 0.12$, the MFD is calculated to be about $3 \mu\text{m}$, which is close to the core diameter of the fiber.

Despite of the many advantages of a diode laser (compact, highly efficient, easy to use, and relatively cheap), the generated beam is usually asymmetric and astigmatic. Taking the diode laser we used as an example, the beam diverges typically 30° vertically and 10° horizontally, leading to an elliptical beam with dimensions of $1.5 \times 3.5 \text{ mm}^2$ after the beam coupler (Fig. 3.5a). In order to obtain a beam with a perfect Gaussian beam profile (Fig. 3.5b), a single-mode fiber (Schäfter + Kirchhoff GmbH) is used as the spatial filter. Inefficiencies when launching the input of the fiber (so-called insertion losses) can be significant. The key requirement is to focus the beam onto the fiber so that there is a complete overlap between the focused beam and the acceptance cone of the fiber [Paw95] (Fig. 3.6). Here the focused beam shape is decided by the laser beam diameter D and focal length of the beam coupler f , while the acceptance cone of the fiber is mainly decided by the NA of the fiber. With the elliptical laser beam from our diode laser, the effective beam diameter can be estimated by

$$D = \sqrt{D_{\perp} \cdot D_{\parallel}}, \quad (3.27)$$

which gives us the value of $D = 2.3$ mm. From Fig. 3.6, we can derive

$$\text{NA} = \sin \alpha \approx \tan \alpha = \frac{D}{2 \cdot f \cdot 0.82}, \quad (3.28)$$

where the factor 0.82 is included for the same reason as in eq. (3.26). With $D = 2.3$ mm and $f = 11$ mm, the optimized NA of fiber is 0.127, which is close to the NA of the fiber we have chosen.

In practice, during the alignment, the center of the fiber at its input end from the integrated beam coupler must be adjusted carefully with adjustment screws until the output power from the fiber reaches its maximum. The average relative intensity fluctuations for the diode laser at the fiber output is stable to about 0.1%.

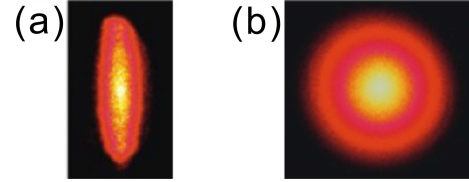


Figure 3.5: Beam shape after leaving a diode laser: (a) laser not coupled to a fiber; (b) laser coupled to a single-mode fiber. (The diagrams are modified from originals provided by PicoQuant GmbH.)

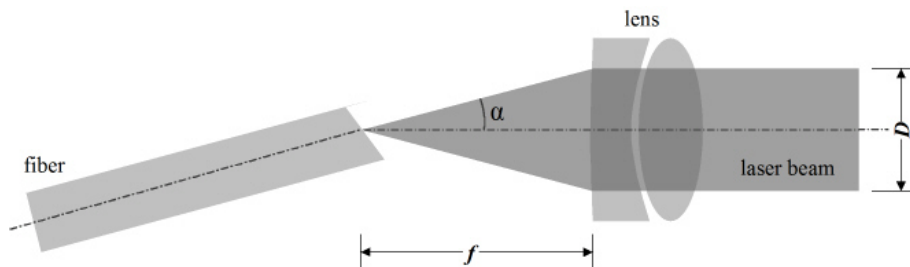


Figure 3.6: Principle of coupling a fiber to a laser beam coupler/collimator.

Fiber collimator. Due to diffraction, the Gaussian beam from the fiber end diverges [Nov06]. For a NA of 0.12, the total angle of divergence (2α) after the fiber can be calculated via

$$\text{NA} = \sin \alpha \quad (3.29)$$

to be $2\alpha \approx 13.8^\circ$. To transform it into a parallel, collimated beam with certain diameter, the end of the fiber is placed at the focal plane of a collimator (60FC-T4-M30-04, Schäfter + Kirchhoff GmbH) (Fig. 3.6). When choosing a collimator, several important parameters should be considered:

1. NA of the collimator. To ensure that the collimator does not cut off part of the incoming beam, a good rule of thumb is to select collimators with a NA at least 50% larger than the fiber, which ensures over 99% transmission. We have chosen a collimator with $\text{NA} = 0.22$, which is 1.8 times of the NA from the fiber.
2. Beam divergence. In practice, it is impossible to obtain a perfectly collimated beam, as all beams will spread out after traveling a certain distance. The total angle of beam divergence θ after a collimator is given by

$$\theta = \frac{\text{MFD}}{f}, \quad (3.30)$$

where f is the focal length of the collimator, and MFD the mode field diameter of the fiber. With $f = 30 \text{ mm}$, and $\text{MFD} = 3 \mu\text{m}$ in our system, $\theta = 0.1 \text{ mrad} \approx 0.006^\circ$, which is much smaller than the divergence angle from the fiber and almost negligible.

3. Beam diameter D after the collimator. To obtain the highest resolution of a confocal microscope, the excitation laser beam should slightly overfill the back aperture of the objective (3 – 6 mm) in order to make use of its full NA (see section 3.1.3). From eq. (3.28) and Fig. 3.6, we can estimate the beam diameter after the collimator to be $D \approx 6 \text{ mm}$, which fulfills the requirement.

The same as for the beam coupler, the relative positions of the fiber and the collimator should be adjusted until maximum output power is reached. In addition, the collimator should be aligned so that the output Gaussian beam propagates exactly along the optical axis of the system.

3.2.1.2 Lens and filter

Lens. When selecting lenses for an optical system, paraxial calculations are usually performed in the first place to estimate critical parameters such as focal length, objective and image positions, and clear aperture (typical 90% of lens diameter). To begin, the thin-lens approximation which neglects the distance between the lens' principal points is applied. The relationship among focal length f , relative distances of the objective s_o and image s_i from the lens is given by the equation

$$\frac{1}{f} = \frac{1}{s_o} + \frac{1}{s_i}, \quad (3.31)$$

while the magnification m is given by

$$m = \frac{s_i}{s_o}. \quad (3.32)$$

For more accurate calculations, the thin-lens approximation is not always applicable and one has to take the deviation of ray when passing through a thick lens into account (see e.g., the Melles Griot catalogue).

Like other optical elements, the performance of a lenses is limited by diffraction. When a positive lens with focal length f is used to focus a collimated light beam with diameter of D , the diffraction-limited spot size d can be calculated from equation

$$d = \frac{1.22\lambda}{\text{NA}} = 2.44\lambda \frac{f}{D}. \quad (3.33)$$

The clear aperture CA of the lens should be larger than the incident beam diameter D to guarantee maximum transmission. The value f/CA is usually referred to as the f-number of a lens, and it is half of the value of $1/\text{NA}$ from the lens. In practice, several types of lens errors affect the resolution, in particular spherical and chromatic aberrations which depend on lens shape and material. The situation can be improved by using achromatic doublets, which are two-lens systems and correct for both spherical and chromatic aberration.

When selecting a lens, aside from the above mentioned focal length, clear aperture and shape, the material of a lens should also be considered. Typical materials used for lens substrates include synthetic fused silica, N-BK7, and several other materials (see the Melles Griot catalogue). They are usually coated with thin layer(s) of special materials to modify the reflection properties. Important factors that should be evaluated include transmission versus wavelength, thermal, mechanical and chemical characteristics, as well as cost.

Filter. Filters are employed to selectively block desired wavelength bands from the incident beam or regulate the intensity of the light. The former, generally referred to as wavelength selective filters, can be classified into two groups: (1) bandpass filters that only transmit a band of wavelengths, and (2) edge filters, which include longpass and shortpass filters. Longpass filters only transmit light with wavelengths longer than a certain wavelength while shortpass filters transmit light with wavelengths shorter than a certain wavelength.

According to the different production techniques, there are mainly two types of filters:

1. Absorption filters. They are generally composed of colored glass (also called absorption glass) or polymers that attenuate light solely by absorption [Paw95]. Such filters are relatively inexpensive and their spectral characteristics are independent of the incident angle. However there is only a limited selection of such materials, and many of them are autofluorescent. In addition, the bandpass types have a poor slope and the peak transmittance is usually low. Also, since they absorb light, these filters might be overheated and crack under intense illumination.
2. Interference filters. They are composed of several layers of special materials (dielectric materials or metal oxides) with a thickness of around a quarter or one-half of the target wavelength and a substrate of optical-grade glass. Light incident on the filter surface is either reflected due to constructive interference or transmitted by destructive interference. As compared to color glass filters, interference filters have improved flexibility of performance and provide very sharp transmission slopes. To obtain the optimal performance, interference filters should be oriented with the reflective, metallic looking surface towards the incident light beam. Additionally, the light beam should pass perpendicularly to the filter surface (so-called normal incident). Otherwise, the spectral characteristics shift to shorter wavelengths and sometimes polarized light is produced.

A combination of neutral-density (ND) filters is often used to regulate the intensity of laser beams equally at all wavelengths. ND filters are made of absorptive gray glass (for low power) or glass coated with a reflective metallic film (for high power). Optical density (OD, also called absorbance), which is related to transmittance (T) by

$$\text{OD} = -\log_{10}(\text{T}), \quad (3.34)$$

is usually used to describe the transmission of light through a ND filter. In our setup, since low power (<1 Watt) is typically applied, five absorptive ND filters (NE02B, NE05B, NE10B, NE20B, and NE40B, Thorlabs) with OD from 0.2 to 4 are combined to adjust light intensity (Fig. 3.7a).

Due to the rather broad spectral width of the laser beam from the diode laser, spectral filtering is crucial and realized by a laser clean-up filter (MaxDiode LD01-473/10-25, Semrock) with center wavelength of 470 nm, bandwidth of 10 nm, and average transmission > 90% in the wavelength range 468 – 478 nm (Fig. 3.7b). Since it is an interference filter, its orientation and the incident angle of the laser beam are important.

Common fluorophores usually have a Stokes shift of 20 to 100 nm [Paw95]. In fluorescence microscopes, in order to transmit the emission from samples and block interference due to scattered and stray light, dielectric mirrors or longpass filters are typically used depending on the Stokes shift of the sample. In principle, monochromators can also be used to serve the purpose, but observation through a filter can often have a signal level 50-fold higher than through a monochromator, because the

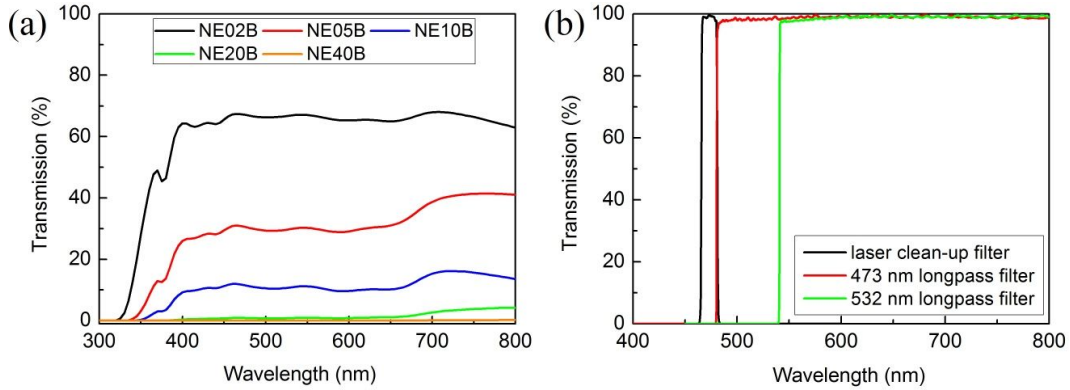


Figure 3.7: Transmission characteristics of (a) ND filters, (b) laser clean-up filter and longpass filters used in this work. (Original data is provided by Thorlabs and Semrock.)

bandpass of the observation is increased and the attenuation due to the monochromator is removed [Lak06]. Since the NCs we investigated usually have PL wavelengths longer than 530 nm, two longpass interference filters with edge wavelength 479.8 nm (RazorEdge LP02-473RS-25, Semrock) and 539.6 nm (RazorEdge LP03-532RS-25, Semrock) are placed before the detectors to block the excitation beam (Fig. 3.7b).

3.2.1.3 Beamsplitter and wave plate

Beamsplitter. Beamsplitters are used to split an incoming light beam into two separate arms – a transmitted beam and a reflected beam. The intensity ratios of the two beams usually vary between 1 : 1 and 1 : 4, and the polarization of the beams depends on the coating materials as well as the nature of the incoming beam. The beamsplitting surface is mounted at a 45° angle to the incoming beam. Beamsplitters are broadly classified into three groups: plate, cube, and pellicle beamsplitters (Fig. 3.8).

In a plate beamsplitter (Fig. 3.8a), a partially reflecting film is deposited on the side facing the incident light, and an antireflecting coating is deposited on the back side. Because the coating materials are usually selected to have negligible absorbance in the visible light region, plate beamsplitters can be used for a wide spectrum range and high-energy applications. However, plate beamsplitters are polarization sensitive, i.e., they have unequal transmission and reflection for p and s polarization components. In addition, ghosting from the antireflection coated surface and shift of the transmitted beam (approximately 0.3 times the thickness of the substrate) can pose potential problems.

A cube beamsplitter (Fig. 3.8b) is composed of two right-angled prisms. A partially reflecting coating is deposited on the hypotenuse surface of one prism. The fact that the reflective surface is protected between the prisms makes a cube beamsplitter more resistant to mechanical damages. This design also eliminates beam offset. In practice, the cube beamsplitter should be placed so that the incident light enters the beamsplitter through the prism that has been coated with reflecting film

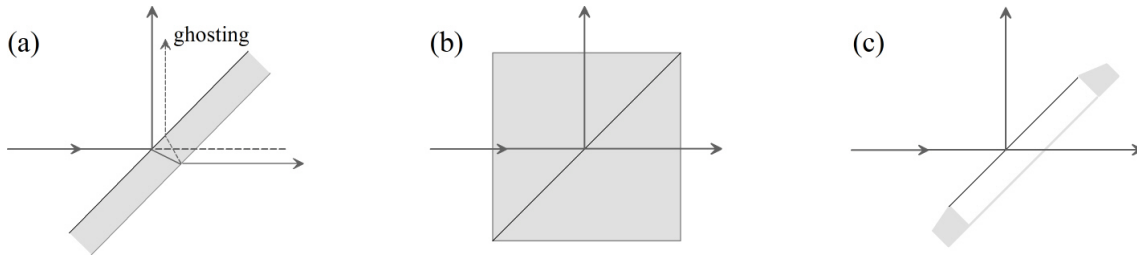


Figure 3.8: Schematic of three main types of beamsplitters: (a) Plate beamsplitter. Both beam offset and ghost reflection exist. (b) Cube beamsplitter. Beam offset is eliminated, but ghost reflection still exists. (c) Pellicle beamsplitter. Both beam offset and ghost reflection are eliminated.

in order to reduce the influence of the optical cement used to glue the prisms together. Antireflection coatings are applied on the entry and exit faces to minimize back reflections, which can also lead to ghost reflections from those faces. Additionally, the power-handling capability of cube beamsplitters is limited due to the cement applied at the bonded interface.

The third important class of beamsplitters is the pellicle beamsplitters (Fig. 3.8c), which consist of a thin ($2 - 10 \mu\text{m}$), elastic membrane (e.g., nitrocellulose) stretched like a canvas over a flat metal frame. A pellicle beamsplitter can virtually eliminate beam offset and ghost images. The drawback is their extremely delicate nature and small power-handling capability. The beamsplitter surface cannot be touched and can only be cleaned by a gentle flow of air.

In this work, since emission from NCs is usually weak and low excitation power is required, a cube beamsplitter (Optarius) with transmittance : reflectance = 2 : 1 is used to transmit and reflect laser beams/emissions. Sometimes, for a two-channel measurement (e.g., anti-bunching measurements, polarization-dependent measurements), a second beamsplitter is placed in front of the SPAD to set up a second detection channel.

Wave plate. Optical wave plates are constructed from birefringent materials and used to transform the polarization state of incoming beam. Birefringent materials are anisotropic crystals that exhibit different refractive indices for its ordinary and extraordinary axes. The axis with lower refractive index is called the fast axis, and the other is called the slow axis. Wave plates are made with the two axes in the plane of surface, so that when incident light propagates perpendicular to the axes, the two orthogonal components along the two axes will propagate at different velocities and a phase shift is induced. Wave plates are characterized by the phase shift (ϕ), which is calculated by the equation

$$\phi = \frac{2\pi\Delta nL}{\lambda_0}, \quad (3.35)$$

where Δn is the birefringence, L the thickness of the crystal, and λ_0 the wavelength of incident light in vacuum.

Two commonly available types of wave plates are the quarter-wave plate and the half-wave plate. A quarter-wave plate creates a phase shift of $\lambda/4$ (90°). When a

linearly polarized beam is aligned 45° to the ordinary (or extraordinary) axis, the output beam will be circularly polarized. Conversely, a circularly polarized beam will be transformed to a linearly polarized one. Half-wave plates create a phase shift of $\lambda/2$ (180°). They are typically used as polarization rotators because, when a linearly polarized beam is normally incident on a half-wave plate at an angle θ with respect to the extraordinary axis, the output beam will still be linearly polarized but the polarization plane will be rotated at an angle of 2θ with respect to the extraordinary axis. Similarly, a clockwise circularly polarized beam will be transformed to a counterclockwise circular polarized beam.

In this work, the laser beam is linearly polarized. Before entering the objective, the laser beam polarization is converted from linear to circular with a polarizer (DGL10, Thorlabs) and a quarter-wave plate (AQWP05M-600, Thorlabs). Here, the polarization plane of the laser beam is first found by rotating the polarizer in the beam path. Then, the quarter-wave plate is inserted between the source and the polarizer, and its fast axis is located at an angle of 45° from the polarization plan of the laser beam. Checking the quality of the output circularly polarized light at the objective by rotating the polarizer, the intensity of light passing through the objective should remain unchanged. Otherwise, it means that the light is probably elliptically polarized and the wave plate should be tilted slightly about its fast axis until constant intensity at the objective is achieved.

3.2.1.4 Microscope objective and scanning stage

Microscope objective. Optical performance of the objective in a microscope is crucial for determining the information content of a measurement. Every objective consists of a number of optical lens elements (as many as 14 for some apochromat objectives) that are carefully aligned and cemented together. Consequently, even the same type of objectives from the same manufacturer can exhibit large performance differences. When selecting an objective, several main parameters need to be considered.

The NA is a measure of the light collecting ability of an objective and determines the resolution limit of a microscope. As mentioned before, it is related to the refractive index of the medium between objective and sample n , and the half objective angular aperture α by the equation $NA = n \sin \alpha$. Although α has a practical upper limit of about 72° , by applying immersion oils, NA can be as much as 1.6. Care should be taken to the medium between the objective and sample because turbulence (e.g. when focusing) or inhomogeneities (e.g. air bubbles in the immersion oil) can be easily created.

Originally in conventional microscopes, tube length refers to the distance between the objective mounting surface and the shoulder of the ocular [Mö5], and the objective is supposed to form an optimized real image at the distance of tube length (160 mm according to the German DIN standard) (Fig. 3.9a). Objectives with such finite tube length can form real images directly without additional tube lenses. Modern objectives are infinity corrected, i.e., if the sample is placed in the front focal plane of the objective, its image is formed at infinity. In order to form a real intermediate image, an additional tube lens is required (Fig. 3.9b). The advantage of an infinity

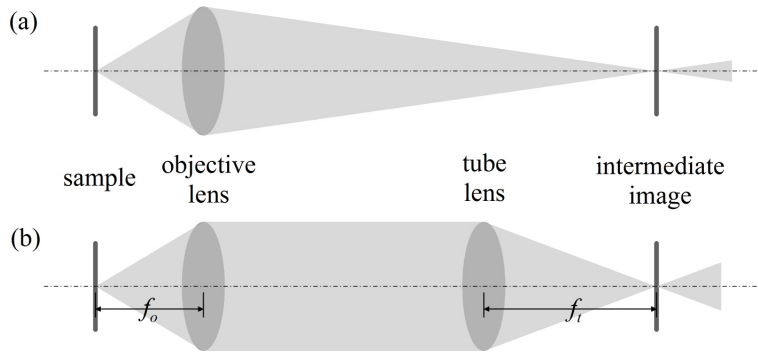


Figure 3.9: Schematic of the light beam path for (a) a finite corrected optical system, and (b) an infinity corrected optical system.

corrected objective is its relative insensitivity to optical components in the telescopic space between the objective and tube lens [Paw95]. In addition, the magnification can be maintained even when the distance between the objective and tube lens is changed.

The magnification (M) of an objective can be calculated from the focal length of the objective f_o and the tube lens f_t by

$$M = \frac{f_t}{f_o}. \quad (3.36)$$

It can be further related to the back aperture D and NA of the objective by equation

$$D = \frac{2 \cdot \text{NA} \cdot f_t}{M \cdot n}. \quad (3.37)$$

For some air objectives with a high NA and a low magnification, values of D can be as large as 20 mm, and are limited by the size of objective mounting threads. This is one of the reasons why some manufacturers (notably Nikon and Leica) have broken from the RMS (Royal Microscopical Society) standard and introduced larger mounting thread sizes. Magnification is also related to the numerical aperture on the objective side (NA) and on the image side (NA') by equation

$$M = \frac{\text{NA}}{\text{NA}'}. \quad (3.38)$$

In some special applications, the working distance (WD), which is defined as the distance between the front of an objective and its focal plane, becomes critical. In general, the WD decreases with increasing magnification and NA. Special long-, extra-long-, super-long-, and ultra-long-working-distance (LWD, ELWD, SLWD and ULWD, respectively) objectives have been developed for specific purposes.

Another important parameter of objectives is their spectral transmission. To increase the transmission, special antireflection coatings are deposited on the lens surfaces. Due to wavelength dependence, transmission of the objective for the excitation and emission light could be different.

Table 3.2: List of objectives used in this work.

manufacturer	type	magnification	NA	immersion medium
Olympus	MplanApo	100x	0.95	air
Zeiss	Achroplan	100x	1.25	oil
Zeiss	A-plan	10x	0.25	air

Due to the complexity of objectives, various types of aberrations exist, the most common of which are spherical aberrations, chromatic aberrations, field curvature, coma and distortion. Those aberrations are usually interconnected, and it is impossible to eliminate them completely within a single objective. According to the types of aberrations that are corrected for, microscope manufacturers have classified various types of objectives into five main groups: achromat, flurite, apochromat, planachromat and planapochromat. Here, “achro” and “apochro” are used to specify the amount of correction for chromatic aberrations: “achro” for two wavelengths and “apochro” for three. The standard wavelengths used for correction are 486.1 nm, 546.1 nm and 656.3 nm [M05]. In addition, “plan” is used to refer to correction for field curvature.

Mainly three different objectives are used in this work for different applications (listed in Table 3.2). Vertical motion of the objective is realized by mounting it onto a motorized piezo actuator (Picomotor Actuator 8303, Newport). Linear resolution of less than 30 nm and maximum travel range of 50.8 mm could be achieved. The main components of the actuator include two jaws that grasp an 80 pitch screw, and a piezoelectric transducer (PZT) (Fig. 3.10). Since slow action of the PZT rotates the screw while fast action causes no rotation, by sending electronic pulses with fast rise time and slow fall time, the PZT will rotate the screw clockwise (Fig. 3.10b). Similarly, to rotate the screw counterclockwise, pulses with slow rise time and fast fall time should be sent (Fig. 3.10c). A homebuilt driver is used to generate electronic pulses and provide control of the actuator. To focus the laser beam, the mirror in front of the camera (DigiMicro 2.0 Scale, dnt GmbH) (M_1 in Fig. 3.3) is moved into the optical beam path so that light from the objective is reflected and focused onto the camera. By moving the objective up or down along the optical axis, optimized focus position can be easily found with the online monitor of the

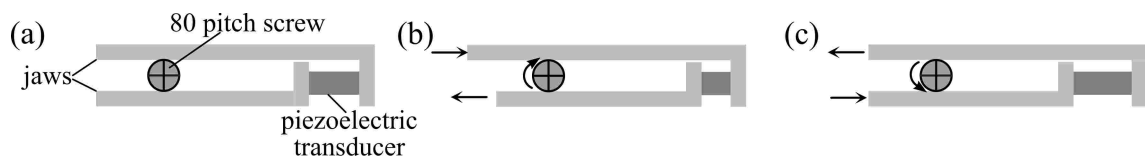


Figure 3.10: Schematic of the action of a piezo actuator. (a) The actuator is mainly composed by two jaws, an 80 pitch screw and a PZT. Slow action of the PZT causes the screw to rotate whereas fast action causes no action. (b) When pulses with fast rise time and slow fall time is sent, the PZT will rotate the screw clockwise. (c) When pulses with slow rise time and fast fall time is sent, the screw will rotate counterclockwise. (The diagrams are modified from originals provided by Newport.)

camera.

Scanning stage. As mentioned in section 3.1.1, sample scanning can be performed in several ways and stage scanning is one of them. In general, a scanning stage should provide high accuracy and vibration stability as well as a sufficient scanning range and enough affordable weight of the sample.

In our setup, the samples are mounted onto a piezo scanning stage (P-527.3CD, PI) with XYZ linear travel ranges up to $200 \times 200 \times 20 \mu\text{m}$ and sub-nanometer resolution. A 3 channel piezo controller system (E-500.00, PI) provides precise control of the XYZ positions, and through an ADwin-gold box (Jäger GmbH), real-time communication to the PC is achieved using program packages written with the LabView programming code. Because this work is mainly about the investigation of single particles deposited on substrate surfaces, only relative positions in x- and y-directions are important and recorded, while the extra control in the z-direction is mainly used to help focus laser beam onto sample. Severe position drift with time is avoided (only $< 10 \mu\text{m}$ overnight) by applying a closed loop feedback. A clear aperture of $66 \times 66 \text{ mm}^2$ of the scanning stage provides sufficient space for fitting in the objective and its holder.

3.2.2 Detection part

3.2.2.1 SPAD

Like the photomultiplier tubes (PMTs), avalanche photodiodes (APDs) are frequently used for the detection of single-photons. In general, an APD is a solid-state semiconductor device that operates by the “avalanche effect”: when an electron-hole pair is generated by the incoming photon, they subsequently accelerate in the opposite directions due to an external reverse voltage that is applied. By random collisions with the lattice of the semiconductor material, a second electron-hole pair is generated by the electron. This effect is called impact ionization. The newly generated electron and hole both obtain kinetic energy from the electric field and create even more electron-hole pairs. Standard APDs operated with the reverse voltage below the breakdown voltage (the minimum reverse voltage to make the diode conduct) can deliver a stable gain on the order of 10^2 to 10^3 [Bec05].

To push the gain to a higher level but retain the stability of the device, the external reverse voltage is deliberately set several volts above the breakdown voltage. As a result, absorption of each photon induces one avalanche breakdown which leads to an easily detectable current pulse, and this makes detection of single photon possible. To avoid the avalanche destroying the diode, an active or passive quenching circuit lowers the avalanche current and restores normal operation after each photon. This kind of principle is often called Geiger mode and it is widely used for SPAD [Bec05]. Silicon SPAD with a stable gain of 10^5 to 10^6 has recently been developed.

So far typical materials applied for SPAD include Si, Ge, InGaAs, and GaN. As with regular photodiodes, the maximum wavelength (λ_{max}) a SPAD can detect is determined by the bandgap energy (E_g) of the semiconductor material with equation

$$\lambda_{\max} = \frac{1240}{E_g}, \quad (3.39)$$

where λ_{\max} is in the unit of nm, and E_g in eV. For wavelengths larger than this value, the energy of the photons is no longer sufficient to excite electron-hole pairs. This wavelength is usually called the cut-off wavelength. Si has an E_g of 1.12 eV. As a result, a commercially available Si SPAD usually has a cut-off wavelength of 1100 nm.

The detection efficiency of a SPAD is usually characterized by its quantum efficiency (QE), which is defined as the fraction of the incident photons that contribute to electron-hole pair generation. It is related to the sensitivity (S_{en}) of the device, which is defined as the minimum detectable optical input power that can be sensed with a SNR of unity, by equation [Bec05]

$$\text{QE} = S_{en} \frac{hc}{e\lambda} = \frac{S_{en}}{\lambda} \cdot 1.24 \cdot 10^{-6} \frac{\text{Wm}}{\text{A}}. \quad (3.40)$$

Here, h is the Planck constant, e the elementary charge, λ the incident wavelength, and c the velocity of light. Fig. 3.11 shows the QE of the two silicon SPADs (PDM 50CT, PicoQuant GmbH) used in this work. At the typical PL wavelength of NCs used in this work (580 – 600 nm), the QE is about 45%, which is relatively low compared to the SPCM-AQR module from Perkin Elmer Inc.

As discussed in section 3.1.2, dark current caused by thermal generation of electrons and holes exists in all semiconductor devices. Shot noise associated with the dark current ultimately determines the limit to the sensitivity of a SPAD. To reduce the dark current, some commercially available detectors are mounted on thermoelectric coolers to keep the temperature a few tens of degrees below 0°C. In addition, since dark count rate increases more than proportionally with the area [Bec05], SPADs are designed with considerably smaller active areas (on the order of 10 to 200 μm in size) than APDs. The sensitivity of the active area is position dependent, usually highest in the center. So it is recommended to focus the light beam to the center of the active area. The SPADs we used have an active area with a diameter of 50 μm and are supplied with thermoelectric coolers, which reduce the dark count rates to < 100 cps.

When SPADs are used for TCSPC measurements, the timing resolution (sometimes called timing jitter) becomes of key importance because it is closely related to IRF of the measurement. It is defined as the width of the statistical distribution of the difference between the photon arrival time and the electrical output of the detector [Li93]. When designing a SPAD, there's a trade-off between high timing

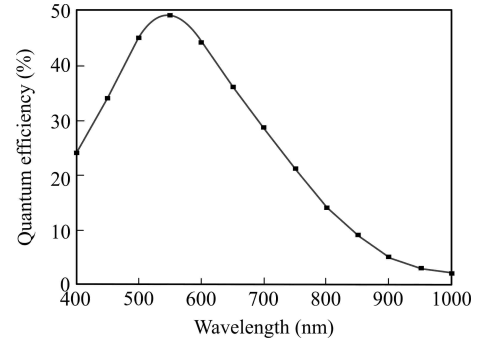


Figure 3.11: Quantum efficiency of the SPADs used in this work as a function of wavelength. (The diagram is modified from original provided by PicoQuant GmbH.)

resolution and high QE. Therefore, ultrafast SPADs usually have low QEs. The timing resolution of the SPADs in this work is 250 ps with TTL counting output (positive long duration pulses) and down to 50 ps with classical NIM timing output (fast negative pulses), which is noticeably better than the SPCM-AQR module from Perkin Elmer Inc.

Another important parameter of SPADs closely related to TCSPC measurement is the dead time, during which the detector is unable to accept a new input event after the detection of a previous one [Bec05]. This is because, in semiconductor materials, defects, such as impurities, dislocations, and vacancies, always exist in the crystal lattice and can give rise to charge trapping levels. When charges trapped during an avalanche are released, a new avalanche will be triggered, even though it is unrelated with the photon arrival. This situation makes it necessary to disable the SPAD for certain time until all the trapped charges have been released. This waiting time is known as the dead time of the SPAD. The counting loss, which refers to the fraction of photons lost in the dead time, is characterized by the counting efficiency E defined as the ratio of the numbers of recorded and detected photons. E can be calculated by equation [Bec05]

$$E = \frac{1}{1 + r_{det} \cdot t_d}, \quad (3.41)$$

with r_{det} as the detector count rate, and t_d the dead time. The dead time of the SPADs used in this work is typically 77 ns.

3.2.2.2 Spectrograph and charge-coupled device (CCD)

Spectrograph. As shown in Fig. 3.3, when the mirror M_2 is flipped into the optical beam path, the emission after passing through the longpass filters will be guided and focused to the spectrograph. The general principle of the grating spectrograph used in this work (SpectraPro-300i, Acton Research) is illustrated in Fig. 3.12. This mounting, called the Čzerny-Turner configuration, is by far the most popular arrangement [Jam07]. After the emission beam is focused on the plane of the input slit by a lens, it is further collimated by a parabolic mirror and diffracted by one of the gratings mounted on a triple turret. A second parabolic mirror focuses the diffracted light onto the plane of the active area of the CCD camera coupled to the

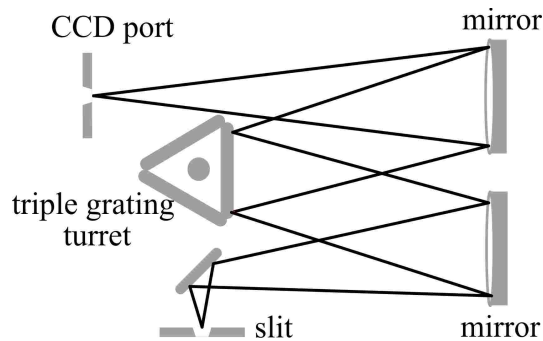


Figure 3.12: Schematic of the principle of a spectrograph with the Čzerny-Turner configuration.

spectrograph to generate a spectrum of the input light. The reason why parabolic mirrors are preferable to spherical ones is that the formers can help to reduce the coma of the system [Jam07]. By rotating the grating, the output wavelength can be varied. Sometimes, the spectrograph can also be used as a monochromator by simply adding an output slit.

At some point, optical performance of a spectrograph is mainly determined by its grating. When a polychromatic beam reaches the grating, diffraction takes place and the angle at which each spectral component is reflected depends on its wavelength. As shown in Fig. 3.13a, parallel rays 1 and 2 with the same wavelength λ incident at an angle θ_i relative to the grating normal of a diffraction grating with groove spacing D . Here the signs of the angles are measured from the grating normal: positive when they are measured counterclockwise from the grating normal and negative when measured clockwise. It is clear that ray 2 travels a different distance from ray 1. The traveling difference in the incident beam path (l_i) and reflected beam path (l_r) can be computed from Fig. 3.13b and Fig. 3.13c as

$$l_i = D \sin \theta_i, \quad (3.42)$$

$$l_r = -D \sin \theta_r. \quad (3.43)$$

Thus, the total difference is

$$\begin{aligned} l_{total} &= l_i - l_r \\ &= D \cdot (\sin \theta_i + \sin \theta_r). \end{aligned} \quad (3.44)$$

For constructive interference to occur, this distance must equal an integer multiple of the wavelength, i.e.,

$$D \cdot (\sin \theta_i + \sin \theta_r) = m \cdot \lambda. \quad (3.45)$$

This equation is called the grating equation, where the integer m is called the diffraction order. When $m = 0$ (zero-order), it can be derived that $\theta_i = -\theta_r$, which indicates that the grating serves as a simple mirror.

Several parameters are frequently used to characterize a grating. The groove

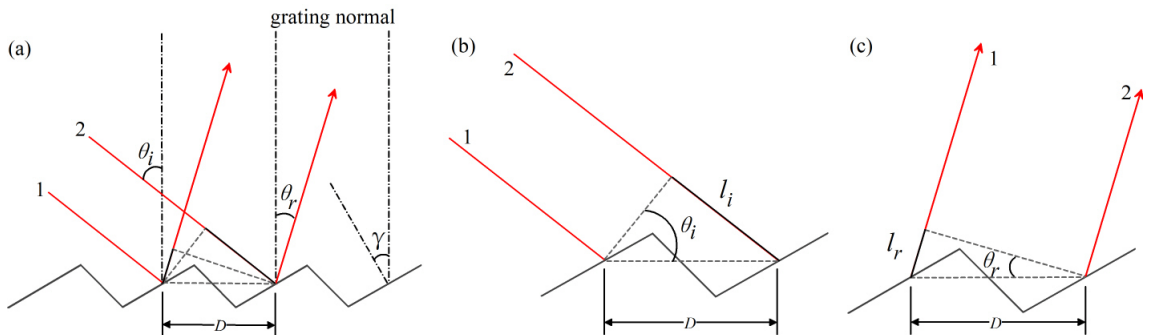


Figure 3.13: (a) Schematic showing the beam path of two rays incident on a diffraction grating. (b) Traveling difference in the incident beam path. (c) Traveling difference in the reflected beam path.

Table 3.3: Main parameters of gratings for SpectraPro-300i used in this work.

grating	groove density (grooves/mm)	blaze wavelength (nm)
1	50	600
2	150	500
3	600	500

density G is defined as $G = 1/D$ and is usually given in “grooves per mm”. The angle γ between the grating normal and the normal of the groove surface is called the blaze angle (Fig. 3.13a). In the special case when the reflected light returns along the same path as the incident light, i.e., $\theta_i = \theta_r = \gamma$, eq. (3.45) can be simplified to

$$2D \sin \gamma = m \cdot \lambda, \quad (3.46)$$

indicating that, for a wavelength λ , most of the reflected light is concentrated to the m th-order. Since in the zero-order ($m = 0$), all wavelengths overlap with each other and are not spectrally resolved, usually maximum efficiency for the 1st-order ($m = 1$) is fulfilled and the corresponding wavelength λ_b is called the blaze wavelength, which can be calculated as $\lambda_b = 2D \sin \gamma$. Thus, for λ_b , all the incident light is reflected into the 1st-order and all other orders (including the zero-order) are suppressed. Main parameters of the gratings used in this work are listed in Table 3.3.

The spectral resolution of a spectrograph R represents the ability of the spectrograph to separate two adjacent spectral lines. If the minimum spectral distance between two lines in the vicinity of λ that can be isolated by the spectrograph is $\delta\lambda$, then R is given by

$$R = \frac{\lambda}{\delta\lambda}. \quad (3.47)$$

Theoretically, spectral resolution is decided by the number of grooves N that exist in the grating [Jam07]:

$$R = N \cdot m. \quad (3.48)$$

However, the imperfections of manufacture make this practically unrealizable. Aside from N , longer optical length traveled by the light beam inside the spectrograph and larger distances between the grating and the slits enhance the spatial separation between the different spectral components and therefore increase spectral resolution. The slit width is also closely related to R . For a smaller slit width, the spectrum width $\delta\lambda$ also decreases, leading to higher resolution. However, it should also be noted that the output intensity and SNR are also lower for smaller slit width.

Sometimes, even though two separate lines are not resolved, spectral features, such as wider, asymmetrical line shapes, indicate the presence of more than one spectral lines. This is often used as a criterion in the determination of single NCs at room temperature.

In practice, the spectrograph resolution is usually set by the width of the CCD pixels and the slit width is chosen to match this width. Starting from eq. (3.45), for a collimated incoming beam with different wavelengths, differentiation of the

equation with respect to λ gives

$$\frac{d\theta_r}{d\lambda} = \frac{m}{D \cos \theta_r}. \quad (3.49)$$

As a result, linear dispersion of the spectrum in focal plane (x direction) of the CCD camera is given by

$$\frac{dx}{d\lambda} \approx f \frac{d\theta_r}{d\lambda} = \frac{f \cdot m}{D \cos \theta_r}, \quad (3.50)$$

with f as the focal length of the camera. For a certain wavelength λ , the width of the input slit can be related to the width of its image by differentiating eq. (3.45) with respect to θ_i :

$$\cos \theta_i d\theta_i = -\cos \theta_r d\theta_r. \quad (3.51)$$

This is called the lateral magnification and should be taken into account during the design [Jam07].

When coupling a spectrograph to the main beam path, the input light cone must match the acceptance cone of the spectrograph. Moreover, to guarantee the whole source is imaged, the slit size must be larger than the image in the input plane. After the spectrograph is installed, the wavelength calibration should be checked regularly. This can be performed with a mercury argon lamp (HG-1, Ocean Optics). During the calibration, in order to increase the precision of wavelength determination and to decrease light intensity, a small slit width should be used. The lamp is placed above the objective and a small amount of the light enters the spectrograph. The dominant Hg lines are located in the spectrum and assigned the corresponding wavelengths. Since there are multiple Hg lines, it sometimes helps to use the laser beam with known wavelength (e.g. 470 nm) together with the Hg lines to make sure that a line is assigned to the correct wavelength.

Charge-coupled device (CCD). Spectrally resolved light from the spectrograph is focused onto the active area of the CCD camera (Imager QE, LaVision) and a spectrum is formed. The basic concept of CCDs is an array of Metal-Oxide-Semiconductor capacitors (MOS capacitors), and each capacitor represents a pixel. A cross-sectional view of a p-type MOS capacitor from a buried-channel CCD is shown in Fig. 3.14a. It consists of a p-type silicon substrate with a thin n-type layer formed on the surface, an insulating silicon dioxide layer, and a metal electrode (gate). When a positive voltage is applied to the gate electrode to reverse bias the p-n junction, holes in p-type silicon substrate and electrons in n-type silicon layer are driven away from the interface of the junction, leaving behind a depletion region. Meanwhile, a potential well is formed in the n-type silicon layer (Fig. 3.14b). Incident photons generate electron-hole pairs in the depletion region and the electrons migrate upwards the n-type silicon layer and are confined in the potential well. The build up of electrons is directly proportional to the number of incident photons.

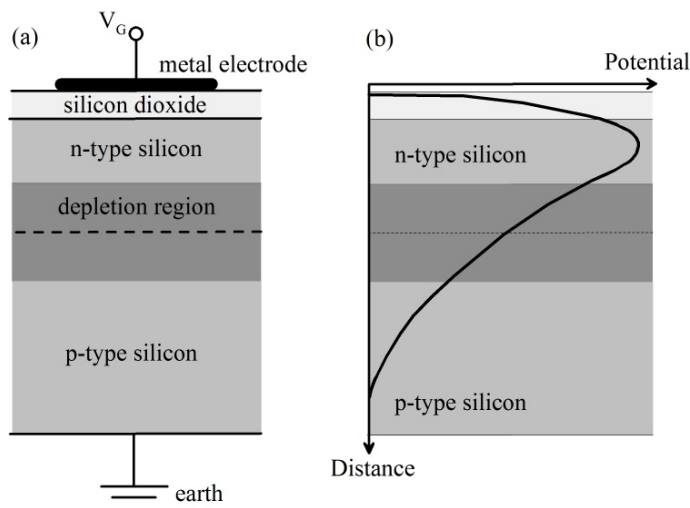


Figure 3.14: (a) Cross-section of a p-type MOS capacitor from a buried-channel CCD. (b) Potential well in a p-type MOS capacitor.

Once the exposure time has elapsed, the trapped charges in the MOS capacitors have to be exported. The charge readout process includes two steps: (1) the charges are moved from one pixel to another pixel across the surface of the capacitor array, and (2) they are read out row by row into an output register prior to being digitized. As shown in Fig. 3.15, the concept of a “bucket brigade” can be used to describe this process [Jan01].

Moving charges across the device is realized by manipulating the voltages applied on the gate electrodes. The detailed procedure is presented in Fig. 3.16. In general, each pixel (MOS capacitor) is divided into three distinct areas called phases (ϕ_1, ϕ_2, ϕ_3). During the exposure time (Fig. 3.16a), the potential applied on phase 1 (V_1) is higher than on the other two (V_2). As a result, there is a deeper depletion region in phase 1 and charges are confined in it. At the end of the exposure time (Fig. 3.16b), when the charges need to be transferred, the potential of phase 2 is enhanced to V_1 , which removes the potential barrier between phase 1 and 2. At this point, charges distribute themselves uniformly over the whole region by diffusion. In the next step (Fig. 3.16c), the potential on phase 1 is decreased to V_2 . Due to the potential difference, the charges are transferred from phase 1 to 2. After the whole process, charges are moved closer to the output by 1/3 pixel. By repeating this process, transferring charges across the device can be realized.

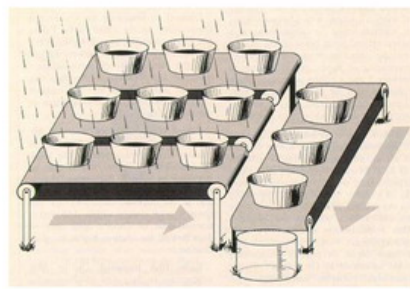


Figure 3.15: Bucket analogy used to describe CCD operation (from [Aig11]). Measuring the incident photon distribution in a CCD can be likened to measuring rainfall on a field with an array of buckets.

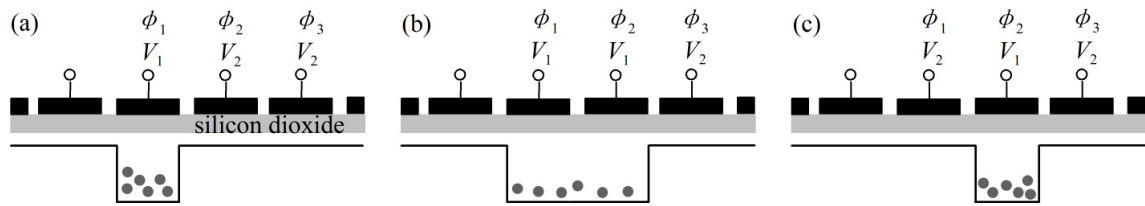


Figure 3.16: Schematic of charge transfers in a CCD.

To read out pixels row by row, an additional row of pixels (called the output register) located between the edge of the device and the top row of pixels is used. When the charges from the top row are moved into the output register, each of the remaining rows of pixels is moved up one row closer to the output. The charge values in the output register are further transferred and converted to digital signals.

Now that we know the basic working principles of CCDs, in the following important performance specifications will be introduced.

1. Dark current. Due to the semiconductor used, dark current in CCDs is inevitable. The activation energy necessary to excite electron-hole pairs differs from pixel to pixel. Pixels with very low activation energies are called “hot” and can show dark current counts several times the average. To minimize dark current, CCD cameras for high precision measurements are usually cooled by thermoelectric coolers. The CCD camera (Imager QE, LaVision) used in this work is cooled to -11°C .
2. Quantum efficiency (QE). It is defined as the ratio of the number of electrons detected and the number of incident photons. Early CCDs typically have maximum QE of about 40 – 50%. By applying back-illumination technique, CCDs with maximum QE of 85% are now commercially available [Paw95]. With Imager QE a maximum QE of $> 62\%$ could be obtained.
3. Blooming. It occurs when a potential well overflows with electrons during the exposure time, and typically an area of saturated pixels are created. This is usually caused by bright objective in the imaged area. The maximum number of charges that each capacitor can store without causing blooming can be estimated by multiplying the pixel area (μm^2) by 600 [Paw95]. Take Imager QE as an example. Its pixel size is $6.45 \times 6.45 \mu\text{m}^2$, which corresponds to a maximum of 25000 electrons/pixel. CCDs with anti-blooming gate protection are commercially available. However, for low light level measurements, e.g., single NC measurements in this work, they are not recommended because of the reduced sensitivity.
4. Frame rate. It is the rate at which a CCD camera acquires an image and then reads the complete image out. The frame rate is of particular importance in tracking rapid processes and taking image sequences.



This page is intentionally left blank.

Chapter 4

Core-shell semiconductor nanocrystals

Core-shell heterostructures commonly show properties that cannot be achieved with only one component. On one hand, coating core NCs with wider bandgap semiconductor materials so that both electrons and holes are confined in the cores can protect the core NCs from the environment. These so-called type I core-shell NCs have the charge carriers confined in the core and usually have higher quantum efficiency and enhanced photostability compared to the bare core NCs. On the other hand, sometimes growth of the shell is used to tune the wavefunction of the NCs, as is in the case of type II core-shell NCs. In this chapter, methods for the preparation of both type I and type II core-shell NCs are described. The synthesized core-shell NCs are characterized by different methods on the ensemble and single NC level.

4.1 Type I core-shell semiconductor nanocrystals

The type I core-shell NCs studied here were synthesized with CdSe NCs as cores. CdS and ZnS as shell materials were overcoated onto the core NCs following the SILAR method [Xie05]. The final products were multishell NCs with CdSe as cores coated with nominally 2 MLs CdS, 3.5 MLs $\text{Cd}_{0.5}\text{Zn}_{0.5}\text{S}$ and 2 MLs ZnS shells.

4.1.1 Experimental

Setup for synthesis. Since many chemicals used in the synthesis of NCs are air-sensitive, inert atmosphere is required. Preparation steps were performed inside a commercial glove box with less than 1% of O_2 and H_2O under slight overpressure of nitrogen at 3 – 4 mbar. The air-free synthesis was carried out in a homebuilt Schlenk system, main part of which is shown in Fig. 4.1. The reaction temperature can be controlled in the range of 20 – 800°C under a continuous argon (Ar) flow.

Characterization methods. Optical properties of the synthesized NC solutions were characterized by UV/Vis and fluorescence spectroscopies. Structures, mainly size distribution of the NCs, were measured under TEM. Individual NCs were also characterized with confocal microscopy. Parameters of the UV/Vis and

fluorescence spectrometers, and TEM are listed in section 5.1 (Table 5.1) together with other characterization methods. Details about the confocal microscope have been discussed in chapter 3.

Synthesis of multishell NCs. CdSe core NCs were first synthesized following the greener approach [Pen01] with some modifications. Typically, a stock solution of Se/TBP (0.2 mol/L) was prepared and stored in the glove box. For the synthesis, 0.0514 g (0.4 mmol) cadmium oxide (CdO) powder, 0.2232 g (0.8 mmol) tetracyclphosphonic acid (TDPA), 3.0 g trioctylphosphine oxide (TOPO), and 1.0 g octadecylamine (ODA) were weighted into a 50 mL three-neck flask. After evacuation for 1 h at room temperature, the mixture was heated to 320°C under Ar flow to form an optical clear solution. Then temperature of the solution was lowered to 270°C, followed by the injection of 4 mL of the Se/TBP stock solution. The reaction temperature was immediately adjusted to 250°C. After certain time, the temperature was lowered to 80°C to stop the reaction. Hexane and methanol were added subsequently to precipitate the NCs. After centrifugation and decantation for three times, the final product was redispersed in hexane.

Size and concentration of the resultant CdSe NCs were roughly estimated following the method reported in [Yu03a]. Once the amount of the core NCs and the volume of the individual core NC were known, the amount of the precursor solution for each monolayer can be deduced from the calculation of the number of the surface atoms [Xie05].

To synthesize multishell NCs, fresh precursor solutions were first prepared. The zinc precursor solution (0.1 M) was prepared by dissolving 0.2034 g ZnO in 6.18 g oleic acid and 18.0 mL octadecene (ODE) at 310°C. Cadmium precursor solution (0.1 M) was prepared by dissolving 0.3204 g CdO in 6.18 g oleic acid and 18.0 mL ODE at 240°C. The Zn/Cd = 1/1 precursor solution (0.1 M) was prepared by dissolving 0.1017 g ZnO and 0.1602 g CdO in 6.18 g oleic acid and 18.0 mL ODE at 300°C. Finally, the sulfur precursor solution (0.1 M) was prepared by dissolving 0.1007 g sulfur in 31.5 mL ODE at 180°C. All the precursor solutions, except for the sulfur solution that was kept under room temperature, were stored at 80°C.

In a typical procedure to synthesize the multishell NCs, 3 mL ODE and 1 g ODA were evacuated at 100°C for 1 h in a 50 mL three-neck flask (Fig. 4.1). After the mixture was cooled to room temperature, the previously synthesized CdSe NC solution (e.g., 2.96 nm in diameter, 1.82×10^{-7} mol) was injected. To remove the hexane and other impurities, evacuation was performed for 1 h at room temperature and 30 min at 100°C. Then the mixture was heated to 235°C under Ar flow.

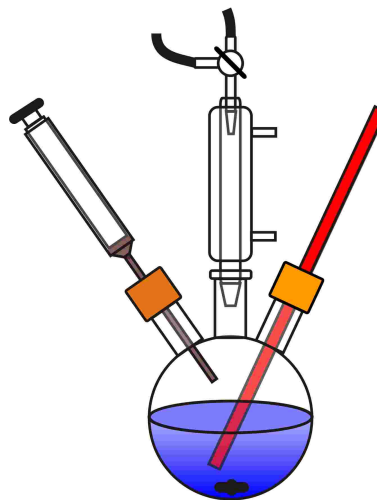


Figure 4.1: Schematic of the reaction setup.

4.1. Type I core-shell semiconductor nanocrystals

Calculated amounts of precursor solutions were injected alternatively with the time interval between each injection being 10 min. After the last injection, the solution was kept at 260°C for another 30 min to let the precursors react completely. In the end, the multishell NCs were purified and redispersed in chloroform.

Sample preparation for individual NC measurements. Glass covers used as substrates were freshly cleaned by subsequent ultrasonication in acetone, isopropanol, and distilled water, respectively. The cleaned glass covers were then flushed with distilled water and dried with nitrogen gas. To protect the NCs from the environment, a chemically inert and optically transparent polymer called Zeonex was dissolved in toluene (6 g/L) and used to dilute the NC solutions. The obtained solution was then spin-coated onto the cleaned glass covers at 3000 rpm so that the NCs were embedded in a thin layer of polymer film. To well resolve the NCs under the confocal microscope, concentration of the diluted sample should be very low so that the density of the NCs on the substrate was about 1 NC/ μm^2 .

4.1.2 Results and discussion

Fig. 4.2 shows a set of absorption and PL spectra of CdSe core NCs (Fig. 4.2a) and multishell NCs (Fig. 4.2b) synthesized from those core NCs.

The absorption spectrum of the CdSe NCs has four distinct peaks (or shoulders), which are due to the discrete sets of electronic levels in the NCs. Electronic transitions corresponding to the peaks (shoulders) marked in the figure are respectively: 1, 1S(e) – 1S_{3/2}(h); 2, 1S(e) – 2S_{3/2}(h); 3, 1P(e) – 1P_{3/2}(h); 4, 1S(e) – 3S_{3/2}(h). From the first absorption peak position (546 nm), size of the NCs calculated according to Ref. [Yu03a] is 2.96 nm. The PL spectrum shows a FWHM of 25 nm and peak position at 552 nm, which means a Stokes shift of 6 nm. By using Rhodamine 6G as the standard, the quantum efficiency of the core NC solution is calculated to be 16.4%.

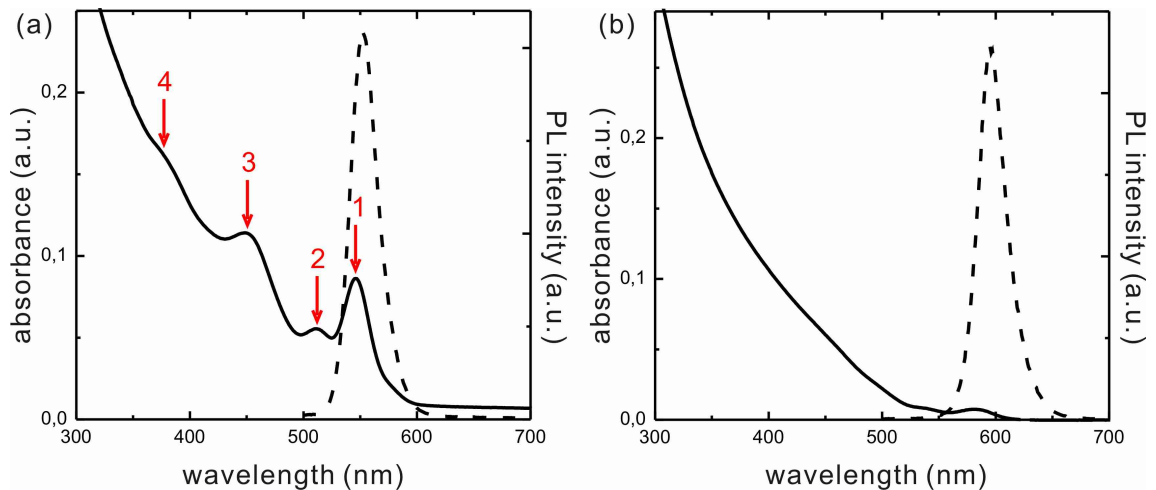


Figure 4.2: Absorption (solid curves) and PL (dashed curves) spectra of (a) CdSe core NCs and (b) the corresponding multishell NCs.

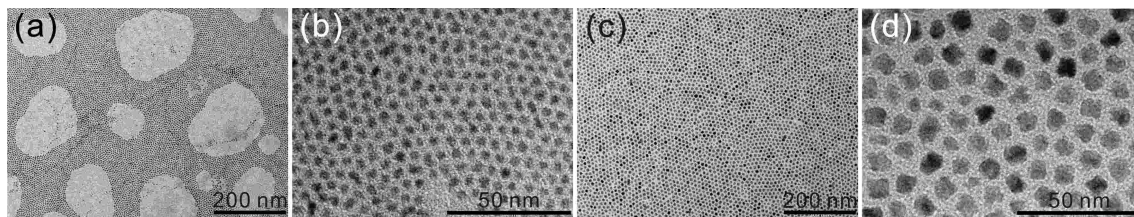


Figure 4.3: TEM images of (a – b) CdSe core NCs and (c – d) corresponding multishell NCs.

Growth of the shell materials makes both the absorption and PL spectra red shifted. Especially for the PL spectrum, the peak position shifts to 595 nm. This is partially due to the growth of the core NCs during the shell growth. Another reason is the extension of the electronic wavefunctions leaking out into the shell materials because of the finite value of the band offsets. The other significant change is that the absorption spectrum of the multishell NCs is almost structureless. Calculation of the quantum efficiency gives the value of 42.3%, much higher than that of the core NCs.

Structures of the NCs were characterized with TEM. As shown in Fig. 4.3, homogeneous size distributions are observed for both CdSe core NCs (Fig. 4.3a, b) and multishell NCs (Fig. 4.3c, d). Size of the core NCs measured from TEM is 3.1 ± 0.2 nm, in consistence with the value calculated from the absorption spectrum. The multishell NCs have the diameter of 6.4 ± 0.4 nm, relatively larger than the calculated value ($(2.96 + 2 \times 0.35 + 3.5 \times 0.33 + 2 \times 0.31)$ nm = 5.44 nm. [Xie05])

Optical properties of the NCs were also studied at the single NC level. In the measurements, an oil objective (100 \times , NA=1.25) was used to optimize the optical performance of the confocal microscope. Fig. 4.4 shows examples of scanned PL images of CdSe core NCs (Fig. 4.4a) and multishell NCs (Fig. 4.4b) on glass covers measured under the same experimental conditions. The scan range for both images is $10 \times 10 \mu\text{m}^2$, and the color scale is 0 – 1000 counts/s. The PL intensity of the core NCs, as marked by circles, is very weak. On the contrary, the multishell NCs show

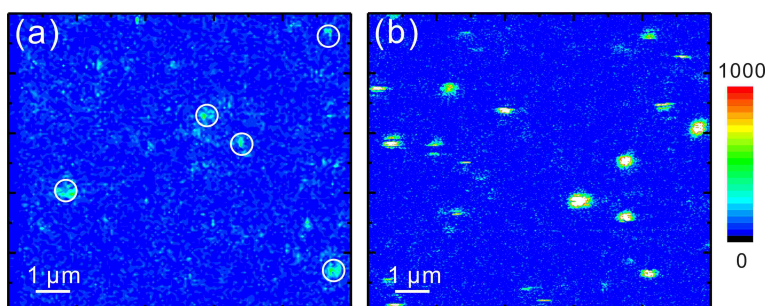


Figure 4.4: Scanned PL images ($10 \times 10 \mu\text{m}^2$) of (a) CdSe core NCs and (b) multishell NCs on glass covers measured under the same experimental conditions. The unit of the color scale is counts/s.

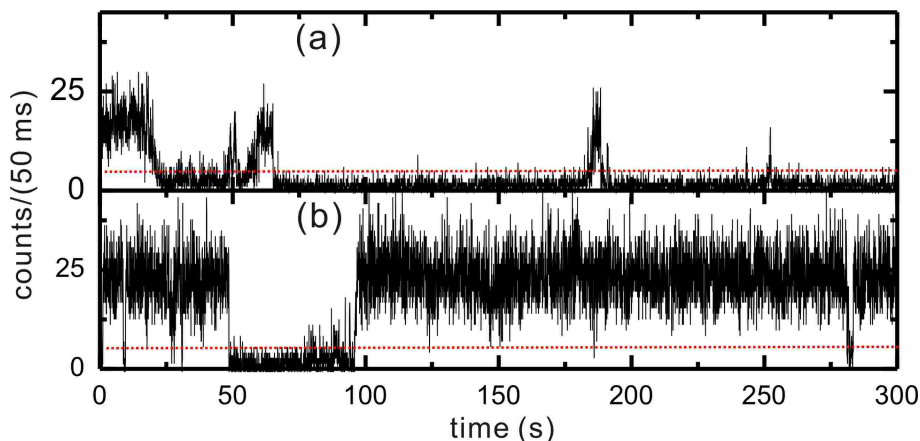


Figure 4.5: Representative time traces from (a) a CdSe core NC and (b) a multishell NC. The time bin is 50 ms. The dashed lines are the thresholds dividing on- and off-states.

much stronger PL intensity. Sometimes only several pixels instead of a complete bright sphere is observed. This is due to the blinking behavior of the observed NCs.

Two representative PL time traces from a CdSe core NC and a multishell NC are shown in Fig.4.5. The experimental conditions for the measurements were the same. Time bin of the time traces is 50 ms. The threshold that divides the on- and off-states is defined as twice the background intensity, as marked by dashed lines in the figure. It can be observed that the PL intensity of the on-state for the multishell NC is about 25 counts/(time bin), higher than the 15 counts/(time bin) from the core NC. The ratio between the time that the NCs are at the on-state during the measurement and the total measurement time (on%) is calculated to be 18.4% and 80.2% for the core and multishell NCs, respectively, indicating improved photostability of the multishell NC as compared to the core NC.

To study the influence of the shells on the recombination rates of the NCs, PL decay curves were also recorded from many individual core and multishell NCs. A representative decay curve (background subtracted) from a multishell NC is shown in Fig. 4.6. It is fitted with a stretched exponential function. From the fitting results, an average lifetime of 23.1 ns is derived. No apparent difference between the lifetimes of the core and multishell NCs is observed. That is probably because although growth of the wider bandgap materials makes wavefunctions more spread out, the change is not significant enough to cause variations in the lifetime.

In conclusion, growth of the multishells of wider bandgap materials on the CdSe core NCs helps to protect the NCs from the environment. Photostability of the NCs is greatly enhanced. Meanwhile, the carrier dynamics of the NCs is preserved.

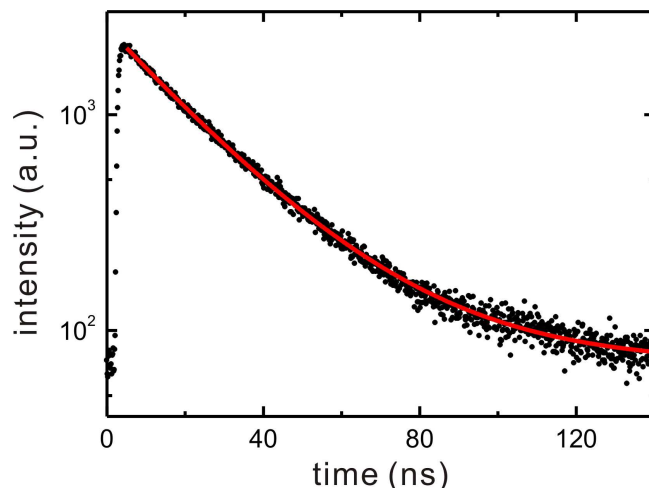


Figure 4.6: Background-subtracted PL decay curve from an individual multishell NC (black dots) fitted with a stretched exponential function (red curve).

4.2 Type II core-shell semiconductor nanocrystals

As discussed earlier, type II core-shell NCs are heterostructures in which charge carriers are spatially separated due to band offsets between the core and shell materials. Such structures lead to certain interesting characteristics, such as a significant red shift of the PL spectrum and a long lifetime. In this work, type II core-shell NCs mainly based on CdTe NCs as cores are studied. The relative positions of valence and conduction band edges of the used materials are shown in Fig. 4.7.

4.2.1 Experimental

Two different groups of core-shell NCs based on CdTe core NCs were synthesized following the SILAR method: CdTe/CdSe core-shell NCs and CdTe/CdS core-shell NCs. Detailed synthesis procedures of these NCs are described in the following.

Synthesis of CdTe NCs. A stock solution of Te/trioctylphosphine (TOP) with the concentration of 0.2 mol/L was prepared and stored in the glove box. To synthesize CdTe NCs, 0.0514 g (0.4 mmol) CdO, 0.2232 g (0.8 mmol) TDPA, 1 g TOPO and 15 mL ODE were added into a 50 mL three-neck flask and evacuated for 1 h at room temperature. The mixture was then heated to 310°C under Ar flow. Once an optical clear solution was formed, the temperature was lowered to 270°C. 2 mL of the Te/TOP stock solution was injected at once and the reaction temperature was immediately lowered to 250°C. After certain time, the reaction was stopped by cooling the mixture to 80°C. The same purification process as in the synthesis of CdSe NCs was performed and the final product was dispersed in toluene.

Coating of shell materials. In principle the procedure is similar to the synthesis of CdSe multishell NCs described in section 4.1.1. However, CdTe NCs are in general

4.2. Type II core-shell semiconductor nanocrystals

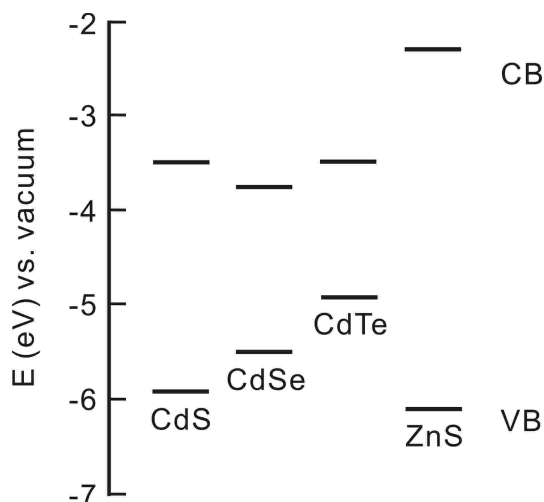


Figure 4.7: Relative positions of valence and conduction band (VB and CB, respectively) edges in CdTe, CdSe, CdS, and ZnS. Data from Ref. [Rei09]

not as stable as CdSe NCs. Therefore, during the growth of shell materials onto CdTe NCs, it is crucial that very low concentrations of O_2 and H_2O exist in the reaction system.

In the synthesis of CdTe/CdSe core-shell NCs, cadmium precursor solution with the concentration of 0.04 M was prepared by dissolving 0.0615 g (0.48 mmol) CdO in the mixture of 1.186 g oleic acid and 10.66 mL ODE at 240°C under Ar flow. The resultant clear solution was kept at 80°C . Selenium precursor solution (0.2 M) was prepared and stored in the glove box for further applications. Different from the synthesis of multishell NCs, the reaction temperature during the growth of CdSe shells was kept at 210°C , because the reactivity of Cd- and Se-precursors were higher than Zn- and S-precursors, respectively. As to CdTe/CdS core-shell NCs, the Cd- and S- precursor solutions were prepared following the method described in section 4.1.1, only that the concentrations were reduced to 0.04 M. The reaction temperature was optimized to 240°C .

Sample preparation. Samples for the optical measurements of individual NCs under confocal microscope were prepared in the same way as in section 4.1.1. As to the lifetime measurements of ensemble NCs, solutions with proper NC concentrations were added into quartz cuvettes with a path length of 1 cm. Due to the thick walls of the cuvettes, a long-working distance objective (Zeiss, $10\times$, $NA = 0.25$) was used.

4.2.2 Results and discussion

Fig. 4.8 shows a set of representative absorption and PL spectra of CdTe core NCs coated with different monolayers of CdSe shells. The absorption spectra are normalized at 480 nm, which is the excitation wavelength of the PL spectra. With the increase of the CdSe shell thickness, a continuous red shift of both the first absorp-

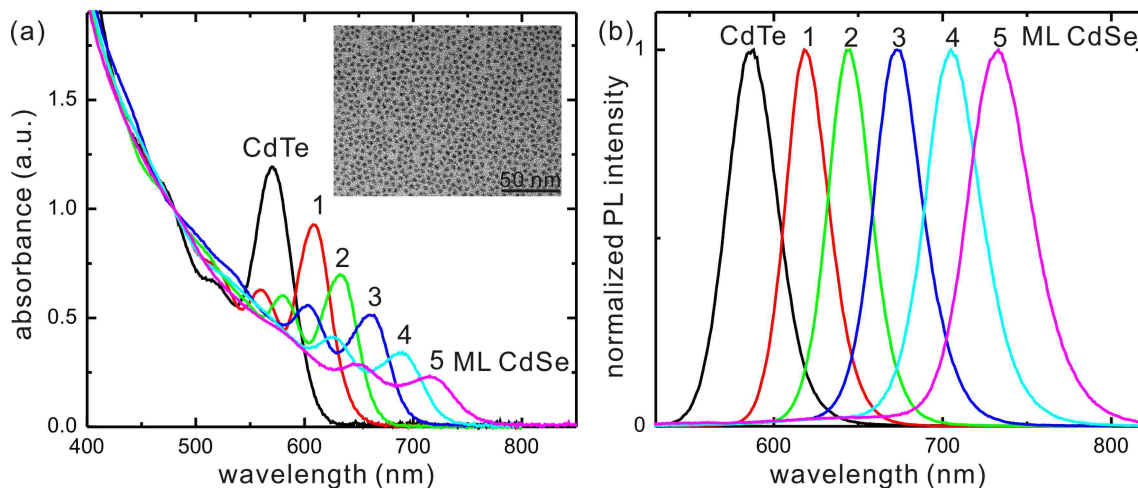


Figure 4.8: (a) Absorption and (b) PL spectra of CdTe NCs coated with different monolayers (MLs) of CdSe shells. The absorption spectra are normalized at 480 nm. The inset in (a) is a TEM image of CdTe NCs coated with 4 ML of CdSe shells.

tion peak and PL peak is observed (Table 4.1). At the same time, an increase in the oscillator strength of the second electronic transition in the absorption spectra in comparison to the first electronic transition is observed with the increase of the shell thickness. This is mainly due to the dramatic decrease in the spatial overlap of the wavefunctions for the first electronic transition. The core-shell NCs have homogeneous size distributions. An example is given in the inset of Fig. 4.8a, where a TEM image of CdTe NCs coated with 4 MLs of CdSe shells is shown.

Quantum efficiencies (QE) of these core-shell NC solutions are calculated using Rhodamine 6G as the standard and plotted in Fig. 4.9. The QE of the CdTe core NCs is 13.3%. After the growth of the first monolayer of CdSe shell, it increases to 19.5%. During the shell growth, two opposite mechanisms affect the overall QE of the NCs. On one hand, due to the spatial separation of the charge carriers, according

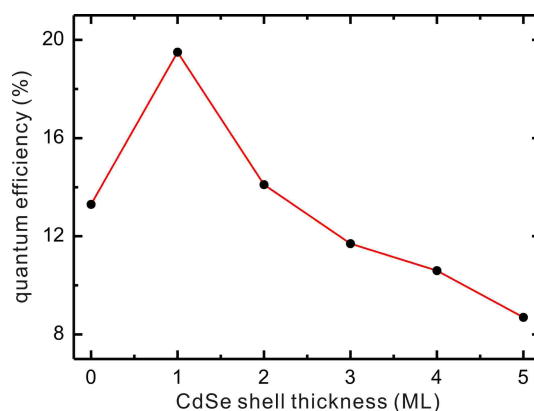


Figure 4.9: Quantum efficiency of CdTe NCs coated with different monolayers (ML) of CdSe shells.

4.2. Type II core-shell semiconductor nanocrystals

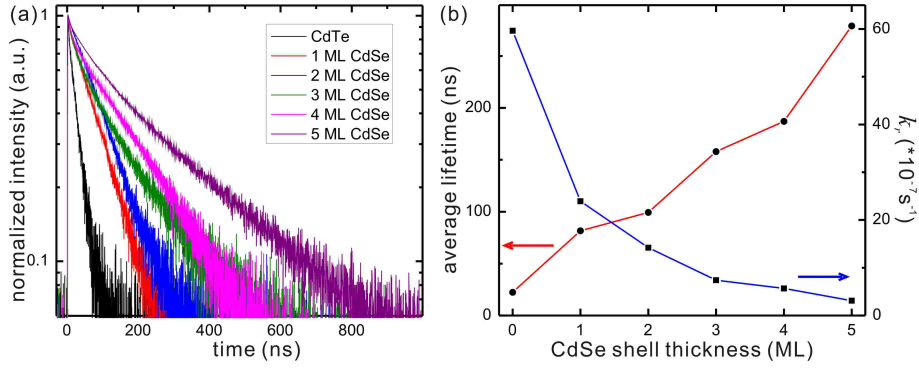


Figure 4.10: (a) Normalized decay curves and (b) average lifetimes (red) and radiative decay rates (blue) calculated from stretched exponential fitting results of CdTe NCs coated with different monolayers (MLs) of CdSe shells.

to the Fermi's golden rule the spontaneous recombination rate (k_r) decreases. Since

$$\text{QE} = \frac{k_r}{k_r + k_{nr}} = \frac{1}{1 + k_{nr}/k_r}, \quad (4.1)$$

if we assume k_{nr} is not changed, then QE decreases with the increase of shell thickness. On the other hand, growth of the shell materials passivates the surface of the NCs, especially for the first monolayer. Since the charge carriers are still mainly localized in the core of the NCs, the passivation effect dominates. Therefore, an increase of the QE is observed. However, when the influence from the decrease of the overlap between the electronic wavefunctions dominates, as in the case of CdTe NCs coated with more than two monolayers of CdSe shells, decrease of the QE occurs. QE values of the core-shell NCs are listed in Table 4.1.

The growth of the CdSe shell is directly related with the recombination dynamics of the core-shell NCs. Decay curves of CdTe NCs coated with different monolayers of CdSe shells were recorded using the TCSPC method, as shown in Fig. 4.10a. The CdTe core NCs have the fastest PL decay. With the increase of the CdSe shell thickness, the decay becomes slower. By fitting the decay curves with stretched exponential functions, the average lifetimes can be deduced from the fitting results. Since the lifetime of the NCs is much longer than the width of the IRF (128 ps), IRF signal is not reconvoluted during the fitting process. Fig. 4.10b (red) shows the

Table 4.1: PL peak, QE, $\langle\tau\rangle$ and k_r of CdTe/CdSe core-shell NCs.

NO. of ML	PL peak (nm)	QE (%)	$\langle\tau\rangle$ (ns)	k_r (s^{-1})
0	588	13.3	22.3	5.96×10^8
1	618	19.5	81.5	2.39×10^8
2	645	14.1	99.3	1.42×10^8
3	673	11.7	157.9	7.41×10^7
4	705	10.6	187.0	5.67×10^7
5	733	8.7	278.9	3.12×10^7

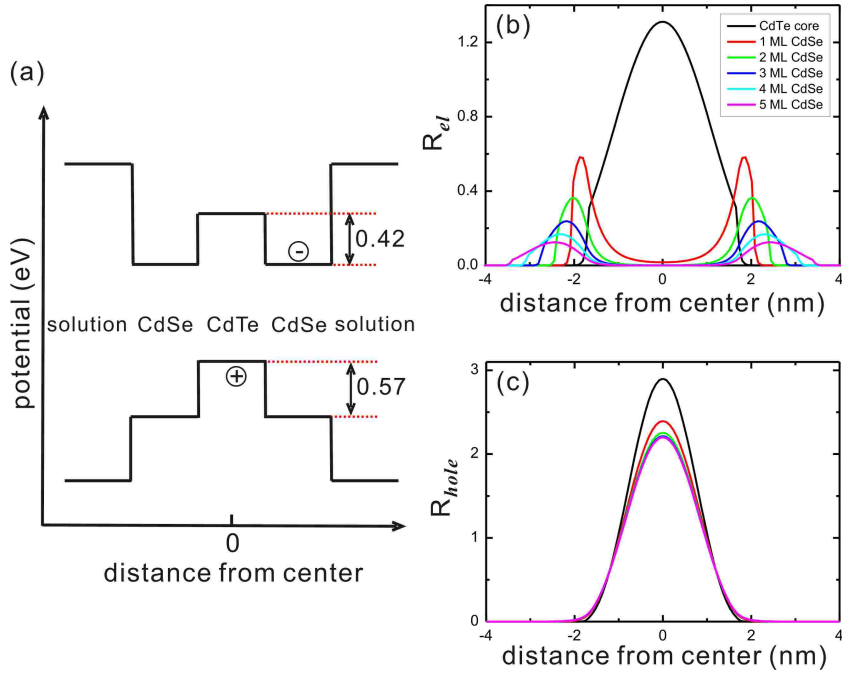


Figure 4.11: (a) Schematic of the geometry and potential in CdTe/CdSe core-shell NCs. Values of band offset are taken from Ref. [Wei00b]. (b, c) Wavefunctions of electrons (b) and holes (c) in CdTe/CdSe core-shell NCs. Diameter of the CdTe cores is 3.4 nm.

CdSe shell thickness dependent average lifetime $\langle\tau\rangle$ of the core-shell NCs (also listed in Table 4.1). As the shell gets thicker, average lifetime of the NCs is dramatically increased. From the equation $k_r = QE \cdot (k_r + k_{nr}) = QE / \langle\tau\rangle$, the radiative decay rate k_r of the NC solutions can also be calculated, as shown in Fig. 4.10b (blue). As expected, k_r decreases with the increase of shell thickness.

To understand these optical behaviors of the CdTe/CdSe core-shell NCs, radial wavefunctions ($R(r)$) of the electrons and holes were calculated according to Ref. [Sch94]. Geometry and relative potentials of the core-shell NCs are plotted in Fig. 4.11a. Diameter of the CdTe core NCs (D_0) was determined from the first absorption peak in Fig. 4.8a [Yu03a] as 3.4 nm. Thickness of each CdSe shell was taken as 0.35 nm. Therefore for 5 MLs the shell thickness was 1.75 nm. Effective masses of the electrons and holes in CdTe were taken as $m_e^* = 0.11 m_0$, and $m_h^* = 0.4 m_0$, respectively, and in CdSe $m_e^* = 0.13 m_0$, $m_h^* = 0.45 m_0$ [Mad99]. The computed results are shown in Fig. 4.11b and c. In CdTe core NCs, both the electrons and holes are localized inside the NCs. With the coating of CdSe shells, although the holes are still mainly located in the CdTe cores, the electrons are located in the CdSe shells. This leads to a dramatic decrease of the overlap between the electron and hole wavefunctions. Therefore, the recombination rates decrease. Meanwhile, in CdTe/CdSe core-shell NCs, since the charge carrier recombination mainly happens between the edge of the conduction band of the CdSe shells and valence band of CdTe cores, from the potential diagram (Fig. 4.11a) it can be seen that the energy of emitted photons is smaller than the recombination energy in either single component. Consequently, red shift of the PL spectra is observed.

4.2. Type II core-shell semiconductor nanocrystals

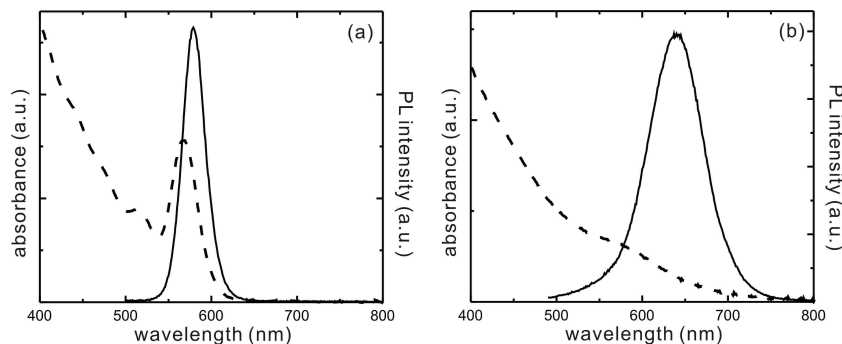


Figure 4.12: Absorption (dashed curves) and PL (solid curves) spectra of (a) CdTe NCs and (b) CdTe/CdS core-shell NCs. The thickness of the CdS shell is nominal 2 MLs.

Measurements of individual CdTe/CdSe core-shell NCs under confocal microscope were tried but did not succeed. The NCs were extremely unstable even when embedded in thick layers of protective polymer. Therefore, a more stable component CdS instead of CdSe was overcoated onto CdTe core NCs. Although lattice mismatch between CdTe and CdS is relatively larger (11.5%) as compared to that between CdTe and CdSe (7.1%) [Cha07], from section 2.2.6 it is known that CdTe is a material with high deformable potential. When a very thin shell is coated onto CdTe NCs, coherent epitaxial growth of the shell is expected and no additional defects due to lattice mismatch should be introduced.

A set of absorption and PL spectra of CdTe core NCs and CdTe cores coated with 2 MLs of CdS shells are shown in Fig. 4.12. Growth of the CdS shells leads to a red shift of the absorption and PL spectra. The PL peak shifted from 579 nm for the CdTe cores to 637 nm for the core-shell NCs. In addition, the absorption spectra of the CdTe/CdS NCs is almost featureless, while the PL spectra is much broader than that of the cores, indicating broader size distribution of the core-shell NCs. Calculation of the quantum efficiency gives the value of 5.1% and 33.3% for the CdTe cores and CdTe/CdS core-shell NCs, respectively. The high quantum efficiency of the core-shell NCs indicates a good surface passivation by the shell materials.

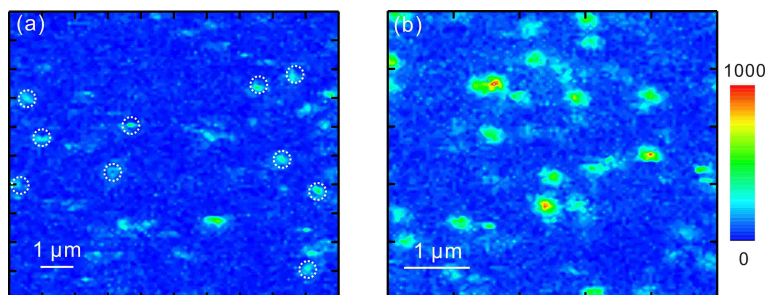


Figure 4.13: Scanned PL images of (a) CdTe core NCs and (b) CdTe/2ML CdS core-shell NCs on glass covers. The size of image (a) is $10 \times 10 \mu\text{m}^2$, of image (b) is $5 \times 5 \mu\text{m}^2$. The color scale in both images is 0 – 1000 counts/s.

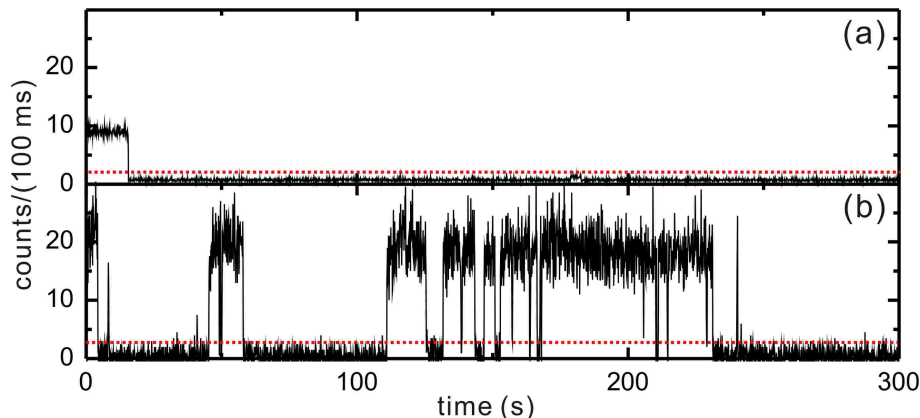


Figure 4.14: Time traces of an individual (a) CdTe core NC and (b) CdTe/2 MLs CdS core-shell NC on glass covers. The time bin is 100 ms. The dashed lines are the thresholds dividing on- and off-states.

Investigation of the individual CdTe/CdS core-shell NCs were performed by embedding the NCs in Zeonex matrices. Fig. 4.13 shows representative scanned PL images of CdTe cores and CdTe/CdS core-shell NCs measured under the same conditions. The size of Fig. 4.13a is $10 \times 10 \mu\text{m}^2$, and of Fig. 4.13b is $5 \times 5 \mu\text{m}^2$. Obviously, the PL intensity of the CdTe/CdS core-shell NCs is much higher than that of the CdTe core NCs.

To investigate in more detail the optical behaviors of the NCs, PL time traces of individual NCs were recorded for certain time. In contrast to CdTe/CdS core-shell NCs, time traces of CdTe cores were very difficult to record, because these core NCs were extremely unstable. Illumination of laser beam immediately bleaches the PL of the NCs. Fig. 4.14 shows two representative time traces from an individual CdTe core NC and a CdTe/CdS core-shell NC. While the time trace of the CdTe/CdS NC features blinking behavior, the PL of the CdTe NC was bleached almost immediately (15.5 s) after the illumination. The threshold used to divide the on- and off-states is defined as twice the background intensity. The most frequent on-state PL intensity of the CdTe core NC is about 9 counts/(time bin), and that of the CdTe/CdSe NC is increased to 20 counts/(time bin). The on-time fraction (on%), which is the ratio between the time the NCs stay at the on-state and the total measurement time, is calculated to be 5.2% and 40.6% for the CdTe core and core-shell NC, respectively.

Aside from the red shift of the PL spectra, the type II characteristics of the CdTe/CdS core-shell NCs were further studied by their recombination dynamics. In Fig. 4.15 background-subtracted decay curves from the two NCs in Fig. 4.14 are shown together. Fitting the decay curves with stretched exponential functions gives average lifetimes of 6.6 ns and 90.3 ns for the CdTe core and CdTe/CdS core-shell NC, respectively. The extremely short lifetime of the CdTe core NC is probably due to the unpassivated surface trap states, which lead to multi-nonradiative recombination channels. The large nonradiative decay rate causes short lifetime of the core NC. The lifetime of the CdTe/CdS NC is much longer than that of the CdTe core. There are mainly two contributions: firstly, the CdS shells passivate the

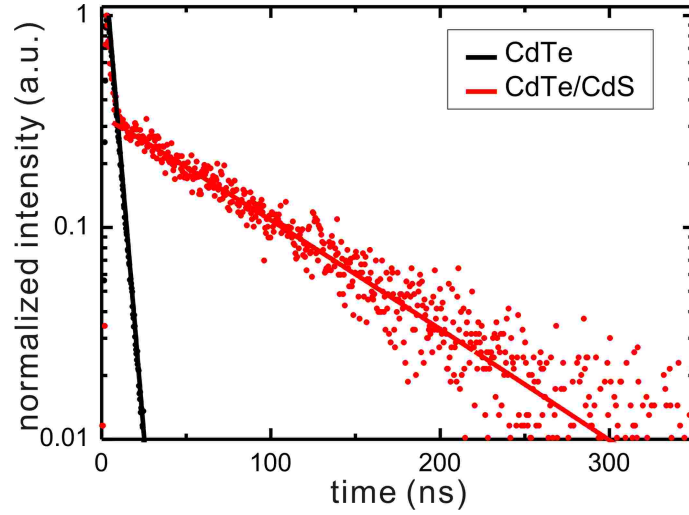


Figure 4.15: Normalized decay curves (dots) of an individual CdTe core NC (black) and a CdTe/2 MLs CdS core-shell NC (red) together with their stretched exponential fittings (curves).

CdTe core and decrease the nonradiative decay rates. Secondly, spatial separation of the electrons and holes causes the decrease of the overlap between the electron-hole wavefunctions. As a result, the spontaneous recombination rate decreases. Overall, the decay rate is decreased and the lifetime is much longer.

Radial wavefunctions of the CdTe/CdS core-shell NCs were calculated to prove their type II characteristics. Values of the effective masses of electrons and holes in CdS were taken as $m_e^* = 0.2 m_0$ and $m_h^* = 0.7 m_0$ [Mad99], respectively. Diameter of the CdTe core was calculated to be 3.4 nm. Thickness of each CdS ML was taken as 0.35 nm [Xie05]. Here the CdS shell thickness was varied from 0 to 2 MLs (0 – 0.7 nm). Fig. 4.16a shows the band offsets in the core-shell NCs [Sch06]. The calculated results are shown in Fig. 4.16b and c. The holes are located in the CdTe core in all cases. The electrons, however, are delocalized over the whole NC with the coating of the CdS MLs. Thus the overlap between the electron and hole wavefunctions decreases significantly with the increase of the shell thickness. This observation is consistent with the increase of the recombination lifetime.

In conclusion, type I and type II core-shell NCs were synthesized and characterized. In the case of type I core-shell NCs, the growth of wider bandgap materials helps to passivate the surface of the core NCs and improves the photostability. Since the charge carriers are mainly confined in the cores of these type I core-shell NCs, the recombination dynamic is similar to the bare core NCs. On the contrary, the charge carriers in type II core-shell NCs are spatially separated. Here, mainly CdTe based type II core-shell NCs were investigated. Calculations of the electron and hole wavefunctions show that in these NCs, holes are mainly located in the cores of the NCs, whereas the electrons are either located in the shells in the case of CdTe/CdSe NCs or delocalized over the whole NCs in the case of CdTe/CdS NCs. Consequently, dramatic red shifts of the PL wavelength and increased lifetimes were observed.

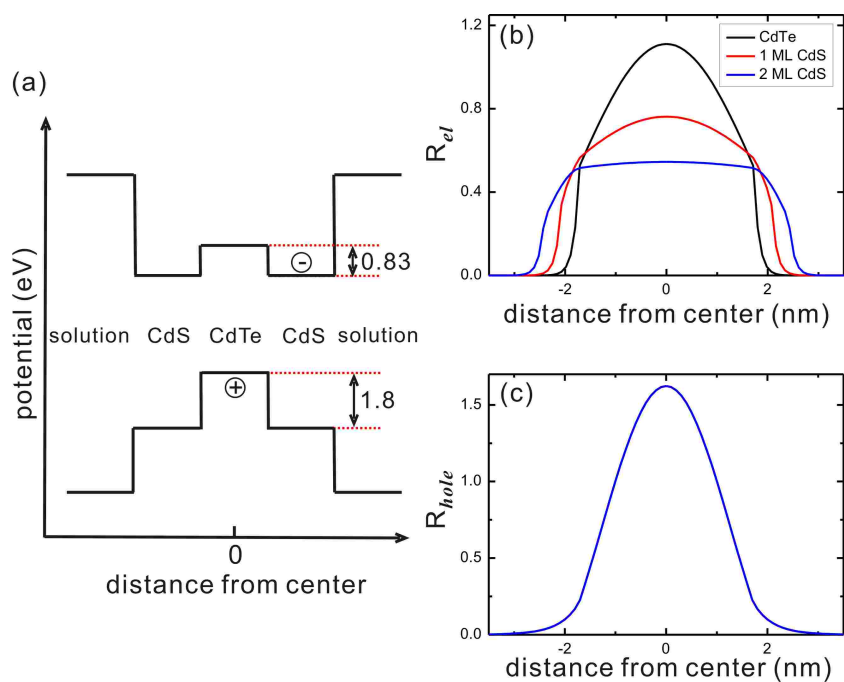


Figure 4.16: (a) Schematic of the geometry and potential in CdTe/CdS core-shell NCs. Values of the band offsets are taken from Ref. [Sch06]. (b, c) Wavefunctions of electrons (b) and holes (c) in CdTe/CdS core-shell NCs. Diameter of the CdTe cores is 3.4 nm.

Chapter 5

Semiconductor nanocrystals on gold nanoparticle films

This chapter studies the influence of self-assembled AuNP films on the optical properties of NCs. To tune the distance between the AuNP films and NCs, homogeneous silica shells with different thicknesses were grown on the surface of NCs. By changing the preparation conditions, AuNP films with different geometries and optical properties were prepared. Detailed descriptions of sample preparation and characterization methods are given in the first section. The prepared samples were then studied with a confocal microscope on the single NC level and the results are discussed in the second section. In the last part, the observed phenomena are discussed in combination with a simple model.

5.1 Samples: preparation and characterization

As the fluorophores in this study, multishell NCs synthesized following the SILAR method were overcoated with silica shells to separate them from AuNP films. The thickness of the silica shell was determined by TEM. Optical properties of the ensemble NC solution, including absorption and PL, were characterized by UV/Vis and fluorescence spectroscopy. On the other hand, AuNP films were prepared by the self-assembly of AuNPs on pre-cleaned glass covers. Detailed information about the structures of those films were determined by TEM, SEM and AFM, while their optical properties were also measured by a UV/Vis spectrometer. For measurements of individual NCs, the silica coated NCs were spin-coated onto the AuNP films under proper conditions. Table 5.1 lists the main characterization methods used here.

Table 5.1: Characterization methods.

method	company	model
UV/Vis spectrum	Varian, Inc	Cary 5000 UV-Vis-NIR Spectrometer
Fluorescence spectrum	Horiba Jobin Yvon GmbH	FluoroMax™-4 Spectrofluorometer
TEM	JEOL Ltd.	JEM-1011
SEM	Carl Zeiss	Leo 1550
AFM	JPK Instruments	NanoWizard®

5.1.1 Silica coated semiconductor nanocrystals

Synthesis. CdSe multishell NCs containing CdSe core (3 nm), nominally 2 monolayers (MLs) CdS (0.7 nm), 3.5 MLs Cd_{0.5}Zn_{0.5}S (1.2 nm), and 2 MLs ZnS (0.6 nm) were prepared following the SILAR method as described in section 4.1.1.

Silica shells were coated onto the surface of NCs following the previously reported microemulsion method [Dar05] with some modifications. In a typical reaction, 7 g cyclohexane and 1.272 g NP-10 were added into a reaction flask and stirred vigorously at 1200 rpm for about 15 min. Then, a small amount of the highly concentrated CdSe multishell NCs dispersed in chloroform (~ 1 nmol) was injected into the flask. After waiting for 15 min, different amounts of TEOS were added and the mixture was stirred for another 30 min. By this time, a stable microemulsion system had formed. To initiate the polymerization process of TEOS, 120 μL ammonia aqueous solution (25 wt.%) was added and the reaction was kept in the dark for more than 20 h to form stable silica-coated NCs (SiNCs). In order to prevent agglomeration of the SiNCs, molecules with special functional groups were then introduced to modify the surface of the SiNCs. Finally, the products were isolated from the microemulsion system by the addition of 1-propanol and centrifugation. After being washed by 1-propanol, ethanol, and water subsequently, the resultant precipitate was dispersed in ethanol or water and stored in the dark for further applications.

Characterization. SiNCs used in this study should fulfill several requirements: (1) monodisperse (including both the NC size and the silica shell thickness); (2) individual NCs in the center of each particle; (3) controlled silica shell thickness; (4) high photostability. Therefore, the experimental conditions have to be carefully selected.

Fig. 5.1 shows the influence of the amount of NCs (V_{NC}) when the other experimental parameters are the same. When the added amount of NCs is small (Fig. 5.1a, b), aside from SiNCs with individual NCs in the middle, many silica particles without NCs also appear. By increasing the amount of NCs (Fig. 5.1c), more SiNCs with individual NCs are formed, although the thickness of the silica shell decreases. Meanwhile, big SiNCs with multiple NCs in the middle are also observed.

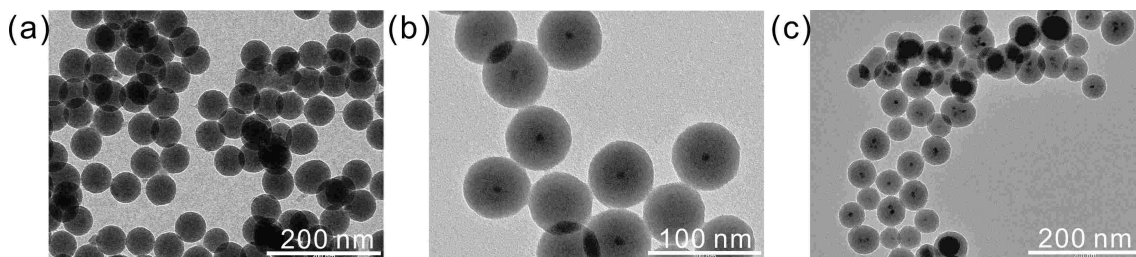


Figure 5.1: TEM images of SiNCs synthesized from different amounts of NCs while the other experimental parameters are the same. The amount of TEOS is 70 μL , and the reaction time is 22 h. (a) $V_{\text{NC}} = 0$ μL ; (b) $V_{\text{NC}} = 50$ μL ; (c) $V_{\text{NC}} = 200$ μL .

5.1. Samples: preparation and characterization

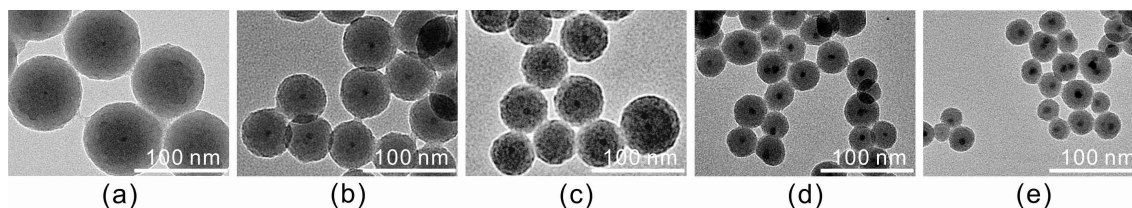


Figure 5.2: TEM images of SiNCs synthesized from different amounts of TEOS while the other experimental parameters are kept constant. The amount of NCs is $60 \mu\text{L}$ and the reaction time is 22 h. (a) $V_{\text{TEOS}} = 100 \mu\text{L}$; (b) $V_{\text{TEOS}} = 60 \mu\text{L}$; (c) $V_{\text{TEOS}} = 40 \mu\text{L}$; (d) $V_{\text{TEOS}} = 20 \mu\text{L}$; (e) $V_{\text{TEOS}} = 10 \mu\text{L}$. The corresponding sizes of SiNCs are (a) 80 nm; (b) 55 nm; (c) 50 nm; (d) 30 nm; (e) 20 nm. The magnifications are the same in all the images.

Aside from the amount of initial NCs, another important parameter is the added amount of TEOS, which is directly related to the thickness of the silica shells. Fig. 5.2 shows the size dependence of the SiNCs on the amount of TEOS (V_{TEOS}). With the decrease of V_{TEOS} , the silica shell gets thinner. However, when V_{TEOS} is too small ($< 10 \mu\text{L}$), no homogeneous silica shell can be formed on the NC surface, and only irregular silica structures can be formed.

Other parameters such as the reaction time and the amount of aqueous ammonia solution (V_{NH_3}) also influence the quality of the final product, but the effect is not as direct and significant as the previous two. Therefore, in the synthesis, the reaction time and V_{NH_3} are often kept constant.

In order to perform optical investigations of individual SiNCs, it is crucial to have the SiNCs separated from one another. However, the synthesized silica particles tend to coagulate and eventually polycondensation of their surface OH groups occurs. Therefore, it is necessary to modify the surface of the SiNCs. Surfactants used to prevent such irreversible agglomeration of the silica nanoparticles mainly include two types. The first type leaves the silica particles chemically inert and consequently prohibits agglomeration. For example, a dense layer of octadecyl alcohol [vH81] or (3-methacryl)oxypropyltrimethoxysilane [Phi89] has been used to coat the surface of silica particles. The generated particles can be dispersed in organic solvents. The other type of surfactants renders the surface of silica nanoparticles with cationic or anionic functional groups, and the electrostatic repulsion of the nanoparticles prevents the agglomeration. The most commonly used functional groups include amine group [Bad90, Wei08, Kum08], carboxylate group [Bec99, Bag06, Kum08], sulfonate group [Wan03], and phosphonate groups [Ger01, Sch02, Bag06].

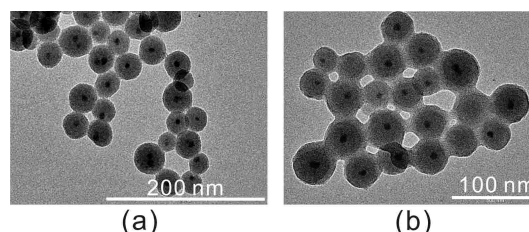


Figure 5.3: TEM images of SiNCs modified by different amounts of APS. $V_{\text{NC}} = 60 \mu\text{L}$; $V_{\text{TEOS}} = 20 \mu\text{L}$; reaction time is 22 h. (a) $V_{\text{APS}} = 1 \mu\text{L}$; (b) $V_{\text{APS}} = 3 \mu\text{L}$.

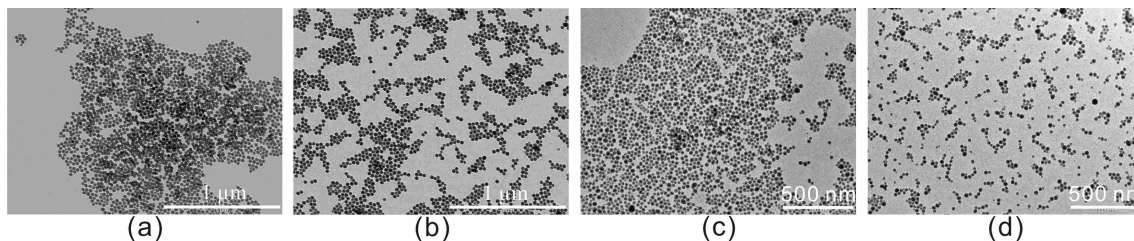


Figure 5.4: TEM images of SiNCs modified with different amounts of THPAP. $V_{\text{NC}} = 50 \mu\text{L}$, and the reaction time is 22 h. (a) $V_{\text{TEOS}} = 20 \mu\text{L}$, $V_{\text{THPAP}} = 1 \mu\text{L}$; (b) $V_{\text{TEOS}} = 20 \mu\text{L}$, $V_{\text{THPAP}} = 2 \mu\text{L}$; (c) $V_{\text{TEOS}} = 10 \mu\text{L}$, $V_{\text{THPAP}} = 1 \mu\text{L}$; (d) $V_{\text{TEOS}} = 10 \mu\text{L}$, $V_{\text{THPAP}} = 2 \mu\text{L}$.

Several types of surfactants were used in this work to prevent agglomeration of SiNCs, one of which was (3-aminopropyl)trimethoxysilane (APS). As shown in Fig. 5.3, with the increase of the amount of APS (V_{APS}), the surface of the SiNCs becomes rougher and crosslinking between neighboring SiNCs becomes significant, which indicates that APS is not the proper surfactant for this study.

Another surfactant mostly studied is the 3-(trihydroxysilyl)propyl methylphosphonate, monosodium salt solution (42 wt.% in H_2O) (THPAP). The phosphonate group from the molecule effectively prohibits the agglomeration of SiNCs. Fig. 5.4 shows that with the increase of the amount of THPAP (V_{THPAP}), the SiNCs become separated from each other and more individual SiNCs can be observed.

However, THPAP is a strong base (e.g. when $V_{\text{THPAP}} : V_{\text{H}_2\text{O}} = 1 : 9$, the pH value is about 10.6). As a result, if the concentration of THPAP in the reaction system is too high, the NCs will dissolve (Fig. 5.5a). Furthermore, the final product should be kept in buffer solution in order to prevent the corrosion from the THPAP left in the solution. Fig. 5.5b shows the THPAP modified SiNCs which are kept in distilled water for 1 week after synthesis. It is clear that the inner layers of silica are dissolved and that the NCs are no longer in the center of the particles.

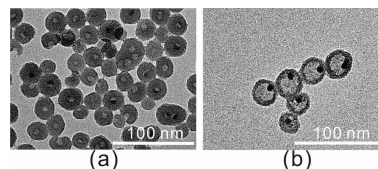


Figure 5.5: (a) SiNCs with the NCs dissolved. (b) SiNCs with inner layers of silica dissolved.

Other surfactants that were also used include 2-(4-Chlorosulfonylphenyl)ethyl-trimethoxysilane, which can also provide efficient electrostatic repulsion between SiNCs because the sulfonate groups can dissociate to provide negative charges on the surface of the SiNCs.

Even though the requirements from the structures are met, the photostability of the SiNCs should be high enough in order to perform single NC optical measurements. During the coating of silica shells, usually the PL intensity of the NCs decreases because of the chemical corrosion from reaction materials (e.g., $\text{NH}_3 \cdot \text{H}_2\text{O}$) and binding of TEOS and NP-10 on the surface of NCs [Koo08]. Therefore, the photostability of the original NCs before silica coating is very important. Fig. 5.6a shows that the absorption spectrum of the SiNCs is broad and almost structureless. When

5.1. Samples: preparation and characterization

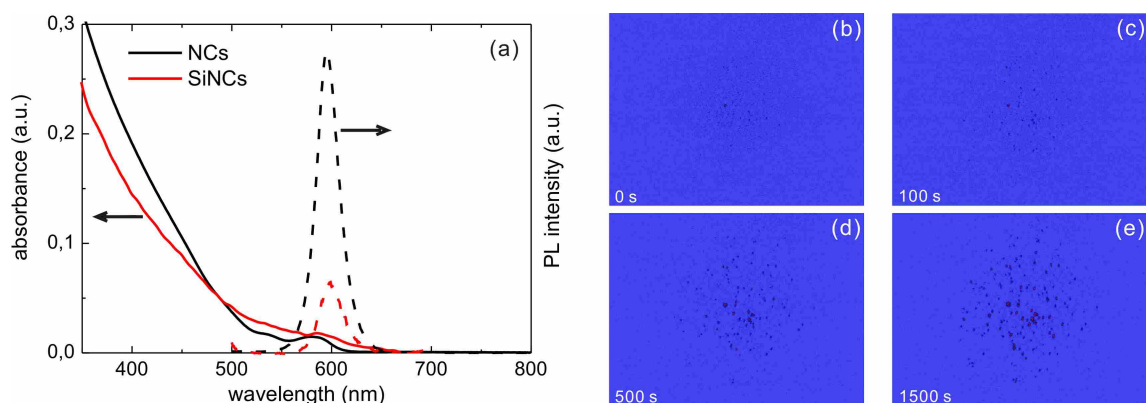


Figure 5.6: (a) Absorption (solid curves) and PL (dashed curves) spectra of NCs before (black) and after (red) coating of silica shells. The absorption spectra are normalized at the excitation wavelength (488 nm). (b – e) PL images of SiNCs on glass covers after being illuminated by expanded laser beam (470 nm) spot for different times. The colorbar range is the same in all four images. Size of the images is about $60 \times 60 \mu\text{m}^2$.

the absorbance at the excitation wavelength (488 nm) is normalized, the PL intensity of SiNCs is lower than that of NCs without silica shell, although no apparent shift in the PL peak is observed. In addition, the synthesized SiNCs typically show photobrightening behavior¹ [Wan04, Dem08], which is shown in Fig. 5.6b – e. When the SiNCs evenly distributed on a glass cover are illuminated by an expanded laser beam spot, the number of emitting SiNCs increases with the illumination time.

5.1.2 Self-assembled gold nanoparticle films

Synthesis. Gold nanoparticles (AuNPs) were prepared according to Ref. [Gra95]. In a typical reaction, 500 mL of 1 mM solution of HAuCl_4 was brought to a rolling boil under vigorous stirring. By the addition of 50 mL of 38.8 mM sodium citrate, the solution color changed swiftly from yellow to colorless. The heating was continued for 10 min until the solution turned red. Then, the heating mantle was removed and the solution was left cool to room temperature. The final products were kept in the dark and used within one month after preparation.

To prepare the AuNP films, glass covers were cleaned in a 70°C piranha solution (3 : 1 (v/v) mixture of concentrated H_2SO_4 and 30% H_2O_2) for 10 min to remove

¹Also known as photoactivation.

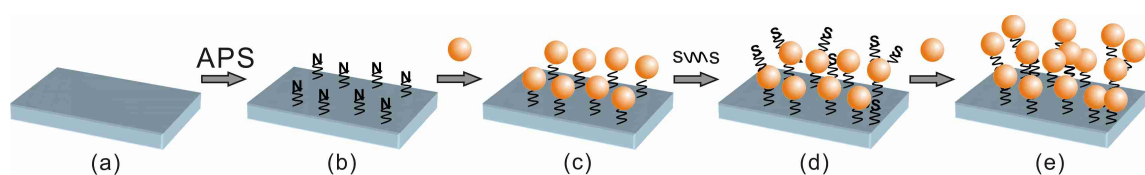


Figure 5.7: Illustration of the preparation of AuNP films.

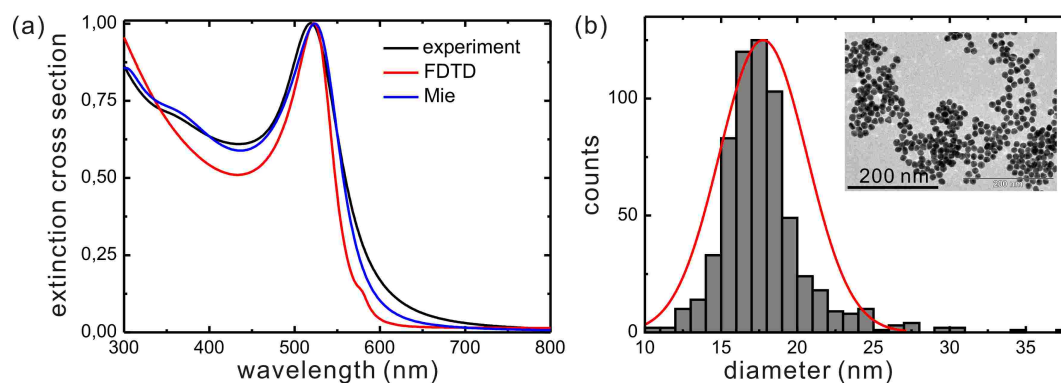


Figure 5.8: (a) Normalized extinction spectra of AuNPs in water from experimental measurement (black), of single AuNP with the diameter of 17 nm in water calculated from FDTD simulation (red) and Mie theory (blue). (b) Histogram of the diameter of the synthesized AuNPs. The inset is a TEM image of the AuNPs.

any organic residues, rinsed thoroughly with distilled water, and then stored in distilled water for future applications. (*Warning:* piranha solution is hazardous and highly reactive. It may explode on contact with organic solvents. Extreme care should be taken at all times.) The cleaned glass covers were then submerged into 1% (v/v) solution of APS in ethanol for 24 h, and then rinsed with ethanol and distilled water to remove the excess molecules on the surface. The functionalized glass covers were then immersed in a solution of AuNPs for 1 h, followed by rinsing with distilled water. To attach more AuNPs, these prepared glass covers were submerged into a 0.1 M solution of 1, 2-ethanedithiol in toluene. After 15 min, the glass covers were taken out, rinsed with toluene, and dried with a nitrogen stream. They were then immersed again in AuNP solution for 1 h, followed by a thorough rinsing with distilled water. The whole preparation method is presented in Fig. 5.7. (Here, the preparation of the AuNP films were mainly performed by Dr. Hua Tan.)

Characterization. The extinction spectrum of the AuNP solution measured by the UV/Vis spectrometer is shown in Fig. 5.8a (black curve). A peak with the wavelength of 520 nm is observed, and the small width of the peak indicates narrow size distribution, which is confirmed by TEM measurements. Fig. 5.8b gives a histogram of the AuNP diameter measured from TEM images. Most of the AuNPs are spherical (inset in Fig. 5.8b) and have diameters in the range of 10 – 25 nm, while the most probable diameter is 17 nm. The extinction spectra calculated with the FDTD simulation and Mie theory for single AuNPs with the diameter of 17 nm is found to be in reasonable agreement with the experimental result.

Absorption spectra of two representative AuNP films are shown in Fig. 5.9a, together with that of AuNPs in solution. The films that were immersed once in AuNP solution have an absorption peak at 526 nm, which is relatively red shifted as compared to the spectrum of the AuNP solution (blue curve). In the following, this type of AuNP films is called Au526. On the other hand, the films that were immersed twice in the AuNP solution have a much broader spectrum with a higher

5.1. Samples: preparation and characterization

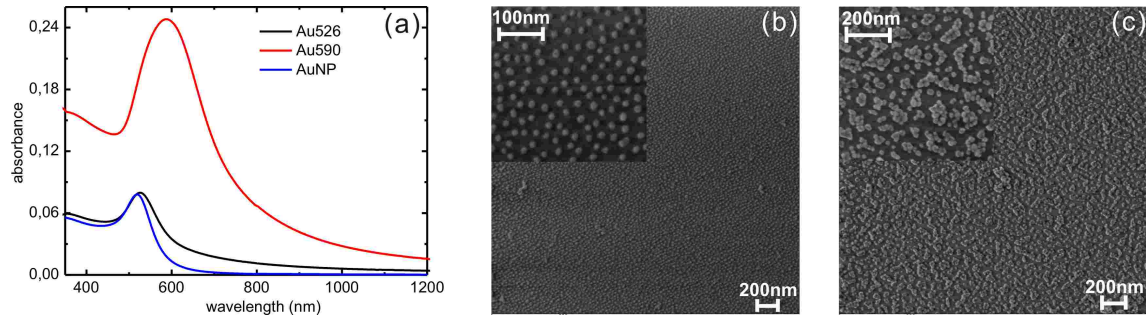


Figure 5.9: (a) Absorption spectra of Au526, Au590, and AuNPs in solution. (b) SEM images of Au526. (c) SEM images of Au590.

absorption intensity (red curve) compared with the spectrum of Au526, and the peak is further red shifted to 590 nm. Consequently, this type of AuNP films is called Au590. The structures of the two types of AuNP films are shown in Fig. 5.9b and c. Au526 mainly have separated AuNPs evenly distributed on the glass cover. However, Au590 have aggregates of AuNPs with different geometries, which explains the broad and red-shifted absorption spectrum.

Structures of the AuNP films were further studied with AFM, and the result is given in Fig. 5.10. Consistent with the SEM images, the AFM height images of Au526 films recorded in air also show small height variation of the AuNP films and homogeneous distribution of the AuNPs on the glass cover. Since the most probable diameter of the AuNPs is 17 nm, it is clear from the profile of height in Fig. 5.10b that only single layer of AuNPs is adsorbed and almost no aggregate is formed.

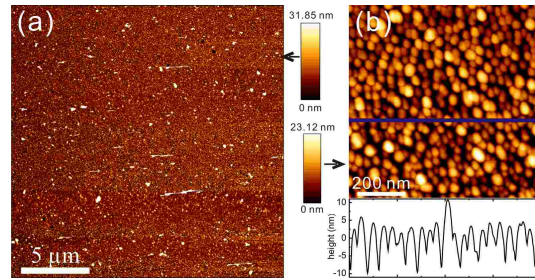


Figure 5.10: (a) AFM height image of a Au526 film ($20 \times 20 \mu\text{m}^2$). (b) AFM height image ($0.8 \times 0.8 \mu\text{m}^2$) of a Au526 film together with the profile of height of the AuNPs marked in the image (blue line).

5.1.3 Sample preparation for optical measurements

In order to prepare samples for optical investigation of individual NCs, previously described SiNCs with QE of 31% and overall diameters of 20 nm and 40 nm were diluted with ethanol. (Here, several batches of SiNCs used for the optical investigation were prepared by Dr. Hua Tan.) The prepared AuNP films (Au526 and Au590) were fixed on a homebuilt spin-coater. Then, 10 – 20 μL of the diluted SiNC solution was spin-coated onto the films at the speed of about 1000 rpm. Due to the limitation of optical resolution, the average spacing between the neighboring SiNCs has to be adjusted to be larger than 1 μm .

To examine if the spin-coating process disrupts the structures of the AuNP films,

the prepared samples were characterized again with SEM and AFM. The same structure and geometry of the AuNP films were observed before and after spin-coating. However, because of the similar sizes of the AuNPs and SiNCs, as well as the relatively low contrast due to the low conductivity of the glass covers in the SEM measurements, it was impossible to distinguish the single SiNCs from AuNPs with these two methods.

5.2 Optical measurements of individual semiconductor nanocrystals

Measurements of the optical properties of individual NCs were performed with the experimental setup described in section 3.2. In particular, to avoid contamination of the samples, an air objective (Olympus, 100 \times , 0.95 NA) was used.

Fig. 5.11 shows scanned PL images of 20 nm sized SiNCs spin-coated on three different substrates and measured under the same conditions. Each image has the size of $10 \times 10 \mu\text{m}^2$, and the integration time for each pixel is 25 ms. The color scale presents the PL intensity of the SiNCs and the range is the same in each image (0 – 2000 counts/s). For the SiNCs on the bare glass covers (Fig. 5.11a), only very few SiNCs can be observed (as marked by circles in the image) and their maximum PL intensity is about 500 counts/s. However on the AuNP films, the maximum PL intensity of the SiNCs increases to 1200 counts/s (Fig. 5.11b) and 2000 counts/s (Fig. 5.11c) for Au526 and Au590, respectively. In the special case of Au590, many more SiNCs are observed compared to the bare glass cover. Aside from the increasing PL intensity of the SiNCs, it is clear that the background signal is also larger in the case of the AuNP films. This is due to the increased scattering and/or impurities introduced by the AuNP films.

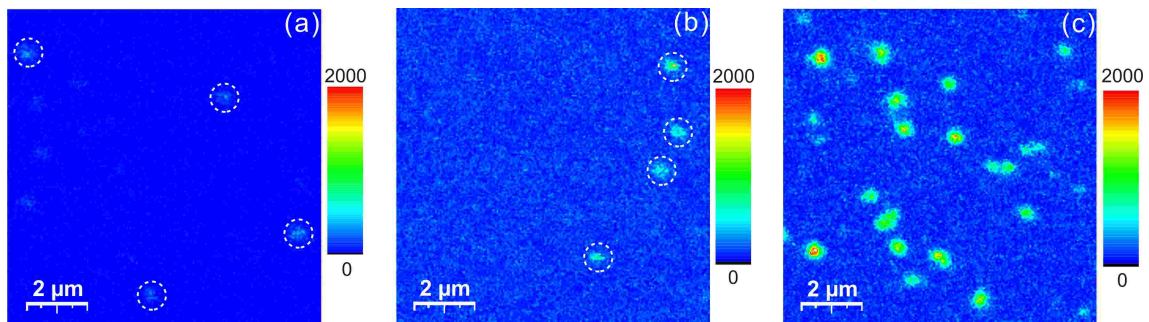


Figure 5.11: Scanned PL images ($10 \times 10 \mu\text{m}^2$) of 20 nm sized SiNCs on (a) bare glass cover, (b) Au526, and (c) Au590. The color scale presents the PL intensity of the SiNCs in the range of 0 – 2000 counts/s

5.2. Optical measurements of individual semiconductor nanocrystals

PL spectra of the individual SiNCs on different substrates were recorded by a CCD camera. Due to the different intrinsic properties of the SiNCs, small deviations in the spectrum peak position and width are observed for different SiNCs, as shown in Fig. 5.12. The spectrum from individual SiNCs can be fitted with single Lorentzian functions and the FWHM is usually smaller than 18 nm. However, no apparent difference is observed for the spectra of SiNCs on the three different types of substrates.

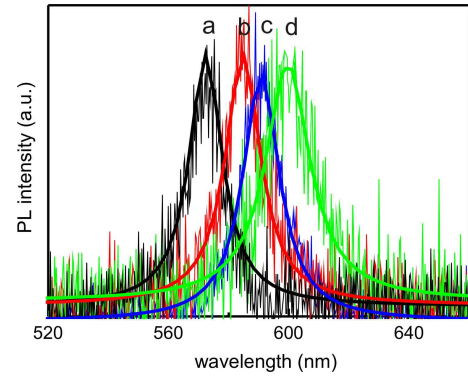


Figure 5.12: PL spectra of individual SiNCs. The smooth curves are Lorentzian fittings.

To study the PL properties of the 20 nm sized SiNCs in more detail, PL time traces recording the temporal evolution of the PL intensity were investigated under the same experimental conditions for many (about 50 for each substrate) individual SiNCs. Fig. 5.13a – c shows a set of typical time traces of individual SiNCs on the three different substrates. The time bin of each time trace is 50 ms. The corresponding count rate histograms (CRHs) are given in Fig. 5.13d – f, which can be roughly approximated by the sum of two Poisson distributions. By defining the threshold dividing the on- and off-states of the NCs as the minimum between the two peaks in the CRHs, it can be computed that the fraction of the on-time for the SiNCs on bare glass cover, on Au526, and on Au590 are 60%, 77%, and 94%, respectively. It can also be observed that the most frequent PL intensity for the on-state of the SiNCs is increased from 32 counts/(time bin) on bare glass cover over 55 counts/(time bin) on Au526 to 104 counts/(time bin) on Au590. Meanwhile, the most frequent PL intensity for the off-state also increases, as listed in Table 5.2. It should be noted that, for the SiNCs on the AuNP films (especially for those on Au590), the intensity of the off-state is significantly higher than the corresponding background signals measured under the same conditions on each corresponding substrate (but at positions without the SiNCs). This is very different from SiNCs on bare glass covers, where no significant difference in the PL intensities of the off-state and background is observed. It can be concluded that those off-periods of the SiNCs on AuNP films are actually low-emitting periods and can be assigned to the so-called gray states [Spi09]. The mechanism behind the

Table 5.2: Information derived from the time traces of 20 nm sized SiNCs on different substrates.

substrate	on-time fraction	on-state PL intensity (counts/(time bin))	off-state PL intensity (counts/(time bin))	background PL intensity (counts/(time bin))
bare glass	60%	32	1	1
Au526	77%	55	8	3
Au590	94%	104	31	14

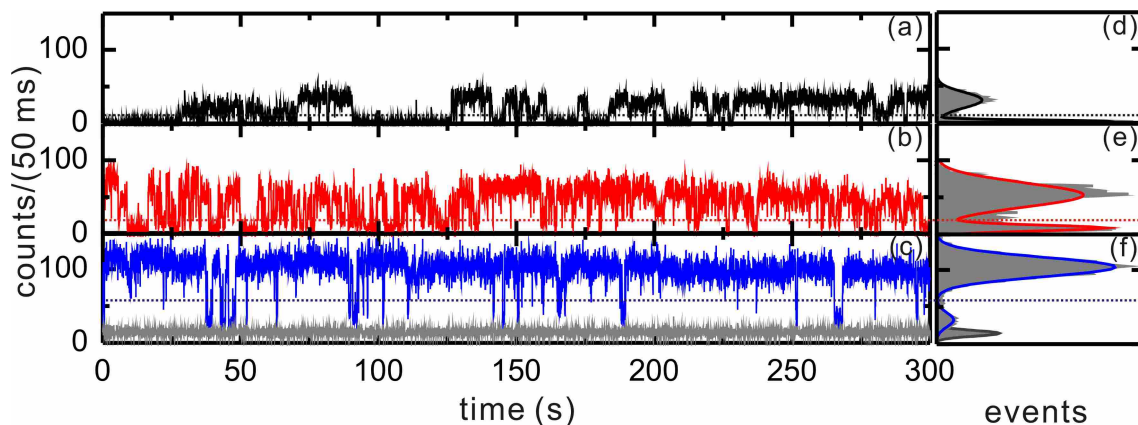


Figure 5.13: (a – c) Typical time traces of individual 20 nm sized SiNCs on glass (a), Au526 (b), and Au590 (c). (d – f) The corresponding count rate histograms. In (c) and (f), the background time trace and the count rate histogram of Au590 are also shown. The dashed lines are the thresholds and the curves in (d – f) are the sum of two Poisson distributions used to fit the count rate histograms.

appearance of such gray states will be discussed in detail in the next section.

As mentioned above, these three time traces are representative examples of many individual 20 nm sized SiNCs that have been investigated. Fig. 5.14 shows histograms of the on-state most frequent PL intensities constructed from the time traces of about 50 single SiNCs on each type of substrate. As can be seen from the figure, for the 20 nm sized SiNCs, the most frequent PL intensity of the on-state increases from bare glass cover to the AuNP films. Similar experiments were also performed on 40 nm sized SiNCs, as shown in Fig. 5.14b. However, different from the 20 nm sized SiNCs, the PL intensity of the 40 nm sized SiNCs is nearly independent of the substrate, indicating that for those SiNCs, the influence from the AuNP films is much weaker as compared to the 20 nm sized SiNCs. On the other hand, preliminary experiments by directly spin-coating NCs without silica shells on AuNP films show an immediate quenching of the fluorescence, which may be attributed to the predominant ultrafast electron transfer from NCs to AuNPs. Therefore, the following discussion will be mainly concentrated on the 20 nm sized SiNCs.

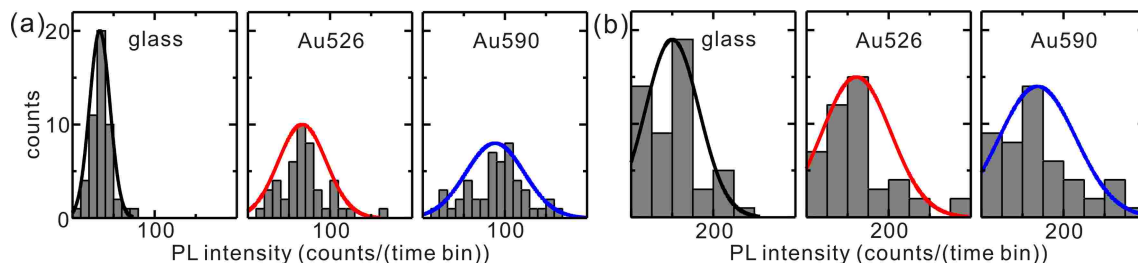


Figure 5.14: Histograms of the on-state most frequent PL intensity of 20 nm (a) and 40 nm (b) sized SiNCs on different substrates. The curves are Gaussian fittings.

5.2. Optical measurements of individual semiconductor nanocrystals

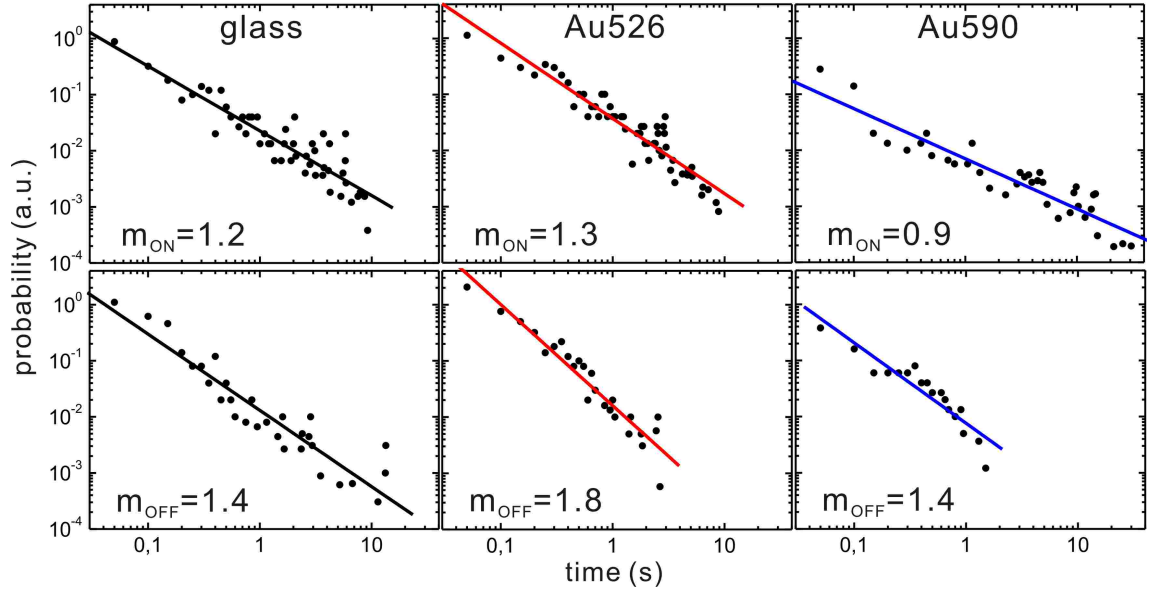


Figure 5.15: On- (upper panels) and off-time (lower panels) probability density plotted on a log-log scale for the time traces in Fig. 5.13a – c. The lines are a linear fit to the data, and the corresponding slopes of the fitted lines are denoted as m_{ON} or m_{OFF} .

From the time traces in Fig. 5.13a – c we can extract the on- and off-time probability densities by defining the threshold as the minimum between the two peaks in the histograms. Since the probability density of shorter on-/off-time is much higher than that of the longer time, in order to avoid overweighting the short time events, each event density is weighted by the average time between nearest neighbor events [Kun01]. The resultant probability densities are plotted on a log-log scale in Fig. 5.15. It can be seen that both the on- and off-time follow the universal power law (section 2.2.4) regardless of the substrates. Further analysis of many other time traces reveals that the exponents (m_{ON} and m_{OFF}) have values in the range of 0.9 to 2.1.

Detailed study was also performed regarding the recombination dynamics of the SiNCs on different substrates by the time-resolved PL spectroscopy. Fig. 5.16a shows the background-subtracted PL decay curves of the very same SiNCs investigated in Fig. 5.13. The background intensity, which is mainly due to impurities and scattering from the substrates, are below 5% of the total PL intensity. Shown as well is the IRF, which has a FWHM of 128 ps. In TCSPC, the detected decay curves represent the convolution of the PL decay function of the sample and the IRF. The IRF can be neglected in the cases when the investigated sample has lifetime much longer than the width of IRF, e.g., CdSe NCs, which usually have room-temperature lifetimes on the order of tens of ns. However, when the lifetime of the sample is comparable to or even shorter than the width of IRF, the experimental data has to be reconvoluted in order to obtain results free from instrumental distortions [McK77, O'C79].

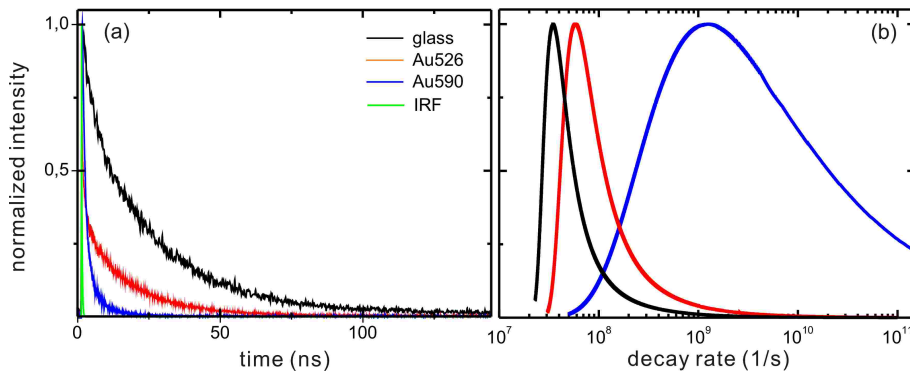


Figure 5.16: (a) PL decay curves of single SiNCs on different substrates together with the IRF. (b) The corresponding rate distributions calculated from the stretched exponential fitting results.

Two methods are used to evaluate the recombination rates of the individual SiNCs. In the first approach, the decay curves in Fig. 5.16a are fitted with a stretched exponential function (eq. (2.39)) by reconvoluting the IRF signal in the FluoFit software (PicoQuant GmbH). The quality of the fits can be judged by the commonly applied chi-square criteria, and the appearance of the normalized deviation and autocorrelation curves for randomness of error. For the single SiNCs on bare glass cover the values of $\tau_{1/e}$ and β_s are determined to be 19.9 ns and 0.84. From eq. (2.40) the average lifetime is computed to be 21.7 ns. The values for SiNCs on the AuNP films are listed in Table 5.3, and it is clear that the corresponding average lifetimes $\langle\tau\rangle$ are shorter than that of the SiNC on glass cover. From these fitting results, the decay rate distributions ($\tau\rho(\tau)$) can be calculated by a direct inverse Laplace transformation of the fitting functions (see section 2.2.5). As shown in Fig. 5.16b, the decay rate and width of the rate distribution increases from the SiNCs on glass cover to these on the AuNP films.

The second approach relies on the previously mentioned TTTR single photon counting technique (see section 2.2.5). In principle, for a time trace recorded for certain time, we can separately collect the PL decay curves for each time bin i and fit them with a single exponential function

$$I_i(t) = A_i \exp(-t/\tau_i). \quad (5.1)$$

Since the total number of photons corresponding to a certain decay process is given by the area below the decay curve, for each time bin, the emitted photons N_i can

Table 5.3: $\tau_{1/e}$, β_s and $\langle\tau\rangle$ computed from the stretched exponential fittings of the decay curves.

substrate	$\tau_{1/e}$ (ns)	β_s	$\langle\tau\rangle$ (ns)
bare glass	19.9	0.84	21.7
Au526	12.7	0.83	14.0
Au590	0.4	0.44	1.1

5.2. Optical measurements of individual semiconductor nanocrystals

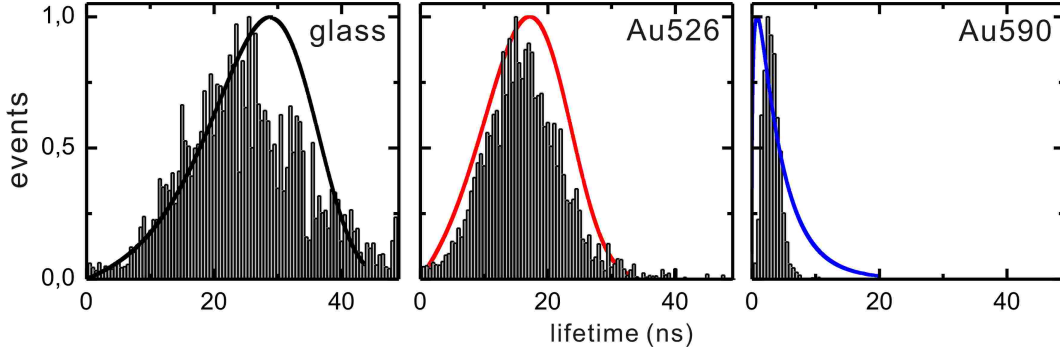


Figure 5.17: PL lifetime distributions of SiNCs on different substrates calculated by fitting decay curves from each time bin with single exponential functions (bars) and from the stretched exponential fittings (lines). For the SiNCs on glass, a time bin of 100 ms instead of 50 ms is used because of the relatively low PL intensity.

be computed from the single exponential fitting results of the decay curves by

$$N_i = \int_0^{\infty} I_i(t) dt. \quad (5.2)$$

Combining eq. (5.1) and eq. (5.2), we obtain

$$N_i = A_i \tau_i \quad (5.3)$$

Therefore, by summing up the values of $A_i \tau_i$ of different time bins having the same τ_i , the total number of photons with lifetime τ_i in the whole recording time of the time trace can be computed to be $\sum_j A_j \tau_i$. The corresponding histogram of the lifetime ($\sum_j A_j \tau_i$ vs. τ_i) can thus be constructed.

Fig. 5.17 shows lifetime distributions of the SiNCs investigated in Fig. 5.13 calculated from the two methods: by fitting decay curves from each time bin with single exponential functions and from the stretched exponential fittings for the decay curves constructed from the whole time traces. For the SiNCs on glass covers, a time bin of 100 ms instead of 50 ms is used because of the comparably low PL intensity. Good correlation between the two methods is observed for SiNCs on the different substrates.

Average lifetimes $\langle \tau \rangle$ can also be computed from the second approach, in which $\langle \tau \rangle$ is defined as

$$\langle \tau \rangle = \frac{\int A_i \tau_i d\tau_i}{\int A_i d\tau_i}. \quad (5.4)$$

For the SiNCs on glass, on Au526, and on Au590, $\langle \tau \rangle$ is computed to be 18.4 ns, 12.5 ns, and 2.7 ns, respectively. These values are in good agreement with those obtained from the stretched exponential approach (Table 5.3).

In addition, it is possible to correlate the PL intensity ($A_i \tau_i$) with the fluorescence lifetime (τ_i). Fig. 5.18a – c shows simple scatter plots of the PL intensity – lifetime

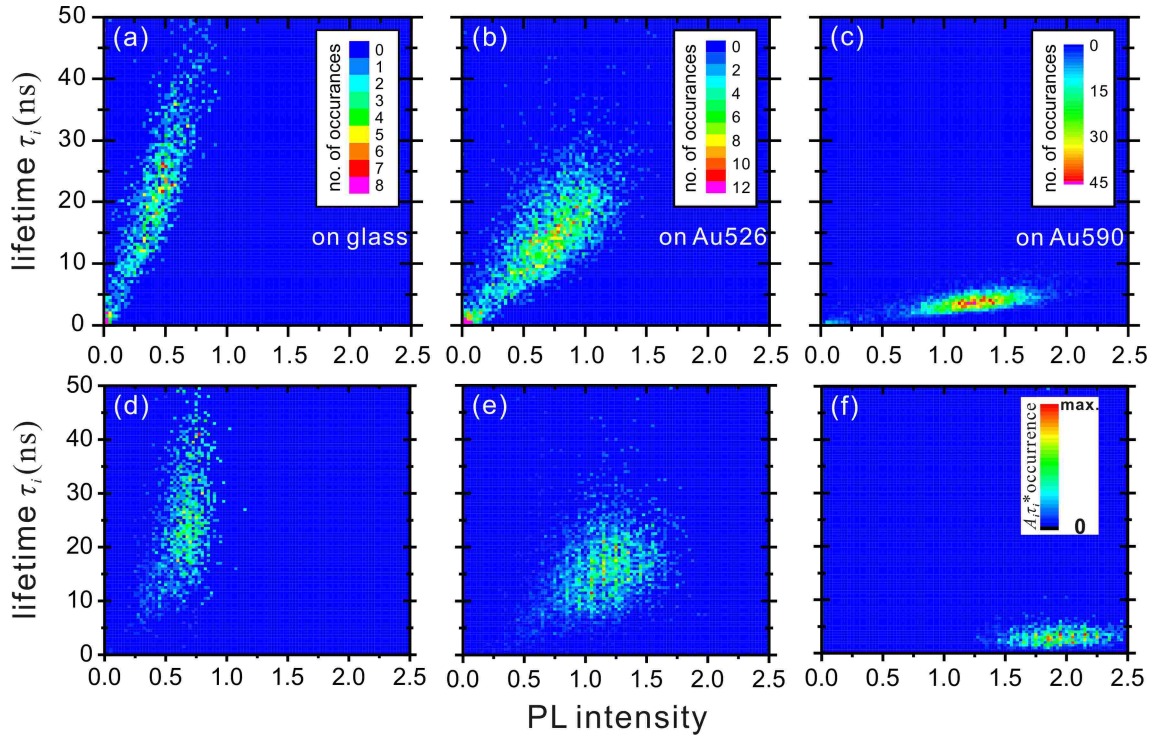


Figure 5.18: (a – c) Unweighted scatter plots of PL intensity ($A_i\tau_i$) – lifetime (τ_i) distributions of the SiNCs on different substrates. (d – f) Weighted PL intensity – lifetime distributions of SiNCs on glass (d), on Au526 (e), and on Au590 (f).

distribution of SiNCs on the three types of substrates. For the SiNCs on glass, a time bin of 100 ms instead of 50 ms is used because of the relatively low PL intensity. Broad distributions of the occurrences are observed and, in general, long lifetimes are correlated with high PL intensities. Since the data points at low PL intensity and short lifetimes are strongly influenced by the background signals, the occurrences at each $A_i\tau_i - \tau_i$ pair are weighted by the number of photons $A_i\tau_i$ and the results are plotted in Fig. 5.18d – f. Compared to the unweighted scatter plots, the noisy signals corresponding to low PL intensity and short lifetime disappear, although the PL behavior that long lifetime correlating to high intensity is still conserved. In this case, the integral over the whole scatter plot gives a measure of the total PL intensity instead of the total number of evaluated decay curves. Constructing lifetime distributions from Fig. 5.18d – f would give the results shown in Fig. 5.17 (bars).

In summary, the experimental findings from the optical measurements of individual SiNCs on different substrates are:

1. Fluorescence enhancement. Compared to the case of the glass cover, the on-state PL intensities of the 20 nm sized SiNCs on Au526 and Au590 are increased by factors of 2 and 3, respectively.
2. Blinking suppression. The SiNCs on AuNP films show a suppressed blinking behavior compared to those on glass covers. The on-time fraction increased from 60% on a glass cover to 94% on Au590.

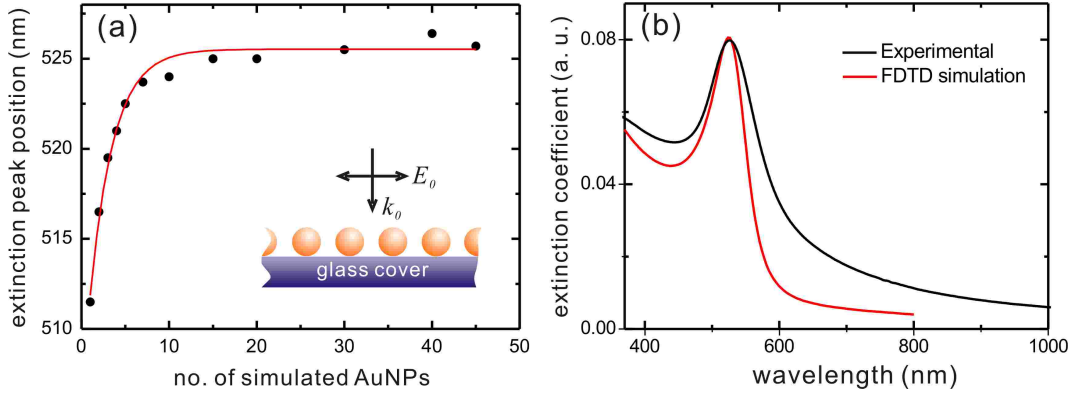


Figure 5.19: (a) Dependence of the extinction peak position on the number of simulated AuNPs in the simulation of Au526. The red curve is guide for the eye by fitting the simulation results with an exponential function $f(x) = c_1 + c_2 \exp(-c_3x)$. The inset is a schematic of the simulated geometry. (b) Extinction spectra of Au526 from experimental measurements and FDTD simulations.

3. Occurrence of gray states. For the SiNCs on AuNP films, especially on Au590, low-emitting periods corresponding to gray states instead of off-states appear.
4. Decreased lifetime and increased recombination rate.

In the following section, the mechanisms to explain these findings will be discussed in detail.

5.3 Theoretical interperation

As previously discussed in section 2.4.1, the near-field interaction between NCs and metallic nanostructures changes both the field applied to the NCs (the excitation process) and the field radiated by them (the emission process). Since the internal conversion, which happens between excitation and emission processes, depends mainly on the intrinsic electronic structure of NCs, it is insensitive to the changes of the local electric field in first approximation. Therefore, when the excitation intensity is below saturation, which is fulfilled in all of the measurements carried out in this study, it is reasonable to treat the excitation and emission processes independently.

Excitation process. For the excitation process, since the excitation rate k_{exc} is proportional to the local electric field intensity $|E|^2$ at the position of the NCs, numerical simulations with 2D FDTD method¹ were performed. The smallest grid size was determined by the method reported by Zhang et al. [Zha07a]. Typically, the total simulation time was set to 200 fs so as to make sure the simulations had sufficient time steps. Meanwhile, the Auto shutoff level was set to 1e-08 so that the simulation can be automatically shut off once the required accuracy was met. A

¹Due to the relatively large size of the AuNP films, 3D FDTD would require too much computing power.

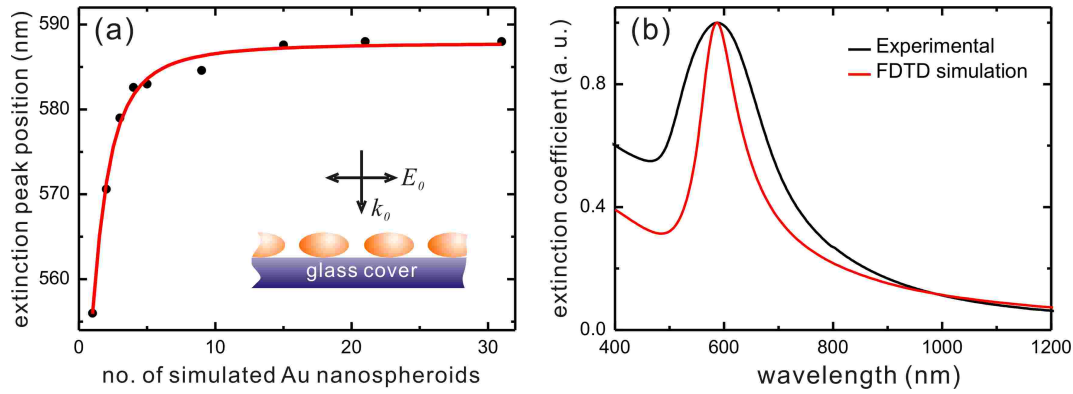


Figure 5.20: (a) Dependence of the extinction peak position on the number of simulated Au nanospheroids in the simulation of Au590. The red curve serves as a guide for the eye by fitting the simulation results with an exponential function $f(x) = c_1 + c_2 \exp(-c_3x)$. The inset is a schematic of the simulated geometry. (b) Extinction spectra of Au590 from experimental measurements and FDTD simulations.

plane wave with wavelength between 300 and 800 nm propagating perpendicularly to the substrate was used as the light source (see inset in Fig. 5.19a).

First of all, the extinction spectra of Au526 and Au590 were simulated and compared to the experimental data in order to prove the validity of the simulations. For Au526, the size and edge-to-edge distance of AuNPs were estimated from the TEM and SEM images (Fig. 5.8 and 5.9) to be 17 nm and 15 nm, respectively. Because of the near field interparticle coupling, the number of simulated AuNPs had a significant influence on the extinction spectra. Fig. 5.19a shows the calculated extinction peak position versus the number of simulated AuNPs (17 nm) which are located 15 nm away from each other. A continuous red shift of the extinction peak is observed with the increasing number of AuNPs, and it remains constant at 526 nm after the number reaches 15. Fig. 5.19b compares the measured extinction spectrum of Au526 with the simulated one of an array of 45 AuNPs. Good agreement is observed, while the broadening of the experimental spectra can be due to the nonuniform distribution of the AuNPs on glass substrate and a variation in the incident direction of light.

Because of the inhomogeneity of the AuNP aggregates, Au590 is not as easy to simulate as Au526. To approximate the structure, a 2D outline of the AuNPs in a $1 \mu\text{m} \times 1 \mu\text{m}$ SEM image area was plotted with ImageJ (NIH, USA). This projected 2D area was then approximated by arrays of spheres which were evenly distributed on the substrate. By making sure the whole area of those spheres were the same as that from the experimental projection, the average diameter of the spheres was calculated to be 60 nm, while the average edge-to-edge distance between the neighboring particles was 15 nm. The height of those aggregates was roughly estimated from SEM to be about 24 nm. Therefore, the Au590 films can be approximated by an array of spheroids with equatorial radius of 30 nm parallel to the surface, a polar radius of 12 nm perpendicular to the surface, and an average edge-to-edge distance between the neighboring AuNP islands of 15 nm (inset of Fig. 5.20a). A similar

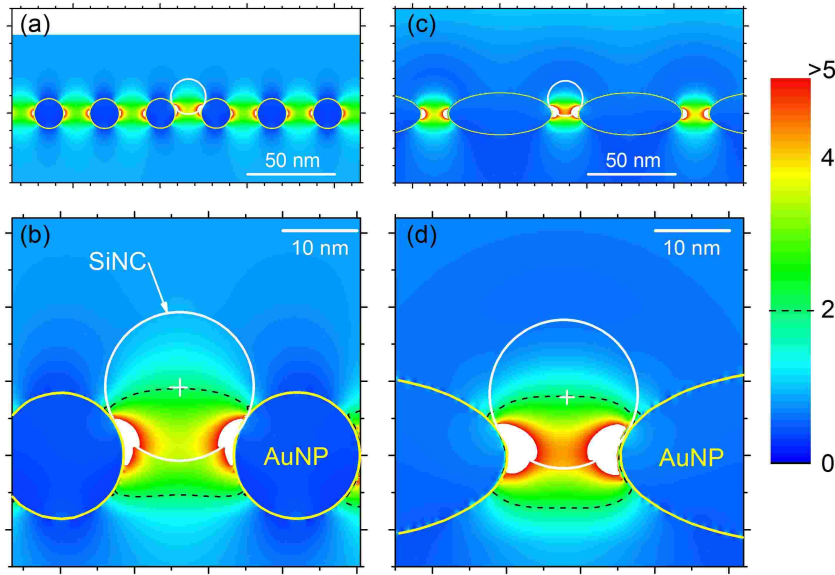


Figure 5.21: Color scale plots of the local electric field intensity enhancement factor of (a) Au526 and (c) Au590. (b) and (d) are the enlarged details of (a) and (c), respectively. The white circles indicate the possible positions of the 20 nm sized SiNCs.

effect of the simulated number of Au nanospheroids on the extinction peak position is also observed as for Au526 (Fig. 5.20a). The extinction spectrum simulated from an array of 45 Au nanospheroids is again in good agreement with the experimental result, as shown in Fig. 5.20b.

Since the simulation was in reasonable agreement with experimental results, also the local electric field enhancement factor γ_{exc} , which is defined as the ratio of the electric field intensity at the excitation wavelength 470 nm and the position of the NCs, to the incident field intensity value in the absence of the metallic nanostructures, was calculated. The simulation result is shown in Fig.5.21. It is apparent that the local field intensity enhancement factor strongly depends on the location of the NCs on the AuNP films. As was discussed in section 5.1.3, the exact position of the SiNCs is difficult to determine. In a special case indicated by the circles in Fig. 5.21, the 20 nm sized SiNCs are located within the gaps of neighboring AuNPs, and the corresponding enhancement factors are computed to be $\gamma_{exc} = 1.9$ and $\gamma_{exc} = 2.0$ for Au526 and Au590, respectively. Visualization of the enhancement factor suggests values of up to 3.5 for Au526 and 5 for Au590. These values are in good agreement with the experimentally observed PL enhancements of different individual SiNCs as shown in Fig.5.14.

The simulation results of the excitation process reveal that the increased local electric field, and hence the increased excitation rate, is at least part of the reason for the experimentally observed enhancement of the on-state PL intensity for the 20 nm sized SiNCs on AuNP films. Here, it should be noted that the excitation wavelength we applied (470 nm) is blue-shifted compared to the extinction peaks of the AuNP films. Therefore, the local field enhancement is an off-resonant effect and is relatively weak.

Emission process. Generally, it is possible to estimate the change of the radiative and nonradiative decay rates of SiNCs on glass cover and on AuNP films if the quantum efficiency (η) of the respective SiNCs is known. For the ensemble solution of the SiNCs, the quantum efficiency was measured to be about 31%. In a very rough approximation, one can assume that this value is the same for individual SiNCs on a glass cover. Taking the on-time fraction of the SiNCs (60%) into account, we obtain the quantum efficiency for the on-state of SiNCs on glass to be $\eta_{on}^{glass} = 31\% / 60\% = 52\%$. Together with the measured average decay rate

$$k_{measured}^{glass} = k_r^{glass} + k_{nr}^{glass} = (21.7 \text{ ns})^{-1} \quad (5.5)$$

obtained from the stretched exponential fitting approach, one can derive the corresponding k_r^{glass} and k_{nr}^{glass} , as listed in Table 5.4. For the 20 nm sized SiNCs on Au590, by calculating the total number of photons emitted in 300 s from the time traces in Fig. 5.13, it is derived that the overall PL intensity of SiNCs on Au590 is increased by a factor of 4.8 compared to those on a bare glass cover. If we take the local electric field enhancement factor as 2, and take the on-time fraction (94%) into account, then the on-state quantum efficiency of the SiNCs on Au590 is calculated to be

$$\eta_{on}^{Au590} = \frac{4.8}{2} \times 31\% \times \frac{1}{94\%} = 79\%. \quad (5.6)$$

Again, using the measured average decay rate $k_{measured}^{Au590} = (1.1 \text{ ns})^{-1}$, we can estimate the radiative and nonradiative decay rates. The calculated results are listed in Table 5.4. Within these considerations based on a very rough approximation of the quantum efficiency η_{on}^{glass} , the coupling of NCs in 10 nm distance to the Au590 film increases the radiative decay rate by a factor of about 30 whereas the nonradiative decay rate is only enhanced by a factor of about 8.

The above results are obtained based on the experimental measurements and a very rough approximation of the quantum efficiency. To theoretically estimate the recombination rates of the 20 nm sized SiNCs on AuNP films, the different models introduced in section 2.4.2 were used to simulate the interactions. The individual SiNCs were treated as point dipoles emitting at the wavelength of 600 nm. The quantum efficiency was again approximated to be 31%.

Table 5.4: Recombination rates for 20 nm sized SiNCs on different substrates.

substrate	η_{on} (%)	$k_{measured}$ (s^{-1})	k_r (s^{-1})	k_{nr} (s^{-1})
glass	52	4.6×10^7	2.4×10^7	2.2×10^7
Au526	47	7.1×10^7	3.3×10^7	3.8×10^7
Au590	79	9.1×10^8	7.2×10^8	1.9×10^8

First, to estimate the validity of the FDTD method, the radiative decay rate of a dipole oriented perpendicularly (k_r^{perp}) to a single AuNP surface with diameter of 17 nm was computed from both the FDTD method and the Gersten-Nitzan model, as shown in Fig. 5.22. Good correlation between the two methods is observed, and the radiative decay rate of dipoles oriented perpendicular to the AuNP surface is expected to be larger than the case without AuNP (dashed curve in Fig. 5.22). When the dipole gets closer to the AuNP surface, k_r^{perp} increases.

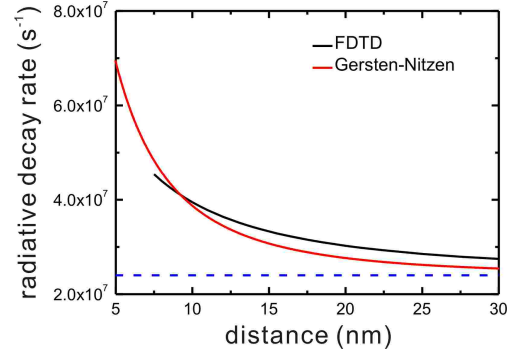


Figure 5.22: Radiative decay rates of a dipole oriented perpendicularly to a AuNP surface calculated from FDTD method and Gersten-Nitzan model. The dashed curve is the radiative decay rate of the dipole on a glass cover ($2.4 \times 10^7 \text{s}^{-1}$).

Radiative decay rates (k_r) of dipoles on AuNP films were then simulated with the FDTD method. Fig. 5.23 shows the local electric field enhancement distribution close to a dipole in a 20 nm sized silica shell oriented parallel to Au526 and Au590 films. The black area indicates regions with decreased electric field intensity as compared to that on a glass cover (< 1). For dipoles on Au590, strong enhancement is observed.

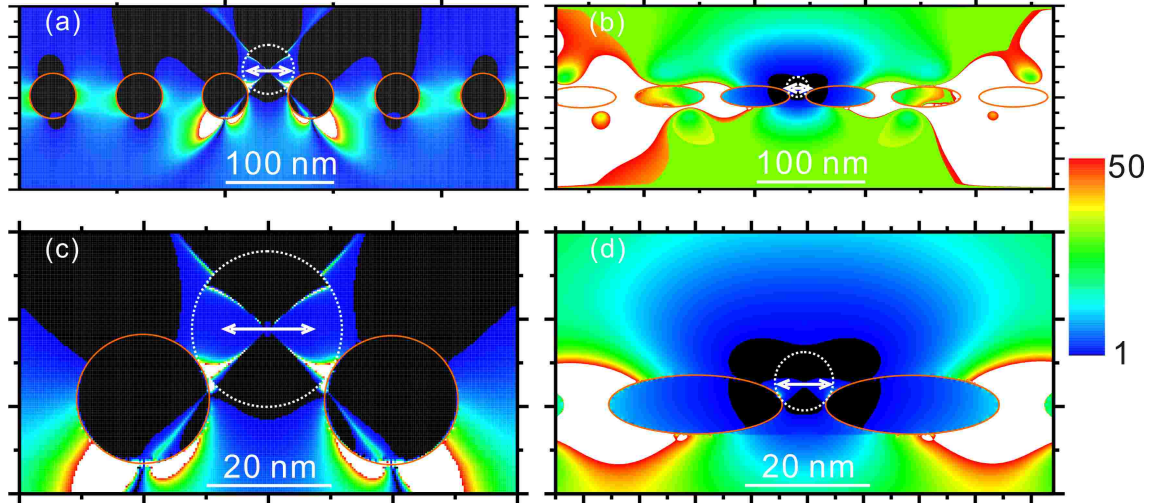


Figure 5.23: Color scale plots of the local electric field intensity enhancement factor of a dipole oriented parallel to (a) Au526 and (b) Au590 as compared to that on a glass cover. (c) and (d) are the enlarged details of (a) and (b). The white circles and arrows indicate the positions of the silica shells and dipoles. The color scale stars from 1, which means the black area indicates decreased local electric field.

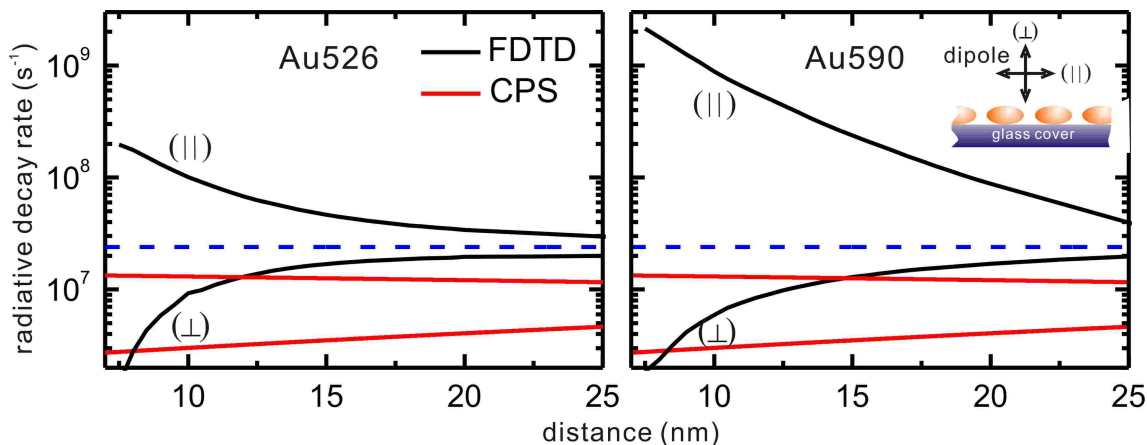


Figure 5.24: Radiative decay rates of dipoles on Au526 and Au590 calculated from FDTD method (black) and CPS model (red). The dashed curves are the radiative decay rate on glass covers. For the curves from the FDTD method, the upper ones correspond to the dipole oriented parallelly (\parallel) to the AuNP film, and the lower ones to the dipole oriented perpendicularly (\perp) to the surface. The same conditions apply for the curves from the CPS model. The inset is a schematic of the simulation geometry.

The calculated radiative decay rate as a function of distance between the dipole and the AuNP films is shown in Fig.5.24. Obviously, orientation of the dipole has big influences on k_r . Dipoles oriented perpendicularly (\perp) to the AuNP film have smaller k_r than those on glass covers, whereas parallel orientation (\parallel) leads to an increase in k_r . Comparing the k_r values of the dipoles on Au526 and Au590, it can be seen that the AuNP film Au590 has stronger influence on the decay rates. Because of the lack of knowledge about the detailed orientation of the dipoles in the NCs, it is difficult to accurately calculate the decay rates. However, since the dipole always has orientations in between the two extreme cases (parallel and perpendicular), one can expect that the value k_r should also be in between the area defined by the two curves corresponding to the two orientations, which is fulfilled by the k_r values from Table 5.4. Shown together in Fig. 5.24 are the k_r values calculated from the CPS model. This model mainly applies for continuous, thick metallic films. Here the calculated k_r values are much smaller than the results from Table 5.4 because of the over-estimated influence from the AuNP films.

In principle, one can also use those methods to calculate the nonradiative and total decay rates, and consequently the quantum efficiency. However, there are several limitations in the calculations:

1. The FDTD method can be used to simulate structures that are closest to the real situation. However, it is valid only for dipoles with unity quantum efficiency [Nov06] and strongly dependent on the exact 3D structure of the system, which is not known at this point.
2. Almost all the methods rely on the exact value of the quantum efficiency of the dipoles. In the above mentioned calculations, the quantum efficiency of 31% from the solution is used. However, for NCs without silica shells it

has been shown that only a portion of the individual NCs show fluorescence at all [Ebe02, Yao05]. Also taking into account that the on-time fraction of those fluorescent NCs is probably below 1, it can be argued that the quantum efficiency of the on-state of NCs should be certainly higher than the quantum efficiency in solution. However, the exact value is still unknown.

3. Transition dipoles in NCs are considered to be 2D, with the formed bright plane being perpendicular to the c axis of the NCs [Emp99]. Orientation of the dipoles has big influence on the interaction between the metallic nanostructures and the dipoles. However, the lack of the knowledge about the orientation of the dipoles makes the accurate calculation difficult.

Suggested model. Based on the above discussions, the experimental findings can be addressed within a simple qualitative model plotted in Fig. 5.25. For NCs, we generally distinguish between the on-state, which allows for the emission of photons, and the off-state, which usually contributes no photons. As discussed in section 2.2.4, despite many different models describing the blinking behavior, the on- and off-states are usually assigned to the neutral and charged NCs, respectively. As shown in Fig. 5.25, when a neutral NC is excited from its ground state $|1\rangle$ to the excited state $|2\rangle$ at the rate of k_{exc} , an exciton is generated. This excitation process is strongly dependent on the local electric field intensity. Since the excitation wavelength used in this work (470 nm) is smaller than the PL wavelength (600 nm), the exciton is excited to higher excitonic states. Only after a very fast intraband relaxation process does it relax to the lowest excitonic states.

Once there, the exciton can relax either radiatively (k_r) or nonradiatively (k_{nr}) to the ground state $|1\rangle$. However, in addition, the NC in the excited state $|2\rangle$ can also transfer to the charged ground state $|1'\rangle$ when one of the charge carriers is trapped. The subsequent photon excitation generates multiexcitons and brings the NC into its excited charged state $|2'\rangle$ at a rate k'_{exc} . From here, in most cases, the ultrafast Auger recombination process, in which the recombination energy from one pair of charge carriers excites the unpaired charge carrier, competes with the radiative recombination process. In the case without AuNP films, k'_{nr} which includes both the intrinsic nonradiative decay rate (e.g., nonradiative recombination through exciton-phonon interactions) and the Auger recombination rate, is much faster than k'_r . Therefore, the NC appears to be dark (off-state). When the NC is placed on the AuNP films, especially on Au590, the radiative decay rate k'_r is significantly increased

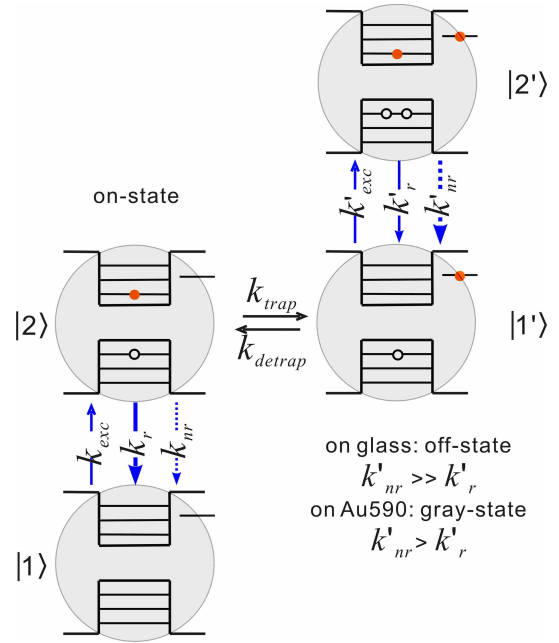


Figure 5.25: Schematic of the theoretical model.

and becomes comparable to the Auger recombination rate, and consequently k'_{nr} . As a result, low emitting periods attributed to the gray-states are observed. In the experiment, due to the small number of photons at the gray-state and the limited time resolution of the setup, we were not able to determine the recombination rates of the gray state. However, from the relative PL intensity of the on- and gray states, it is possible to correlate the quantum efficiency of the gray state (η_{gray}^{Au590}) to the on-state (η_{on}^{Au590}) as $\eta_{gray}^{Au590}/\eta_{on}^{Au590} = 19\%$.

The observation of the suppressed blinking behavior can also be explained on the basis of this model. When NCs are placed on AuNP films, the increase of the recombination rate including both k_r and k_{nr} inhibits the possibility of the charge carriers being trapped ($k_r + k_{nr} \gg k_{trap}$). Therefore, the NC stays more often in the on-state. However, because of the increased excitation rate of the charged NCs (k'_{exc}), the reverse process (recovery from the off- or gray states) may also be inhibited ($k'_{exc} \gg k_{detrap}$), which means long off-states are also possible.

In conclusion, the presence of AuNP films significantly influences the optical properties of the nearby NCs, which show increased on-state PL intensity, decreased lifetime, suppressed PL blinking, and emission from the gray state when compared to the NCs without nearby AuNP films. These observations are explained by the complex interactions between the metallic nanostructures and the NCs. For further investigation, it would be useful to know the exact 3D orientations of the NCs and the metallic nanostructures relative both to each other and to the external electromagnetic fields. By carefully choosing the studied system, the long-discussed blinking mechanism of NCs can possibly be revealed.

Chapter 6

Semiconductor nanocrystals attached to gold nanoparticles

The complex interactions between NCs and metallic nanostructures strongly depend on the geometry of the two relative to each other and to the external electromagnetic field. In order to unambiguously study the interaction mechanism, well-defined hybrid nanostructures comprised of individual NCs and AuNPs were prepared and investigated with confocal microscopy at the single NC level. Different from the case in chapter 5, the silica shells of different thicknesses used to adjust the distance between NCs and AuNPs were coated on the AuNP surface. The very same investigated hybrid nanostructures were further imaged in TEM to study the corresponding geometries. In this way, we were able to correlate optical and structural properties of the hybrid nanostructures. In what follows, detailed sample preparation and characterization methods will be described in the first part. Optical results are then correlated with the structural properties, followed by theoretical simulation with the FDTD method and the Gersten-Nitzan model.

6.1 Samples: preparation and characterization

In order to obtain hybrid nanostructures with defined distance between NCs and AuNPs, silica shells with different thicknesses were coated on the surface of AuNPs, which were then surface modified with positive ligands (these AuNPs coated with silica shells are abbreviated as AuNP@SiO₂ in the following). CdSe multishell NCs with negative ligands were attached onto the AuNP@SiO₂ by electrostatic interactions. By controlling the ratio between the two kinds of solutions and preparation parameters, hybrid nanostructures with individual NCs attached to single AuNP@SiO₂ can be obtained. Optical properties of the ensemble solutions were characterized by UV/Vis and fluorescence spectroscopy as in chapter 5. The structures of AuNP@SiO₂ and the hybrid nanostructures were extensively investigated with TEM, while the latter was further studied with high resolution TEM (HRTEM) and energy dispersive X-ray (EDX) (Philips CM 300, 80 kV).

6.1.1 Silica coated gold nanoparticles

Synthesis. Differently sized spherical AuNPs were synthesized following the seed-mediated growth method reported in Ref. [Bro00, RF06]. First, seed AuNPs were synthesized by the Turkevich method as described in chapter 5. By reducing HAuCl_4 with ascorbic acid at the temperature of 35°C in the presence of the seed AuNPs, bigger AuNPs were produced. The diameter of those AuNPs can be tuned in certain range by varying the ratio between the amount of the seed AuNPs and the precursor solution. To synthesize AuNPs with even larger diameters, AuNPs from the second step of the growth were used as seeds for further growth. In all of the seed growth steps, cetyltrimethylammonium bromide (CTAB) was used as the surfactant to stabilize the AuNPs. In addition, when using AuNPs from the second step as seeds, usually shape separation has to be carried out first to remove side products such as nanorods and planar shapes.

During this study, three different approaches were used to coat AuNPs with silica (or polymer) shells:

1. The first method relies on the direct coating of silica on the AuNP surface using the sol-gel process [Lu02]. Silica sols were generated by ammonia catalyzed hydrolysis of TEOS. In a typical procedure, $200\ \mu\text{L}$ previously synthesized AuNP (average diameter: $55\ \text{nm}$) solution was added into $2\ \text{mL}$ 2-propanol under vigorous stirring ($1200\ \text{rpm}$), followed by the addition of various amounts of TEOS. $15\ \text{min}$ later, $50\ \mu\text{L}$ ammonium solution ($25\ \text{wt}\%$) was added to speed up the hydrolysis of TEOS. The reaction was allowed to proceed at room temperature for different times and then stopped by the addition of excess ethanol. The particles were separated from the reaction medium by centrifugation, and then washed first with 1-propanol and then with ethanol. The final product was dispersed in $1\ \text{mL}$ ethanol for further applications.
2. The second approach uses polyelectrolytes as building blocks to encapsulate the AuNPs with polymer bilayers through the layer-by-layer assembly process [Jin09]. For each polyelectrolyte bilayer, two different polymers with opposite charges were deposited subsequently: polystyrene sulfonate (PSS) and poly(allylamine hydrochloride) (PAH). In a typical synthesis, PAH and PSS stock solutions were prepared by dissolving the respective polymer in a $1\ \text{mM}$ NaCl solution ($10\ \text{mg/mL}$). The CTAB-stabilized $55\ \text{nm}$ sized AuNPs were washed twice to remove the excess surfactants. Since the AuNPs stabilized by CTAB possessed a high positive charge, the polymer deposition started with the addition of PSS stock solution which contained negative sulfonate groups into the AuNP solution. The volume ratio of the polymer to AuNP solutions was optimized to be $1 : 2$. After incubation for $30\ \text{min}$, the particles were washed three times with distilled water to remove the unbound PSS polymers. It should be noted that the centrifugation speed during the washing procedure should not exceed $1500\ \text{rpm}$ to avoid aggregation. The washed sample was redispersed in water and used for the deposition of the next half layer with the PAH polymer by the same process. The same procedure was repeated for additional layers of polyelectrolyte bilayers. The final product was dispersed in water for future applications.

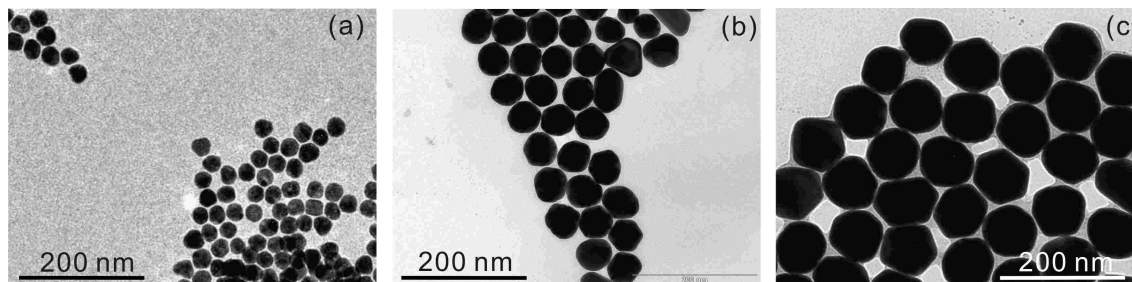


Figure 6.1: TEM images of AuNPs with average diameters of (a) 13 nm, (b) 55 nm, and (c) 88 nm. The magnifications are the same in all three images.

- The third approach follows the procedure reported in Ref. [FL09]. A special coupling agent methoxy-poly(ethylene glycol)-thiol (mPEG-SH) was used to transfer AuNPs from water into ethanol, in which silica shells were then coated on the AuNP surface through the standard Stöber process.

In order to attach NCs, the silica (or polymer) coated AuNPs were surface modified with APS or polyelectrolyte (PAH), which makes the particle surface positively charged.

Characterization. Since in this study mainly the influence of individual AuNPs on NCs is investigated, among the most important structural parameters are the size of the AuNPs and the silica (or polymer) shell thickness.

Shown in Fig. 6.1 are the TEM images of different sized AuNPs synthesized by the Tukevich method (Fig. 6.1a) and the seed mediated method (Fig. 6.1b, c). The diameters of the AuNPs synthesized by the Tukevich method (Fig. 6.1a) are determined to be 13 ± 3 nm by measuring 100 AuNPs from the TEM images. Most of the particles appear to be spherical. Those AuNPs were used as seeds to grow bigger AuNPs that are shown in Fig. 6.1b. The resultant AuNPs have diameters of 55 ± 5 nm (100 particles, TEM). After purification, the 55 nm sized AuNPs were used for the further growth of 88 ± 6 nm (100 particles, TEM) sized AuNPs (Fig. 6.1c).

Unlike the synthesis of the small AuNPs (13 nm), the seed mediated method

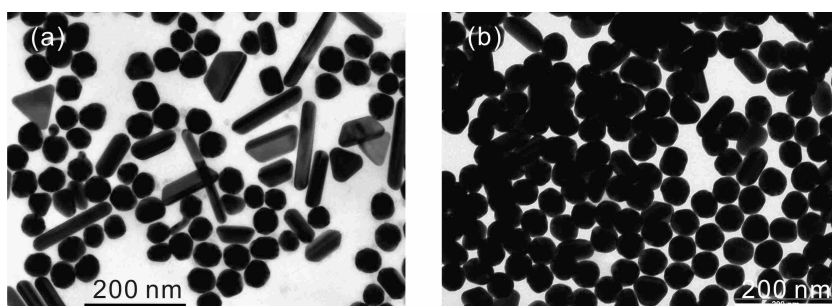


Figure 6.2: TEM images of 55 nm sized AuNPs before (a) and after (b) purification. The magnifications are the same in both images.

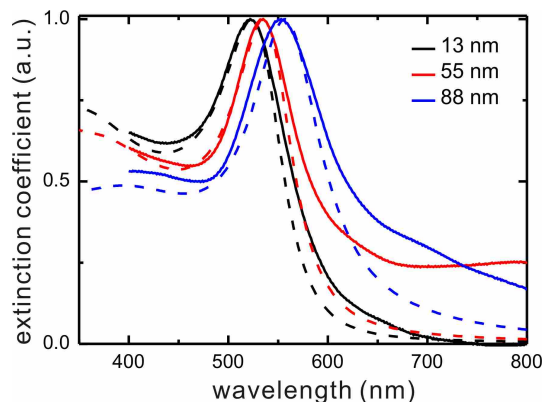


Figure 6.3: Normalized extinction spectra of 13 nm (black), 55 nm (red), and 88 nm (blue) sized AuNPs in water obtained from experimental measurements (solid curves) and Mie theory (dashed curves).

usually yields many side products, such as nanorods and platelets. To use the product for further applications, these side products have to be separated from the spherical AuNPs. This is achieved by repeated addition of an excess of hot saturated CTAB solution into a concentrated mixture containing differently shaped particles. Due to the CTAB assisted self-assembly, nanorods and platelets precipitate easily from the mixture, leaving the spherical particles in solution [Jan03]. Fig. 6.2 shows TEM images of the 55 nm sized AuNPs before (Fig. 6.2a) and after (Fig. 6.2b) the separation of side products.

Extinction spectra of the differently sized AuNPs measured by a UV/Vis spectrometer are shown in Fig. 6.3 (solid curves). A continuous red shift of the spectrum is observed with the increase of the AuNP size: for the 13 nm sized AuNPs, the extinction peak position is at 522 nm, whereas for the 55 nm and 88 nm sized AuNPs, the peak shifts to 535 nm and 555 nm, respectively. The spectra are also calculated with the complete Mie theory (dashed curves). As shown in Fig. 6.3, good correlation between the experimental and theoretical results is observed. The broadening of the experimental results can be due to the inhomogeneous size and shape distributions of the particles in the solution.

To control the distance between NCs and AuNPs, silica or polymer shells were coated on the surface of the synthesized AuNPs. In this work, mainly the 55 nm sized AuNPs were used because, in these AuNPs, the scattering effect exceeds the absorption effect. According to the radiating plasmon model (section 2.4.2), PL enhancement under certain conditions can be expected. In chapter 5, we learned that the interaction between NCs and metallic nanostructures is strongly dependent on the distance between the two. Therefore, the thickness of the shell on AuNP surface should be carefully controlled. In the following, the results from the three coating approaches will be discussed.

When coating silica shells according to the first approach, i.e., direct coating of silica on the AuNP surface, the amount of added TEOS and the reaction time are directly related to the silica shell thickness. Fig. 6.4a – d shows the influence of the amount of added TEOS on the silica shell thickness when the other experimental

6.1. Samples: preparation and characterization

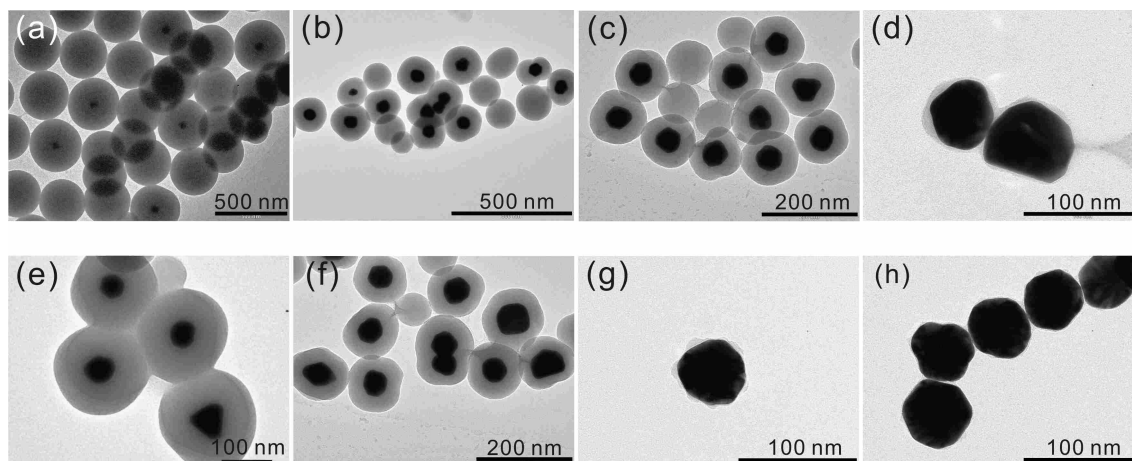


Figure 6.4: TEM images of AuNP@SiO₂ synthesized from different amounts of TEOS and reaction times when the other reaction conditions are the same. In (a – d), the reaction time is 2 h. The amount of added TEOS is (a) 10 μL , (b) 0.6 μL , (c) 0.2 μL , and (d) 0.1 μL . The corresponding silica shell thicknesses are (a) 150 nm, (b) 50 nm, (c) 30 nm, and (d) < 10 nm. In (e – h), the amount of TEOS is 1 μL , and the reaction time is (e) 2 h, (f) 1 h, (g) 30 min, and (h) 10 min. The corresponding shell thicknesses are (e) 65 nm, (f) 25 nm, (g) and (h) < 10 nm.

conditions are the same. When too much TEOS is added, lots of empty silica spheres are formed. With the decrease of the amount of TEOS, the silica shell thickness and the amount of empty silica spheres also decreases. The reaction time also plays an important role on the shell thickness, as shown in Fig. 6.4e – h. With the increase of reaction time, the silica shell becomes thicker. However, from Fig. 6.4d, g, and h, it is observed that when the silica shell is very thin (< 10 nm), the shell becomes inhomogeneous.

Fig. 6.5 shows TEM images of 55 nm sized AuNPs coated with different bilayers of polyelectrolytes following the second approach. Because of the charges on the surface introduced by the polymers, the AuNPs become separated from each other (Fig. 6.5a). Thin and homogeneous shells are formed on the AuNP surface (Fig. 6.5b – d). For the AuNPs coated with 1 bilayer of polyelectrolytes (Fig. 6.5b), the shell thickness is determined to be 2 ± 0.5 nm by measuring 50 particles in the TEM

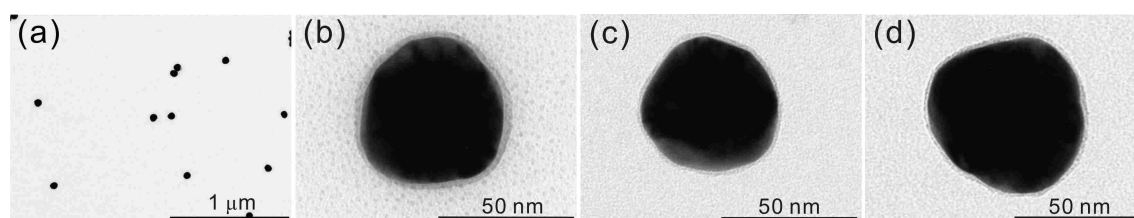


Figure 6.5: TEM images of AuNPs coated with (a – b) 1 bilayer, (c) 1.5 bilayers, and (d) 2 bilayers of polyelectrolytes.

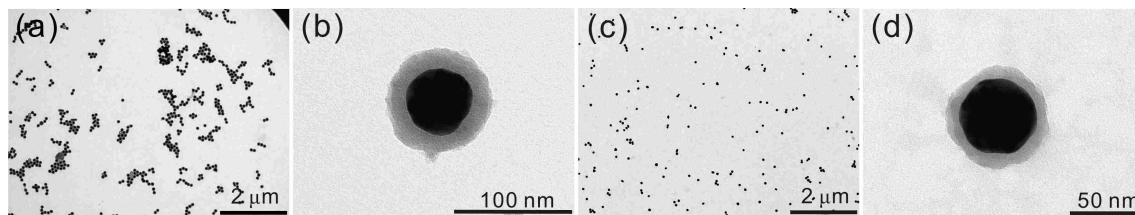


Figure 6.6: TEM images of AuNPs coated with silica shells and surface modified with (a – b) APS or (c – d) PAH.

images. Theoretically, the deposition of more bilayers should increase the shell thickness. However, from Fig. 6.5c and d we see that no apparent increase in the shell thickness is observed. This might be attributed to the fact that during the coating procedure many AuNPs were washed away as a result of the purification process. This makes it difficult to accurately determine the amount of remaining AuNPs in the solution.

The AuNPs were also coated with silica shells following the third approach. Fig. 6.6 shows the resultant AuNPs coated with silica shells and then surface modified with APS (Fig. 6.6a, b) or PAH (Fig. 6.6c, d). (The two samples shown here are provided by the group of Prof. Luis M. Liz-Marzán.) It can be observed that silica shell with thickness below 20 nm is evenly coated on the surface of the AuNPs. Compared to AuNP@SiO₂ surface modified with APS, those modified with PAH have a relatively thin shell (< 15 nm) and the particles are separated from each other because of the high surface charges.

In conclusion, among the three approaches coating AuNP surface with shell materials, the first approach can only generate thick (> 20 nm) homogeneous silica shells, while on contrast the second approach only produces extremely thin (< 5 nm) polymer shells. Only the third approach is able to provide homogeneous silica shells with reasonable thickness (< 20 nm). Therefore in the following study, mainly AuNP@SiO₂ synthesized following the third approach were used.

6.1.2 Sample preparation

Fluorophores used in this work are multishell NCs coated with negatively charged polyisoprene-poly(ethylene oxide)-COOH (PI-PEO-COOH) block copolymers as ligands (CAN GmbH, 10 μM). The multishell NCs are composed of 3.8 nm sized CdSe cores, nominally 1.2 MLs CdS shells and 1.8 MLs ZnS shells. The average diameter of the multishell NCs is 6±0.4 nm and the surface ligands have a thickness of about 2 nm. Fig. 6.7a shows a TEM image of the multishell NCs. The PL peak of the solution is at 580 nm, as shown in Fig. 6.7b, and it has a quantum efficiency of 26%. Representative PL spectra of two individual NCs are shown in Fig. 6.7c. They are fitted with single Lorentzian functions. The FWHM of the two spectra are both 14 nm. Shown as well in Fig. 6.7b is the extinction spectrum of the above mentioned PAH modified AuNP@SiO₂ solution which has a localized surface plasmon band centered at 540 nm. The average diameter of the AuNPs is 55±5 nm, and the

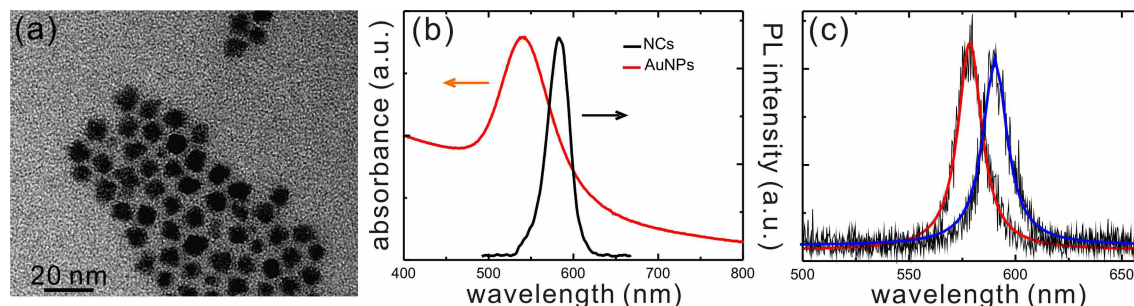


Figure 6.7: (a) TEM image of the CdSe/CdS/ZnS multishell NCs. (b) PL spectrum of the multishell NCs (black) and absorption spectrum of the PAH modified Au@SiO₂ (red). (c) PL spectra of two individual NCs (black) fitted by single Lorentzian functions (red and blue).

silica shell thickness is smaller than 15 nm.

In a typical procedure to prepare the hybrid nanostructures, 100 μL of the diluted NC solution (0.1 μM) was added dropwise to 1 mL of the AuNP@SiO₂ colloid solution. After incubation for 2 h to allow electrostatic interaction between the NCs and AuNP@SiO₂, the sample was centrifuged at low speed. Most of the excess NCs not binding onto AuNP@SiO₂ were left in the solution and discarded. The precipitates mainly including hybrid nanostructures were re-dispersed in distilled water and kept in dark for further applications. The prepared hybrid samples were usually used within one week.

In order to localize and investigate the same nanostructures with both confocal microscopy and TEM (ultimately HRTEM and EDX), the prepared samples should be deposited on substrates that fulfill several requirements. The substrates should

1. be highly transparent and mechanical stable for the electron beams in TEM and HRTEM measurements.
2. exhibit low autofluorescence at the excitation wavelength and not quench PL of the NCs. For example, preliminary experiments show that the normal carbon films strongly quench PL of the NCs. Therefore, they are not suitable for the correlation experiments here.
3. be resistant to solvents and robust enough for multiple handling.
4. be easy to trace the same position back.

Due to those reasons, the substrates used here were ultrathin (15 nm) silicon nitride (Si₃N₄) membranes containing 9 windows, each with the size of $100 \times 100 \mu\text{m}^2$ (Plano GmbH). In addition, 1D CdSe semiconductor nanowires (NWs) with PL centered at about 700 nm (Fig. 6.8a, black curve) were used as markers to locate the same NCs in the confocal microscope and in TEM. Their elongated structures as well as the fact that their PL wavelength is far away from that of NCs (580 nm) makes them ideal candidates as markers. The NWs were prepared according to the standard solution-liquid-solid method [Li09]. Fig. 6.8b and c show TEM images of the randomly distributed NWs. A scanned PL image of the CdSe NWs is plotted in Fig. 6.8d. The spectrum of the NW at the marked position together with the corresponding Gaussian fitting are shown in Fig. 6.8a (red curve).

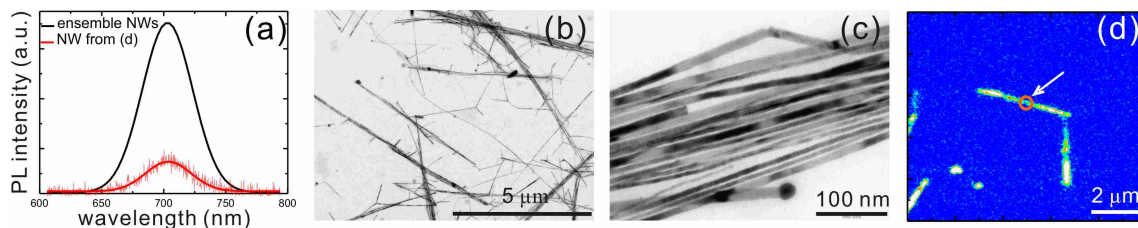


Figure 6.8: (a) PL spectra of CdSe NWs. (b – c) TEM images of randomly distributed CdSe NWs. (d) A scanned PL image of CdSe NWs. The PL spectrum (red curve) in (a) is recorded from the position marked with a red circle in (d) and fitted with a Gaussian function.

To prepare samples for the measurements, the Si_3N_4 membrane was first treated with oxygen plasma (PDC-002, Harrick Plasma, Inc.) for 40 s to remove organic contaminants and generate a hydrophilic surface. 10 μL of the above mentioned sample containing hybrid nanostructures was then slowly (300 – 400 rpm) spin-coated onto the membrane. Once the sample was dry, 10 μL diluted solution of CdSe NWs in toluene was also spin-coated onto the same membrane and used as markers.

6.2 Optical measurements of individual semiconductor nanocrystals

Optical properties of the NCs were measured under the same experimental conditions as in chapter 5. To avoid contamination of the membranes, an air objective was again used.

The sequence of the different characterization methods is very important in this correlation approach. Because of the strong electron beam in the TEM measurements, usually PL from the NCs and NWs can no longer be detected after TEM. Therefore, it is crucial to perform optical investigation prior to the TEM measurements. During this study, only the NCs that exhibited typical PL behaviors that are characteristic for a single NC (blinking, single peak PL spectra with FWHM smaller than 18 nm) were further investigated by TEM.

An example of the correlation between optical measurements and TEM imaging of a hybrid nanostructure is given in the following. A raster scanned PL image with the size of $10 \times 13 \mu\text{m}^2$ and a corresponding TEM image of the exact same position on the membrane are shown in Fig 6.9a and b, respectively. The elongated nanostructures are the luminescent CdSe NWs which were used as markers during the relocation process. The circles in both images indicate a hybrid nanostructure comprising a single CdSe NC attached to an individual AuNP that is embedded in a 7 nm thick silica shell ($\text{AuNP}@\text{SiO}_2$ -7), as shown in Fig. 6.9c.

6.2. Optical measurements of individual semiconductor nanocrystals

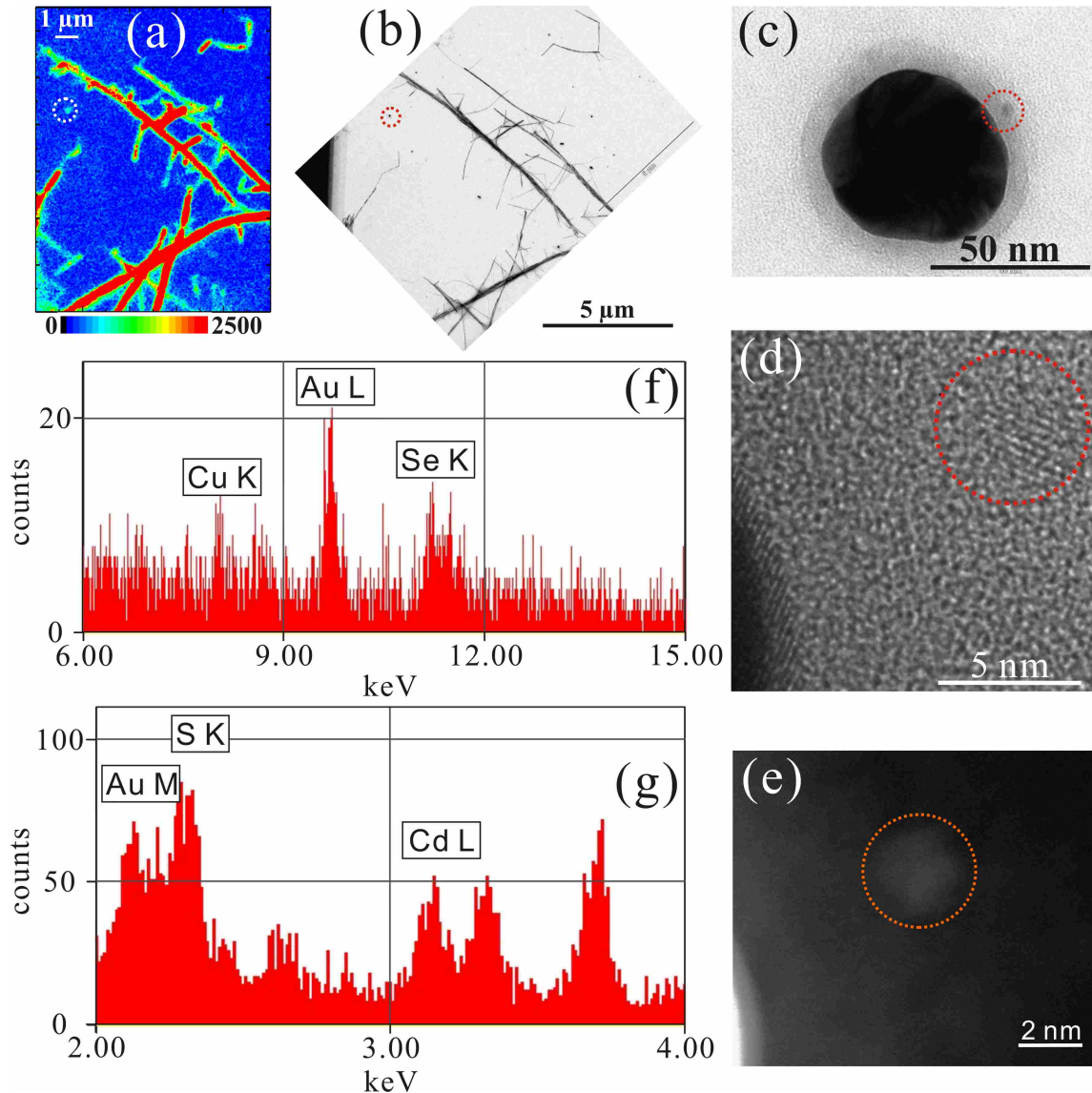


Figure 6.9: (a) A scanned PL image of the sample on a Si_3N_4 membrane. The elongated nanostructures are the CdSe NWs. (b) A TEM image of the sample at the very same position as in (a). (c) A TEM image of a single NC (marked by red circles) attached to a single AuNP embedded in a 7 nm thick silica shell. The circles in (a) and (b) indicate the position of the hybrid nanostructure shown in (c). (d, e) A HRTEM image (d) and a corresponding STEM image (e) of the NC marked in (c). (f, g) EDS spectra obtained from the NC marked in (e). Peaks corresponding to cadmium (Cd), selenium (Se), sulfur (S), and gold (Au) are marked.

To further confirm the very existence of the individual NCs on the surface of AuNP@SiO_2 , both energy dispersive X-ray spectroscopy (EDS) and HRTEM were used to characterize the samples. As shown in Fig. 6.9d, the HRTEM image shows crystal lattice fringes at the position of the NC in the hybrid nanostructure from Fig. 6.9c in contrast with the amorphous background of the silica shell, which gives clear evidence for the existence of the NC. Fig. 6.9e shows a scanning transmission

electron microscopy (STEM) image of the same NC shown in Fig. 6.9d. The corresponding EDS spectra were taken at the position of the NC and shown in Fig. 6.9f and g. Aside from the signal of the element Au from the nearby AuNP@SiO₂, X-ray emission peaks of the corresponding elements of the NC (Cd, Se, S) can also be observed. It should be noted, however, that a quantification is not possible due to the weak signals of the individual NCs.

During this study, altogether 23 NCs attached to individual AuNPs coated with silica shells of different thicknesses were investigated. As control experiments, 143 isolated NCs in the absence of AuNPs were also investigated. Individual NCs attached to AuNP dimers were rarely observed (less than 5%). Nevertheless, some of the results are also shown here because of the interesting optical properties of those NCs. In what follows, four representative NCs with and without AuNP@SiO₂ are discussed in detail.

Fig. 6.10 shows a set of representative PL time traces with time bin of 50 ms from individual NCs without AuNP@SiO₂ (Fig. 6.10a), attached to a AuNP coated with a 7 nm thick silica shell (AuNP@SiO₂-7, the hybrid nanostructure from Fig. 6.9c) (Fig. 6.10b), a AuNP coated with a 14 nm thick silica shell (AuNP@SiO₂-14) (Fig. 6.10c), and a AuNP dimer coated with a 14 nm thick silica shell (Fig. 6.10d). All the time traces were measured under the same experimental conditions for 300 s. Together shown next to the time traces are the respective histograms of photon counts per time bin (Fig. 6.10e – h). The geometries of the individual NCs attached to AuNP@SiO₂-14 and AuNP dimer are given in Fig. 6.11.

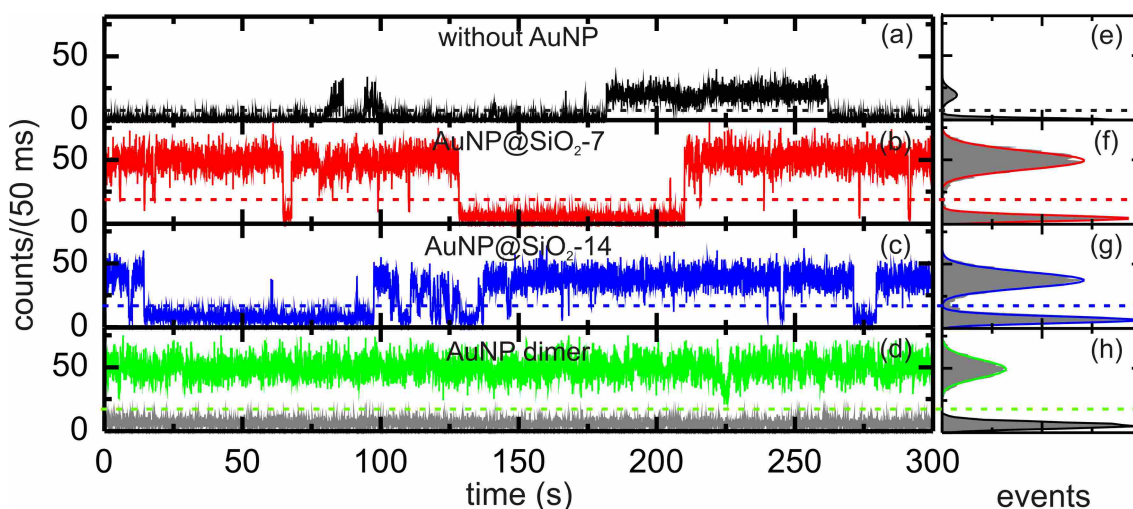


Figure 6.10: Representative time traces of PL intensity (a – d) and the corresponding histograms of photon counts per time bin (e – h) from individual NCs without a AuNP (a, e), attached to a AuNP@SiO₂-7 (b, f), to a AuNP@SiO₂-14 (c, g), and to a AuNP dimer coated with a 14 nm thick silica shell (d, h). In (d) and (h), the time trace (gray) and corresponding histogram of the background signal are also shown. The time bin is 50 ms. The curves in (e – h) are Poisson distributions fitted for the histograms. The dashed lines are the thresholds separating the on- and off-states.

6.2. Optical measurements of individual semiconductor nanocrystals

The time traces in Fig. 6.10a – c feature distinct on/off switching of the PL intensity, and the corresponding histograms can be roughly fitted by the sum of two Poisson distribution functions (the curves in Fig. 6.10e – g). From the peak values of the Poissonian approximation, we can derive the most frequent PL intensities of the on- and off-states of the NC without AuNP as 20 counts/(time bin) and 1 count/(time bin). These values are representative of the 143 isolated NCs. A histogram of the on-state PL intensity of these NCs is shown in Fig. 6.12a. For the NCs attached to AuNP@SiO₂-7 and AuNP@SiO₂-14, the peak values corresponding to the on-state increase up to 50 counts/(time bin) and 38 counts/(time bin), respectively. At the same time, the mean value of the off-state also shifts to 5 counts/(time bin), which is consistent with the intensity of the background signal measured at positions close to the NCs. This increase in background intensity can be due to impurities in the solution which were left in the vicinity of the hybrid nanostructures during the spin-coating process. Subtracting the on-state PL intensities with the corresponding background intensities, the net PL intensities of the on-state from individual NCs without AuNP@SiO₂, attached to a AuNP@SiO₂-7, and to a AuNP@SiO₂-14 are 19, 45, and 33 counts/(time bin). As a result, comparing NCs with and without AuNP@SiO₂, an enhancement factor of 2.4 and 1.7 can be derived for the NCs attached to AuNP@SiO₂-7 and AuNP@SiO₂-14, respectively. On the other hand, with the NC attached to a AuNP dimer, both the histograms from time traces of the NC and the background signal can be approximated by single Poisson functions. The peak values are derived to be 49 and 5 counts/(time bin), respectively. The results are summarized in Table 6.1.

From the time traces it is also possible to calculate the fraction of time the NCs stay at the on-/off-states. For the time traces in Fig. 6.10a – c, the threshold dividing the on- and off-states is defined as the minimum between the two peaks in the histogram. The fraction of on-time for the NC without AuNP@SiO₂ is determined to be 37%, which is close to the mean value of the 143 NCs without AuNP@SiO₂

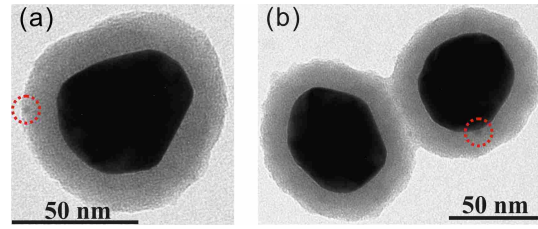


Figure 6.11: TEM images of individual NCs attached to (a) a AuNP@SiO₂-14 and (b) a AuNP dimer coated with 14 nm thick silica shell. The circles indicate the locations of the NCs.

Table 6.1: PL intensity and enhancement factor derived from time traces in Fig. 6.10 (unit for the PL intensities: counts/(time bin)).

	on-state PL intensity	off-state (background) PL intensity	net PL intensity	enhancement factor
NC	20	1	19	
NC+AuNP@SiO ₂ -7	50	5	45	2.4
NC+AuNP@SiO ₂ -14	38	5	33	1.7
NC+AuNP dimer	49	5	44	2.3

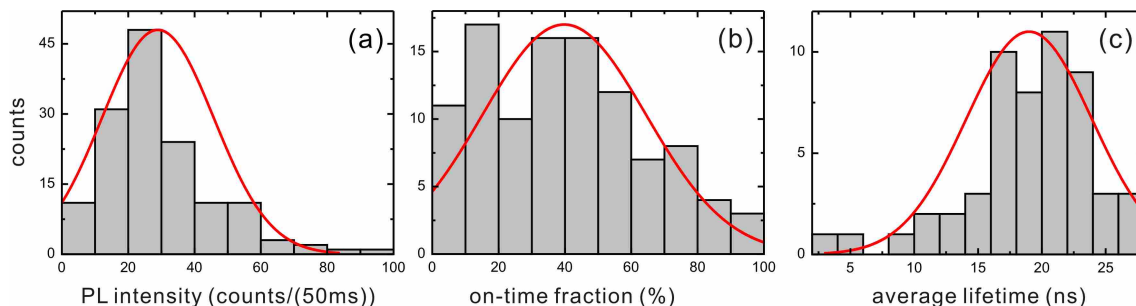


Figure 6.12: Histograms of (a) on-state PL intensity, (b) on-time fraction, and (c) average lifetime of isolated individual NCs.

(Fig. 6.12b). For the NCs attached to AuNP@SiO₂-7 and AuNP@SiO₂-14, the values increase to 71% and 63%, indicating dramatically suppressed off-states. Since there is no apparent off-state observed for the NC attached to AuNP dimer, the threshold is defined as twice the mean background signal. No off-time is observed in the time trace during the observation time and the NC remains in the on-state.

The above mentioned PL behavior is closely related to the recombination dynamics of the individual NCs during the emission process. Decay curves of the NCs were recorded by the TCSPC method. Fig. 6.13a shows the background-subtracted PL decay curves of the same NCs investigated in Fig. 6.10. The IRF with a FWHM of 128 ps is also shown. The decay curves are reconvoluted by the IRF signal and fitted with stretched exponential functions (eq. (2.39)). The fitting results are listed in Table 6.2. Average lifetimes are also computed according to eq. (2.40) from the fitting results. For the NC without AuNP@SiO₂, the values derived for $\tau_{1/e}$ and β_s are 20.7 ns and 0.97, respectively, which gives an average lifetime $\langle\tau\rangle$ of 21.0 ns. This value is representative of the many isolated NCs investigated, as shown in Fig. 6.12c. The average lifetimes of the NCs attached to AuNP@SiO₂-7, AuNP@SiO₂-14, and AuNP dimer are computed to be 5.4 ns, 15.9 ns, and 1.3 ns, respectively. These values are much shorter than those for NCs without AuNPs. From the fitting results, the corresponding rate distributions are also calculated and plotted in Fig. 6.13b. It can be observed that the recombination rates of the NCs with AuNPs in the vicinity, especially the ones attached to AuNP@SiO₂-7 and AuNP dimer, are higher than that of the isolated one.

In principle, these results from the optical measurements of individual NCs attached to AuNP@SiO₂ can be summarized as the following:

1. Enhanced PL intensity. For the NCs attached to AuNP@SiO₂-7 and AuNP

Table 6.2: Results calculated from the stretched exponential fittings of the decay curves.

	β_s	$\tau_{1/e}$ (ns)	$\langle\tau\rangle$ (ns)
NC	0.97	20.7	21.0
NC+AuNP@SiO ₂ -7	0.71	4.3	5.4
NC+AuNP@SiO ₂ -14	0.90	15.2	15.9
NC+AuNP dimer	0.67	1.0	1.3

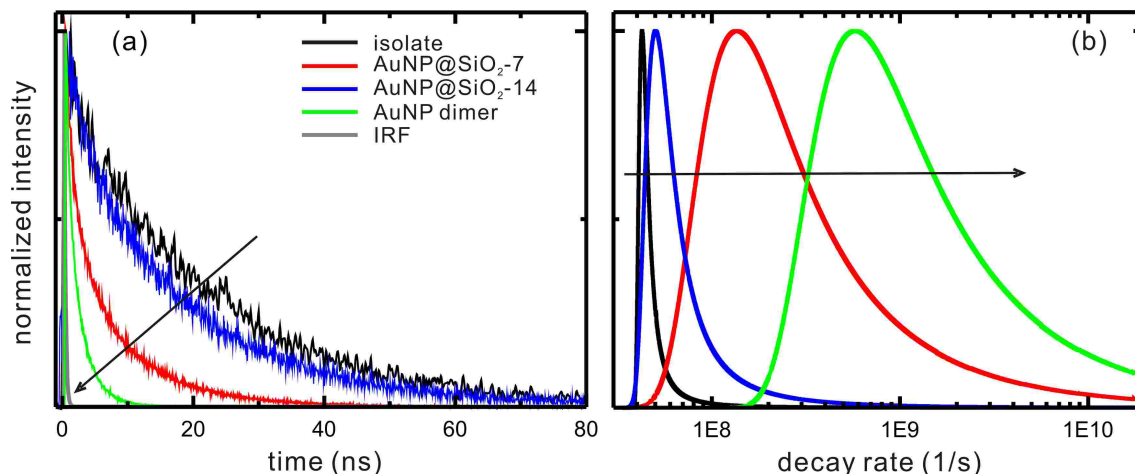


Figure 6.13: (a) Background-subtracted PL decay curves of the individual NCs without AuNP (black), attached to a AuNP@SiO₂-7 (red), attached to a AuNP@SiO₂-14 (blue), and attached to a AuNP dimer (green) together with the IRF (gray). (b) The corresponding decay rate distributions calculated from the fitting results of the stretched exponential functions.

- @SiO₂-14, enhancement factors of 2.4 and 1.7 are observed when compared to isolated NCs.
- 2. Decreased lifetime/enhanced recombination rate. For the NCs attached to AuNP dimers, the average lifetime is decreased by about one order of magnitude as compared to the isolated NC.
- 3. Suppressed blinking.

In the next section, those optical findings will be discussed and explained in combination with the corresponding geometries of the hybrid nanostructures.

6.3 Correlation between optical and structural properties

Following the procedure explained in section 5.3, here the excitation and emission processes are also treated separately.

Excitation process. The excitation rate is proportional to the local electric field intensity at the position of the NCs. To estimate the change of excitation rate under the influence of nearby AuNPs, precise simulations with 3D FDTD were performed to calculate the local electric field enhancement factor γ_{exc} , which is defined as the ratio of the electric field intensity at the excitation wavelength 470 nm around the AuNPs to the incident field intensity in the absence of the AuNPs. The step size was set to be 1 nm, and a 470 nm plane wave incident from the top (along z-axis) with the polarization parallel to the x-axis was employed as the light source.

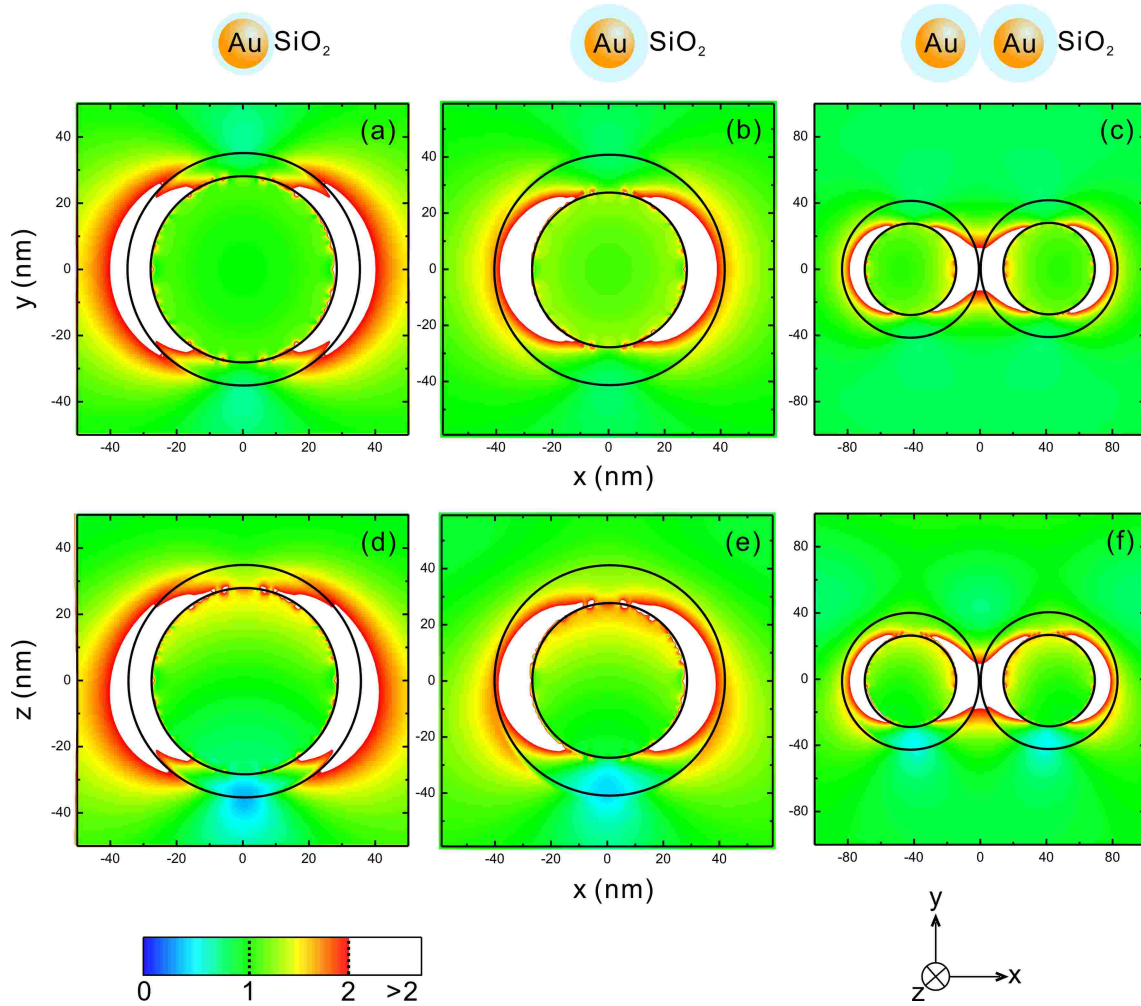


Figure 6.14: Local electric field enhancement factor distributions near (a, d) a AuNP@SiO₂-7, (b, e) a AuNP@SiO₂-14, and (c, f) a AuNP dimer coated with a 14 nm silica shell simulated by 3D FDTD method. The nanoparticles are illuminated by a 470 nm plane wave incident from above along the z-axis with the polarization parallel to the x-axis. The circles indicate that relative positions of the AuNPs and silica shells.

The simulation results for the local electric field enhancement factor near a AuNP@SiO₂-7, a AuNP@SiO₂-14, and a AuNP dimer with 14 nm silica shell are shown in Fig. 6.14. Apparently, the value of γ_{exc} is strongly dependent on the position of NCs relative to the AuNP and incident light. Both enhancement ($\gamma_{exc} > 1$) and reduction ($\gamma_{exc} < 1$) of the local electric field intensity can be observed. Due to the high dielectric constant of silica, the electric field is mostly confined within the silica shells coating the AuNPs. Comparing AuNP@SiO₂-7 and AuNP@SiO₂-14, the γ_{exc} value on the surface of AuNP@SiO₂-7 along x-axis (> 2) is much stronger than on the surface of AuNP@SiO₂-14 (about 1.5). As with the AuNP dimer, the coupling effect leads to hot spots between the AuNPs.

However, TEM images can only provide topography of the hybrid nanostructures projected on the image plane. Due to the insufficient information of the exact location of the NCs with respect to AuNPs and incident light, it is difficult to

6.3. Correlation between optical and structural properties

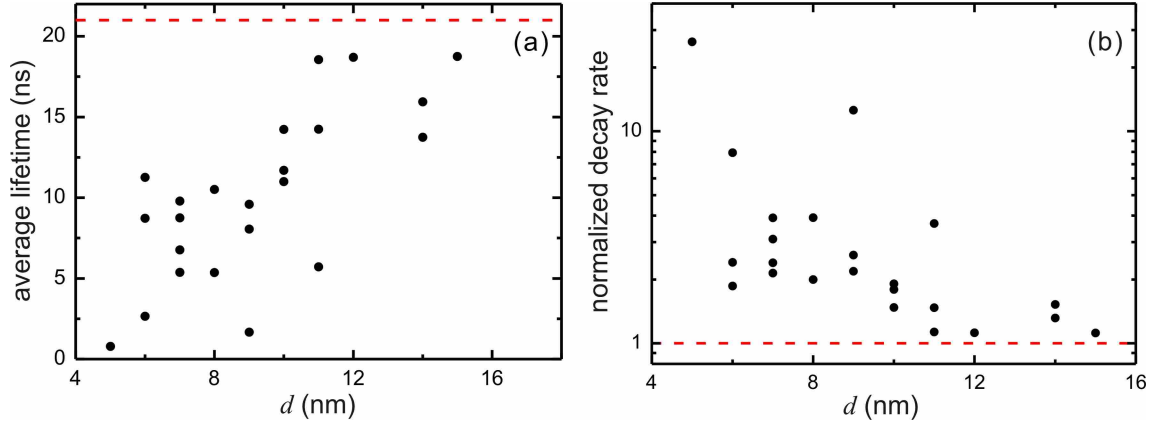


Figure 6.15: (a) Dependence of average lifetime on silica shell thickness d . The average lifetimes are calculated from the stretched exponential fitting results. The dashed line indicates the average lifetime of isolated NCs (from Table 6.2). (b) Normalized decay rate (k/k_0) as a function of silica shell thickness d . The dashed curve corresponds to the value from isolated NCs, i.e., $k/k_0 = 1$.

determine γ_{exc} values corresponding to the NCs. In addition, the excitation process is only part of the reason for the change in the optical properties of the NCs. The recombination rates in the emission process also affect the PL intensity.

Emission process. Average lifetimes of the 23 individual NCs attached to AuNP@SiO₂ are computed from the stretched exponential fitting results of the decay curves. Since decay rate is inversely proportional to lifetime, the decay rate of NCs attached to AuNP@SiO₂ (k) can be normalized to the decay rate of the isolated NCs (k_0) by

$$\frac{k}{k_0} = \frac{\tau_0}{\tau}, \quad (6.1)$$

where τ and τ_0 are the lifetimes of the NCs with and without nearby AuNPs. In this calculation, we take the representative τ_0 from Table 6.2, which means that $\tau_0 = 21.0$ ns. By imaging the hybrid nanostructures in TEM after the optical measurements, thicknesses of the silica shells (d) are determined and plotted against the corresponding average lifetimes (τ) (Fig. 6.15a) and normalized decay rates (k/k_0) (Fig. 6.15b). From the plots it can be seen that lifetimes of the NCs attached to AuNP@SiO₂ (Fig. 6.15a, black dots) are shorter than that of isolated NCs (Fig. 6.15a, dashed line). With the decrease of d , influence from the nearby AuNPs becomes larger. Hence, the lifetimes of the NCs decrease and correspondingly the decay rates increase.

Sometimes, different lifetimes for one specific d are observed. This, to some extent, can be attributed to the different intrinsic recombination rates¹ of the NCs. Another likely reason is the various orientations of the transition dipoles of the NCs with respect to the AuNPs.

¹Recombination rates of NCs without the influence from AuNPs.

As discussed in section 2.2.4, in the case that CdSe NCs are assumed to be spherical and have a ZB lattice structure, the lowest excited state of the NC should be eightfold degenerate [Nor04]. However, in reality, this state is split into five levels by the crystal shape asymmetry, the intrinsic crystal field, and the electron - hole exchange interaction. Of the five states, two are optically forbidden (dark excitons), whereas the other three are optically active (bright excitons). [Efr96] Since two of the three optically active states are degenerate (both with an angular momentum projection along the c axis of the crystal structure), two potential transition dipole orientations exist in CdSe NCs: a linear dipole oriented along the c -axis of the NC; a 2D degenerate dipole located in a plane perpendicular to the c -axis. [Emp99] Experiments at both low temperature [Emp99] and room temperature [Chu03, Kob03] have found that transition dipoles of NCs are 2D degenerate, with the formed bright plane being perpendicular to the c -axis of the NCs¹. Therefore, in CdSe NCs, although the PL emission of single NCs originates from linear transition dipoles, the spatial distribution of the emission is 2D, different from that of a linear dipole emitter with a fixed dipole axis.

In order to evaluate the orientational dependence of the PL lifetime, two extreme situations are considered: the bright plane being perpendicular to the AuNP surface (\perp), and the bright plane being parallel to the AuNP surface (\parallel). Results from any other orientations will be in between the two extreme situations. Take the situation that the bright plane is perpendicular to the AuNP surface as an example (Fig. 6.16). For any linear dipole on the bright plane, the radiative ($k_{r,\theta}$) and nonradiative ($k_{nr,\theta}$) decay rates can be expressed as a function of the orientation angle θ (the angle between the linear dipole and the perpendicular direction) by [Ger81b, Vos09]

$$k_{r,\theta} = k_{r,\parallel} \sin^2 \theta + k_{r,\perp} \cos^2 \theta, \quad (6.2)$$

$$k_{nr,\theta} = k_{nr,\parallel} \sin^2 \theta + k_{nr,\perp} \cos^2 \theta. \quad (6.3)$$

Here, $k_{r,\parallel}$, $k_{nr,\parallel}$ and $k_{r,\perp}$, $k_{nr,\perp}$ are the radiative and nonradiative decay rates of linear dipoles oriented parallel and perpendicular to the AuNP surface, respectively. Therefore, the orientation averaged rate of a 2D transition dipole with the bright

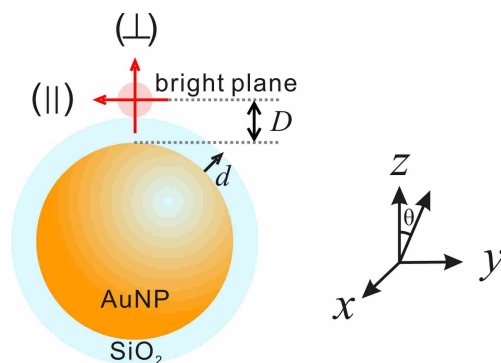


Figure 6.16: Schematic representation of a 2D transition dipole oriented perpendicular to the AuNP surface.

¹Although some groups [Sch05, Pat05] have also argued that the transition dipole in a CdSe NC is a complex 2D plus 1D transition moment, here only a 2D transition dipole is considered.

6.3. Correlation between optical and structural properties

plane lying perpendicular to the AuNP surface is

$$\langle k_r \rangle_{\perp} = \frac{2}{\pi} \int_0^{\pi/2} (k_{r,\parallel} \sin^2 \theta + k_{r,\perp} \cos^2 \theta) d\theta = \frac{k_{r,\parallel} + k_{r,\perp}}{2}, \quad (6.4)$$

$$\langle k_{nr} \rangle_{\perp} = \frac{2}{\pi} \int_0^{\pi/2} (k_{nr,\parallel} \sin^2 \theta + k_{nr,\perp} \cos^2 \theta) d\theta = \frac{k_{nr,\parallel} + k_{nr,\perp}}{2}, \quad (6.5)$$

$$\langle k \rangle_{\perp} = \langle k_r \rangle_{\perp} + \langle k_{nr} \rangle_{\perp} = \frac{k_{\parallel} + k_{\perp}}{2}, \quad (6.6)$$

with $k_{\parallel} = k_{r,\parallel} + k_{nr,\parallel}$, and $k_{\perp} = k_{r,\perp} + k_{nr,\perp}$. Similarly, the orientation averaged rate of a 2D transition dipole with the bright plane oriented parallel to the AuNP surface is

$$\langle k \rangle_{\parallel} = \frac{k_{\parallel} + k_{\parallel}}{2} = k_{\parallel}. \quad (6.7)$$

To estimate the dependence of $\langle k \rangle_{\perp}$ and $\langle k \rangle_{\parallel}$ on the distance between the NCs and AuNPs, two different approaches were employed to simulate the system. From each approach, k_{\parallel} and k_{\perp} can be calculated as a function of the distance. The first approach was the Gersten-Nitzan model introduced in section 2.4.2. In this method, the diameter of the AuNPs was taken as 55 nm. It should be noted that the distance D between the transition dipole and the AuNP surface is the sum of the silica shell thickness d and the radius of the NCs r , which was estimated from TEM to be 5 nm (thickness of surface ligands included), i.e., $D = d + 5$. The quantum efficiency of the individual NCs was taken as 1. Taking $\tau_0 = 21.0$ ns, it can be calculated that the radiative ($k_{r,0}$) and nonradiative ($k_{nr,0}$) decay rates of NCs in the absence of AuNPs were $k_{r,0} = 4.762 \times 10^7 \text{ s}^{-1}$ and $k_{nr,0} = 0 \text{ s}^{-1}$, respectively. Using these parameters, d dependent PL lifetimes of 2D transition dipoles with the bright plane oriented parallel and perpendicular to the AuNP surface were calculated.

The other approach used the 3D FDTD method, which is also introduced in section 2.4.2. In the simulation, a linear electric dipole with wavelength of 580 nm was placed at different orientations (parallel or perpendicular) and distances from the AuNP surface. The mesh size of the simulation was 0.5 nm. Span size of the power monitors used to calculate P_{tot} was set to be 4 nm, because the light source requires a certain amount of space to inject the fields (at least 2 mesh cells) and within this region the fields are not physically meaningful.

Fig. 6.17 shows the calculation results from the two approaches for 2D transition dipoles placed close to bare AuNPs (without silica shells). The surrounding medium was taken either as air (Fig. 6.17a) or silica (Fig. 6.17b). When the surrounding medium is air, good agreement between the two methods is observed. However, for 2D transition dipoles in silica oriented parallel to the AuNP surface, lifetimes calculated from the Gersten-Nitzan model are much shorter than those from the FDTD method. This is probably due to the fact that the Gersten-Nitzan model can sometimes overestimate the nonradiative decay rates [Dul02]. Comparing Fig. 6.17a and b it can be seen that increase of the medium dielectric constant leads to larger decay rates.

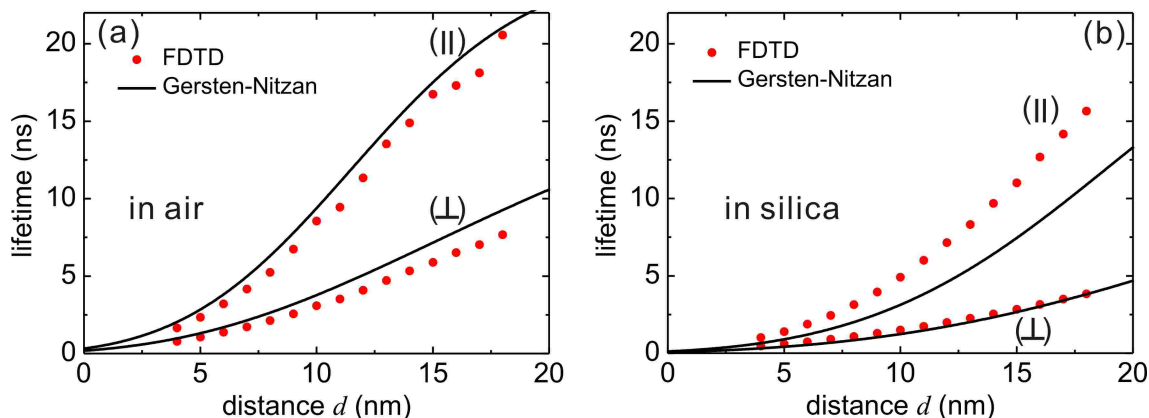


Figure 6.17: Lifetime dependence on the distance between NCs and AuNPs ($d = D - 5$) in air (a) and silica (b). The lifetimes were calculated from the Gersten-Nitzan model (curves) and the 3D FDTD method (dots). For each set of data from the simulations, the upper and lower curves correspond to dipoles with the bright plane oriented parallel (||) and perpendicular (\perp) to the AuNP surfaces, respectively.

From Fig. 6.17 it can also be observed that with the increase of the silica shell thickness, the calculated lifetimes get closer to the lifetime of the isolated NCs (21.0 ns). Orientation of the dipole has big influence on the lifetime. When the dipole is oriented perpendicular to the AuNP surface, interaction between the dipole and the excited plasmon from the AuNP is stronger than in the case where the dipole has a parallel orientation. Consequently, decay rates of dipoles oriented perpendicular to the AuNP surface are larger than those of the parallel ones. This effect is well illustrated by the local electric field intensity enhancement factor distribution near the AuNPs when a linear dipole is placed close to the AuNP surface (Fig. 6.18). The local electric field intensity enhancement factor is defined as the ratio between the electric field intensity in the presence and absence of AuNPs, calculated from the 3D FDTD method. Much stronger electric field intensity enhancement is observed when the linear dipole is oriented perpendicular (Fig. 6.18c, d) to the AuNP surface.

To include the influence of the silica shells around the AuNPs, PL lifetimes of the hybrid nanostructures comprising NCs (2D transition dipoles) and AuNPs@SiO₂ in the air are calculated with the 3D FDTD method, and the calculation results are compared with the experimental data, as shown in Fig. 6.19. Simulated lifetimes for both orientations (|| and \perp) from the 3D FDTD method are much smaller than the experimental results. The possible reason for this could be that the treatment of the CdSe NCs as perfect dipoles may be too crude. As discussed in section 2.4.2, one prerequisite of this method for the calculation of lifetime is that the intrinsic quantum efficiency of the simulated fluorophore should be unity ($QE = 1$). Although some studies have argued that the intrinsic quantum efficiency of the on-state of NCs should be close to unity [Bro04, Yao05], in reality it is very unlikely that the nonradiative process can be completely excluded. Other reasons could be that the calculations were performed for single frequencies (580 nm for the PL of the NCs) instead of considering the spectral overlap [Dul02].

6.3. Correlation between optical and structural properties

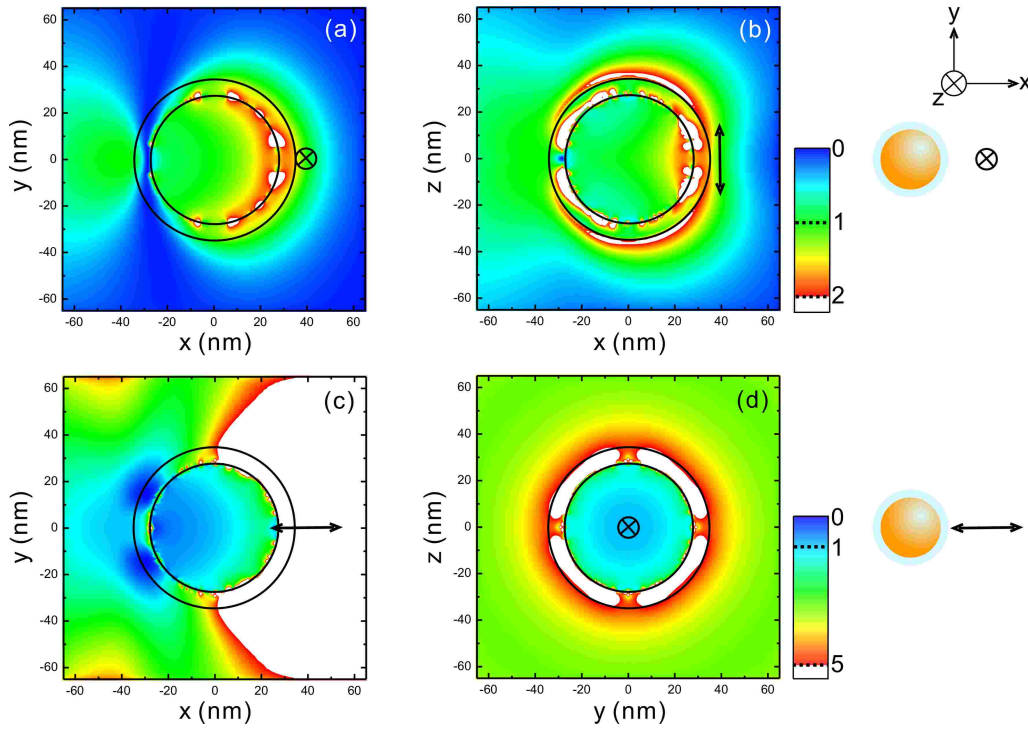


Figure 6.18: Local electric field intensity enhancement factor distribution near a linear electric dipole oriented parallel to (a, b) z-axis and (c, d) x-axis next to a AuNP@SiO₂-7 simulated by 3D FDTD method. The schemes on the right side represent the relative orientations of the dipole and AuNP@SiO₂. The AuNP@SiO₂-7 is centered at (0, 0, 0). The circles and arrows in (a – d) indicate the positions and orientations of the AuNP@SiO₂-7 and dipole.

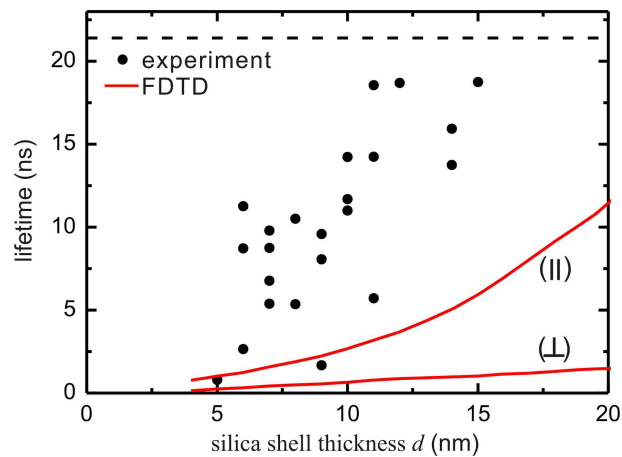


Figure 6.19: PL Lifetime dependence on the silica shell thickness d . The lifetimes are calculated from the experimental results (dots) and the 3D FDTD method (curves). For the data from the FDTD simulations, the upper and lower curves correspond to dipoles with the bright plane oriented parallel (\parallel) and perpendicular (\perp) to the AuNP surface, respectively. The dashed line indicates the experimental lifetime of NCs without nearby AuNP@SiO₂.

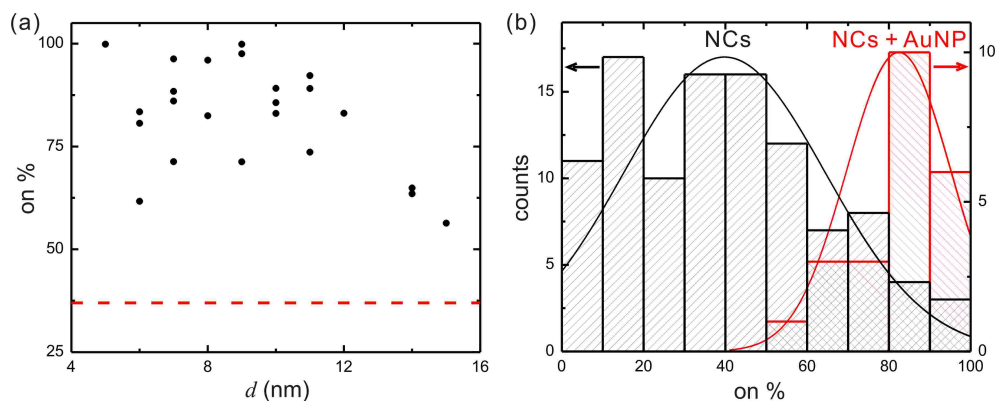


Figure 6.20: (a) Experimental results of the time percentage of NCs stay at the on-state (on%) over 300 s as a function of silica shell thickness. The dashed line indicated the average on% value of isolated NCs. (b) Histograms of on% of isolated NCs (black) and NCs attached to AuNP@SiO₂ (red). The curves are Gaussian fitting of the histograms.

One change in the PL behavior of the NCs directly related to the increased recombination rate is that the NCs attached to AuNP@SiO₂ stay more often in the on-state than those without nearby AuNPs, as shown in Fig. 6.20. This finding is consistent with the results from the previous chapter. In general, when an exciton is formed in a NC, the electron and hole can recombine radiatively or nonradiatively. In addition, however, the charge carriers can also be captured by trapping states. Such a NC can still absorb photons, but the subsequently excited electrons and holes mainly recombine through the ultrafast, nonradiative Auger recombination process, which leads to the off-state of the NCs. Only when the trapped charges are neutralized does the NC return to the on-state. However, when the NCs are attached to AuNP@SiO₂, especially to those coated with thin silica shells, the increased recombination rates efficiently inhibit the possibility of the charge carriers being trapped. Hence, the NCs remain in the on-state more often.

However, due to the insufficient knowledge of the detailed orientation of the transition dipoles in NCs, it is difficult to estimate the contributions from the radiative and nonradiative recombination processes. Since the overall PL intensity is determined by both the excitation and emission processes, even though the previous simulation with FDTD shows that the excitation rate might be increased due to enhanced local electric field intensity near the NCs caused by the excited plasmons in AuNPs, still one cannot argue about the exact enhancement factor of the PL intensity.

In conclusion, in this work, hybrid nanostructures composed of individual CdSe multishell NCs and silica coated AuNPs were prepared. By using both confocal microscopy and TEM, unambiguous correlation between the optical properties and the corresponding structures of the very same hybrid nanostructures was performed. As compared to isolated NCs, those attached to AuNP@SiO₂ exhibited enhanced on-state PL intensity. Meanwhile, the recombination rates of the NCs increased with the decrease of the silica shell thickness, which can be used to explain the suppressed off-states observed for NCs attached to AuNP@SiO₂. The PL lifetimes

6.3. Correlation between optical and structural properties

of the NCs as a function of the distance between the NCs and AuNPs were simulated with the Gersten-Nitzan model and the 3D FDTD method, and the results were compared with the experimental data. This experimental approach may be useful for selective designs of hybrid complexes as well as for comparison with recent theoretical calculations.



This page is intentionally left blank.

Chapter 7

Summary and outlook

The chemical synthesis of high-quality colloidal NCs, especially CdSe and CdTe NCs, has now become a routine procedure. This offers direct analysis of the NCs at individual NC level, which leads to the discovery of numerous effects that are inaccessible in ensemble detection. Unfortunately, the potential of individual NC measurements is often restricted by two factors: PL blinking and PL bleaching. Therefore, learning about and inhibiting these behaviors of NCs are crucial.

In this study, two different methods have been used to manipulate the PL from NCs. In the first method, stable semiconductor materials have been overcoated onto the NCs to passivate their surfaces, forming the so-called core-shell NCs. Depending on the relative band offsets of the core-shell materials, either type I or type II core-shell NCs have been produced. Type I core-shell NCs have improved photostability, although the recombination dynamics is similar to the core NCs. The photostability and recombination dynamics in type II core-shell NCs are more complicated. In general, charge carriers in type II core-shell NCs are spatially separated, leading to the red shift of the PL spectrum and longer lifetime. The overall quantum efficiency is determined by the balance between surface passivation and reduction in the overlap of electron-hole wavefunctions.

In the second approach, surface plasmons excited in metallic nanostructures have been used to manipulate the PL from NCs. Mainly two systems were investigated: silica coated CdSe multishell NCs spin-coated on self-assembled AuNP films, and CdSe multishell NCs attached to silica coated individual AuNPs via electrostatic interaction. For the NCs coupled to the self-assembled AuNP films, an increase in the on-state PL intensity and a decrease in the PL lifetime were observed. In addition, these NCs showed PL from gray states and a strong blinking suppression. These optical behaviors can be explained by the variations of excitation and recombination rates of NCs induced by surface plasmons. As to the NCs attached to individual AuNPs, aside from enhanced on-state PL intensity and suppressed blinking of the NCs, the decrease of lifetime was found to be dependent on the distance between the NCs and AuNPs. A simple model has been proposed to explain these phenomena.

In future work, the exact blinking mechanism of NCs needs further investigation, possibly with the assist of ultra-fast measurements of individual NC lifetimes. By systematically altering the interaction between NCs and metallic nanostructures and consequently the radiative lifetimes of the NCs, the charge carrier trapping dynamics closely related to the blinking behavior of the NCs might be revealed.



This page is intentionally left blank.

Appendix

A. Matlab[®] scripts for the CPS model

```
clc
clear
close all
global e1 e2 n1 lambda q d
e1=1; % medium
e2=(0.21+3.272*j)^2; % metal
n1=1;
lambda=600; % unit nm
q=0.31; % quantum efficiency
d_array=0.01:0.01:40; % unit nm

for ii=1:length(d_array)
    d=d_array(ii);
    kr_perp(ii)=q-3/2*q*imag(quadgk(@kr_perp_integrand, 0, 1));
    knr_perp(ii)=(1-q)-3/2*q*imag(quadgk(@kr_perp_integrand, 1, inf));
    kr_para(ii)=q+3/4*q*imag(quadgk(@kr_para_integrand, 0, 1));
    knr_para(ii)=(1-q)+3/4*q*imag(quadgk(@kr_para_integrand, 1, inf));
end

d_array=d_array';
kr_perp=kr_perp';
knr_perp=knr_perp';
kr_para=kr_para';
knr_para=knr_para';
save d_array.txt d_array -ASCII
save kr_perp.txt kr_perp -ASCII
save knr_perp.txt knr_perp -ASCII
save kr_para.txt kr_para -ASCII
save knr_para.txt knr_para -ASCII

function result=kr_perp_integrand(u)
global e1 e2 n1 lambda q d
k1=2.*pi.*n1./lambda;
d_hat=k1.*d;
L1=-j.*(1-u.^2).^.(1./2);
L2=-j.*(e2./e1-u.^2).^.(1./2);
R_para=(e1.*L2-e2.*L1)./(e1.*L2+e2.*L1);
result=R_para.*exp(-2.*L1.*d_hat).*u.^3./L1;

function result=kr_para_integrand(u)
global e1 e2 n1 lambda q d
k1=2.*pi.*n1./lambda;
d_hat=k1.*d;
L1=-j.*(1-u.^2).^.(1./2);
L2=-j.*(e2./e1-u.^2).^.(1./2);
R_para=(e1.*L2-e2.*L1)./(e1.*L2+e2.*L1);
R_perp=(L1-L2)./(L1+L2);
result=u./L1.*exp(-2.*L1.*d_hat).*(R_perp+(1-u.^2).*R_para);
```

B. Mathematica™ scripts for the Gersten-Nitzan model

```

c = 3.0 * 10^8;
hbar = 1.054571 * 10^(-34);
h = 6.626069 * 10^(-34);
wavelength = 600 * 10^(-9);
angularFreq = 2 * Pi * c / wavelength;
energyJ = h * c / wavelength;
energyeV = 4.135667 * 10^(-15) * c / wavelength;
emedia = 1; (dielectric constant of medium)
emetal = 5222.89361 - 21709.67407 * energyeV + 38087.00036 * energyeV^2 -
37588.35430 * energyeV^3 + 23121.14990 * energyeV^4 - 9216.91166 * energyeV^5 +
2385.83431 * energyeV^6 - 387.42356 * energyeV^7 + 35.87699 * energyeV^8 -
1.44609 * energyeV^9 + I * (-558.27355 + 2888.04152 * energyeV -
6122.57020 * energyeV^2 + 7155.78252 * energyeV^3 - 5131.09093 * energyeV^4 +
2352.05993 * energyeV^5 - 691.32786 * energyeV^6 + 125.98511 * energyeV^7 -
12.95343 * energyeV^8 + 0.57414 * energyeV^9); (dielectric constant of metal)
qy = 1; (quantum yield)
lifetime = 21.7 * 10^(-9); (lifetime)
kr0 = qy / lifetime; (radiative decay rate)
knr0 = 1 / lifetime - kr0; (nonradiative decay rate)
u0 = Sqrt[3 * c^3 * hbar * kr0 / angularFreq^3];
a = 1.5 * c^3 * kr0 / (angularFreq^4);
r = 8.5 * 10^(-9); (radius of metal particle)

deltaPer[d_] = (a / (r + d)^3) * Sum[((emetal - emedia) * (n + 1)^2 * (r / (r + d))^(2 * n + 1)) /
(emetal + emedia * (n + 1) / n), {n, 100}];
krPer[d_] = angularFreq^3 * (Abs[u0])^2 *
(Abs[1 + 2 * (r / (r + d))^3 * ((emetal - emedia) / (emetal + 2 * emedia))])^2 /
(3 * hbar * c^3 * (Abs[1 - deltaPer[d]])^2);
kETPer[d_] = -((Abs[u0])^2 / (2 * hbar * r^3 * (Abs[1 - deltaPer[d]])^2)) *
Sum[(2 * n + 1) * ((n + 1)^2 / n) * (Im[emedia / (emetal + emedia * (n + 1) / n)]) *
(r / (r + d))^(2 * n + 4)], {n, 100}];

deltaPar[d_] = (a / (2 * r^3)) * Sum[n * (n + 1) * (emetal - emedia) *
(r / (r + d))^(2 * n + 4) / (emetal + emedia * (n + 1) / n), {n, 100}];
krPar[d_] = angularFreq^3 * (Abs[u0])^2 *
(Abs[1 - (emetal - emedia) * (r / (r + d))^3 / (emetal + 2 * emedia)])^2 /
(3 * hbar * c^3 * (Abs[1 - deltaPar[d]])^2);
kETPar[d_] = -((Abs[u0])^2 / (4 * hbar * r^3 * (Abs[1 - deltaPar[d]])^2)) * Sum[(n + 1) *
(2 * n + 1) * (r / (r + d))^(2 * n + 4) * Im[emedia / (emetal + emedia * (n + 1) / n)], {n, 100}];

startd = 10^(-10);
endd = 40 * 10^(-9);
di = N[(-startd + endd) / 1000];
SetDirectory["D:\"];

Export["rad - ET - rate - forPerp.dat ",
Transpose[{Table[d*10^9, {d, startd, endd, di}],
Table[Evaluate[krPer[d]], {d, startd, endd, di}],
Table[Evaluate[kETPer[d]], {d, startd, endd, di}]}], "table "
rad-ET-rate-forPerp.dat
Export["rad - ET - rate - forParallel.dat ",
Transpose[{Table[d*10^9, {d, startd, endd, di}],
Table[Evaluate[krPar[d]], {d, startd, endd, di}],
Table[Evaluate[kETPar[d]], {d, startd, endd, di}]}], "table "
rad-ET-rate-forParallel.dat

```

C. FDTD scripts for computing P_{rad} and P_{tot}

```
# Script for the calculation of decay rates in 3D.
f=getdata("monitor2","freqDFT"); # get frequency data
lam=c/f*1e9; # convert to wavelength in nm.
# Calculate power flowing outwards in each direction of the dipole.
Pdipole_top = transmission("dipole-top");
Pdipole_bottom = -transmission("dipole-bottom");
Pdipole_left = -transmission("dipole-left");
Pdipole_right = transmission("dipole-right");
Pdipole_back = transmission("dipole-back");
Pdipole_front = -transmission("dipole-front");
# Calculate total power flowing out of the dipole.
Pdipole = Pdipole_top + Pdipole_bottom + Pdipole_left + Pdipole_right + Pdipole_back + Pdipole_front;
# Calculate radiative power flowing out in each direction in total field.
Pradiative_top = transmission("top");
Pradiative_bottom = -transmission("bottom");
Pradiative_left = -transmission("left");
Pradiative_right = transmission("right");
Pradiative_back = transmission("back");
Pradiative_front = -transmission("front");
# Calculate total radiative power flowing outwards.
Pradiative = Pradiative_top + Pradiative_bottom + Pradiative_left + Pradiative_right + Pradiative_back + Pradiative_front;
# Calculate non_radiative power.
Pnon_radiative = (Pdipole - Pradiative);
# Plot results.
plot(lam, Pradiative, Pnon_radiative, Pradiative + Pnon_radiative, Pdipole, "Wavelength (nm)", "Normalized total radiated power");
legend("Radiative", "Non-radiative", "radiative+nonradiative", "dipole");
#write the data to text files.
write("Normalized radiative power.txt","wavelength(nm), Normalized radiated power");
write("Normalized radiative power.txt",num2str(lam) + "," + num2str(Pradiative));
write("Normalized non-radiative power.txt","wavelength(nm), Normalized non-radiated power");
write("Normalized non-radiative power.txt",num2str(lam) + "," + num2str(Pnon_radiative));
write("Normalized total power.txt","wavelength(nm), Normalized total power");
write("Normalized total power.txt",num2str(lam) + "," + num2str(Pradiative + Pnon_radiative));
```



This page is intentionally left blank.

Bibliography

- [Aig11] Laboratoire Pierre Aigrain. *How a CCD Works*. <http://www.lpa.ens.fr/spip/spip.php?article256> (accessed 7 March 2011).
- [Ang06] P. Anger, P. Bharadwaj and L. Novotny. *Enhancement and Quenching of Single-Molecule Fluorescence*. Phys. Rev. Lett. **96**, 113002 (2006).
- [Ash76] N. W. Ashcroft and N. D. Mermin. *Solid State Physics*. Cengage Learning Services (1976).
- [Asl05] K. Aslan, Z. Leonenko, J. R. Lakowicz and C. D. Geddes. *Annealed Silver-Island Films for Applications in Metal-Enhanced Fluorescence: Interpretation in Terms of Radiating Plasmons*. J. Fluoresc. **15**, 643 (2005).
- [Bad90] R. D. Badley, W. T. Ford, F. J. McEnroe and R. A. Assink. *Surface Modification of Colloidal Silica*. Langmuir **6**, 792 (1990).
- [Bag06] R. P. Bagwe, L. R. Hilliard and W. Tan. *Surface Modification of Silica Nanoparticles to Reduce Aggregation and Nonspecific Binding*. Langmuir **22**, 4357 (2006).
- [Ban99] U. Banin, M. Bruchez, A. P. Alivisatos, T. Ha, S. Weiss and D. S. Chemla. *Evidence for a Thermal Contribution to Emission Intermittency in Single CdSe/CdS Core/Shell Nanocrystals*. J. Chem. Phys. **110**, 1195 (1999).
- [Ban04] U. Banin and O. Millo. *Optical and Tunneling Spectroscopy of Semiconductor Nanocrystal Quantum Dots*. In V. I. Klimov, Editor, *Semiconductor and Metal Nanocrystals*. Marcel Dekker (2004).
- [Bar98] W. L. Barnes. *Fluorescence near Interfaces: the Role of Photonic Mode Density*. J. Mod. Opt. **45**, 661 (1998).
- [Bat02] D. Battaglia and X. Peng. *Formation of High Quality InP and InAs Nanocrystals in a Noncoordinating Solvent*. Nano Lett. **2**, 1027 (2002).
- [Baw92] M. G. Bawendi, P. J. Carroll, W. L. Wilson and L. E. Brus. *Luminescence Properties of CdSe Quantum Crystallites: Resonance between Interior and Surface Localized States*. J. Chem. Phys. **96**, 946 (1992).
- [Bea11] M. C. Beard. *Multiple Exciton Generation in Semiconductor Quantum Dots*. J. Phys. Chem. Lett. **2**, 1282 (2011).
- [Bec99] C. Beck, W. Härtl and R. Hempelmann. *Covalent Surface Functionalization and Self-Organization of Silica Nanoparticles*. Angew. Chem. Int. Ed. **38**, 1297 (1999).
- [Bec05] W. Becker. *Advanced Time-Correlated Single Photon Counting Techniques*. Springer (2005).
- [Bha09] P. Bharadwaj, B. Deutsch and L. Novotny. *Optical Antennas*. Adv. Opt. Photon. **1**, 438 (2009).
- [Bie06] A. Biebricher, M. Sauer and P. Tinnefeld. *Radiative and Nonradiative Rate Fluctuations of Single Colloidal Semiconductor Nanocrystals*. J. Phys. Chem. B **110**, 5174 (2006).
- [Boh83] C. F. Bohren and D. R. Huffman. *Absorption and Scattering of Light by Small Particles*. John Wiley & Sons, New York (1983).
- [Bor99] M. Born and E. Wolf. *Principles of Optics*. Cambridge (1999).
- [Bro00] K. R. Brown, D. G. Walter and M. J. Natan. *Seeding of Colloidal Au Nanoparticle Solutions. 2. Improved Control of Particle Size and Shape*. Chem. Mater. **12**, 306 (2000).
- [Bro04] X. Brokmann, L. Coolen, M. Dahan and J. P. Hermier. *Measurement of the Radiative and Nonradiative Decay Rates of Single CdSe Nanocrystals through a Controlled Modification of their Spontaneous Emission*. Phys. Rev. Lett. **93**, 107403 (2004).
- [Bru84] L. E. Brus. *Electron-Electron and Electron-Hole Interactions in Small*

- Semiconductor Crystallites: The Size Dependence of the Lowest Excited Electronic State.* J. Chem. Phys. **80**, 4403 (1984).
- [Bru94] M. Brust, M. Walker, D. Bethell, D. J. Schiffrin and R. Whyman. *Synthesis of Thiol-derivatised Gold Nanoparticles in a Two-phase Liquid-Liquid System.* J. Chem. Soc., Chem. Commun. 801–802 (1994).
- [Bry88] G. W. Bryant. *Excitons in Quantum Boxes: Correlation Effects and Quantum Confinement.* Phys. Rev. B **37**, 8763 (1988).
- [BS05] M. N. Berberan-Santos, E. N. Bodunov and B. Valeur. *Mathematical Functions for the Analysis of Luminescence Decays with Underlying Distributions 1. Kohlrausch Decay Function (Stretched Exponential).* Chem. Phys. **315**, 171 (2005).
- [Cal05] M. Califano, A. Franceschetti and A. Zunger. *Temperature Dependence of Excitonic Radiative Decay in CdSe Quantum Dots: The Role of Surface Hole Traps.* Nano Lett. **5**, 2360 (2005).
- [Cal07] M. Califano, A. Franceschetti and A. Zunger. *Lifetime and Polarization of the Radiative Decay of Excitons, Biexcitons, and Trions in CdSe Nanocrystal Quantum Dots.* Phys. Rev. B **75**, 115401 (2007).
- [Cha75] R. R. Chance, A. H. Miller, A. Prock and R. Silbey. *Fluorescence and Energy Transfer near Interfaces: the Complete and Quantitative Description of the Eu^{+3} /Mirror Systems.* J. Chem. Phys. **63**, 1589 (1975).
- [Cha78] R. R. Chance, A. Prock and R. Silbey. *Molecular Fluorescence and Energy Transfer near Interfaces.* Adv. Chem. Phys. **37**, 1 (1978).
- [Cha07] J.-Y. Chang, S.-R. Wang and C.-H. Yang. *Synthesis and Characterization of CdTe/CdS and CdTe/CdSe Core/Shell Type-II Quantum Dots in a Noncoordinating Solvent.* nanotechnology **18**, 345602 (2007).
- [Che86] N. Chestnoy, T. D. Harris, R. Hull and L. E. Brus. *Luminescence and Photophysics of Cadmium Sulfide Semiconductor Clusters: the Nature of the Emitting Electronic State.* J. Phys. Chem. **90**, 3393 (1986).
- [Che08] Y. Chen, J. Vela, H. Htoon, J. L. Casson, D. J. Werder, D. A. Bussian, V. I. Klimov and J. A. Hollingsworth. *"Giant" Multishell CdSe Nanocrystal Quantum Dots with Suppressed Blinking.* J. Am. Chem. Soc. **130**, 5026 (2008).
- [Cho07] M. H. Chowdhury, S. K. Gray, J. Pond, C. D. Geddes, K. Aslan and J. R. Lakowicz. *Computational Study of Fluorescence Scattering by Silver Nanoparticles.* J. Opt. Soc. Am. B **24**, 2259 (2007).
- [Cho08] M. H. Chowdhury, J. Pond, S. K. Gray and J. R. Lakowicz. *Systematic Computational Study of the Effect of Silver Nanoparticle Dimers on the Coupled Emission from Nearby Fluorophores.* J. Phys. Chem. C **112**, 11236 (2008).
- [Chr71] N. E. Christensen and B. O. Seraphin. *Relativistic Band Calculation and the Optical Properties of Gold.* Phys. Rev. B **4**, 3321 (1971).
- [Chu03] I. Chung, K. T. Shimizu and M. G. Bawendi. *Room Temperature Measurements of the 3D Orientation of Single CdSe Quantum Dots Using Polarization Microscopy.* Proc. Natl. Acad. Sci. U.S.A. **100**, 405 (2003).
- [Cic07] F. Cichos, C. von Borczyskowski and M. Orrit. *Power-Law Intermittency of Single Emitters.* Curr. Op. Coll. Int. Scie. **12**, 272 (2007).
- [Cox86] I. J. Cox and C. J. R. Sheppard. *Information Capacity and Resolution in an Optical System.* J. Opt. Soc. Am. A **3**, 1152 (1986).
- [Cro10] C. H. Crouch, O. Sauter, X. Wu, R. Purcell, C. Querner, M. Drndic and M. Pelton. *Facts and Artifacts in the Blinking Statistics of Semiconductor Nanocrystals.* Nano Lett. **10**, 1692 (2010).
- [Dab97] B. O. Dabbousi, J. Rodriguez-Viejo, F. V. Mikulec, J. R. Heine, H. Matoussi, R. Ober, K. F. Jensen and

- M. G. Bawendi. *(CdSe)ZnS Core-Shell Quantum Dots: Synthesis and Characterization of a Size Series of Highly Luminescent Nanocrystallites*. J. Phys. Chem. B **101**, 9463 (1997).
- [Dan04] M.-C. Daniel and D. Astruc. *Gold Nanoparticles: Assembly, Supramolecular Chemistry, Quantum-Size-Related Properties, and Applications toward Biology, Catalysis, and Nanotechnology*. Chem. Rev. **104**, 293 (2004).
- [Dar05] M. Darbandi, R. Thomann and T. Nann. *Single Quantum Dots in Silica Spheres by Microemulsion Synthesis*. Chem. Mater. **17**, 5720 (2005).
- [Dem08] S. Dembski, C. Graf, T. Krüger, U. Gbureck, A. Ewald, A. Bock and E. Rühl. *Photoactivation of CdSe/ZnS Quantum Dots Embedded in Silica Colloids*. Small **4**, 1516 (2008).
- [Don09] C. d. M. Donega and R. Koole. *Size Dependence of the Spontaneous Emission Rate and Absorption Cross Section of CdSe and CdTe Quantum Dots*. J. Phys. Chem. C **113**, 6511 (2009).
- [Doo03] S. Doose. *Single-Molecule Characterization of Photophysical and Colloidal Properties of Biocompatible Quantum Dots*. Ruprecht-Karls-Universität Heidelberg PhD thesis (2003).
- [Dra94] B. T. Draine and P. J. Flatau. *Discrete Dipole Approximation for Scattering Calculations*. J. Opt. Soc. Am. A **11**, 1491 (1994).
- [Dra00] B. T. Draine. *The Discrete Dipole Approximation for Light Scattering by Irregular Targets*. In M. I. Mishchenko, J. W. Hovenier and L. D. Travis, Editoren, *Light Scattering by Nonspherical Particles: Theory, Measurements, and Geophysical Applications*, 131–145. Academic Press, New York (2000).
- [Dre70a] K. H. Drexhage. *Influence of a Dielectric Interface on Fluorescence Decay Time*. J. Luminesc. **1-2**, 693 (1970).
- [Dre70b] K. H. Drexhage. *Monomolecular Layers and Light*. Sci. Am. **222**, 108 (1970).
- [Dre74] K. H. Drexhage. *Interactions of Light with Monomolecular Dye Layers*. In E. Wolf, Editor, *Progress in Optics*, Volume XII, 165–232. North-Holland, Amsterdam (1974).
- [Dre03] M. Dressel and G. Grüner. *Electrodynamics of Solids*. Cambridge (2003).
- [Dul02] E. Dulkeith, A. C. Morteani, T. Niedereichholz, T. A. Klar and J. Feldmann. *Fluorescence Quenching of Dye Molecules near Gold Nanoparticles: Radiative and Nonradiative Effects*. Phys. Rev. Lett. **89**, 203002 (2002).
- [Dul04] E. Dulkeith. *Optische Charakterisierung von Hybridsystemen aus Gold Nanopartikeln und Farbstoffmolekülen*. Dissertation, Ludwig-Maximilians-Universität München (2004).
- [Ebe02] Y. Ebenstein, T. Mokari and U. Banin. *Fluorescence Quantum Yield of CdSe/ZnS Nanocrystals Investigated by Correlated Atomic-Force and Single-Particle Fluorescence Microscopy*. Appl. Phys. Lett. **80**, 4033 (2002).
- [Efr82] Al. L. Efros and A. L. Efros. *Interband Absorption of Light in a Semiconductor Sphere*. Sov. Phys. Semicond. **16**, 772 (1982).
- [Efr95] A. L. Efros, V. A. Kharchenko and M. Rosen. *Breaking the Phonon Bottleneck in Nanometer Quantum Dots: Role of Auger-Like Processes*. Solid State Commun. **93**, 281 (1995).
- [Efr96] Al. L. Efros, M. Rosen, M. Kuno, M. Nirmal, D. J. Norris and M. G. Bawendi. *Band-edge Exciton in Quantum Dots of Semiconductors with a Degenerate Valence Band: Dark and Bright Exciton States*. Phys. Rev. B **54**, 4843 (1996).
- [Efr97] Al. L. Efros and M. Rosen. *Random Telegraph Signal in the Photoluminescence Intensity of a Single Quantum Dot*. Phys. Rev. Lett. **78**, 1110 (1997).
- [Efr00] Al. L. Efros and M. Rosen. *The Electronic Structure of Semiconductor Nanocrystals*. Annu. Rev. Mater. Sci. **30**, 475 (2000).

References

- [Efr04] Al. L. Efros. *Fine Structure and Polarization Properties of Band-Edge Excitons in Semiconductor Nanocrystals*. In V. I. Klimov, Editor, *Semiconductor and Metal Nanocrystals*. Marcel Dekker (2004).
- [Emp96] S. A. Empedocles, D. J. Norris and M. G. Bawendi. *Photoluminescence Spectroscopy of Single CdSe Nanocrystallite Quantum Dots*. Phys. Rev. Lett. **77**, 3873 (1996).
- [Emp99] S. A. Empedocles, R. Neuhauser and M. G. Bawendi. *Three-dimensional Orientation Measurements of Symmetric Single Chromophores Using Polarization Microscopy*. Nature **399**, 126 (1999).
- [Far57] M. Faraday. *Experimental Relations of Gold (and Other Metals) to Light*. Philos. Trans. R. Soc. London **147**, 145 (1857).
- [Fis04] B. R. Fisher, H.-J. Eisler, N. E. Stott and M. G. Bawendi. *Emission Intensity Dependence and Single-Exponential Behavior in Single Colloidal Quantum Dot Fluorescence Lifetimes*. J. Phys. Chem. B **108**, 143 (2004).
- [FL09] C. Fernández-López, C. Mateo-Mateo, R. A. Álvarez Puebla, J. Pérez-Juste, I. Pastoriza-Santos and L. M. Liz-Marzán. *Highly Controlled Silica Coating of PEG-Capped Metal Nanoparticles and Preparation of SERS-Encoded Particles*. Langmuir **25**, 13894 (2009).
- [For84] G. W. Ford and W. H. Weber. *Electromagnetic Interactions of Molecules with Metal Surfaces*. Phys. Rep. **113**, 195 (1984).
- [Fra08] P. Frantsuzov, M. Kuno, B. Janko and R. A. Marcus. *Universal Emission Intermittency in Quantum Dots, Nanorods and Nanowires*. Nature Phys. **4**, 519 (2008).
- [Fre73] G. Frens. *Controlled Nucleation for the Regulation of the Particle Size in Monodisperse Gold Suspensions*. Nature: Phys. Sci. 20–22 (1973).
- [G06] D. E. Gómez, M. Califano and P. Mulvaney. *Optical Properties of Single Semiconductor Nanocrystals*. Phys. Chem. Chem. Phys. **8**, 4989 (2006).
- [Gap98] S. V. Gaponenko. *Optical Properties of Semiconductor Nanocrystals*. Cambridge (1998).
- [Ged10] C. D. Geddes. *Metal-Enhanced Fluorescence*. John Wiley & Sons, Inc. (2010).
- [Gen80] L. Genzel and U. Kreibig. *Dielectric Function and Infrared Absorption of Small Metall Particles*. Z. Physik B **37**, 93 (1980).
- [Ger80] J. Gersten and A. Nitzan. *Electromagnetic Theory of Enhanced Raman Scattering by Molecules Adsorbed on Rough Surfaces*. J. Chem. Phys. **73**, 3023 (1980).
- [Ger81a] J. Gersten and A. Nitzan. *Mathematical Appendix to Spectroscopic Properties of Molecules Interacting with Small Dielectric Particles*. J. Chem. Phys. **75**, 1139 (1981).
- [Ger81b] J. Gersten and A. Nitzan. *Spectroscopic Properties of Molecules Interacting with Small Dielectric Particles*. J. Chem. Phys. **75**, 1139 (1981).
- [Ger01] D. Gerion, F. Pinaud, S. C. Williams, W. J. Parak, D. Zanchet, S. Weiss and A. P. Alivisatos. *Synthesis and Properties of Biocompatible Water-Soluble Silica-Coated CdSe/ZnS Semiconductor Quantum Dots*. J. Phys. Chem. B **105**, 8861 (2001).
- [Gha08] A. Ghatak and K Thyagarajan. *An Introduction to Fiber Optics*. Cambridge (2008).
- [Gho07] S. K. Ghosh and T. Pal. *Interparticle Coupling Effect on the Surface Plasmon Resonance of Gold Nanoparticles: from Theory to Applications*. Chem. Rev. **107**, 4797 (2007).
- [Gra95] K. C. Grabar, R. G. Freeman, M. B. Hommer and M. J. Natan. *Preparation and Characterization of Au Colloid Monolayers*. Anal. Chem. **67**, 735 (1995).
- [Gu96] M. Gu. *Principles of Three-Dimensional Imaging in Confocal Microscopes*. World Scientific (1996).

- [Hö93] H. Hövel, S. Fritz, A. Hilger, U. Kreibig and M. Vollmer. *Width of Cluster Plasmon Resonances: Bulk Dielectric Functions and Chemical Interface Damping*. Phys. Rev. B **48**, 18178 (1993).
- [Hin96] M. A. Hines and P. Guyot-Sionnest. *Synthesis and Characterization of Strongly Luminescing ZnS-Capped CdSe Nanocrystals*. J. Phys. Chem. **100**, 468 (1996).
- [Hu06] M. Hu, J. Chen, Z. Y. Li, L. Au, G. V. Hartland, X. Li, M. Marquez and Y. Xia. *Gold Nanostructures: Engineering their Plasmonic Properties for Biomedical Applications*. Chem. Soc. Rev. **35**, 1084 (2006).
- [Jac99] J. D. Jackson. *Classical Electrodynamics*. Wiley (1999).
- [Jam07] J. F. James. *Spectrograph Design Fundamentals*. Cambridge (2007).
- [Jan01] N. R. Jana, L. Gearheart and C. J. Murphy. *Seeding Growth for Size Control of 5 - 40 nm Diameter Gold Nanoparticles*. Langmuir **17**, 6782 (2001).
- [Jan03] N. R. Jana. *Nanorod Shape Separation Using Surfactant Assisted Self-assembly*. Chem. Commun. 1950–1951 (2003).
- [Jin09] Y. Jin and X. Gao. *Plasmonic Fluorescent Quantum Dots*. Nat. Nanotechnol. **4**, 571 (2009).
- [Joh72] P. B. Johnson and R. W. Christy. *Optical Constants of the Noble Metals*. Phys. Rev. B **6**, 4370 (1972).
- [Jor92] J. Jortner. *Cluster Size Effects*. Z. Physik D **24**, 247 (1992).
- [Kam07] F. Kaminski, V. Sandoghdar and M. Agio. *Finite-Difference Time-Domain Modeling of Decay Rates in the Near Field of Metal Nanostructures*. J. Comput. Theor. Nanosci. **4**, 635 (2007).
- [Kat94] J. E. B. Katari, V. L. Colvin and A. P. Alivisatos. *X-ray Photoelectron Spectroscopy of CdSe Nanocrystals with Applications to Studies of the Nanocrystal Surface*. J. Phys. Chem. **98**, 4109 (1994).
- [Kaw66] A. Kawabata and R. Kubo. *Electronic Properties of Fine Metallic Particles. II. Plasma Resonance Absorption*. J. Phys. Soc. Jpn. **21**, 1765 (1966).
- [Kay88] Y. Kayanuma. *Quantum-Size Effects of Interacting Electrons and Holes in Semiconductor Microcrystals with Spherical Shape*. Phys. Rev. B **38**, 9797 (1988).
- [Kli03] V. I. Klimov. *Nanocrystal Quantum Dots: From Fundamental Photophysics to Multicolor Lasing*. Los Alamos Science **28**, 214 (2003).
- [Kob03] F. Koberling, U. Kolb, G. Philipp, I. Potapova, T. Basché and A. Mews. *Fluorescence Anisotropy and Crystal Structure of Individual Semiconductor Nanocrystals*. J. Phys. Chem. B **107**, 7463 (2003).
- [Koo08] R. Koole, M. M. van Schooneveld, J. Hilhorst, C. de Mello Donegá, D. C. Hart, A. van Blaaderen, D. Vanmaekelbergh and A. Meijerink. *On the Incorporation Mechanism of Hydrophobic Quantum Dots in Silica Spheres by a Reverse Microemulsion Method*. Chem. Mater. **20**, 2503 (2008).
- [Kum08] R. Kumar, I. Roy, T. Y. Ohulchanskyy, L. N. Goswami, A. C. Bonoiu, E. J. Bergey, K. M. Tramposch, A. Maitra and P. N. Prasad. *Covalently Dye-Linked, Surface-Controlled, and Bioconjugated Organically Modified Silica Nanoparticles as Targeted Probes for Optical Imaging*. ACS Nano **2**, 449 (2008).
- [Kun00] M. Kuno, D. P. Fromm, H. F. Hamann, A. Gallagher and D. J. Nesbitt. *Nonexponential "Blinking" Kinetics of Single CdSe Quantum Dots: A Universal Power Law Behavior*. J. Chem. Phys. **112**, 3117 (2000).
- [Kun01] M. Kuno, D. P. Fromm, H. F. Hamann, A. Gallagher and D. J. Nesbitt. *"On"/"Off" Fluorescence Intermittency of Single Semiconductor Quantum Dots*. J. Chem. Phys. **115**, 1028 (2001).
- [Kun05] M. Kuno. *Introduction to Nanoscience and Nanotechnology: A Workbook* (2005).

References

- [Lak05] J. R. Lakowicz. *Radiative Decay Engineering 5: Metal-Enhanced Fluorescence and Plasmon Emission*. Anal. Biochem. **337**, 171 (2005).
- [Lak06] J. R. Lakowicz. *Principles of Fluorescence Spectroscopy*. Springer (2006).
- [LaM50] V. K. LaMer and R. H. Dinegar. *Theory, Production and Mechanism of Formation of Monodispersed Hydrosols*. J. Am. Chem. Soc. **72**, 4847 (1950).
- [Lee09] S. F. Lee and M. A. Osborne. *Brightening, Blinking, Bluing and Bleaching in the Life of a Quantum Dot: Friend or Foe?* Chem. Phys. Chem. **10**, 2174 (2009).
- [Li93] L. Li and L. M. Davis. *Single Photon Avalanche Diode for Single Molecule Detection*. Rev. Sci. Instrum. **64**, 1524 (1993).
- [Li03] J. J. Li, Y. A. Wang, W. Guo, J. C. Keay, T. D. Mishima, M. B. Johnson and X. Peng. *Large-Scale Synthesis of Nearly Monodisperse CdSe/CdS Core/Shell Nanocrystals Using Air-Stable Reagents via Successive Ion Layer Adsorption and Reaction*. J. Am. Chem. Soc. **125**, 12567 (2003).
- [Li09] Z. Li, ö. Kurtulus, N. Fu, Z. Wang, A. Kornowski, U. Pietsch and A. Mews. *Controlled Synthesis of CdSe Nanowires by Solution-Liquid-Solid Method*. Adv. Funct. Mater. **19**, 3650 (2009).
- [Lin80] C. P. Lindsey and G. D. Patterson. *Detailed Comparison of the Williams-Watts and Cole-Davidson Functions*. J. Chem. Phys. **73**, 3348 (1980).
- [Lip90] P. E. Lippens and M. Lanoo. *Comparison between Calculated and Experimental Values of Lowest Excited Electronic State of Small CdSe Crystallites*. Phys. Rev. B **41** (1990).
- [Lu02] Y. Lu, Y. Yin, Z. Li and Y. Xia. *Synthesis and Self-Assembly of Au@SiO₂ Core-Shell Colloids*. Nano Lett. **2**, 785 (2002).
- [M05] M. Müller. *Introduction to Confocal Fluorescence Microscopy*. SPIE (2005).
- [Mad99] O. Madelung, U. Rössler and M. Schulz, Editoren. *Landolt-Börnstein, Group III Condensed Matter Numerical Data and Functional Relationships in Science and Technology*, Volume 41B: II-VI and I-VII Compounds; Semimagnetic Compounds. Springer (1999).
- [Mah08] B. Mahler, P. Spinicelli, S. Buil, X. Quelin, J. P. Hermier and B. Dubertret. *Towards non-Blinking Colloidal Quantum Dots*. Nature Mater. **7**, 659 (2008).
- [Mal01] M. A. Malik, N. Revaprasadu and P. O'Brien. *Air-Stable Single-Source Precursors for the Synthesis of Chalcogenide Semiconductor Nanoparticles*. Chem. Mater. **13**, 913 (2001).
- [Mar06] G. Margolin, V. Protasenko, M. Kuno and E. Barkai. *Power Law Blinking Quantum Dots: Stochastic and Physical Models*. Adv. Chem. Phys. **133**, 327 (2006).
- [McB20] J. W. McBain and C. S. Salmon. *Colloidal Electrolytes, Soap Solutions and Their Constitution*. J. Am. Chem. Soc. **42**, 426 (1920).
- [McG08] J. A. McGuire, J. Joo, J. M. Pietryga, R. D. Schaller and V. I. Klimov. *New Aspects of Carrier Multiplication in Semiconductor Nanocrystals*. Acc. Chem. Res. **41**, 1810 (2008).
- [McK77] A. E. McKinnon, A. G. Szabo and D. R. Miller. *The Deconvolution of Photoluminescence Data*. J. Phys. Chem. **81**, 1564 (1977).
- [Med05] I. L. Medintz, H. T. Uyeda, E. R. Goldman and H. Mattoussi. *Quantum Dot Bioconjugates for Imaging, Labelling and Sensing*. Nat. Mater. **4**, 435 (2005).
- [Mei83] M. Meier and A. Wokaun. *Enhanced Fields on Large Metal Particles: Dynamic Depolarization*. Opt. Lett. **8**, 581 (1983).
- [Mie08] G. Mie. *Beiträge zur Optik trüber Medien, speziell kolloidaler Metallösungen*. Ann. Phys. **25**, 377 (1908).
- [Min57] M. Minsky. *Microscopy Aparatus*. U.S. Patent 3013467 (1957).

- [Mir96] J. Mirmal, B. O. Dabbousi, M. G. Bawendi, J. J. Macklin, J. K. Trautman, T. D. Harris and L. E. Brus. *Fluorescence Intermittency in Single Cadmium Selenide Nanocrystals*. Nature **383**, 802 (1996).
- [Mit10] F. Mitschke. *Fiber Optics: Physics and Technology*. Springer (2010).
- [Mor74] H. Morawitz and M. R. Philpott. *Coupling of an Excited Molecule to Surface Plasmons*. Phys. Rev. B **10**, 4863 (1974).
- [Mor02] E. Moreno, D. Erni, C. Hafner and R. Vahldieck. *Multiple Multipole Method with Automatic Multipole Setting Applied to the Simulation of Surface Plasmons in Metallic Nanostructures*. J. Opt. Soc. Am. A **19**, 101 (2002).
- [Mor07] G. Morello, M. Anni, P. D. Cozzoli, L. Manna, R. Cingolani and M. De Giorgi. *Picosecond Photoluminescence Decay Time in Colloidal Nanocrystals: The Role of Intrinsic and Surface States*. J. Phys. Chem. C **111**, 10541 (2007).
- [Mos85] M. Moskovits. *Surface-Enhanced Spectroscopy*. Rev. Mod. Phys. **57**, 783 (1985).
- [Mur93] C. B. Murray, D. J. Norris and M. G. Bawendi. *Synthesis and Characterization of Nearly Monodisperse CdE (E = Sulfer, Selenium, Tellurium) Semiconductor Nanocrystallites*. J. Am. Chem. Soc. **115**, 8706 (1993).
- [Nir95] M. Nirmal, D. J. Norris, M. Kuno, M. G. Bawendi, A. L. Efros and M. Rosen. *Observation of the "Dark Exciton" in CdSe Quantum Dots*. Phys. Rev. Lett. **75**, 3728 (1995).
- [Nir96] M. Nirmal, B. O. Dabbousi, M. G. Bawendi, J. J. Macklin, J. K. Trautman, T. D. Harris and L. E. Brus. *Fluorescence Intermittency in Single Cadmium Selenide Nanocrystals*. Nature **383**, 802 (1996).
- [Nor04] D. J. Norris. *Electronic Structure in Semiconductor Nanocrystals*. In V. I. Klimov, Editor, *Semiconductor and Metal Nanocrystals*. Marcel Dekker (2004).
- [Nov97] L. Novotny, R. X. Bian and X. S. Xie. *Theory of Nanometric Optical Tweezers*. Phys. Rev. Lett. **79**, 645 (1997).
- [Nov06] L. Novotny and B. Hecht. *Principles of Nano-Optics*. Cambridge (2006).
- [Noz08] A. J. Nozik. *Multiple exciton generation in semiconductor quantum dots*. Chem. Phys. Lett. **457**, 3 (2008).
- [O'C79] D. V. O'Connor, W. R. Ware and J. C. Andre. *Deconvolution of Fluorescence Decay Curves. A Critical Comparison of Techniques*. J. Phys. Chem. **83**, 1333 (1979).
- [Oka01] T. Okamoto. *Near-Field Spectral Analysis of Metallic Beads*. In S. Kawata, Editor, *Near-Field Optics and Surface Plasmon Polaritons. Topics in Applied Physics*, Volume 81, 97–122. Springer (2001).
- [Pan08] A. Pandey and P. Guyot-Sionnest. *Slow Electron Cooling in Colloidal Quantum Dots*. Science **322**, 929 (2008).
- [Pap79] G. C. Papavassiliou. *Optical Properties of Small Inorganic and Organic Metal Particles*. Prog. Solid State Chem. **12**, 185 (1979).
- [Pat05] D. Patra, I. Gregor and J. Enderlein. *Defocused Imaging of Quantum-Dot Angular Distribution of Radiation*. Appl. Phys. Lett. **87**, 101103 (2005).
- [Paw95] J. B. Pawley. *Handbook of Biological Confocal Microscopy*. Plenum (1995).
- [Pen97] X. Peng, M. C. Schlamp, A. V. Kadavanich and A. P. Alivisatos. *Epitaxial Growth of Highly Luminescent CdSe/CdS Core/Shell Nanocrystals with Photostability and Electronic Accessibility*. J. Am. Chem. Soc. **119**, 7019 (1997).
- [Pen98] X. Peng, J. Wickham and A. P. Alivisatos. *Kinetics of II-VI and III-V Colloidal Semiconductor Nanocrystal Growth: "Focusing" of Size Distributions*. J. Am. Chem. Soc. **120**, 5343 (1998).
- [Pen01] Z. A. Peng and X. Peng. *Formation of High-Quality CdTe, CdSe, and CdS Nanocrystals Using CdO as Precursor*. J. Am. Chem. Soc. **123**, 183 (2001).

- [Phi75] M. R. Philpott. *Effect of Surface Plasmons on Transitions in Molecules*. J. Chem. Phys. **62**, 1812 (1975).
- [Phi89] A. P. Philipse and A. Vrij. *Preparation and Properties of Nonaqueous Model Dispersions of Chemically Modified, Charged Silica Spheres*. J. Colloid Interface Sci. **128**, 121 (1989).
- [Pil00] M. P. Pileni. *II-VI Semiconductors Made by Soft Chemistry: Syntheses and Optical Properties*. Catal. Today **58**, 151 (2000).
- [Pre08] O. V. Prezhdo. *Multiple Excitons and the Electron-phonon Bottleneck in Semiconductor Quantum Dots: An Ab Initio Perspective*. Chem. Phys. Lett. **460**, 1 (2008).
- [Pyy04] P. Pyykkö. *Theoretical Chemistry of Gold*. Angew. Chem. Int. Ed. **43**, 4412 (2004).
- [Qu01] L. Qu, Z. A. Peng and X. Peng. *Alternative Routes toward High Quality CdSe Nanocrystals*. Nano Lett. **1**, 333 (2001).
- [Ray71] J. W. S. Rayleigh. *On the Scattering of Light by Small Particles*. Philos. Mag. **41**, 447 (1871).
- [Ray07] J. W. S. Rayleigh. *On the Dynamical Theory of Gratings*. Proc. R. Soc. London, Ser. A **79**, 399 (1907).
- [Reg10] M. Regulacio and M.-Y. Han. *Composition-Tunable Alloyed Semiconductor Nanocrystals*. Acc. Chem. Res. **43**, 621 (2010).
- [Rei03] P. Reiss, S. Carayon, J. Bieuse and A. Pron. *Low Polydispersity Core/Shell Nanocrystals of CdSe/ZnSe and CdSe/ZnSe/ZnS Type: Preparation and Optical Studies*. Synth. Met. **139**, 649 (2003).
- [Rei09] P. Reiss, M. Protiere and L. Li. *Core/Shell Semiconductor Nanocrystals*. Small **5**, 154 (2009).
- [RF06] J. Rodríguez-Fernández, J. Pérez-Juste, F. J. García de Abajo and L. M. Liz-Marzán. *Seeded Growth of Submicron Au Colloids with Quadrupole Plasmon Resonance Modes*. Langmuir **22**, 7007 (2006).
- [Rod06] E. Roduner. *Size Matters: Why Nanomaterials are Different*. Chem. Soc. Rev. **35**, 583 (2006).
- [Rog00] A. L. Rogach, D. Nagesha, J. W. Ostlander, M. Giersig and N. A. Kotov. *"Raisin Bun" - Type Composite Spheres of Silica and Semiconductor Nanocrystals*. Chem. Mater. **12**, 2676 (2000).
- [Rog07] A. L. Rogach, T. Franzl, T. A. Klar, J. Feldmann, N. Gaponik, V. Lesnyak, A. Shavel, A. Eychmüller, Y. P. Rakovich and J. F. Donegan. *Aqueous Synthesis of Thiol-Capped CdTe Nanocrystals: State-of-the-Art*. J. Phys. Chem. C **111**, 14628 (2007).
- [Rog08] A. Rogach. *Semiconductor Nanocrystal Quantum Dots: Synthesis, Assembly, Spectroscopy and Applications*. Springer (2008).
- [Roy] Faraday Museum, The Royal Institution of Great Britain, London, U.K. .
- [Sö1] C. Sönnichsen. *Plasmons in Metal Nanostructures*. Dissertation, Ludwig-Maximilians-Universität München (2001).
- [San94] D. R. Sandison and W. W. Webb. *Background Rejection and Signal-to-Noise Optimization in Confocal and Alternative Fluorescence Microscopes*. Appl. Opt. **33**, 603 (1994).
- [San95] D. R. Sandison, D. W. Piston, R. M. Williams and W. W. Webb. *Quantitative Comparison of Background Rejection, Signal-to-Noise Ratio, and Resolution in Confocal and Full-Field Laser Scanning Microscopes*. Appl. Opt. **34**, 3576 (1995).
- [Sat10] K. D. Sattler. *Handbook of Nanophysics: Nanoparticles and Quantum Dots*. CRC Press Inc. (2010).
- [Sch81] G. Schmid, R. Pfeil, R. Boese, F. Bandermann, S. Meyer, G. H. M. Calis and J. W. A. van der Velden. *Au₅₅[P(C₆H₅)₃]₁₂Cl₆ - ein Goldcluster ungewöhnlicher Größe*. Chem. Ber. **114**, 3634 (1981).

- [Sch86] G. Schmid and N. Klein. *Novel Modifications of Gold, Rhodium, and Ruthenium- M_{13} Clusters as Building Blocks of "Superclusters"*. *Angew. Chem. Int. Ed. Engl.* **25**, 922 (1986).
- [Sch87] G. Schmid. *Von Metallclustern und Clustermetallen*. *Nachr. Chem. Tech. Lab.* **35**, 249 (1987).
- [Sch94] D. Schooss, A. Mews, A. Eychmüller and H. Weller. *Quantum-Dot Quantum Well CdS/HgS/CdS: Theory and Experiment*. *Phys. Rev. B* **49**, 17072 (1994).
- [Sch02] G. Schlegel, J. Bohnenberger, I. Potapova and A. Mews. *Fluorescence Decay Time of Single Semiconductor Nanocrystals*. *Phys. Rev. Lett.* **88**, 137401 (2002).
- [Sch04] G. Schmid. *Nanoparticles: From Theory to Application*. Wiley-VCH, Weinheim (2004).
- [Sch05] R. Schuster, M. Barth, A. Gruber and F. Cichos. *Defocused Wide Field Fluorescence Imaging of Single CdSe/ZnS Quantum Dots*. *Chem. Phys. Lett.* **413**, 280 (2005).
- [Sch06] O. Schöps, N. L. Thomas, U. Woggon and M. V. Artemyev. *Recombination Dynamics of CdTe/CdS Core-Shell Nanocrystals*. *J. Phys. Chem. B* **110**, 2074 (2006).
- [Sha07] V. M. Shalaev and S. Kawata. *Nanophotonics with Surface Plasmons*. Elsevier (2007).
- [Shi01] K. T. Shimizu, R. G. Neuhauser, C. A. Leatherdale, S. A. Empedocles, W. K. Woo and M. G. Bawendi. *Blinking Statistics in Single Semiconductor Nanocrystal Quantum Dots*. *Phys. Rev. B* **63**, 205316 (2001).
- [Smi09] A. M. Smith, A. M. Mohs and S. M. Nie. *Tuning the Optical and Electronic Properties of Colloidal Nanocrystals by Lattice Strain*. *Nat. Nanotechnol.* **4**, 56 (2009).
- [Smi10] A. M. Smith and S. Nie. *Semiconductor Nanocrystals: Structure, Properties, and Band Gap Engineering*. *Acc. Chem. Res.* **43**, 190 (2010).
- [Som49] A. Sommerfeld. *Partial Differential Equations of Physics*. Academic Press, New York (1949).
- [Spi09] P. Spinicelli, S. Buil, X. Quélin, B. Mahler, B. Dubertret and J.-P. Hermier. *Bright and Grey States in CdSe-CdS Nanocrystals Exhibiting Strongly Reduced Blinking*. *Phys. Rev. Lett.* **102**, 136801 (2009).
- [Ste05a] F. D. Stefani, W. Knoll and M. Kreiter. *Quantification of Photoinduced and Spontaneous Quantum-Dot Luminescence Blinking*. *Phys. Rev. B* **72**, 125304 (2005).
- [Ste05b] F. D. Stefani, X. Zhong, W. Knoll, M. Han and M. Kreiter. *Memory in Quantum-Dot Photoluminescence Blinking*. *New J. Phys.* **7**, 197 (2005).
- [Ste09] F. D. Stefani, J. P. Hoogenboom and E. Barkai. *Beyond Quantum Jumps: Blinking Nanoscale Light Emitters*. *Phys. Today* 34–39 (2009).
- [Sug87] T. Sugimoto. *Preparation of Monodispersed Colloidal Particles*. *Adv. Colloid Interf. Sci.* **28**, 65 (1987).
- [Sve09] V. K. Svetlana, S. K. Dmitri and V. P. Oleg. *Breaking the Phonon Bottleneck in PbSe and CdSe Quantum Dots: Time-Domain Density Functional Theory of Charge Carrier Relaxation*. *ACS Nano* **3**, 93 (2009).
- [Taf00] A. Taflove and S. C. Hagness. *Computational Electrodynamics: The Finite-Difference Time-Domain Method*. Artech House, Boston (2000).
- [Tal04] D. V. Talapin, I. Mekis, S. Götzinger, A. Kornowski, O. Benson and H. Weller. *CdSe/CdS/ZnS and CdSe/ZnSe/ZnS Core-Shell-Shell Nanocrystals*. *J. Phys. Chem. B* **108**, 18826 (2004).
- [Tan05] J. Tang and R. A. Marcus. *Diffusion-Controlled Electron Transfer Processes and Power-Law Statistics of Fluorescence Intermittency of Nanoparticles*. *Phys. Rev. Lett.* **95**, 107401 (2005).
- [Tur51] J. Turkevich, P. C. Stevenson and J. Hillier. *A Study of the Nucleation*

- and Growth Processes in the Synthesis of Colloidal Gold*. Discuss. Faraday Soc. **11**, 55 (1951).
- [Und01] D. F. Underwood, T. Kippeny and S. J. Rosenthal. *Ultrafast Carrier Dynamics in CdSe Nanocrystals Determined by Femtosecond Fluorescence Upconversion Spectroscopy*. J. Phys. Chem. B **105**, 436 (2001).
- [Ura01] J. Urayama, T. B. Norris, J. Singh and P. Bhattacharya. *Observation of Phonon Bottleneck in Quantum Dot Electronic Relaxation*. Phys. Rev. Lett. **86**, 4930 (2001).
- [vD05] A. F. van Driel, G. Allan, C. Delerue, P. Lodahl, W. L. Vos and D. Vanmaekelbergh. *Frequency-Dependent Spontaneous Emission Rate from CdSe and CdTe Nanocrystals: Influence of Dark States*. Phys. Rev. Lett. **95**, 236804 (2005).
- [vD07] A. F. van Driel, I. S. Nikolaev, P. Vergeer, P. Lodahl, D. Vanmaekelbergh and W. L. Vos. *Statistical Analysis of Time-Resolved Emission from Ensembles of Semiconductor Quantum Dots: Interpretation of Exponential Decay Models*. Phys. Rev. B **75**, 035329 (2007).
- [Ver02] R. Verberk, A. M. van Oijen and Orri M. *Simple Model for the Power-Law Blinking of Single Semiconductor Nanocrystals*. Phys. Rev. B **66**, 233202 (2002).
- [vH81] A. K. van Helden, J. W. Jansen and A. Vrij. *Preparation and Characterization of Spherical Monodisperse Silica Dispersions in Nonaqueous Solvents*. J. Colloid Interface Sci. **81**, 354 (1981).
- [Vis05] R. Viswanatha, S. Sapra, T. Saha-Dasgupta and D. D. Sarma. *Electronic Structure of and Quantum Size Effect in III-V and II-VI Semiconducting Nanocrystals Using a Realistic Tight Binding Approach*. Phys. Rev. B **72**, 045333 (2005).
- [Vos09] W. L. Vos, A. F. Koenderink and I. S. Nikolaev. *Orientation-Dependent Spontaneous Emission Rates of a Two-Level Quantum Emitter in any Nanophotonic Environment*. Phys. Rev. A **80**, 053802 (2009).
- [Wan03] W. Wang, B. Gu, L. Liang and W. A. Hamilton. *Fabrication of Near-Infrared Photonic Crystals Using Highly-Monodispersed Submicrometer SiO₂ Spheres*. J. Phys. Chem. B **107**, 12113 (2003).
- [Wan04] Y. Wang, Z. Tang, M. A. Correa-Duarte, I. Pastoriza-Santos, M. Giersig, N. A. Kotov and L. M. Liz-Marzán. *Mechanism of Strong Luminescence Photoactivation of Citrate-Stabilized Water-Soluble Nanoparticles with CdSe Cores*. J. Phys. Chem. B **108**, 15461 (2004).
- [Wan09] X. Wang, X. Ren, K. Kahen, M. A. Hahn, M. Rajeswaran, S. Maccagnano-Zacher, J. Silcox, G. E. Cragg, A. L. Efros and T. D. Krauss. *Non-Blinking Semiconductor Nanocrystals*. Nature **459**, 686 (2009).
- [Wei00a] S.-H. Wei and S. B. Zhang. *Structure Stability and Carrier Localization in CdX (X=S, Se, Te) Semiconductors*. Phys. Rev. B **62**, 6944 (2000).
- [Wei00b] S.-H. Wei, S. B. Zhang and A. Zunger. *First-Principles Calculation of Band Offsets, Optical Bowings, and Defects in CdS, CdSe, CdTe, and their Alloys*. J. Appl. Phys. **87**, 1304 (2000).
- [Wei08] O. Weichold, B. Tigges, M. Bertmer and M. Möller. *A Comparative Study on the Dispersion Stability of Aminofunctionalised Silica Nanoparticles Made from Sodium Silicate*. J. Colloid Interface Sci. **324**, 105 (2008).
- [Wes88] A. R. West. *Basic Solid State Chemistry*. Wiley (1988).
- [Wik11] Wikipedia. *Cauchy Distribution*. http://en.wikipedia.org/wiki/Cauchy_distribution (accessed 18 March 2011).
- [Wui04] S. F. Wuister, C. d. M. Donega and A. Meijerink. *Local-Field Effects on the Spontaneous Emission Rate of CdTe and CdSe Quantum Dots in Dielectric Media*. J. Chem. Phys. **121**, 4310 (2004).

-
- [Xie05] R. Xie, U. Kolb, J. Li, T. Basché and A. Mews. *Synthesis and Characterization of Highly Luminescent CdSe-Core CdS/Zn_{0.5}Cd_{0.5}S/ZnS Multishell Nanocrystals*. J. Am. Chem. Soc. **127**, 7480 (2005).
- [Yao05] J. Yao, D. R. Larson, H. D. Vishwasrao, W. R. Zipfel and W. W. Webb. *Blinking and Nonradiant Dark Fraction of Water-Soluble Quantum Dots in Aqueous Solution*. Proc. Natl. Acad. Sci. U.S.A. **102**, 14284 (2005).
- [Yee66] K. S. Yee. *Numerical Solution of Initial Boundary Value Problems Involving Maxwell's Equations in Isotropic Media*. IEEE Trans. Antennas Propag. **14**, 302 (1966).
- [Yeh92] C.-Y. Yeh, Z. W. Lu, S. Froyen and A. Zunger. *Zinc-blende - Wurtzite Polytypism in Semiconductors*. Phys. Rev. B **46**, 10086 (1992).
- [Yu02] W. W. Yu and X. Peng. *Formation of High-Quality CdS and Other II-VI Semiconductor Nanocrystals in Non-coordinating Solvents: Tunable Reactivity of Monomers*. Angew. Chem. Int. Ed. **41**, 2368 (2002).
- [Yu03a] W. W. Yu, L. Qu, W. Guo and X. Peng. *Experimental Determination of the Extinction Coefficient of CdTe, CdSe, and CdS Nanocrystals*. Chem. Mater. **15**, 2854 (2003).
- [Yu03b] W. W. Yu, Y. A. Wang and X. Peng. *Formation and Stability of Size-, Shape-, and Structure-Controlled CdTe Nanocrystals: Ligand Effects on Monomers and Nanocrystals*. Chem. Mater. **15**, 4300 (2003).
- [Zha06] K. Zhang, H. Chang, A. Fu, A. P. Alivisatos and H. Yang. *Continuous Distribution of Emission States from Single CdSe/ZnS Quantum Dots*. Nano Lett. **6**, 843 (2006).
- [Zha07a] J. Zhang, Y. Fu, M. H. Chowdhury and J. R. Lakowicz. *Metal-Enhanced Single-Molecule Fluorescence on Silver Particle Monomer and Dimer: Coupling Effect between Metal Particles*. Nano Lett. **7**, 2101 (2007).
- [Zha07b] Y. Zhang, K. Aslan and M. J. R. Preville. *Metal-Enhanced Fluorescence: Surface Plasmons can Radiate a Fluorophore's Structured Emission*. Appl. Phys. Lett. **90**, 053107 (2007).
- [Zha08] J. Z. Zhang and C. D. Grant. *Optical and Dynamic Properties of Undoped and Doped Semiconductor Nanostructures*. In G. Cao and C. J. Brinker, Editoren, *Annual Review Of Nano Research*, Volume 2, 1–61. World Scientific (2008).



This page is intentionally left blank.

Acknowledgements

I would like to express my gratitude to all those people who have made this thesis possible.

My special thanks go to Prof. Alf Mews for introducing me to the fascinating world of nanoscience and being a constant source of knowledge and support. His valuable advices and stimulating suggestions have guided me through the thesis and will always inspire me.

Thanks also go to Dr. Herbert Knepe for his help in designing and building the confocal microscope.

I would also like to thank all the other people in the University of Siegen, in particular Prof. W.H.E. Schwarz for the warm and friendly welcome and all the helps he offered during my first year in Siegen, Dipl.-Ing. Gregor Schulte, Dr. Lars Birlenbach, and Rosy Neidhardt, who were always there to help.

I am also very grateful to Dr. Tobias Kipp, whose enlightening ideas have contributed a lot to this work. Extensive and stimulating discussions with him have always been joyful.

Sincere thanks to all the collaborators without whom most of the results described in the thesis would not have been obtained. To Dr. Hua Tan for preparing some of the ideal semiconductor nanocrystal samples and gold nanoparticle films. To Prof. Luis M. Liz-Marzán, Marcin Grzelczak, and Dr. Andrés Guerrero-Martínez from Universidade de Vigo for experimental advices and providing the gold nanoparticle samples. To Dipl.-Ing. Andreas Kornowski for the HRTEM and SEM measurements and related discussions. To Dr. Zheng Li and Jelena Dimitrijević for the TEM measurements. To CAN GmbH for the semiconductor nanocrystal samples. To Zhe Wang for the semiconductor nanowire samples. To Dr. Tobias Vossmeier for helpful discussions regarding gold nanoparticles. To Michael Ijeh and Dr. Neus G. Bastus for providing me with different gold nanoparticle samples.

I would like to thank all the fellow group members for support and good working atmosphere, in particular Sandra Flessau, Sebastian Schäfer, Nadine Bohn, Zhe Wang, Jessica Völker, Natalia Reim, Jens Böttcher, Anton Myalitsin, Christian Strelow, and Dennis Franz. I would like to thank Katharyn (Katie) Fletcher for her assistance in the last part of measurements. The correction of this thesis has been done by Sandra, Sebastian, Nadine, and Katie, to whom I owe my thanks.

Last but not least, I would like to give my special thanks to my friends, my family, and my husband, whose understanding and patient love have supported me to complete this work.

This page is intentionally left blank.